

# Mechanical Testing and Finite Element Simulation of Laser-drilled TBC Systems

## Mechanische Untersuchung und Finite-Elemente-Simulation von lasergebohrten TBC-Systemen

Von der Fakultät für Maschinenwesen der Rheinisch-Westfälischen Technischen  
Hochschule Aachen zur Erlangung des akademischen Grades eines Doktors der  
Ingenieurwissenschaften genehmigte Dissertation

vorgelegt von

**Vahid Ebrahimzade Isfahani**

Berichter:

Univ.-Prof. Dr.-Ing. Lorenz Singheiser

Univ.-Prof. Dr.-Ing. Manja Krüger

Tag der mündlichen Prüfung: 29. August 2018

Diese Dissertation ist auf den Internetseiten der Universitätsbibliothek online  
verfügbar.





# Abstract

Cooling holes in gas turbine components prevent the superalloy from exposure to very high temperatures that could lead to degradation of the thermomechanical properties. There are around 100.000 cooling holes in a gas turbine, and if their quality is not sufficient, this might lead to a premature failure of the whole system. This is the main reason to optimize drilling of cooling holes. Recently, laser drilling has been used to drill such holes, since it provides a faster and more productive solution in comparison to conventional methods, such as electro discharge/chemical machining (EDM/ECM).

The behavior of laser-drilled TBC systems under thermomechanical loading has not been studied in detail in literature, which is the focus of this PhD thesis. In the current work, as an initial step to assess laser drilling effects in the as-drilled state, flat specimens were drilled with long-pulsed and ultra-short pulsed laser set-ups, and a microstructural analysis was performed to permit selection of the best laser-drilling method. In an extension of the first test series, a second set of specimens was cyclic oxidized, in order to understand the effect of thermal load on TBC adherence in the vicinity of laser drilled holes. Specimens were drilled with long-pulsed laser sources (flash lamp and fiber laser) and with different drilling modes such as percussion as well as trepanation mode. As the third step, LCF tests of specimens undrilled and laser-drilled by flash lamp laser, trepanation mode, as well as ultra-short pulsed laser at two angles,  $30^\circ$  and  $90^\circ$ , were performed at  $850^\circ\text{C}$  with different mechanical strain ranges, 0.38% and 0.67%, in order to analyze the quality of laser drilling quality on the life time and failure mechanism. Additionally, Finite Element Method (FEM) simulations were performed to improve the understanding of the experimental observations of laser-drilled TBC coated superalloy under thermal loading conditions. 3D simulations were performed to study the influence of angle of the hole as well as recast layer on the stress distribution, in order to aid further optimization of laser drilling processes. 2D FEM simulations were also performed to do a sensitivity analysis studying the effect of coefficient of thermal expansion (CTE), creep rate, elastic moduli, and TGO thickness on the stress distribution, thereby validating the experimental results.

# Zusammenfassung

Kühlluftbohrungen in Gasturbinenkomponenten schützen die Superlegierung davor, zu hohen Temperaturen ausgesetzt zu werden, die zur Degradation der thermomechanischen Eigenschaften führen können. Es gibt ungefähr 100.000 Kühlluftbohrungen in einer Gasturbine, vorzeitiges Versagen des gesamten Systems ist möglich, wenn deren Qualität im Hinblick auf Durchmesser, Gleichmäßigkeit, und Rissfreiheit der Bohrung nicht hinreichend ist. In jüngster Zeit wurde Laserbohren verwendet zur Herstellung solcher Löcher, da es eine schnelle und produktivere Lösung im Vergleich zu konventionellen Methoden darstellt, wie z.B. Funkenerosion/chemische Bearbeitung (EDM/ECM).

Das Verhalten von lasergebohrten Wärmedämmschicht-Systemen unter thermomechanischer Belastung wurde in der Literatur bisher kaum untersucht und steht daher im Fokus der Untersuchungen in der vorliegenden Promotionsschrift. In dieser Arbeit wurden Flachproben mit lang-gepulsten und Ultrakurzzeit-gepulsten Laserbohraufbauten hergestellt und Mikrostrukturanalysen durchgeführt, um die Auswahl der besten Laserbohrmethode zu identifizieren. In einer Erweiterung der ersten Testserie wurde eine zweite Probengruppe zyklisch oxidiert, um den Einfluss der thermischen Belastung auf die Wärmedämmschicht-Haftung in der Umgebung der lasergebohrten Löcher zu verstehen. Proben wurden mit lang-gepulsten Laserquellen (Blitzlampen und Faserlaser) sowohl mittels Perkussionsverfahren als auch Trepanier-Modus gebohrt. Im dritten Schritt wurden LCF-Versuche durchgeführt an Proben sowohl im ungebohrten Zustand als auch gebohrt mit Blitzlampen-Laser und Trepanierverfahren, sowie mit Ultrakurzzeit-gepulstem Laser, um den Einfluss der Qualität der Laserbohrung auf Lebensdauer und Versagensmechanismus TBC-beschichteter Superlegierungen zu analysieren. Die Proben wurden mit zwei Winkeln ( $30^\circ$  und  $90^\circ$ ) gebohrt und mit zwei mechanischen Dehnungsschwingbreiten von 0.38% und 0.67% unter LCF-Bedienungen bei  $850^\circ\text{C}$  untersucht. Zusätzlich wurden Finite Element Methode (FEM) Simulationen durchgeführt, um das Verständnis der Versagens lasergebohrter TBC-beschichteter Proben unter thermischer Belastung zu unterstützen. 3D Simulationen wurden durchgeführt, um den Einfluss des Winkels der Bohrung auf die Spannungsverteilung in der Umgebung von Bohrungen zu ermitteln. Zusätzlich wurden 2D FEM Simulationen hinsichtlich einer Sensitivitätsanalyse über den Einfluss von thermischen Ausdehnungskoeffizienten (CTE), Kriechraten, elastischen Moduli und der TGO Dicke auf die Spannungsverteilung durchgeführt, um die experimentellen Ergebnisse zu validieren.

# Contents

1	Introduction and Problem Definition . . . . .	1
2	Literature review of thermal barrier coating (TBC) systems and their material response under extreme conditions . . . . .	4
2.1	TBC systems for stationary gas turbines . . . . .	4
2.1.1	High temperature alloys for gas turbine applications . . . . .	5
2.1.2	Oxidation resistant metallic coatings for TBC systems . . . . .	10
2.1.3	Ceramic TBC layer . . . . .	12
2.2	Degradation mechanisms of TBC systems . . . . .	14
2.2.1	Oxidation of BC . . . . .	14
2.2.2	Interdiffusion between BC and superalloys . . . . .	16
2.2.3	Sintering effect in TBC systems . . . . .	16
2.2.4	Thermal fatigue of TBC-coated superalloy . . . . .	18
2.2.5	Thermomechanical Fatigue of TBC-coated superalloys . . . . .	23
2.2.5.1	LCF loading . . . . .	23
2.3	FEM simulation of TBC systems . . . . .	26
2.3.1	Fundamentals . . . . .	27
2.3.2	Stress analysis . . . . .	30
2.4	Processing of cooling holes for TBC-coated components . . . . .	34
2.4.1	Flash lamp laser . . . . .	36
2.4.2	Fiber laser . . . . .	38
2.4.3	Ultra-short pulsed (USP) laser . . . . .	39
2.4.4	Percussion and trepanation drilling . . . . .	40
3	Experimental method and FEM modelling of thermomechanical response of TBC-coated superalloy . . . . .	41
3.1	Laser drilling systems . . . . .	41
3.1.1	Flash lamp laser . . . . .	41
3.1.2	Fiber laser . . . . .	42
3.1.3	USP laser . . . . .	44
3.2	Laser drilling of TBC systems . . . . .	45
3.3	Cyclic oxidation of laser-drilled TBC systems . . . . .	46
3.4	Influence of LCF loading on life time of laser-drilled TBC systems . . . . .	49
3.4.1	Measurement of temperature gradient during LCF test at 850°C . . . . .	52
3.5	FEM simulations . . . . .	55
3.5.1	Material system . . . . .	55
3.5.2	Axisymmetric model . . . . .	56
3.5.3	Influence of cooling hole diameter under thermal loading on stress distribution at cooling hole . . . . .	59

---

3.5.4	3D FEM model . . . . .	60
4	Results and Discussion . . . . .	62
4.1	Laser drilling of TBC systems . . . . .	62
4.2	Cyclic oxidation of TBC systems . . . . .	66
4.2.1	Thermography measurements of specimens drilled with different parameters and hole angle . . . . .	66
4.2.2	Microstructure analysis of laser-drilled TBC-coated superalloy before and after cyclic oxidation tests . . . . .	68
4.2.3	Thermography measurements of specimens drilled with different diameters . . . . .	72
4.2.4	Microstructure analysis of specimens drilled with different diameters . . . . .	73
4.3	LCF testing of undrilled and laser-drilled TBC systems . . . . .	76
4.3.1	Damage analysis by microstructural investigation of LCF tests . . . . .	83
4.4	FEM results of TBC systems with cooling holes under thermomechanical loading . . . . .	95
4.4.1	Influence of angle with 3D FEM model . . . . .	95
4.4.2	Influence of hole diameter with 2D FEM model . . . . .	96
4.4.3	Influence of recast layer with 3D model . . . . .	98
4.4.4	Influence of recast layer with 2D model . . . . .	100
5	Conclusion and Outlook . . . . .	107
A	Additional Results . . . . .	111
A.1	Laser drilling of TBC systems . . . . .	111
A.2	Cyclic oxidation of laser drilled TBC systems . . . . .	112
A.2.1	Thermography measurements . . . . .	112
A.2.2	Microstructure analysis . . . . .	114
	Bibliography . . . . .	117

# Chapter 1

## Introduction and Problem Definition

Currently, the electricity demand is growing three times faster than the world's population. The need for electricity is predicted to increase by 37 % with an average annual rate of 1.1 % by 2040 [1]. Therefore, making available the necessary energy resources is a top goal of many industrial countries. Renewable energy sources play the most important role in the future. Nowadays, the use of renewable energies is increasing remarkably, which is also associated with possible fluctuations in their output, for example when wind is insufficient. Gas turbines are a good solution to this problem, since they can support the power circuit within minutes.

Using gas-fired energy power plants is much better in terms of the relatively low CO<sub>2</sub> emission in contrast to coal-dependent energy sources, which play a key role in the air pollution. It is also possible to ramp up such power plants fast, which is another important advantage.

Basically, nickel-based superalloys are used in the associated turbine components. However, they can usually function only at temperatures maximally up to 1000 °C, otherwise their high mechanical properties decrease substantially [2]. Above this temperature, Thermal Barrier Coatings (TBC) together with an oxidation protective layer typically are used, in order to increase the hot corrosion and oxidation resistance and reduce the temperature of the superalloy. As an additional cooling strategy, a portion of the compressed air is passed through approximately 100.000 cooling holes in the gas turbine components to decrease the temperature further. Such cooling holes can be drilled with Electrochemical Machining (ECM) and Electrodischarge Machining (EDM) as well as laser drilling, which is the current preferred technique. ECM and EDM drilling has to be performed before the ceramic TBC coating, that can be applied using electron beam-physical vapor deposition (EB-PVD) coating or air plasma spraying (APS), which may result in partial closure of cooling holes by powder particles. Laser drilling of cooling holes as the last processing step of TBC coated components offers economic advantages as well as design advantages to shape cooling holes according to aerodynamic design of the components. However, it has been shown that the life-time of the laser-drilled components can be reduced (6 to 9 times) compared to components without such holes [3], see Fig. 1.1, which shows the relationship between applied strain range in a LCF test and number of cycles to failure,  $N_f$ .

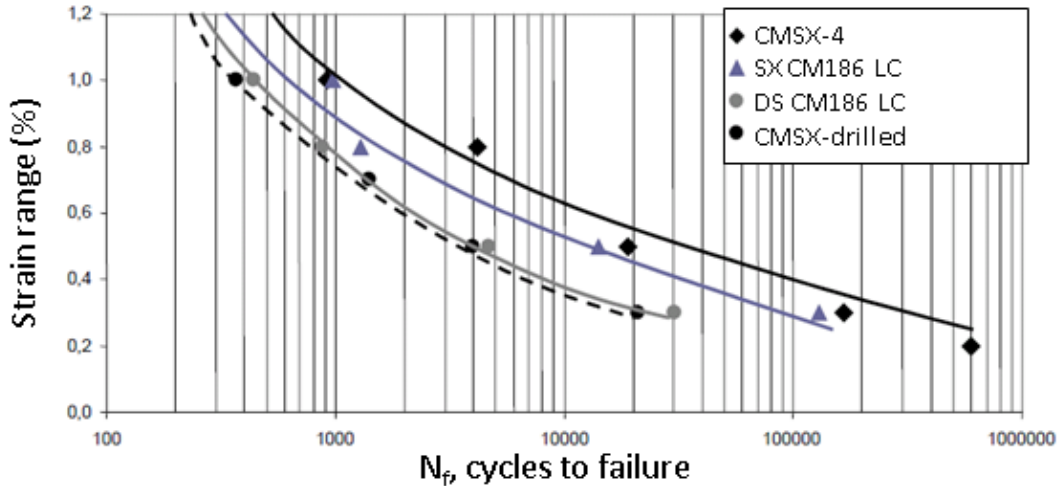


Figure 1.1: Total strain range versus cycles to failure for laser-drilled and undrilled specimens out of CMSX-4 in comparison with SX CM186 LC and DS CM186 LC [3], DS: directionally solidified, SX: single crystal.

Currently, main problems using laser drilling techniques appear to be the limited quality of cooling holes, which makes them a critical life limiting factor [3]. The limited quality of such holes is mainly related to material removal process during long-pulsed laser drilling, which is melting-dominant [4–6] and induces defects such as geometrical imperfections, recast layers, oxide layers, heat affected zone (HAZ), and cracks at interfaces and/or grain boundaries of the substrate [6]. The defect density can be affected by different laser parameters such as hole angle, trepanation/percussion drilling, peak power, assist gas, pulse frequency etc. [7–9].

Trepanation drilling, i.e. laser drilling with a circular movement of the nozzle, has been suggested in literature [10–12] as a method to provide better quality holes than percussion drilling, i.e. laser drilling with fixed movement. Trepanation can also be used to drill larger holes with good quality, as it is more similar to a conventional cutting process. However, a detailed comparison of these two drilling modes appears not to be available in literature, which is hence one of the focuses of this study.

A number of studies have aimed towards an understanding of the influence of the angle on the quality of laser-drilled holes, leaving still some questions open. Very few studies concentrated on the behavior of laser-drilled TBC systems under thermal cycling conditions [13–15]. Nonetheless, thermal cycling of laser-drilled TBC systems as well as the delamination behavior of the coating at the holes with different qualities, angles, and diameters have not been in focus so far, which is hence analyzed in this thesis as well.

Recently, new technologies of laser drilling, such as ultra-short pulsed (USP) laser [16–18], have been developed, to enhance the removal of molten material out of narrow cooling holes and to avoid crack formation at cooling holes.

In the frame of this thesis, the quality of cooling holes produced by different laser drilling methods in the Chair of Laser Technology in RWTH Aachen University will be investigated in detail by metallographic analysis of drilled as well as cyclic oxidized

coated samples, and by finite-element-method (FEM) calculation of thermal stresses around cooling holes with different diameter and inclination during thermal loading of laser-drilled TBC coated samples. FEM simulations of stress and strain development during thermal cycling extend the work of P. Bednarz et al. [23] and state of the art simulations published in literature [24–28]. All previous simulations have been performed on undrilled systems. Interpretation of the experiments on TBC systems with cooling holes require detailed information of stress and strain development around cooling holes, which will be discussed in this thesis as well. FEM simulations of laser-drilled TBC coated superalloy under LCF loading conditions was not performed, since it was not in the project plan.

The behavior of TBC systems under thermomechanical loading conditions modes has already been studied to some extent [13, 19–22]. However to our knowledge, material behavior of laser-drilled TBC systems under low cycle fatigue (LCF) conditions has not been in the focus up until now. Selected LCF experiments on undrilled and laser-drilled TBC coated components were also performed at 850°C with different strain ranges, in order to allow an enhanced understanding of the influence of application relevant loading conditions on TBC coated components.

In Chapter 2, the material behavior of the components of a TBC system is described, followed by the review of literature on the related damage mechanisms under test conditions. To get familiar with the role of laser processing on the quality of holes, details on different laser methods will be also presented. In Chapter 3, the experimental aspects such as detailed test parameters, different material systems, as well as the FEM models used in the simulations will be described. In Chapter 4, the results of the experiments as well as numerical studies will be presented and discussed. In Chapter 5, conclusions and outlook of the work will be drawn.

# Chapter 2

## Literature review of thermal barrier coating (TBC) systems and their material response under extreme conditions

### 2.1 TBC systems for stationary gas turbines

A TBC system usually consists of 3 components: a ceramic TBC, an oxidation protective layer or bond coating (BC), and a substrate. During very high temperature exposure of the BC, an oxide layer grows between TBC and BC layer, which is termed thermally grown oxide (TGO) layer, see Fig. 2.1. In this section, each of these components is described in details.

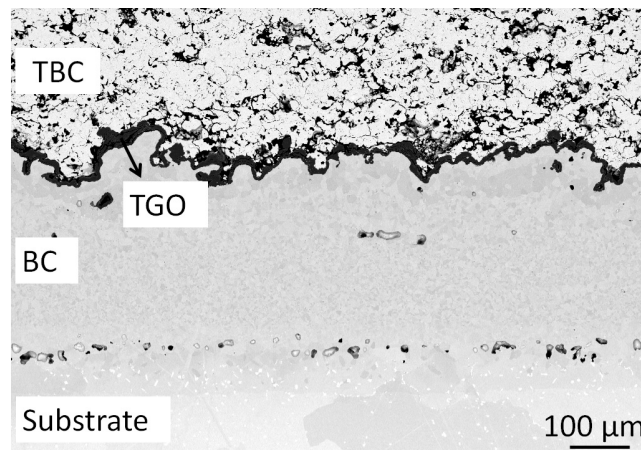


*Figure 2.1: Components of a typical TBC system consisting of a nickel-based superalloy IN 792 CC as the substrate, a MCrAlY bond coating, LCO22, and an air plasma sprayed (APS) yttria-stabilized-zirconia (YSZ) TBC, see results section 4.1 for more details.*

The top layer of a TBC system usually consists of a yttria-stabilized zirconia ceramic, with a low thermal conductivity of around 1 W/mK [19]. Typical TBC thickness can



be between 50 to 300  $\mu m$ , which results in a cooled metallic components below the TBC of around 200°C [19]. The application of the ceramic coating is either by air plasma spraying (APS) or electron beam physical vapor deposition (EB-PVD).

MCrAlY (M=Ni,Co,) bond coatings have a high oxidation resistance, mainly due to their high Al-content, which leads to a very stable, slow growing  $Al_2O_3$ -scale formation at high temperature exposure [29] that protects the superalloy from severe oxidation. They also provide a good adhesion between the superalloy and TBC.

### 2.1.1 High temperature alloys for gas turbine applications

In gas turbines, the compressor increases the pressure of the incoming air. The compressed air is then mixed with fuel and ignited. In this phase, the temperature and pressure of air is increased significantly, which causes extreme conditions for the turbine components. In modern gas turbines, the inlet temperature can be enhanced to 1350-1400 °C, whereas superalloys can only maintain their mechanical properties approximately up to 1000 °C [2]. In an environment with higher temperatures, superalloys can be damaged by various mechanisms such as fatigue, creep, hot corrosion, erosive wear, and oxidation. For this reason, materials should be used that can still maintain their properties under these extreme conditions, therefore mostly nickel-based superalloys are used for such applications. Superalloys (nickel- or cobalt-based alloys) can retain their properties up to around 80% of their melting temperature. Nickel-based superalloys consist of a stable fcc crystal structure, while the cobalt-based alloys have a hexagonal closed packed structure which can be transformed to fcc structure by adding of alloying elements. Therefore, cobalt-based superalloys have typically lower high temperature strength than the nickel-based version.

Nickel-based superalloys consist usually of Ni as basis, Cr, W, Ta,  $Y_2O_3$ , Al, Re, Pt, Ti, Nb, Si, C, Zr, B, and Y. The matrix of superalloys consists of fcc  $\gamma$ -phase including high amount of Co, Cr, Mo, W, etc [20], see Fig. 2.2a. In this matrix, the strengthening intermetallic particles  $\gamma'$  –  $Ni_3Al$  with a  $L1_2$  crystal structure (from here on, referred to as  $\gamma'$ ) are embedded [20, 30], see Fig. 2.2b.

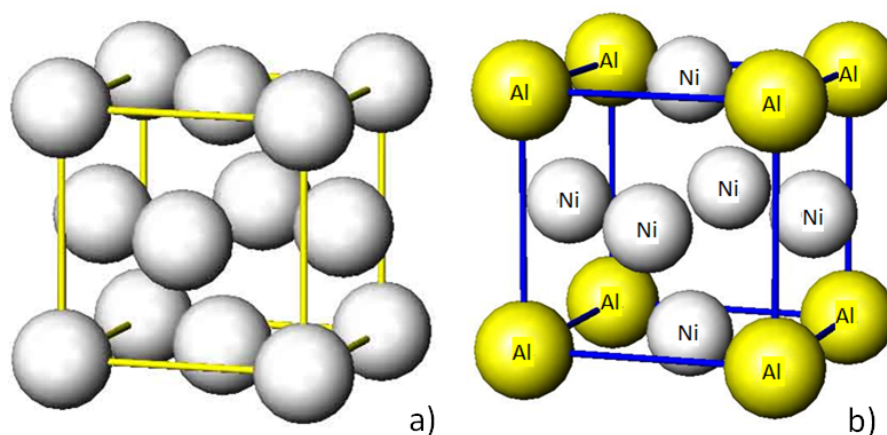


Figure 2.2: Crystal structure of a) the fcc- $\gamma$  and b) the  $\gamma'$  –  $Ni_3Al$  phase with a  $L1_2$  type structure.

Besides  $\gamma'$  phase, other factors can play also an important role in determining the strength of the superalloy, which are the alloying elements, the lower density of grain boundaries, the amount of dendrites, i.e. tree-like crystal growth during solidification of molten material [31], and the eutectics. Eutectics are mixed phases such as interdendritic  $\gamma/\gamma'$  eutectic phase, which are observed after casting process, that must be avoided with the suitable heat treatment, since they are characterized with a lower melting temperature and can accordingly lead to defects during high temperature exposure [32]. The effect of the alloying elements are categorized below [33]:

- Al and Cr are used to enhance the resistance against oxidation and corrosion.
- Al, Re, Cr, Nb, Co, Fe, Ta, Mo, and W increase the hardness of the alloy.
- C, Cr, Mo, W, Nb, Ta, and Ti increase the volume fraction of hardening carbides, especially at grain boundaries.
- Co decreases the stacking fault energy and accordingly the probability of dislocation climb.
- Co, Cr, and Fe can substitute with Ni in  $\gamma'$  phases. Ta, Nb, Ti, and Fe can substitute Al in  $\gamma'$  phase. Therefore,  $\gamma'$  phases increase in volume fraction.
- Ta, Si, Y, Al, Cr, Y, Hf, and Zr improve the corrosion properties; Ta decreases the growth rate of alumina, Si increases the internal oxidation resistance, Y provides a better oxide layer adherence, and finally Al and Cr promote to build up a corrosive protective layer based on  $\text{Al}_2\text{O}_3$  or  $\text{Cr}_2\text{O}_3$ .

The outstanding feature of  $\gamma'$  phases is its high thermally stability which is due to the coherent connection between these phases with the  $\gamma$  matrix, resulting in a low surface energy [20]. Size, shape, and distribution of  $\gamma'$  phases play an important role in determining the creep and fatigue strength of superalloys [19]. The yield strength of nickel-based superalloys hardened with  $\gamma'$  precipitates either remains relatively constant, with low to average  $\gamma'$  volume fraction, or increases up to 750 °C, with high  $\gamma'$  volume fraction. One of the reasons for such an increase in yield strength is suggested to be the increase in density of immobile cross-slip dislocations in coarse  $\gamma'$  phases [34, 35]. Above 850°C, the strength starts to decrease due to activation of slip mechanisms of dislocations in the superalloy matrix, see Fig. 2.3.

To increase the creep strength of nickel-based superalloys, two different strengthening approaches are used:

1. Precipitation hardening by  $\gamma'$ -particles with an average size of approximately 1  $\mu\text{m}$ .
2. Solid solution hardening using elements with large atom diameters such as W, Ta, Re, Ru enhances the long term creep resistance due to absence of precipitate coarsening, which is typical for  $\gamma'$ -particles.

Polycrystalline superalloys are not very suitable for rotating components of gas turbines, since cracks can be initiated from the grain boundaries perpendicular to the centrifugal forces and hence a premature failure can occur [37]. For instance, in a conventionally cast polycrystalline IN 792 superalloy, the  $\gamma'$  phase is not precipitated in the  $\gamma$  phase homogeneously after heat treatment, reducing its fatigue resistance, in contrast to single

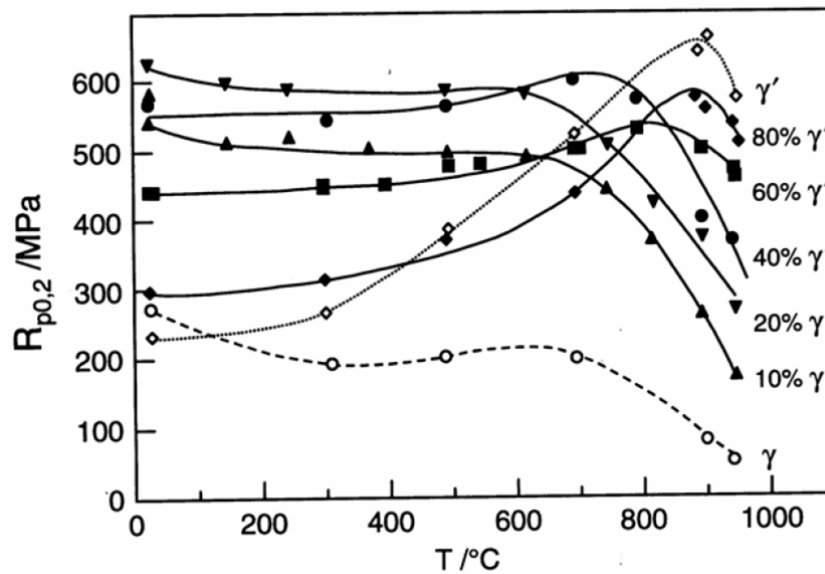


Figure 2.3: Yield strength for different  $\gamma'$ -phase volume fraction in nickel-based superalloys versus temperature [36].

crystals shown in see Fig. 2.4. The thickness of the  $\gamma'$  precipitations is about 0.5 to 10  $\mu\text{m}$  for different geometries. Elongated metal carbides will be also formed in polycrystals [38].

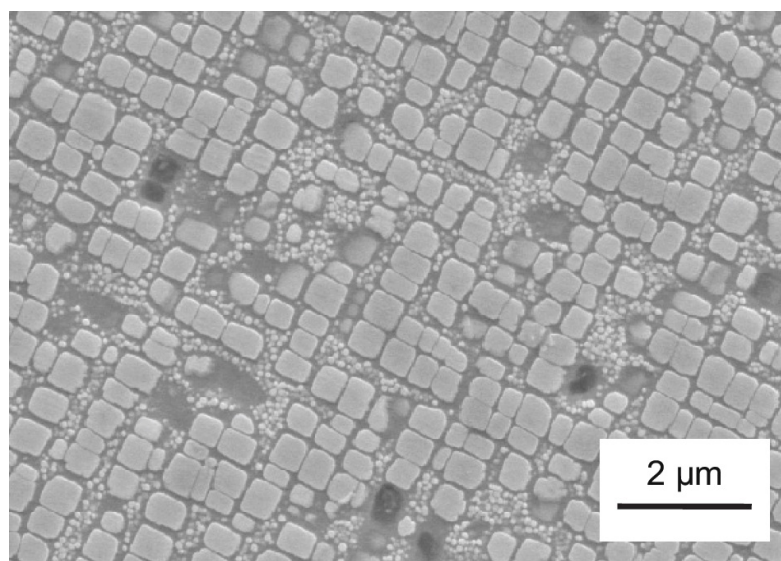


Figure 2.4: Microstructure of cubic  $\gamma'$  precipitations (in light gray) in the  $\gamma$  matrix (in dark gray) for a heat-treated IN 792 CC, image is obtained using SEM [39].

Directionally solidified (DS) substrates have columnar grains in radial or the main loading direction, which increases the life-time of the components. Such microstructures, for example in IN 792 DS, have a volume fraction of around 60% of  $\gamma'$  precipitates, whereas in a polycrystal, for example IN 738 LC (Low Carbon), it is up to 45%. In single crystals this fraction is around 80% [40]. The increase in  $\gamma'$  volume fraction in combination with

the decrease in grain boundary density in single crystals or DS superalloys, compared with polycrystals, leads to their higher creep and fatigue strength. This higher strength makes it possible to increase the turbine inlet temperature (TIT) approximately by 40°C [39].

DS microstructures are produced by pulling the mold out of the furnace, with a slow speed of around 30 cm per hour, and landing the solidification front of the molten material on a chill plate, which produces a high temperature gradient between the liquidus and solidus temperatures at the interface, Fig. 2.5 [37]. The slow movement of the material and the existing high temperature gradient results in typical long grains. On the contrary, the casting process is done with higher cooling rate for polycrystals.

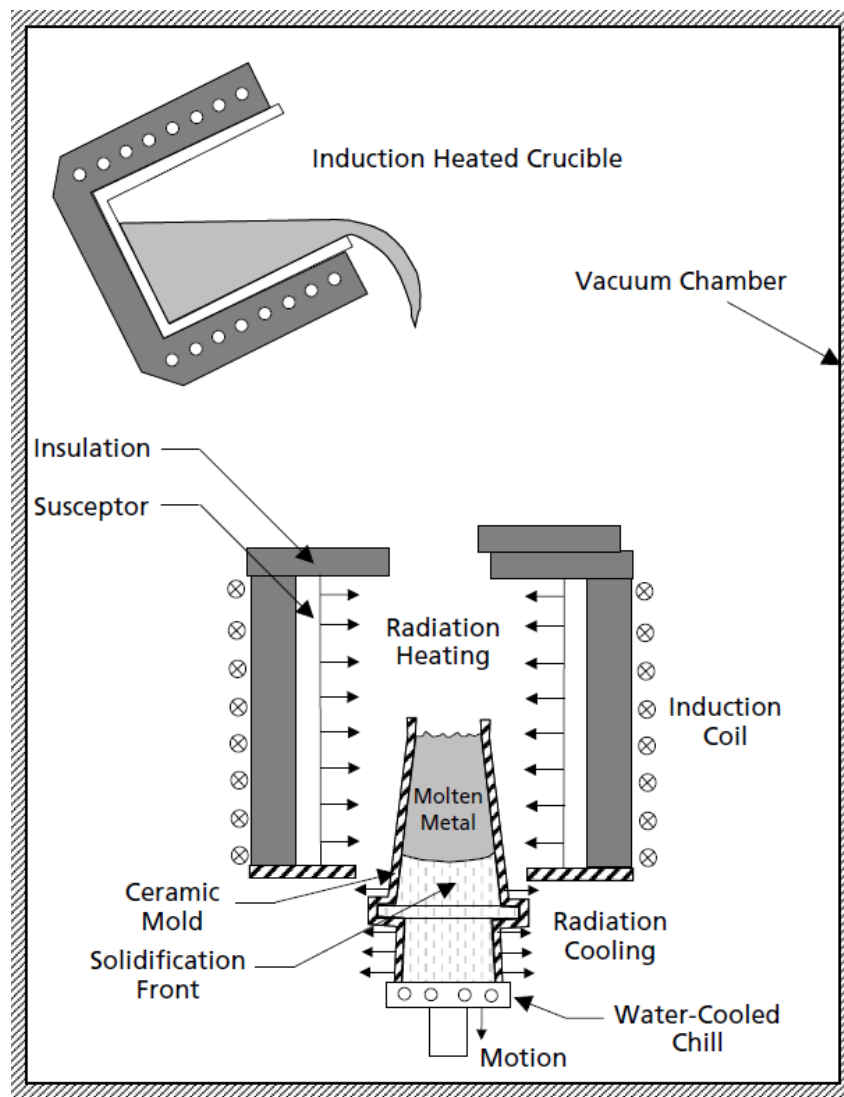


Figure 2.5: Process of directional solidification for superalloy castings [41].

For single crystals, the casting process is similar to the casting of DS alloys, where different grains nucleate and grow parallel. To produce a single crystal with defined orientation, a helical tube, the so-called pig tail, at the chill plate will be used which results in selection of a single grain with well defined orientation, see Fig. 2.6. Seeding is another method to form single crystals. In this method, a cast single crystal, so-called seed crystal, is

placed on the chill plate in order for the molten material to accept its orientation by the solidification process, see Fig. 2.6. The advantage of this method is that the orientation of the final crystal can be controlled by that of seed crystal.

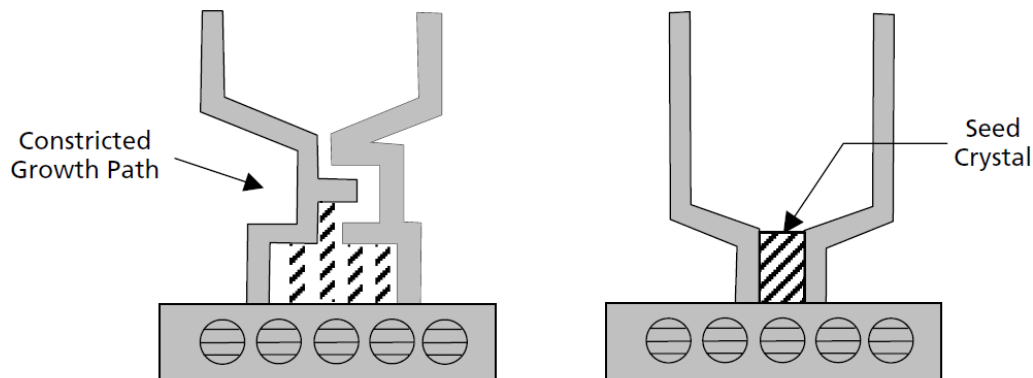


Figure 2.6: Casting of single crystal superalloys using helical tube (left figure), and seed crystal (right figure) [37].

All  $\gamma'$ -hardened alloys are heat treated after casting process. Only in few cases this step is omitted, where the amount of improvement in the mechanical properties in comparison to the heat treatment cost is not economically reasonable. Heat treatment process is performed to optimize and homogenize the chemical composition and mechanical properties [32]:

- optimization of  $\gamma'$  size and form, and its homogeneous distribution,
- precipitation of carbides at grain boundaries,
- homogeneous distribution of alloying elements in order to achieve a balanced solidus temperature,
- reduction or elimination of  $\gamma/\gamma'$  eutectics,
- releasing of residual stresses,
- retrieving of the microstructure after the coating process, as well as improving the bond between the coating and substrate,
- retrieving the goal microstructure and elimination of unnecessary precipitations after application.

Fig. 2.7 shows the dendrite structure before and after heat treatment. It can be seen that the alloying elements will be more homogeneous distributed in material after the heat treatment process. After casting, the volume fraction of  $\gamma'$  building elements are higher in interdendritic regions, which diffuse during heat treatment towards dendrites. The process consists of a step-wise heat treatment, which in comparison with a one-step process results in a more homogeneous microstructure and prevents melting of eutectic phases with low melting temperature by redistributing them. Fig. 2.7c shows the result

of the following precipitation hardening performed after solution heat treatment, which is performed to achieve a more homogeneous microstructure by further solution of  $\gamma'$  particles with relative large sizes, i.e. primary  $\gamma'$  [31].

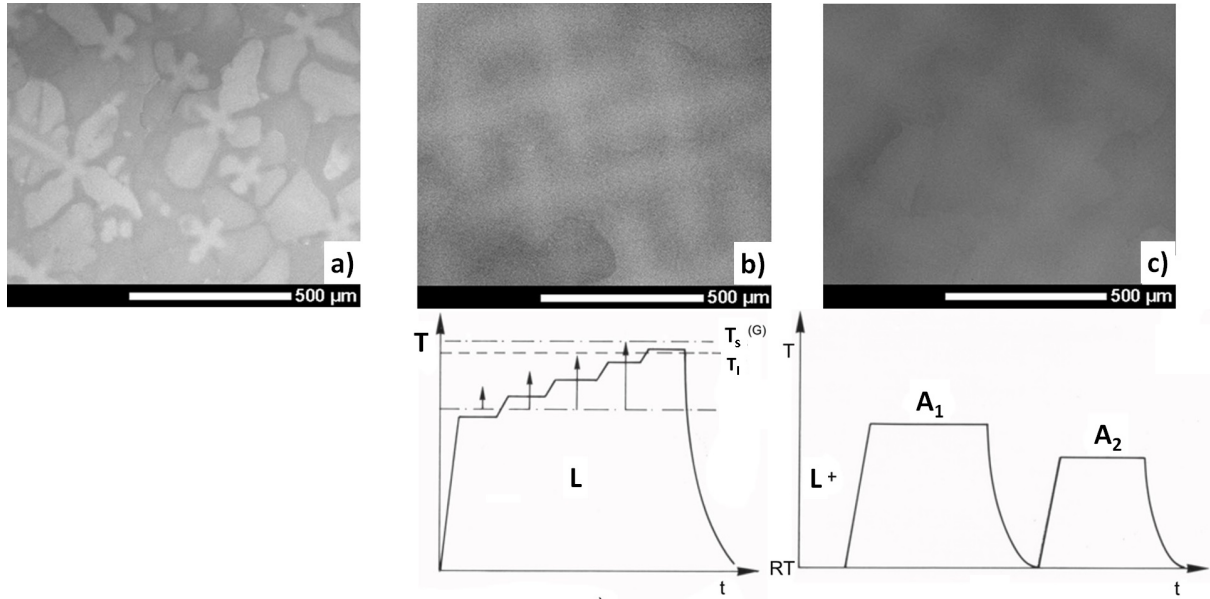


Figure 2.7: Development of the dendritic microstructure of the single crystal nickel-based superalloy CMSX-4 due to heat treatment, a) as-cast, b) solution heat treated, and c) solution heat treated and precipitation hardened leading to a more homogeneous microstructure by further solution of large  $\gamma'$  particles [31].

### 2.1.2 Oxidation resistant metallic coatings for TBC systems

The bond coating or BC is used in the TBC system to prevent oxidation and corrosion of the substrate, which can occur at extremely high temperature exposure. Responsible for the excellent oxidation resistance is the formation of a dense, slowly growing alumina scale by the appropriate Al-content in the coating. Moreover, by mechanical bonding at the rough TBC/BC interface, a good adhesion between TBC and substrate can be achieved [42, 43]. The typical material for a BC are MCrAlY (M=Ni or Co) alloys. The main typical elements in BCs are listed in Table 2.1. Addition of Y, Hf, Zr, and also recently Re provides a better oxidation resistance [44]. Yttrium results also in an improved adhesion between the oxide layer and BC [45–47].

Element	Volume fraction %
Al	8-12
Cr	15-22
Co	10-30
Y	0.2-0.5

Table 2.1: Typical element percentage in a MCrAlY BC [19].

The BC is typically deposited using electron beam physical vapor deposition (EB-PVD)



or plasma spraying in vacuum (VPS) to prevent oxidation of Al [19]. At very high temperature, for instance 1050°C or higher, the  $\beta$ -aluminum rich phases become depleted, and alumina ( $\text{Al}_2\text{O}_3$ ) will be formed at the TBC/BC interface, see Fig. 2.8b. Alumina is very stable with a slow growth rate as well as a good adhesion to the bond coating. Additionally, the BC induces a diffusion zone between itself and the substrate, which resists the vertical cracks starting at TBC/BC interface to grow further to the substrate [19], see for more details section 2.2.2. Moreover, due to the high temperature exposure during the spraying process such diffusion zone already forms [48].

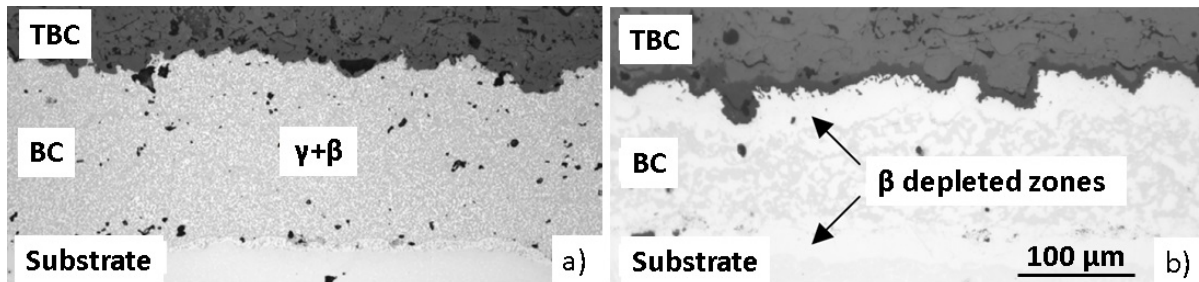


Figure 2.8: a) Typical microstructure of BC, b) formation of the dark TGO layer by exposure of the BC to extreme high temperatures. TBC system: IN 792 CC substrate, LCO22 BC, and APS TBC [19].

Typically, the elastic modulus of BC drops if temperature increases as shown in Fig. 2.9 for different types of the coating. The main characteristics of BC is its high ductility and low creep strength at high temperatures, whereas  $E$ -modulus and thermal expansion coefficient are similar to nickel-based superalloys.

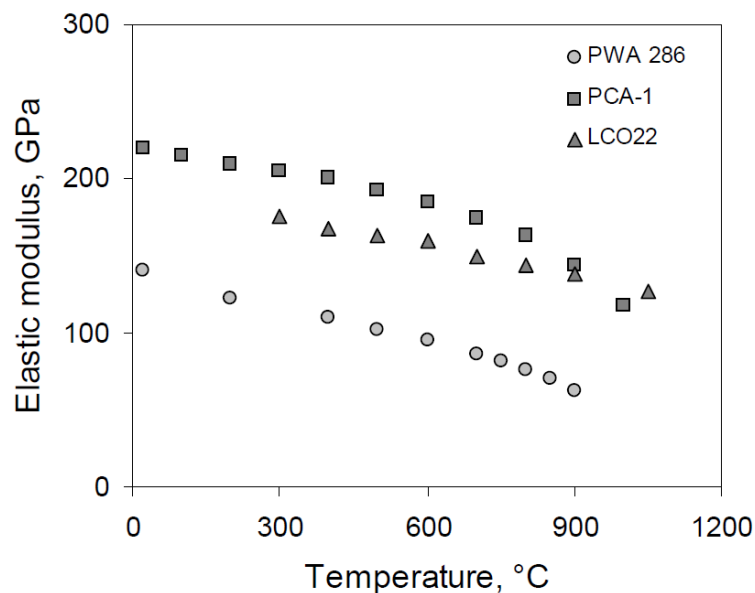


Figure 2.9: Temperature dependence of elastic modulus for three MCrAlY bond coating alloys [49–51].

The ductile-brittle transition temperature (DBTT) is determinant for strain tolerance of

the coating, which can be defined as a temperature range where fracture strain changes from relatively low (brittle material) to high (ductile material) values. DBTT depends on the composing elements and the production process of the bond coating. For example, if the concentration of Al increases, DBTT also increases, see Fig. 2.10.

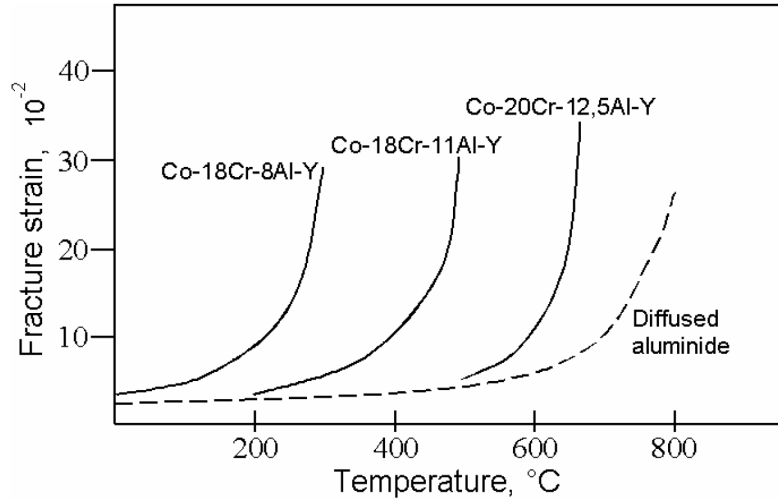


Figure 2.10: Temperature dependence of fracture strain for various bond coatings [49–51].

### 2.1.3 Ceramic TBC layer

As it was briefly mentioned in Chapter 1, a ceramic TBC is used for gas turbine components to protect the metallic parts from undergoing very high temperature exposure and the corresponding damage modes. There are basically two ways to deposit TBCs or BC layers on the substrate: air plasma spraying (APS) [52] and electron beam-physical vapor deposition (EB-PVD) [53]. In this work, TBC layers are deposited using the APS method. Fig. 2.11a shows the structure of APS TBCs. For APS TBCs, the grains have a lamellar shape with an aspect ratio of around 10:1 or more, in the direction parallel to the coating deposition plane. The intersplat cracks can be seen parallel to the coating plane, where on the contrary the intrasplat cracks are perpendicular to the interface [19]. APS TBCs, due to their large pore density and lamellar parallel structure, have the advantage of featuring a lower thermal conductivity than EB-PVD coatings, which have a columnar structure see Fig. 2.11b. However, the columnar microstructure of EB-PVD TBCs provides good strain tolerance and durability.

Among ceramic materials, zirconia ( $\text{ZrO}_2$ ) has a relatively high coefficient of thermal expansion (CTE) ( $1 \times 10^{-5} \text{K}^{-1}$ ) [55, 57], and therefore is used vastly in APS TBC systems. This results in lower thermal mismatch, i.e. lower thermal stresses. Plasma spraying of zirconia layers can be performed in air, since the powder will not be oxidized, which makes this a method of reasonable cost for large components [20]. The typical porosity of such TBC layer is in the range of 16-40 %. The microstructure of the TBC, such as porosity, depends on the velocity and temperature of the particles, which is also dependent on the spraying distance and the plasma powder [56].



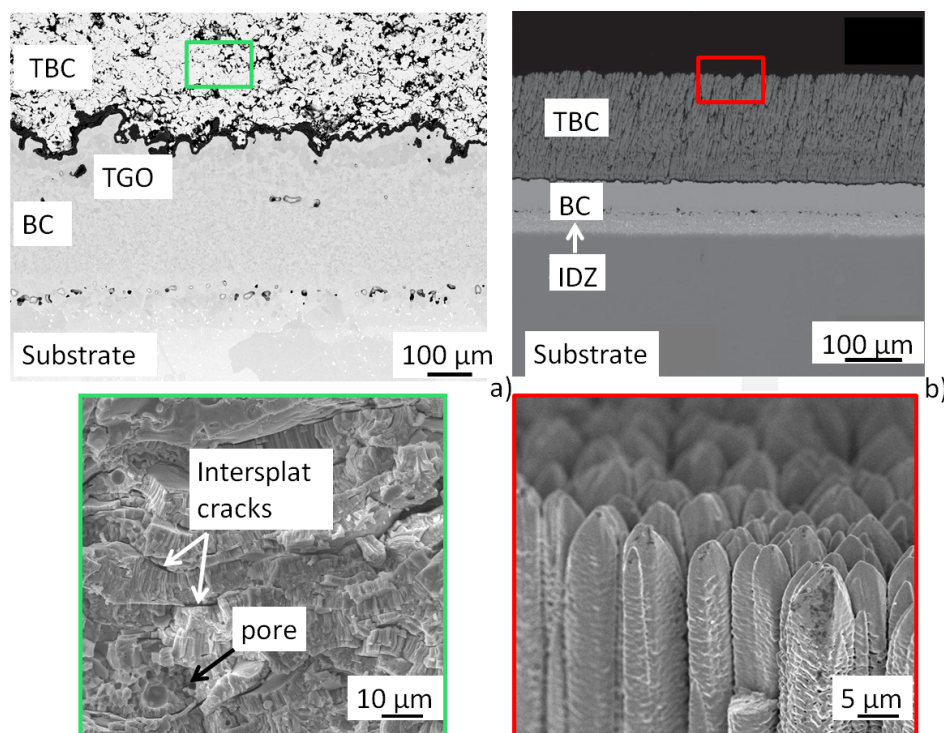


Figure 2.11: a) Lamellar microstructure of APS as well as b) columnar structure EB-PVD TBC in the as-deposited state [54, 55].

Zirconia can be found in three lattice arrangements: monoclinic (at low temperatures), tetragonal (at intermediate temperature), and cubic (at high temperatures) [58]. Tetragonal-to-monoclinic transformation at around  $1200^{\circ}\text{C}$  causes a volume change of 8 % [20], which can lead to large stresses and induce failure. To prevent such transformations several oxide additives can be used, such as  $\text{Y}_2\text{O}_3$ ,  $\text{CeO}_2$ , and  $\text{MgO}$  [59]. In a fully stabilized zirconia, the cubic phases weight percentage is 100 %, which are stable over the application-relevant temperature ranges, avoiding any phase transformation. Yttria-stabilized zirconia (YSZ) with wt. 7% experiences the longest life-time under thermal cycling conditions [59–61].

A partially stabilized zirconia with yttria ( $\text{Y}_2\text{O}_3$ ) is observed to be better than the fully stabilized with  $\text{MgO}$  or  $\text{CeO}_2$ . In a partially stabilized zirconia, monoclinic and cubic phases coexist. Tetragonal precipitation in the cubic matrix increases the material strength and fracture toughness. These precipitations are meta-stable at room temperature ( $25^{\circ}\text{C}$ ), which can change into the martensitic monoclinic phase by absorbing a certain amount of deformation energy, where due to the resulting volume expansion, compressive stresses will be applied on the defects and cracks, and hence a high fracture strength will be obtained [60].

An APS TBC layer is formed of many thin zirconia splats, usually with the width of  $20\ \mu\text{m}$  to  $100\ \mu\text{m}$ , and a thickness of around  $10\ \mu\text{m}$ . Based on the manufacturing process, there are cracks and pores between the splats, which favorably reduce the thermal conductivity. On the other hand, tensile stresses are formed due to the high cooling rate of the sprayed layers. These stresses induce segmentation cracks. Existence of the described defects decreases the strength of the material [62]. Many groups have measured the elastic

modulus between room temperature and 1200 °C. As Fig. 2.12 shows, it decreases with increasing temperature. At high temperature, stresses in TBC will be relaxed due to creep mechanisms, with the primary creep being the main deformation regime [63].

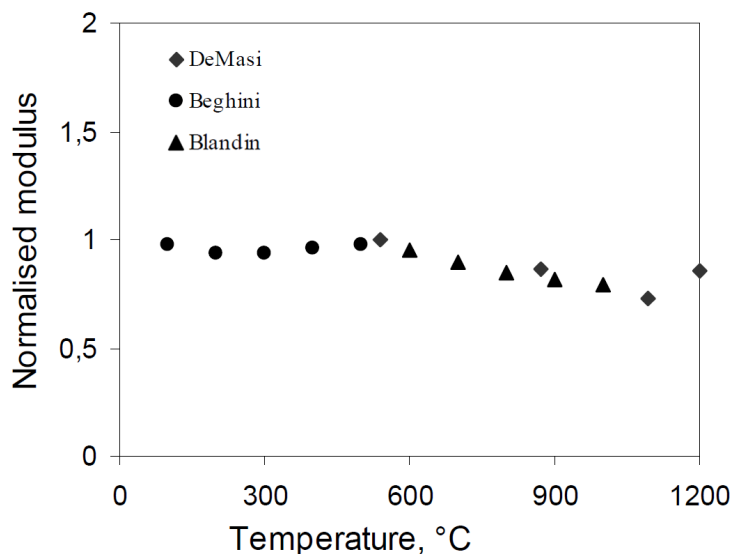


Figure 2.12: Normalized elastic modulus of TBCs as a function of temperature [64–67].

## 2.2 Degradation mechanisms of TBC systems

In the following, a literature review on the behavior of TBC systems under thermal fatigue loading will be given. Not many groups have studied so far the fatigue behavior of drilled or even notched TBC systems as well as the influence of laser-drilled holes on the life time, which makes this work an edge moving study.

### 2.2.1 Oxidation of BC

When the BC is exposed to high temperatures (around 900 °C or higher), an alumina oxide layer begins to grow at the TBC/BC interface. The growth, the rate of growth, and the microstructure of TGO affects substantially the life-time of TBC systems [68, 69]. Due to the diffusion of aluminum from BC to TBC/BC interface,  $\beta$ -Al rich phases in BC will be depleted and alumina,  $\text{Al}_2\text{O}_3$ , will be formed [19]. The growth rate is typically parabolic, i.e. it is relatively high at the beginning phase of high temperature exposure, whereas it reduces after further oxidation of the BC [29], see Fig. 2.13a. Under ideal conditions, the growth rate of alumina follows a parabolic rate law based on inward diffusion of oxygen along grain boundaries of the TGO. Fig. 2.13b and c show the TBC system with a very thin and thick TGO layer, respectively, where for the latter a delamination crack can be observed.

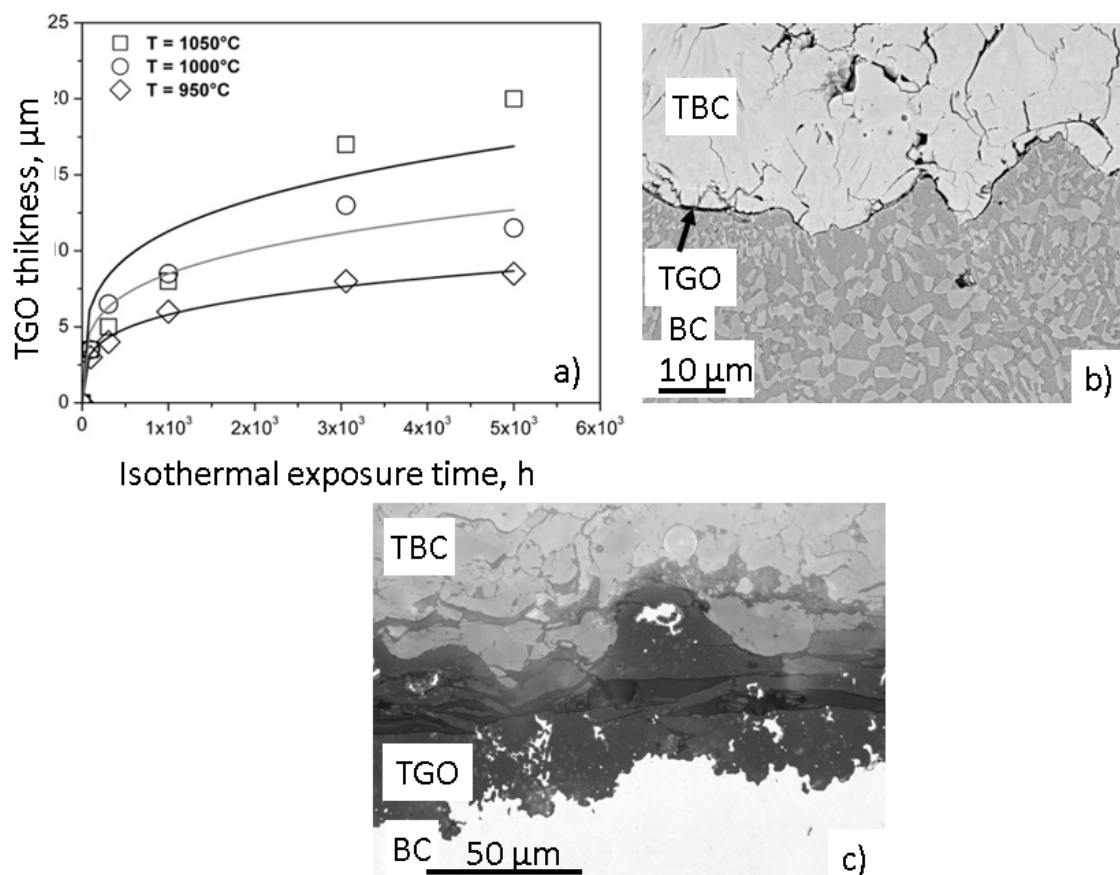


Figure 2.13: a) Isothermal TGO growth of alumina scale at various temperatures [29], TBC system with b) very thin and c) thick TGO layer

Spinel type oxides, also called transition oxides, such as  $\alpha$ -chromia or (Co)(Cr, Al) spinel, can be formed depending on oxygen pressure and temperature. They contribute to TBC failure due to their lower mechanical strength as well as the volumetric change when they change to more stable phases [70]. Shillington et al. [70] have shown that the interfacial fracture toughness of TBC/spinel and TBC/Cr<sub>2</sub>O<sub>3</sub> interfaces is lower than that of TBC/Al<sub>2</sub>O<sub>3</sub> interface. The growth rate of such oxide is higher than that of alumina, which makes it crucial to avoid them and the resulting break-away point due to excessive oxidation. Lack of internal cooling causes formation of these scales much faster, as will be reported in the experimental results, see section 4.2.2.

For MCrAlY coatings, the oxidation kinetics can vary significantly by providing some additives such as Y and Zr or trace elements, for example Si and Ti. They can enhance the scale adherence, reduce the growth rate and increase selective oxidation in the yttria-containing alloys [42]. It is possible that other types of alumina will be formed initially, which happens at certain temperatures and surface conditions [71]. Different forms of alumina are  $\gamma$ -,  $\theta$ -,  $\alpha$ -, and  $\delta$ -Al<sub>2</sub>O<sub>3</sub>.  $\alpha$ -Al<sub>2</sub>O<sub>3</sub> is the thermodynamically most stable modification that has the lowest growth rate.

### 2.2.2 Interdiffusion between BC and superalloys

Interdiffusion is the diffusion of elements at the BC/substrate interface due to concentration gradients across BC and substrate. The process occurs already during the coating process improving coating adherence to the base alloy and accelerates during high temperature exposure. Trunova [19] studied a TBC system with a single crystal substrate, an EB-PVD MCrAlY alloy bond coating and an APS TBC. Due to the concentration gradients of the material elements over the BC/substrate interface, Cr and Al diffused from BC to the substrate, while Ni and Re together with some refractory elements diffused in the opposite direction. Interdiffusion basically caused the depletion of mostly  $\beta$  phases in BC and formation of  $\gamma'$  in substrate at the interface. It is observed that the substrate on the interface loses its single crystal  $\gamma/\gamma'$  structure, and a continuous recrystallized region of  $\gamma'$  phase is formed. Around this area, the regions containing high percentage of W have a round or elongated shape, which are assumed to be  $\mu$  phase based on EDS investigations.  $\mu$  phase contains high contents of Re and Ta [19]. The areas where W and Re contents are lower and Cr content is higher are recognized as  $\sigma$  phase.

### 2.2.3 Sintering effect in TBC systems

The influence of annealing (often called sintering), which is mainly a result of surface diffusion, will be described in this section. Sintering effects can be observed by a reduction in crack and dislocation density, defect density between splat layers, and grain growth [62, 72–75]. Since the microstructure of APS-TBC usually features various micro- and macro-cracks, pores, impurities, and lamellar splat morphology, sintering processes can affect its mechanical properties significantly. The intensity of sintering depends on exposure temperature and annealing time.

Gas turbine components often undergo high temperature exposure. Many researchers have implemented annealing tests to measure material strength for temperatures above 1000 °C, where heat treatment induces an increasing trend in the elastic modulus [72, 76–78], see Fig. 2.14. The first stage with the lower trend can be traced back to the healing between the splats. At this stage, the elastic modulus is still relatively low due to the existence of the micro-cracks. On the other hand, the observations show that above 1300° C, both intersplat material bonding and healing of the microcracks occurs, hence yielding a larger positive slope in the curve. With increasing temperature, the increase rate in the elastic modulus also enhances. With the increasing  $E$ -modulus the stresses in TBC increase as well, which enhances the probability of damage initiation.

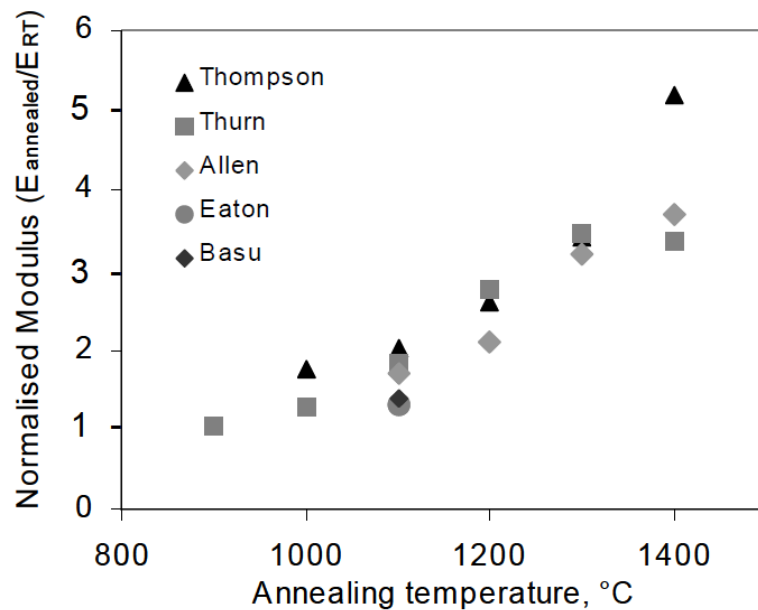


Figure 2.14: Normalized elastic modulus of TBC as function of annealing temperature for an exposure of max. 100 hours [72, 76–78].

Choi et al. [79] studied the influence of sintering on several parameters such as elastic modulus, Poisson’s ratio, mode I and mode II fracture toughness, density, micro-hardness, surface structure and phase stability. Except for phase stability, all the other properties increased for an annealing time of 5 h to 100 h at 1316 °C. Due to sintering, the structure was strengthened, Fig. 2.15a, and changed from a porous material to a more dense aggregate, Fig. 2.15b, leading to larger thermal conductivity [74, 80, 81], Fig. 2.16. The porosity is reported to be affected at around 1050-1300 °C [81, 82], while crack healing occurred around 900 °C.

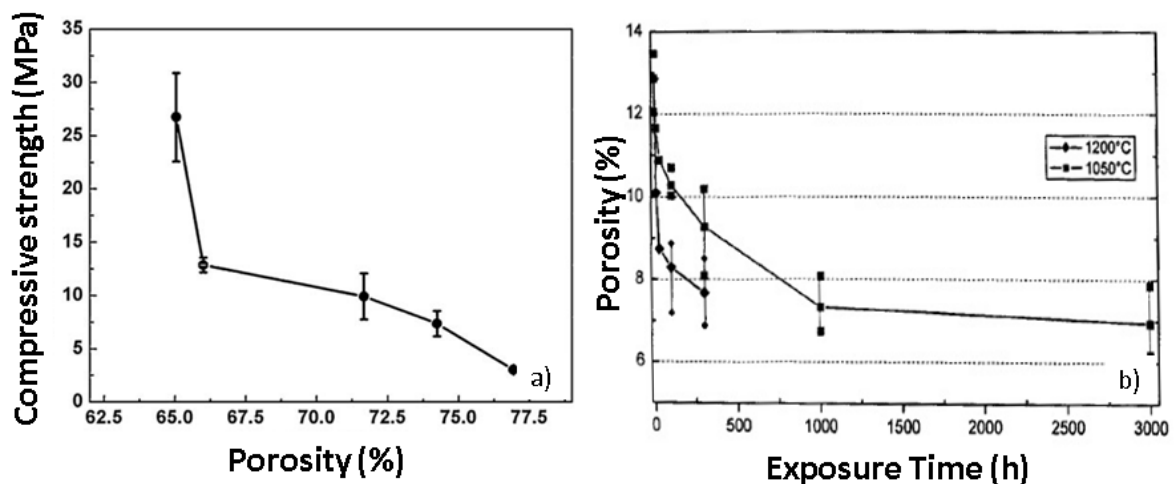


Figure 2.15: a) Compressive strength versus porosity [80], and b) time and temperature dependent evolution of porosity of APS-TBC system [81].

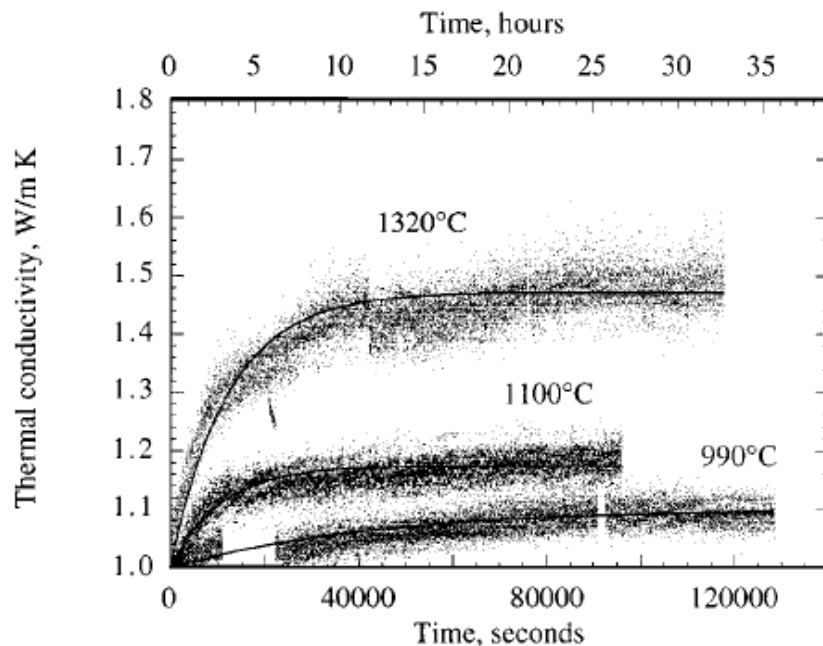


Figure 2.16: The overall thermal conductivity change of a YSZ TBC determined by the real time laser heat flux testing [74].

On the other hand, sintering causes the TBC to shrink, which results in in-plane tensile stresses, that increase by the increased elastic modulus of the TBC. This might correspondingly lead to the formation of vertical cracks in TBC/TGO interface [83].

#### 2.2.4 Thermal fatigue of TBC-coated superalloy

Thermal fatigue can be defined as thermal cycling of a material system, meaning the material's temperature changes from a minimum value to a maximum value back and forth until failure occurs. In the case of thermal cycling exposure, thermal stresses play an important role, which is due to the thermal mismatches between the components of the TBC system, see Fig. 2.17, as well as oxidation of the BC.

Trunova [19] has performed thermal fatigue tests on TBC-coated substrate from CMSX-4 with and without holding time. Without any holding time at the maximum temperature, the life-time of the tested specimen has been reported to be very high; 23500 cycles. This is due to the fact that the TGO layer has not grown enough to weaken the TBC/BC interface substantially, see in Fig. 2.18a the experimental observations, and in Fig. 2.19a the schematic presentation of typical damage modes. The typical failure mode is the delamination in the TBC layer above TBC/BC interface. Additionally, thermal fatigue cracks, perpendicular to the coating interface, have been observed in the BC, which originate from the valleys of the TGO/BC interface because of the stress concentration at this position due to in-plane tensile stress in the BC [21]. The critical stresses at the lowest temperature after cooling play an important role for crack initiation and propagation. On the other hand at high temperatures, the stress level is lower due to plasticity and stress relaxation. Based on the finite-element-method (FEM) calculations, TBC systems with a thin TGO layer experience high tensile stresses at the peaks of the TBC/BC interface



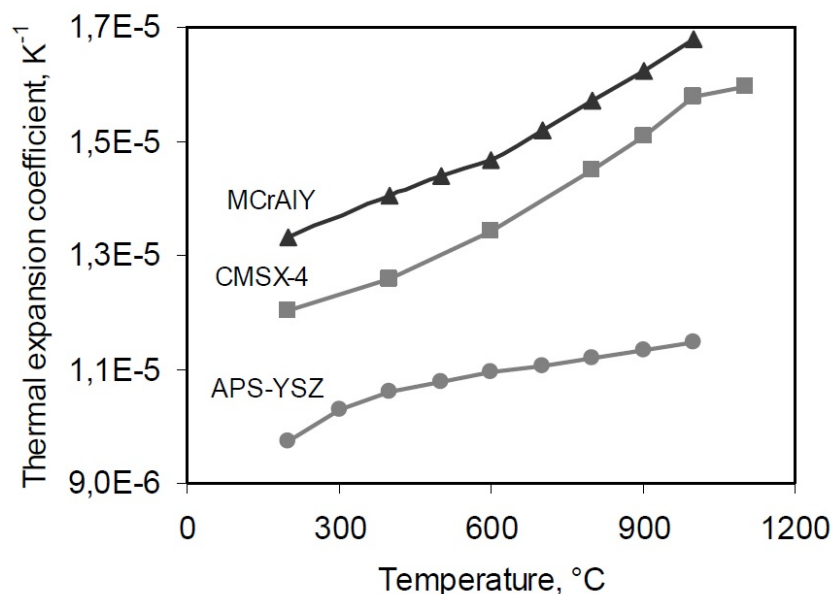


Figure 2.17: Variation of CTE versus temperature for a TBC system [39].

at low temperatures [24]. Mainly the TGO layer remains thin during operation, due to internal cooling in gas turbine components and the temperature gradient in TBC, where the temperature of BC is around 950 °C [19, 29]. Therefore, the BC will not be oxidized considerably.

If a hold time is applied at the maximum temperature, the TGO layer will grow to a larger extent than in case without hold time, see Fig. 2.18b and Fig. 2.19b. Hence, it decreases significantly the interfacial fracture toughness of the interface. Therefore, the delamination plane will shift to the TBC/BC interface, where it takes place partly in the TGO and partly in the TBC [19, 69, 84]. The life-time decreases drastically, which shows the deteriorating effect of oxidation. In contrast to the case without holding time, no vertical cracks were found in the bond coating, which is due to oxidation of the TGO/BC interface and a lower notch effect at valleys as a consequence of a thin alumina scale [19]. Yamazaki et al. [85] tested TBC specimens with different hold time at the max. temperature of 1050 °C. They observed crack formation at the beginning in TBC and after the test at the weakened TBC/TGO interface. With less hold time, there was a higher possibility to see a white failure (fracture in TBC), while with more hold time one could see the crack at TBC/TGO interface.

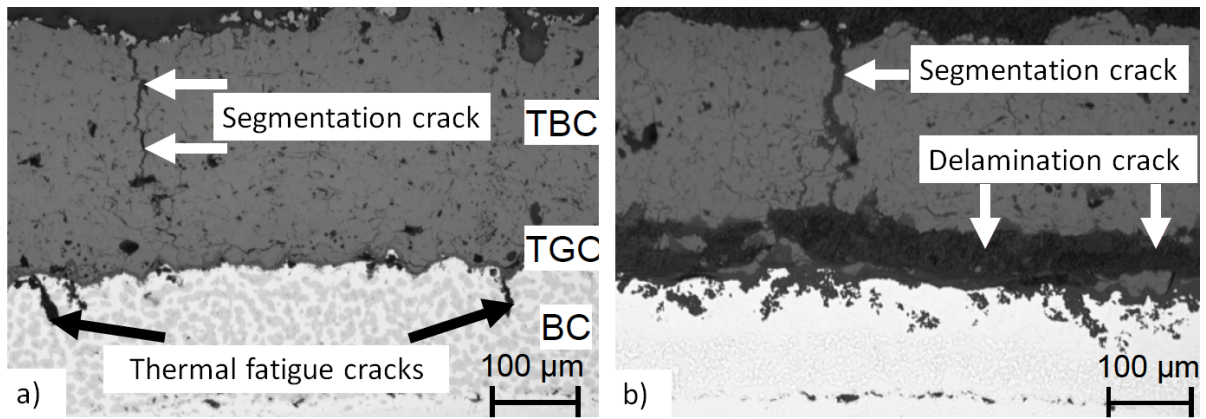


Figure 2.18: SEM image of failure state after (a) thermal cycling and (b) cyclic oxidation [19].

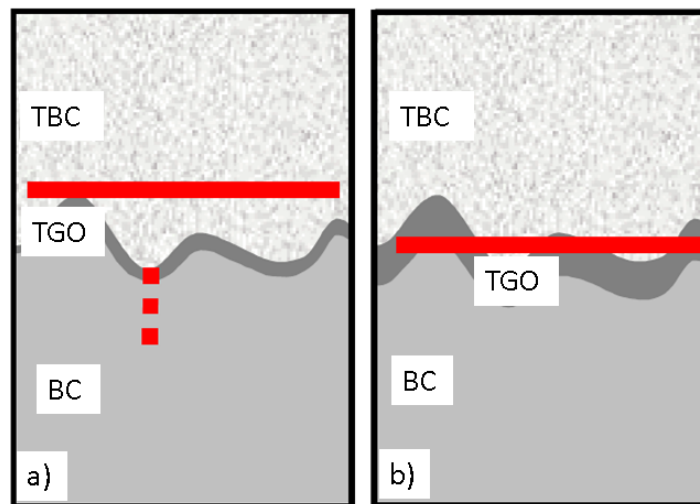


Figure 2.19: Schematic presentation of typical damage modes induced by (a) thermal cycling without hold time and (b) cyclic oxidation [19].

The damage evolution of a TBC system under cyclic oxidation loading conditions is shown in Fig. 2.20. Regarding as-received state, micro-defects such as pores and micro-cracks can be found in the TBC layer. During long time exposure at high temperature, the cracks will be formed within TGO or at the TBC/BC interface at peaks and propagate further. Above a certain TGO thickness, such microcracks will coalesce which is favored by a low roughness of the bond coating. Near the end of life time the macro delamination crack will grow further up to a point where spallation occurs.

The cracking mechanism of such TBC system can be categorized in two phases. In the first phase, where the microcracks initiate and extend, the propagation rate is relatively slow and determined by their growth within TGO, see Fig. 2.21 [86]. At the second phase, the cracks coalesce and grow further within the ceramic TBC at a higher growth rate.



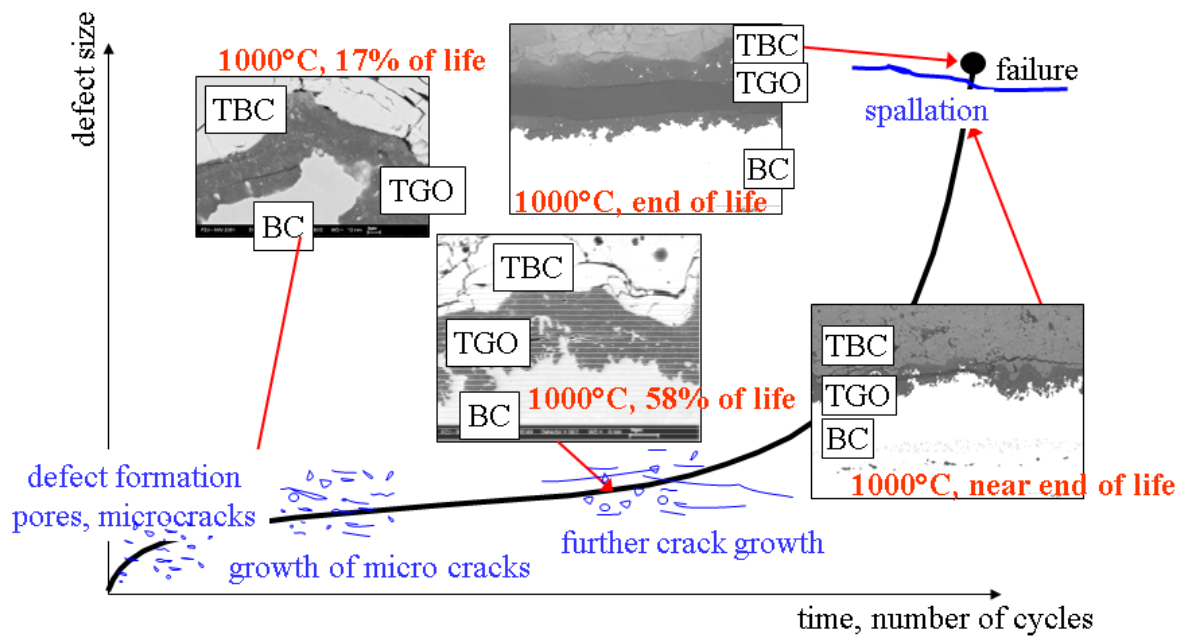


Figure 2.20: Cracking mechanism due to TGO growth and thermal misfit.

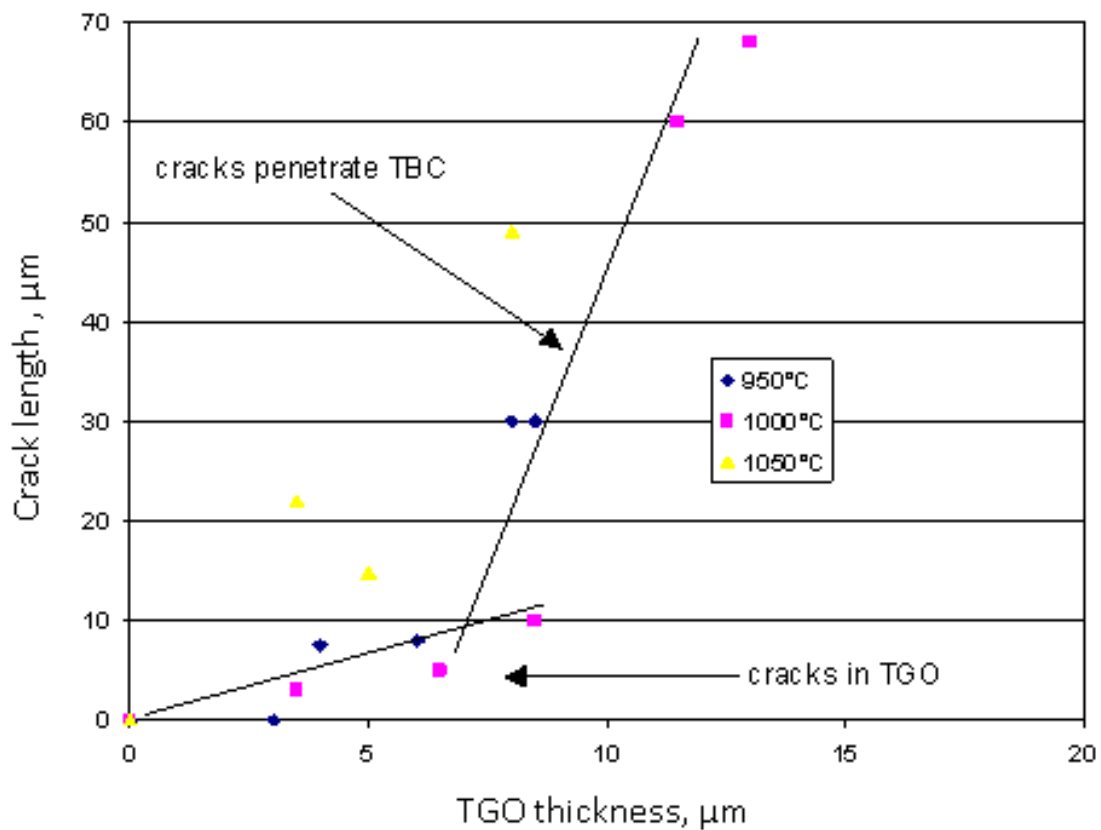


Figure 2.21: Max. crack length vs. TGO thickness for isothermal oxidation ( $T = 950^\circ\text{C}$ ,  $1000^\circ\text{C}$ ,  $1050^\circ\text{C}$ ) [86].

R. Herzog et al. [86] developed a model for describing damage evolution of TBC system under high temperature exposure based on the mechanisms described above. If TGO thickness is less than one fourth of the interface roughness,  $R_z/4$ , the cracking mechanism is in the first phase, where only microcracks form at peaks, see Fig. 2.22a. When the TGO thickness is around  $R_z/4$  TGO cracks propagate and penetrate to TBC layer, see Fig. 2.22b. This is promoted by change of the original tensile stress on the top hill of BC and compressive stress in valley of BC in the opposite direction with increasing oxide scale thickness. With further TGO growth cracks join together leading to delamination and spallation of TBC layer.

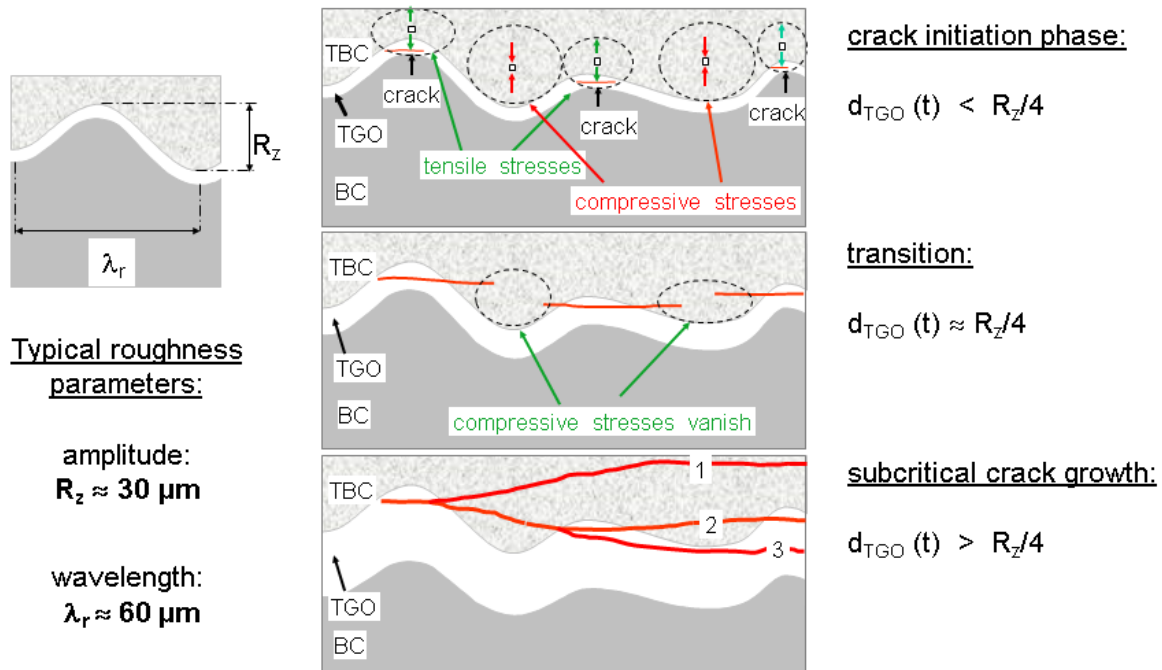


Figure 2.22: Cracking mechanism and stress development due to oxidation [86].

The edge effects in thermal loading tests are of importance, where delamination cracks initiate mostly at edges due to the higher local stresses. Li et al. [87] performed thermal shock tests on EB-PVD TBC systems for several maximum temperatures including 1050°C. They observed delamination cracks for the tests at this temperature, which occurred mainly at the edges or the fixture hole. Khan et al. [88] performed thermal shock tests at 1020 °C with APS TBC systems. The failure started also at the edges due to higher residual stresses at these positions. Zhu et al. [89] analyzed different TBC systems including various BC types by performing FEM simulations, in order to understand the failure and damaging mechanisms for improving the life time. They also found higher stresses and initial cracks at the edge. However, no considerable data regarding thermal cycling of laser-drilled TBC systems, which is one of the focus points of this work, could be found in literature.

## 2.2.5 Thermomechanical Fatigue of TBC-coated superalloys

TBC-coated components of a gas turbine undergo thermal as well as mechanical fatigue loading scenarios during operation. Therefore, it is important to study the behavior of drilled and undrilled TBC systems under such loading conditions. In the following, a literature review of the important studies regarding LCF tested TBC-coated nickel-based superalloys is presented.

### 2.2.5.1 LCF loading

Performing isothermal mechanical fatigue test for life times lower than  $10^6$  is typically called low cycle fatigue or LCF. LCF testing, under application relevant conditions such as high temperature and high strain ranges, is a suitable method to examine the influence of laser-drilled holes on the life time of TBC-coated superalloys, as gas turbine components. Fig. 2.23 shows a typical loading profile during a LCF test. The test temperature,  $T_{\text{test}}$ , is constant during the test. Over the cycle time,  $t_c$ , the specimen is under mechanical cyclic loading, which can be either stress- or strain-controlled, i.e. the case in Fig. 2.23. The total strain range, considering the  $R = \epsilon_{\text{min}}/\epsilon_{\text{max}} = -1$  can be defined as  $\Delta\epsilon_{\text{tot}} = 2\epsilon_m$ .

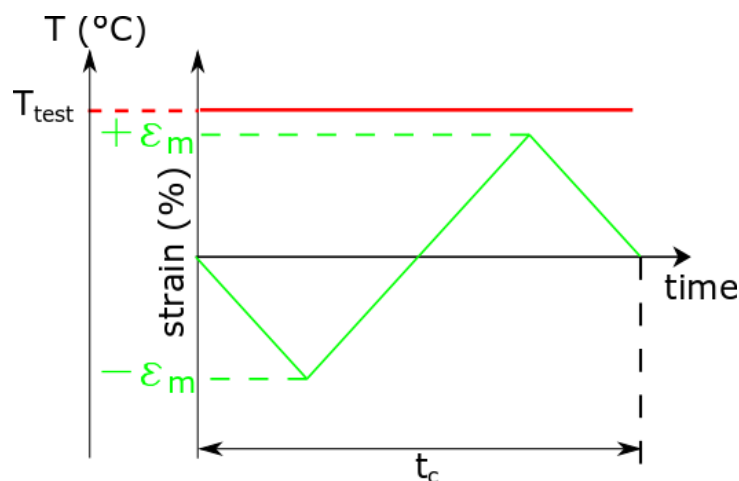


Figure 2.23: Typical LCF loading over a single cycle time,  $t_c$ , at a constant test temperature,  $T_{\text{test}}$ , under a strain-controlled mechanical cyclic loading. The total strain range is defined in this case ( $R = -1$ ) as  $\Delta\epsilon_{\text{tot}} = 2\epsilon_m$ .

Klabbers [3] performed strain-controlled LCF tests on specimens from three different materials, CMSX-4, CM186LC SX, and CM186LC DS, at  $950^\circ\text{C}$  using an induction heating system. The tests were performed with a strain rate of  $6\%/min$  with different strain ranges,  $0.5\%$ ,  $0.8\%$ , and  $1.0\%$ , with a failure criterion of  $10\%$  stress reduction.

As shown in Fig. 2.24, it can be seen that with the lower strain range, the average crack length at the inner surface of the base alloy as well as at TBC/BC interface increases.

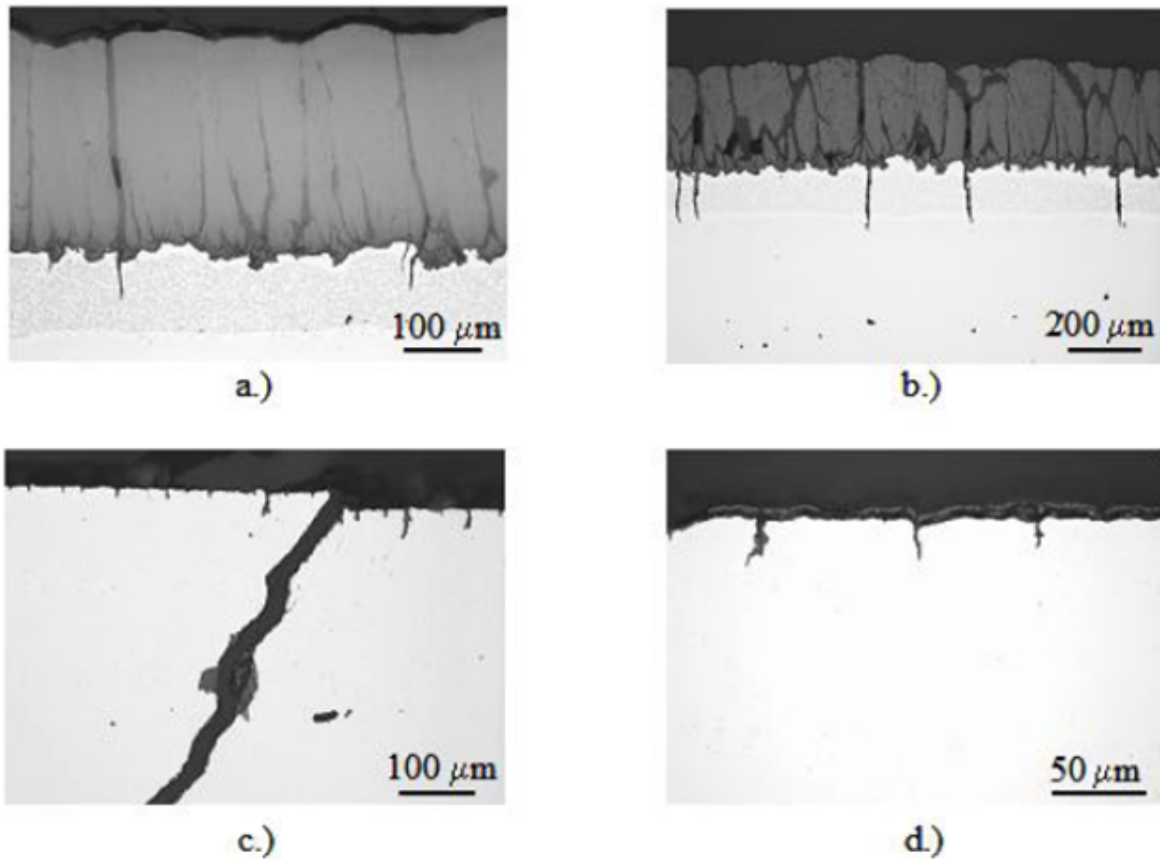


Figure 2.24: SEM images of the secondary cracks in the superalloy CMSX-4 with TBC coating after LCF testing, a) outer side with  $\Delta\epsilon = 0.8\%$  and  $N_f = 1703$ , b) outer side with  $\Delta\epsilon = 0.5\%$  and  $N_f = 7967$ , c) inner side with the primary crack with  $\Delta\epsilon = 0.8\%$  and  $N_f = 1703$ , d) inner side with  $\Delta\epsilon = 0.5\%$  and  $N_f = 7967$  [3].

In Fig. 2.25 the SEM images of the BC-coated superalloy CM186LC DS is shown. The primary crack has propagated through both the BC and the base alloy. For the specimens tested with higher strain ranges, it can be observed that the primary crack has initiated from the inner surface of the base alloy, since the secondary cracks can be found on the inner surface. For the lower strain range 0.5%, the cracks which initiated at TBC/BC interface as well as the ones at the inner surface of the superalloy, have almost similar length.

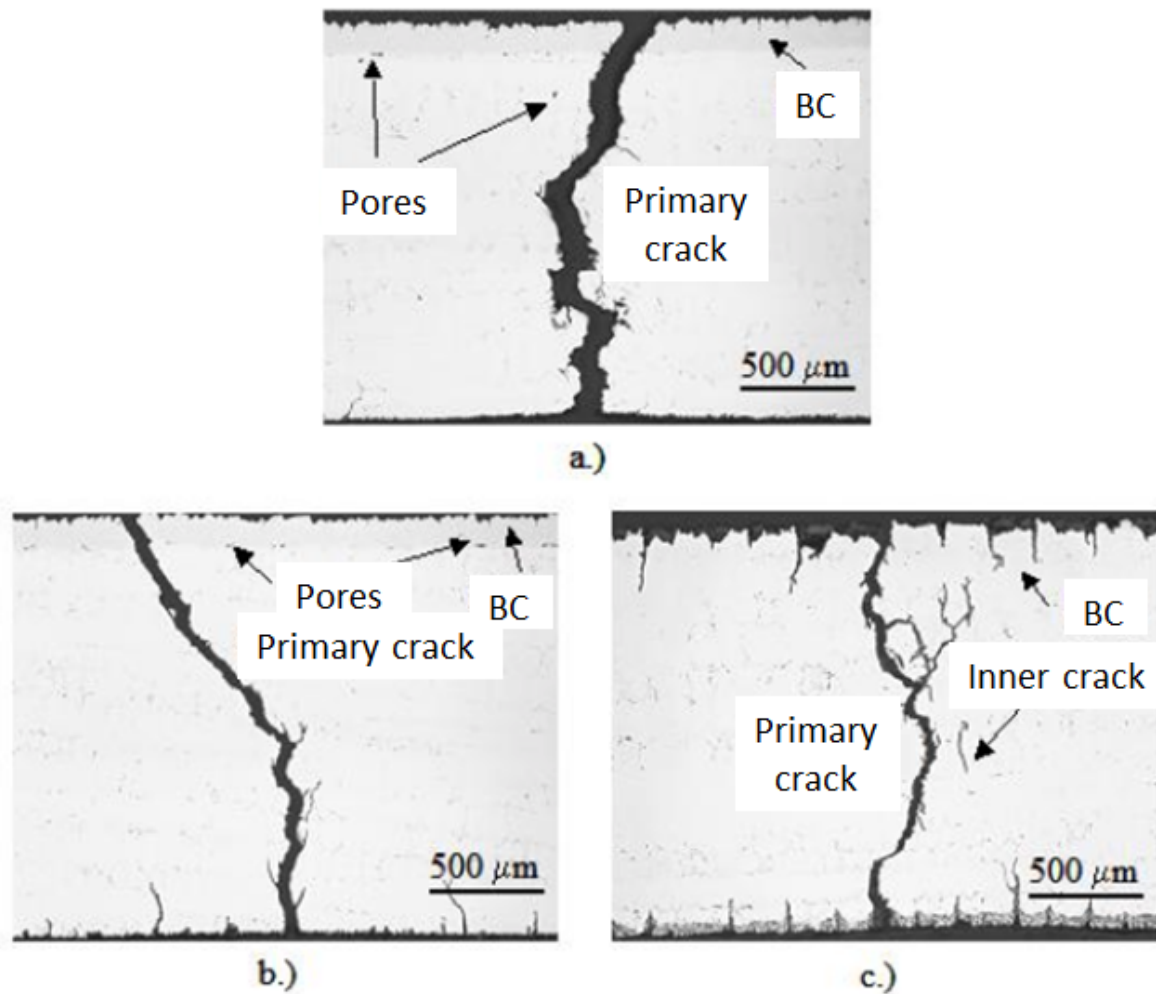


Figure 2.25: SEM images of the primary crack and initiated cracks for different strain ranges for the superalloy CM186LC DS with only BC after LCF testing, a)  $\Delta\epsilon = 1.0\%$  and  $N_f = 260$ , b)  $\Delta\epsilon = 0.8\%$  and  $N_f = 730$ , c)  $\Delta\epsilon = 0.5\%$  and  $N_f = 3178$  [3].

Klabbers [3] also tested laser-drilled and undrilled uncoated flat specimens from the single crystal superalloy CMSX-4 with LCF loading at  $950^\circ\text{C}$  and different strain ranges, see Fig. 2.26. It was observed that cracks appeared at the laser-drilled cooling holes. A reduction of around 9 times in the life time of drilled specimen in comparison with the undrilled specimen was observed, shown in Fig. 1.1.

Heckmann [39] performed also strain-controlled LCF tests at  $450^\circ\text{C}$  and  $950^\circ\text{C}$  on coated and uncoated superalloys IN 792 CC and CMSX-4. LCF testing at the higher temperature resulted in a lower life time than the tests with the lower temperature. The cracks in the specimens tested at the higher temperature were relatively open and oxidized, whereas for the specimens tested at the lower temperature the cracks had the opposite characteristics, indicating the deteriorating effect of oxidation on the life time. An increase in the crack density and crack length in the BC was also observed for smaller strain ranges. No spallation of the TBC coating was observed in the failed specimens.

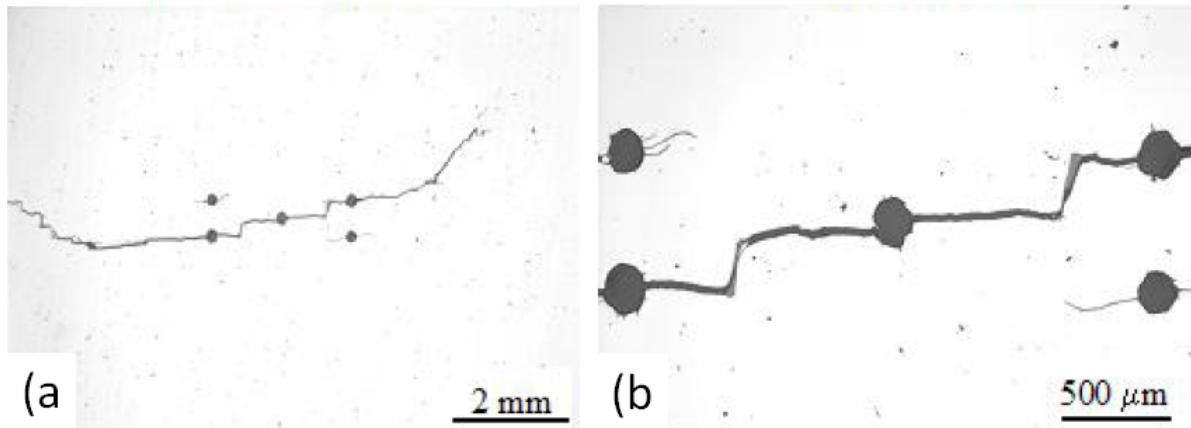


Figure 2.26: a) Crack propagation path of laser-drilled uncoated specimen from CMSX-4, tested by LCF at  $950^{\circ}\text{C}$  with  $\Delta\epsilon = 1.0\%$  and  $N_f = 371$ , b) magnified image of the cracking at the holes in (a).

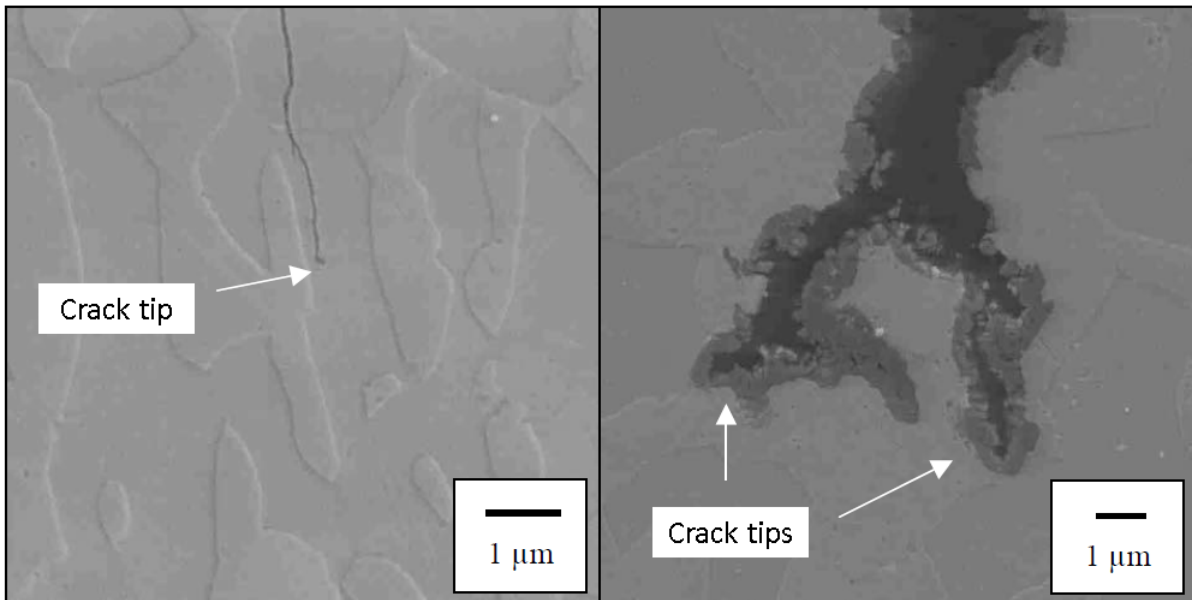


Figure 2.27: Crack tips in the BC on CMSX-4 after LCF loading at  $450^{\circ}\text{C}$  and  $950^{\circ}\text{C}$ ,  $\Delta\epsilon = 0.99\%$ ,  $N_f = 4321$  cycles (left),  $950^{\circ}\text{C}$ ,  $\Delta\epsilon = 0.98\%$ ,  $N_f = 2460$  cycles (right) [39].

## 2.3 FEM simulation of TBC systems

In the following, the fundamentals and theory of finite element method is described. Afterwards, a literature review on stress analysis of TBC systems using FEM is presented.

### 2.3.1 Fundamentals

The principle of minimum potential energy is used in finite element method to calculate the deformation of the physical system under external forces. According to the second law of thermodynamics, the direction of deformation will be towards a state with the minimum potential energy. We can write the total potential energy,  $\Pi$ , as below

$$\Pi = \underbrace{\Pi_{in}}_{\int_{\Omega} \Psi(\boldsymbol{\epsilon}) dV} + \underbrace{\Pi_{out}}_{-\int_{\Omega} \mathbf{b} \cdot \mathbf{u} dV - \int_{\Omega} \mathbf{t}^* \cdot \mathbf{u} dA}, \quad (2.1)$$

where  $\Pi_{in}$  indicates the free energy of the system, which is the energy stored in the material.  $\Pi_{out}$  is the change in the potential energy by exertion of external forces [90]. Total potential energy is defined as the potential stored in the material without external forces, therefore the external potential has a negative sign.

As stated above, the system deforms by minimizing  $\Pi$

$$\begin{aligned} \delta\Pi &= \int_{\Omega} \frac{\partial\Psi}{\partial\boldsymbol{\epsilon}} : \delta\boldsymbol{\epsilon} dV - \int_{\Omega} \mathbf{b} \cdot \delta\mathbf{u} dV - \int_{\Omega} \mathbf{t}^* \cdot \delta\mathbf{u} dA = 0 \\ &= \int_{\Omega} \boldsymbol{\sigma} : \delta\boldsymbol{\epsilon} dV - \int_{\Omega} \mathbf{b} \cdot \delta\mathbf{u} dV - \int_{\Omega} \mathbf{t}^* \cdot \delta\mathbf{u} dA = 0 \\ &= \mathbf{f}_{int} - \mathbf{f}_{ext} = 0, \end{aligned}$$

where  $f_{int}$  and  $f_{out}$  are the internal and external forces. The physical coordinate system in a FE model is approximated by transforming the physical coordinates of material points to the so-called natural coordinate system using the shape functions  $\mathbf{N}$  for  $i = 1, \dots, n$ , where  $n$  is the number of nodes of an element. The physical coordinates and the deformation field can be then formulated as below

$$\mathbf{x} = \sum_i \hat{x}_i^e N_i(\boldsymbol{\zeta}) \quad (2.2)$$

$$\mathbf{u} = \sum_i \hat{u}_i^e N_i(\boldsymbol{\zeta}), \quad (2.3)$$

where  $\hat{x}_i^e$  is the corresponding physical coordinate and  $\hat{u}_i^e$  deformation value of element  $e$  and node  $i$ , and  $\boldsymbol{\zeta}$  is the natural coordinate vector. Shape function of node  $i$ ,  $n_i$ , is normalized at this node, i.e.  $N_i(\mathbf{n}_i) = 1, \mathbf{n}_i = (\boldsymbol{\zeta}_{n_i})$ . Shape function  $N_i$  is however zero at the other nodes,  $\mathbf{n}_j$ , i.e.  $N_i(\mathbf{n}_j) = 0, j \neq i$ . Assuming a linear problem, strains are relatively small, and the strain field for a 2-dimensional case writes



$$\boldsymbol{\epsilon} = \frac{1}{2} (\nabla \mathbf{u} + \mathbf{u} \nabla) \quad (2.4)$$

$$= \nabla^s \cdot \mathbf{u} = \nabla^s \mathbf{N} \cdot \mathbf{u}^e \quad (2.5)$$

$$\begin{pmatrix} \epsilon_{11} \\ \epsilon_{22} \\ \epsilon_{12} \end{pmatrix} = \underbrace{\begin{pmatrix} \frac{\partial}{\partial x_1} & 0 \\ 0 & \frac{\partial}{\partial x_2} \\ \frac{\partial}{\partial x_2} & \frac{\partial}{\partial x_1} \end{pmatrix} \begin{pmatrix} N_i & 0 \\ 0 & N_i \end{pmatrix}}_{\mathbf{B}} \begin{pmatrix} u_1^e \\ u_2^e \end{pmatrix} \quad (2.6)$$

$$= \mathbf{B} \mathbf{u} \quad (2.7)$$

where  $\mathbf{B}$  is the matrix multiplication of derivative tensor and shape function tensor. The concept of FEM is to discretize the model into finite elements, where each element is constructed by linking specific nodes to another.

The typical procedure, which is performed in each analysis in the FEM software ABAQUS, is shown in Fig. 2.28. The computations can consist of one or more steps each divided into increments, i.e. time intervals which build up a step.

At each increment, the internal force tensor for each element will be calculated, and afterwards the global internal and external force tensor will be built up assembling the local tensors.

$$\mathbf{F}^{int} = \bigcup_{i=1}^{n_{el}} \mathbf{f}^{int} \quad \text{and} \quad \mathbf{F}^{ext} = \bigcup_{i=1}^{n_{el}} \mathbf{f}^{ext}. \quad (2.8)$$

For the whole domain, the equilibrium equation for all the elements is shown by equation 2.9, which by using a implicit method will be solved by an iteration method, i.e. typically Newton-Raphson (NR) method.  $\mathbf{R}$  is the residual force tensor, which should be less than a defined tolerance, TOL, after an iteration in order to reach convergence in results, see step (e) in Fig. 2.28. If convergence is not achieved, the system of equations will be solved in the next iteration using NR method, starting from step (f). In each time step, the external load  $\mathbf{F}^{ext}$  will be changed based on its evolution over time and the time increment  $\Delta t$ .

$$\mathbf{R} = \mathbf{F}^{int} - \mathbf{F}^{out} = 0 \quad (2.9)$$

The algorithm for an each iteration is summarized below.

- (a) Specify the initial value of the current step,  $n + 1$ ,  $\mathbf{u}_{n+1}^0$ , by assigning the converged value of the previous step,  $n$ ,  $\mathbf{u}_n$ . If it is the first step, then  $\mathbf{u}_{n+1}^0 = 0$ , in the case of no external load at the initial state.

$$\mathbf{u}_{n+1}^0 = \mathbf{u}_n \quad (2.10)$$



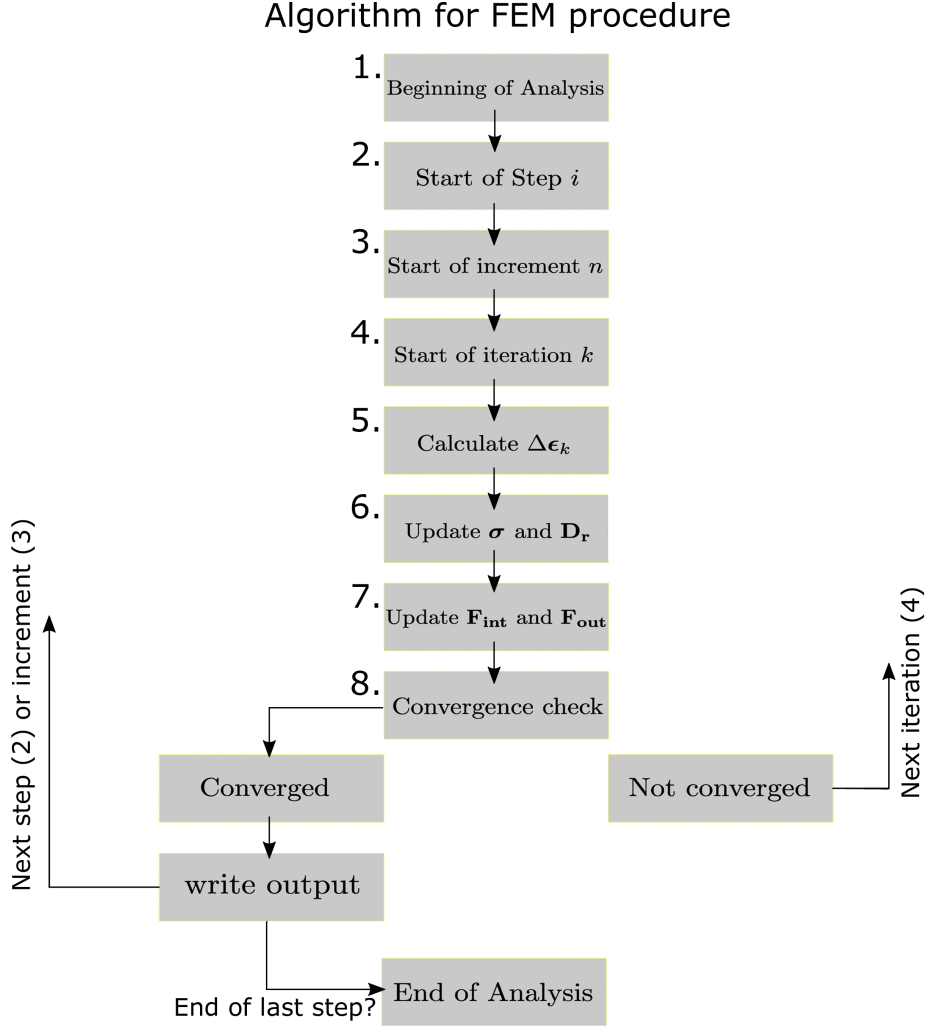


Figure 2.28: Typical analysis procedure in ABAQUS.

(b) Calculate the initial displacement increment using NR method

$$\Delta \mathbf{u}_{n+1}^1 = - \left. \frac{\partial \mathbf{R}_u}{\partial \mathbf{u}} \right|_{\mathbf{u}=\mathbf{u}_{n+1}^0}^{-1} \mathbf{R}_u(\mathbf{u}_{n+1}^0) \quad (2.11)$$

(c) Update  $\mathbf{u}$  for the first iteration

$$\mathbf{u}_{n+1}^1 = \mathbf{u}_{n+1}^0 + \Delta \mathbf{u}_{n+1}^1 \quad (2.12)$$

(d) Calculate the local internal forces by utilizing the constitution laws, and build the global internal and external force tensors by assembling the local tensors for iteration m

$$\mathbf{F}^{int} = \bigcup_{i=1}^{n_{el}} \mathbf{f}^{int}(\boldsymbol{\sigma}_{n+1}^m, \mathbf{u}_{n+1}^m, \boldsymbol{\epsilon}_{n+1}^m) \quad \text{and} \quad \mathbf{F}^{ext} = \bigcup_{i=1}^{n_{el}} \mathbf{f}^{ext} \quad (2.13)$$

- (e) Solve the system of equations and check convergence

$$\mathbf{R}_u = \|\mathbf{F}^{int} - \mathbf{F}^{ext}\| \leq TOL \quad (2.14)$$

If converged,

$$\mathbf{u}_{n+1} = \mathbf{u}_{n+1}^m \quad (2.15)$$

$$\boldsymbol{\sigma}_{n+1} = \boldsymbol{\sigma}_{n+1}^m \quad (2.16)$$

and go to step (a) for the next step if it is the case. If not, go to step (g) for the next iteration.

- (f) Calculate the next deformation increment  $\Delta \mathbf{u}_{n+1}^{m+1}$ , update the deformation,  $\mathbf{u}_{n+1}^{m+1}$ , and go to step (d)

$$\Delta \mathbf{u}_{n+1}^{m+1} = - \underbrace{\frac{\partial \mathbf{R}_u}{\partial \mathbf{u}} \Big|_{\mathbf{u}=\mathbf{u}_{n+1}^{m+1}}^{-1}}_{\mathbf{K}_{n+1}^{e,m+1}} \mathbf{R}_u(\mathbf{u}_{n+1}^{m+1}) \quad (2.17)$$

$$\mathbf{u}_{n+1}^{m+1} = \mathbf{u}_{n+1}^m + \Delta \mathbf{u}_{n+1}^{m+1} \quad (2.18)$$

where  $\mathbf{K}_{n+1}^{e,m+1}$  is the stiffness matrix and defined below

$$\begin{aligned} \mathbf{K}_{n+1}^{e,m+1} &= \frac{\partial}{\partial \mathbf{u}} \left( \mathbf{F}^{int}(\boldsymbol{\sigma}_{n+1}^{m+1}) - \mathbf{F}^{ext} \right) = \frac{\partial \mathbf{F}^{int}(\boldsymbol{\sigma}_{n+1}^{m+1})}{\partial \mathbf{u}} \\ &= \frac{\partial}{\partial \mathbf{u}} \int_{\Omega} \mathbf{B}^T \boldsymbol{\sigma}_{n+1}^{m+1} \delta \mathbf{u} dV \\ &= \int_{\Omega} \mathbf{B}^T \frac{\partial \boldsymbol{\sigma}_{n+1}^{m+1}}{\partial \boldsymbol{\epsilon}_{n+1}^{m+1}} \frac{\partial \boldsymbol{\epsilon}_{n+1}^{m+1}}{\partial \mathbf{u}_{n+1}^{m+1}} \delta \mathbf{u} dV \end{aligned} \quad (2.19)$$

The simulations in this work were done with the commercial CAE Software ABAQUS from DASSAULT SYSTEMS.

### 2.3.2 Stress analysis

Stress states of TBC systems, especially at room temperature, play an important role regarding life-time of cooled components. Using FEM, it is possible to calculate how the stress distribution is influenced in the case of different geometries, e.g. interface roughness, coating thickness, as well as changes in various material parameters such as creep properties,  $E$ -modulus, thermal expansion coefficients, etc.

Chang et al. [91] performed stress analysis using FEM calculations by considering only elastic behavior of the components of the TBC system, where the stresses were mainly

a result of thermal mismatches. On the basis of high out-of-plane stresses at the tip of peaks in a TBC coating with a thin TGO layer, and also high shear stresses at off-peak areas, they made predictions for crack initiation and propagation, see Fig. 2.29 below. The thermal expansion coefficient of a BC is usually higher than that of substrate and TBC. Thus, typically after cooling to room temperature, the BC shrinks more and induces in-plane compressive stresses in the TBC. On the contrary, in-plane tensile stress is induced in the BC, which induces vertical cracks especially at valleys due to stress concentration effect. In normal direction for a negligible TGO layer, at peaks, BC is similar to a sphere coated with TBC, and at valleys, similar to a coating on a cylindrical TBC sphere. Therefore, due to shrinking of BC at peak and valley during cooling, tensile and compressive out-of-plane stresses, respectively, will be induced [20, 92, 93].

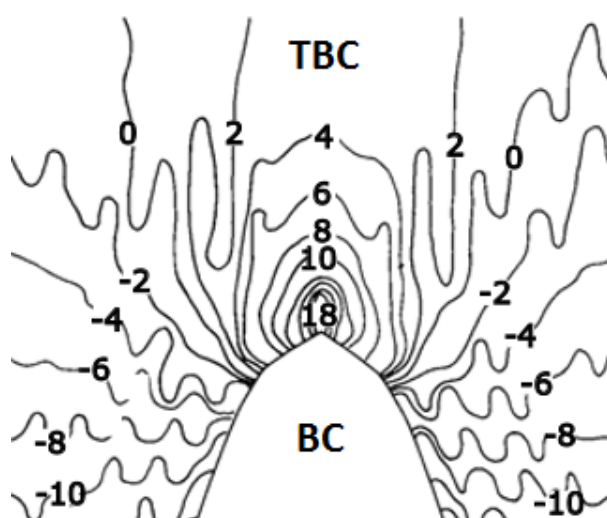


Figure 2.29: Stress distribution (in MPa) in the perpendicular direction to a TBC/BC interface at the peak position [91].

It is however too simple to consider the material behavior of a TBC system as purely elastic. The complexity of the stress situation in such a system was illustrated afterwards by Chang et al. [94]. The more realistic stresses in this case were lower than the stresses in the elastic case. Inelastic deformation such as plastic as well as viscoplastic behavior of the components of the TBC system should be taken into account, which allows the irreversible deformation of the topology of the TBC/BC interface. Freborg et al. [95] analyzed the TBC system under thermal loading taking into account the visco-plastic and elastic behavior of the components. They showed that stress relaxation at high temperature reduces the stress state at room temperature at the TBC/BC interface, while the TGO growth at high temperature intensifies the stresses. The crack mechanism was thought to be due to the linkage of the cracks formed over valleys at the final stages in the existence of oxide layer, with the cracks formed early over the peaks. Such mechanism in TBC systems under thermomechanical loading is due to coupling of different phenomena such as elastic, plastic and creep deformation. As a summary [23], Fig. 2.30 shows different TBC systems with these different material behavior, where the explained differences in stress distributions can be observed.

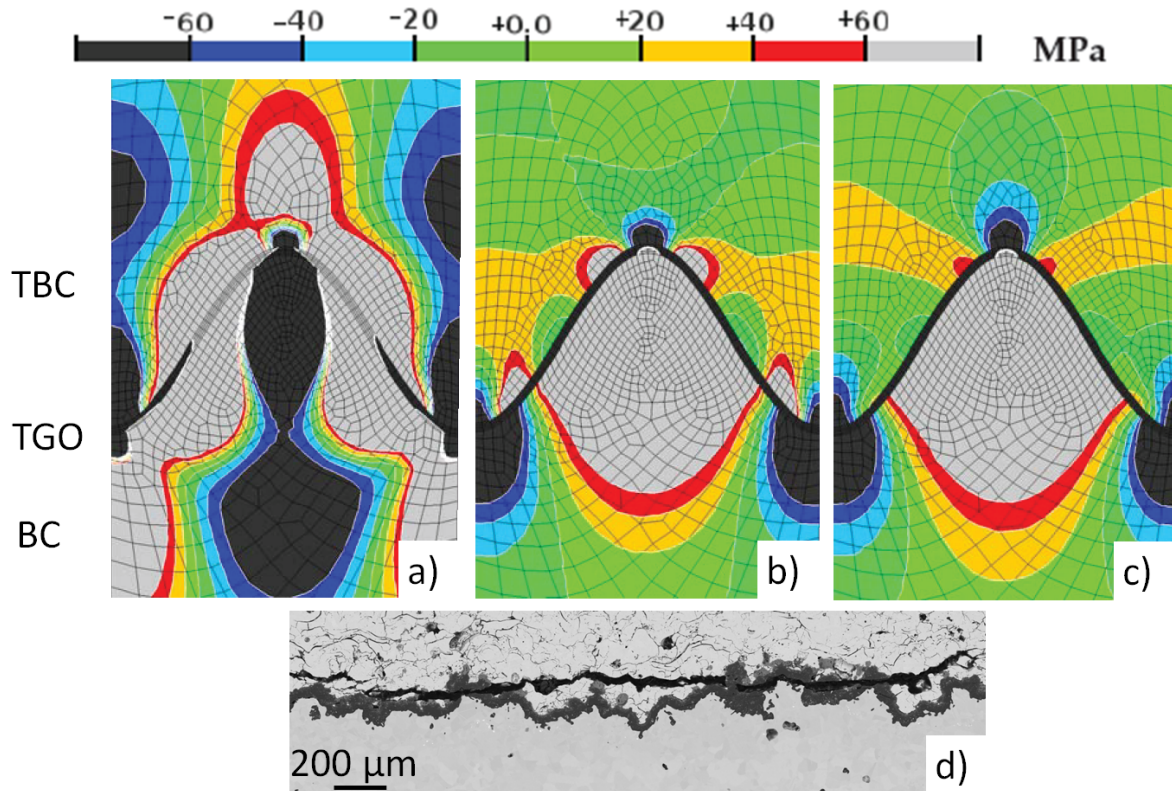


Figure 2.30: Different stress distributions including (a) complete elastic behavior, (b) consideration of BC and TGO plasticity, (c) viscoelastic and plastic material behavior [23], d) typical delamination crack of a TBC system.

Bednarz [23] studied deeply the effect of material parameters, such as creep rates and plasticity data as well as different interface asperities. It was concluded that, in order to reduce stresses, TBC porosity should be higher and sintering rate lower. TGO plasticity could decrease the stress in BC and TGO considerably. TBC creep reduced the geometrical instabilities due to oxidation kinetics. BC creep reduced the pace of formation of tensile stress in TBC. He also showed that by changing the CTE of the components the stress changed strongly.

The switching of the stress state at TBC/BC interface was shown in several works [24, 91, 96, 97]. In the first cracking phase, the TGO thickness is relatively low. At peaks, the material experiences tensile stress which usually leads to microcracks in TGO or TBC. However, such cracks do not grow further due to the off-peak region which is under compressive stress, see Fig. 2.31a. With increasing TGO growth, the off-peak region will be under tensile stress and the cracks penetrate into the TBC layer and coalesce, which leads to delamination of the TBC layer, see Fig. 2.31b. Gupta et al. [98] simulated the real interface of TBC/BC interface via object oriented FEM, where they also found the same stress evolution due to TGO growth as reported by Bednarz for a sinusoidal roughness profile [23]. Since TGO thickness plays an important role in limiting TBC life, normally there is a tendency to state a critical TGO thickness at which the end of life-time is reached. It was indicated that interface irregularities influence the critical TGO thickness, which is around 8 μm [92].

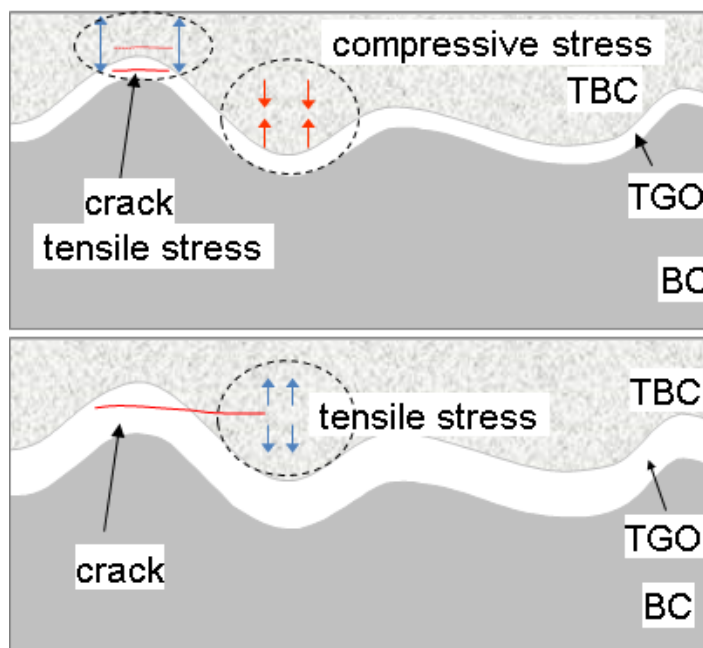


Figure 2.31: Cracking mechanism versus stress development due to oxidation [86].

Bäcker et al. [99] analyzed different aspects of TBC systems. Three interface geometries were chosen, out of which the sine-shaped interface showed the smoothest stress distribution. It was also suggested that, since life-time limiting cracks usually form at low temperature, implementing large stress relaxation at high temperature can compensate for uncertainties in material behavior at such conditions. Eriksson et al. [100] analyzed similarly different interface geometries including triangular, cosine, and ellipse. They showed that stress intensities were close to each other for these cases. However, cosine interface had values between the other two. Therefore, such interface geometry provides a more realistic stress distribution in the TBC systems.

Wang et al. [27] analyzed the stress state with and without cracks in different TBC systems. They found larger tensile out-of plane and shear stress at the edges. High in-plane compressive stresses at edges were also reported to be critical for coating buckling. Jiang et al. [28] analyzed the stress distribution for a TBC system with a flat interface between top coat and BC, using an axisymmetric model and an elastic material system. It was shown that there is high in-plane stress gradient in tangential and shear direction at the TBC/BC interface at the hole, see Fig. 2.32. It was also derived that greater hole diameter leads to higher stresses near the hole at the interfaces. Wu et al. [101] studied the residual stress after the coating process especially at the edge. It was similarly found that there is relatively high out-of-plane stress at the edge over TBC/BC interface. There was also a high stress gradient at the edge near the interface.

The stress response and failure behavior of TBC systems at edges and holes in detail, especially with sinusoidal interface, has been studied only to a limited extend [27, 28, 101], which is one of the focus points of this work by considering a more application relevant FEM model. The influence of defects at the hole, such as recast layers, and a sensitivity analysis of material parameters on the stress distribution will also be analyzed.

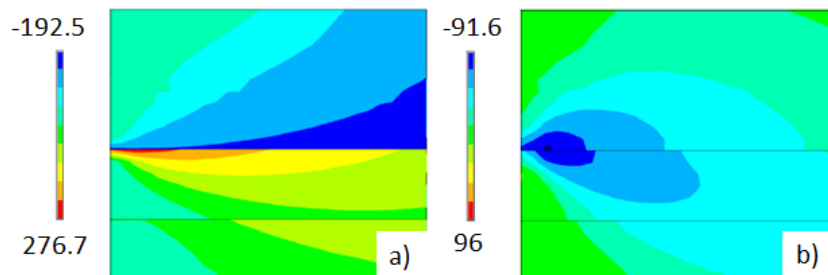


Figure 2.32: (a) Tangential and (b) shear stress distribution with an elastic TBC system at a hole edge [28].

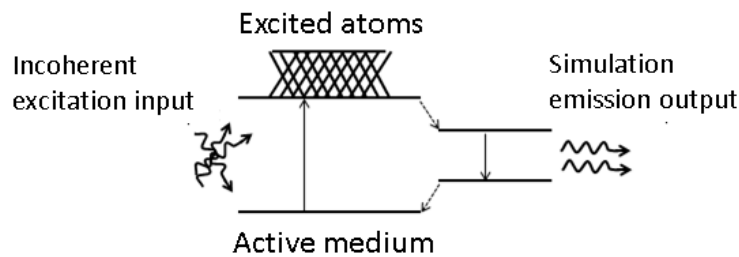
## 2.4 Processing of cooling holes for TBC-coated components

Cooling holes are drilled typically using one of the following three techniques: electrochemical machining (ECM), electro-discharge machining (EDM) and laser drilling [102]. The ECM process consists mainly of four components: power supply, workpiece, cutting tool, and electrolyte. The cutting tool is the negative electrode, cathode, where the workpiece acts as the positive electrode, anode, which is connected to the DC power supply. The electrolyte is flown rapidly between the electrodes, and material removal occurs due to high electric potential between the cutting tool and workpiece, resulting in its anodic dissolution [103]. In the EDM process the workpiece, anode, and the tool, cathode, are connected similarly to a power supply. The electrodes are immersed in a dielectric solution (kerosene for instance). When the distance between the electrodes decreases to a certain threshold, the dielectric solution breaks down and an electron current forms from the anode (tool) to cathode electrode (workpiece). The electrons will ionize the dielectric fluid and build a spark, which induces material removal of the workpiece. The dielectric liquid acts as the cooling fluid as well, and removes eroded material [103].

A laser system provides optical radiation with defined frequency which is controllable. There are basically three components in a laser system: an amplifying medium, an exciting medium, and an optical resonator [104], see Fig. 2.33. The amplifying medium (1) has the task to provide coherent laser pulses with a specific wavelength. For this purpose, typically irradiation of incoherent light (2) is used to create excited atoms in the medium. The emitted light from the medium is not already monochromatic and unidirectional as is the case by a laser light beam. These characteristics are produced by placing the medium in an optical resonator (3), for instance two parallel mirrors where the light will move back and forth through the excited atoms in between, and hence a coherent laser beam will be formed, which can be of high energy and used for material machining. The output laser is then transmitted to the target (in this case specimen surface) using a beam handling system, i.e. reflective or transmissive optics, which have to be able to tolerate intense laser beams. As a cooling system for the components exposed to extreme conditions water or air, for example, are used.



1. Amplifying medium: The means to amplify light by converting an incoherent to a coherent light beam



2. Incoherent light: The source for excitation of the atoms of medium to produce light with specific wave length

3. Optical resonator (mirrors): The means to oscillate the light for a coherent light beam

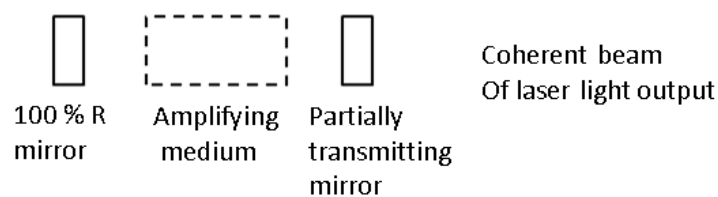


Figure 2.33: Three main parts of a laser system [104].

For EDM/ECM, the specimen should be fully electrically conductive, which is a problem for TBC-coated superalloys used in gas turbine components. For this purpose, the base material needs to be drilled first, and afterwards coated with TBC, resulting in the partial closure of the cooling holes. Additionally, drilling tools have to be used to open partially closed holes after TBC deposition. This makes EDM/ECM drilling more time consuming than faster methods such as laser drilling. Moreover, the electrolyte used by ECM is not environment friendly making this method not ideal [102]. The machining rate of EDM is lower than laser machining. These advantages of laser drilling versus EDM/ECM has increased the focus towards this method, despite its related problems which are recast layer formation as a result of incomplete molten material removal, as well as crack formation especially at the TBC/BC and BC/superalloy interfaces [105]. Fig. 2.34 shows, as an example, an inclined laser-drilled hole, showing typical cracks at interfaces on both leading edge and trailing edge.



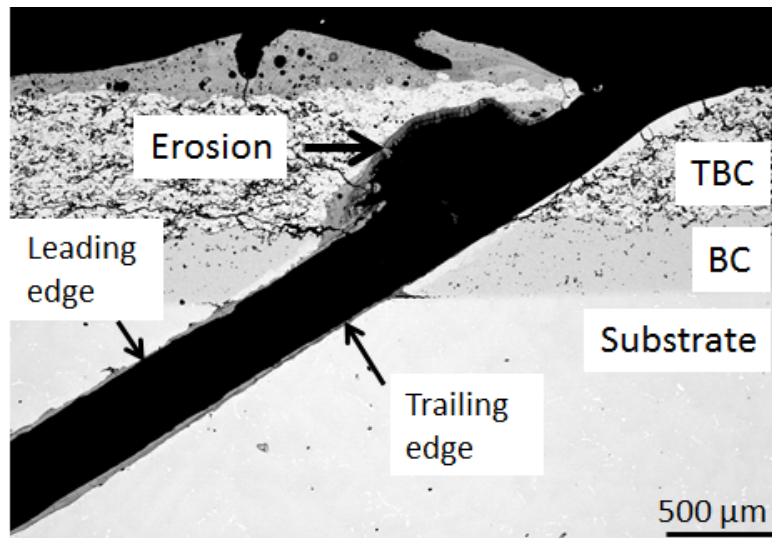


Figure 2.34: A typical laser-drilled hole in a TBC-coated superalloy (PWA 1483) with bond coating (Sicoat 2464), and an APS TBC, see section 4.1.

### 2.4.1 Flash lamp laser

By laser drilling of cooling holes, using pulses in range of milliseconds, the process of material removal is dominated by melting, see Fig. 2.35. The reason is that the laser pulse width is larger than the threshold needed for heat transfer from laser to the material. Additional to melting, part of the material becomes also vaporized. Due to vaporization, a pressure will be applied to the melt and causes its ablation. A remaining recast layer on the hole wall is a consequence of this ablation process [106].

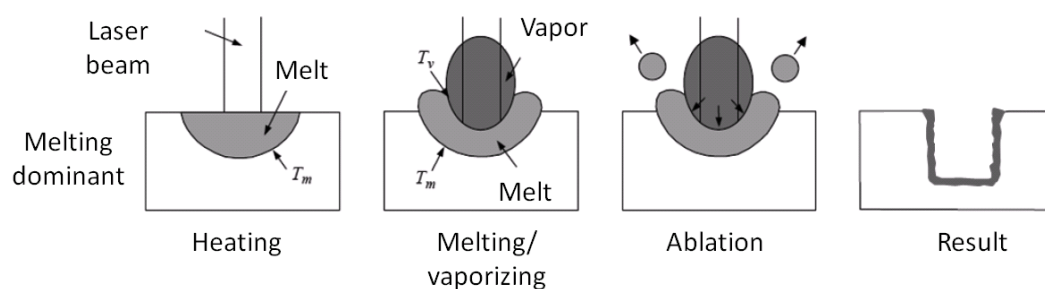


Figure 2.35: Process of a melting-dominant laser drilling [18].

Applying flash lamp laser drilling, typically a Nd:YAG crystal laser is used as the amplifying medium. Typically there is Xenon or Krypton in the lamps, which can radiate the wavelengths that are optimally received by the crystal laser. There are several problems that warrant improvement in the current state of laser drilling technology, which will be described in the following [104]. Typical damages experienced by the TBC system after long-pulsed drilling are illustrated in Fig. 2.36.

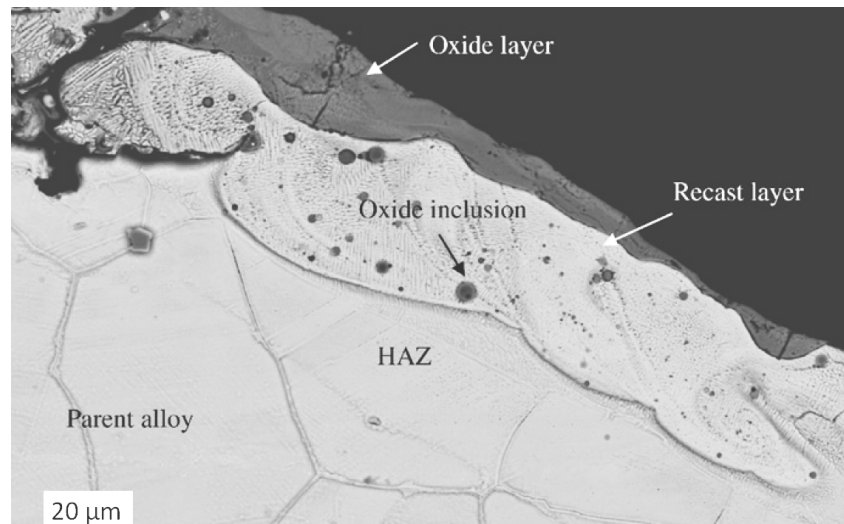


Figure 2.36: Typical defects after laser drilling; alumina formation due to oxidation, spinel oxides, heat affected zone (HAZ), substrate and zirconia recast layer [6].

There is a heat affected zone (HAZ) at the laser-drilled hole, where the material microstructure is slightly affected by the energy of the laser pulses. A recast layer, on top of HAZ, is obviously the resolidified molten material, which could not be ejected from the hole during laser drilling. Oxide inclusions can be found in this layer as well. On top of the recast layer, oxide layer can be formed during laser processing [6]. After laser drilling, a zirconia recast layer might be observed on the hole wall as well, especially on TBC, BC, and partly on the substrate [5, 107].

As already mentioned, these defects are mostly related to the incomplete ejection of molten or vaporized material from the hole [4–6]. Several research works have been focused on the aspect of the hole angle and its relationship to the formation of cracks after drilling [5, 6, 108, 109]. For coated materials, delamination of TBCs, especially on the leading edge of inclined holes appears to be a critical issue [5, 6], see Fig. 2.37 and Fig. 2.38. Such cracks can act as nucleation sites and grow during service of the turbine blade, especially under the respective thermomechanical loading conditions, leading to a lifetime reduction [3]. Kamalu et al. [109] suggested a two phase mechanism for formation and propagation of cracks. Cracks are suggested to be induced by the thermal mismatches between the ceramic TBC, metallic BC, and the superalloy, already during the first laser pulse, and in the next phase the cracks propagate due to the mechanical stress related to the explosive recoil pressure of the subsequent laser pulses. Sezer et al. [5] performed a CFD analysis for melt ejection during drilling process, where they suggested that such delamination cracks are a result of higher velocity gradients of molten material on the leading edge, which induced higher forces and shear stresses, challenging the bond strength of TBC/BC and BC/substrate interfaces. Owing to a higher normal and shear stress at the hole entrance near to the leading edge, due to vortex formation, erosion of TBC was also observed, see Fig. 2.34. Girardot et al. [107] tried to quantify the cracking mechanism associated with laser drilling. Using numerical calculations, they showed how the forces of the molten material change when the laser beam angle is varied. The forces are higher in case of a smaller angle to the surface, independent of TBC thickness. However, the applied moment due to such forces is higher in case

of a thicker TBC, implying that a thinner coating is beneficial in this respect. Thus, the crack propagation was concluded to be mostly due to mechanical stresses associated mainly with the subsequent laser pulses. Drilling inclined holes increases the oxide layer, recast layer, and heat affected zone [6], see Fig. 2.37.

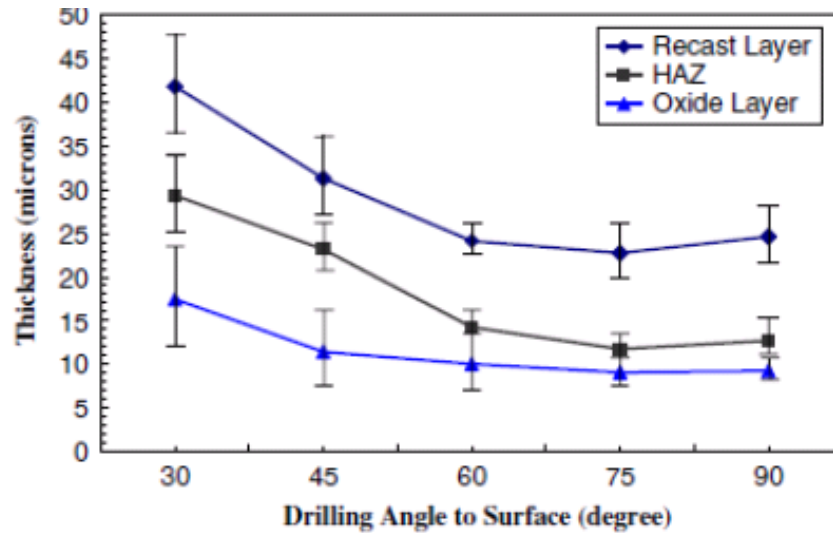


Figure 2.37: The effect of cooling hole angle on HAZ, oxide and recast layer [6].

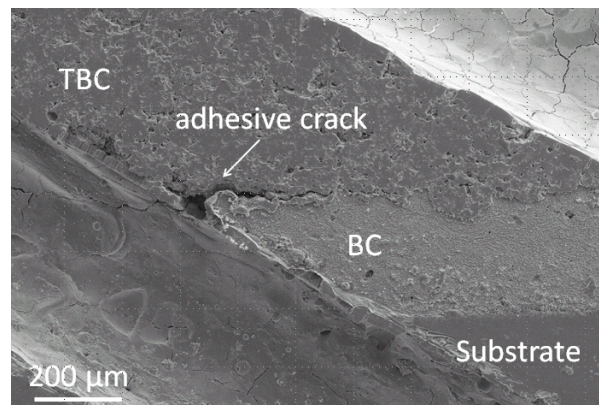


Figure 2.38: Delamination crack near the TBC/BC interface at the leading edge; TBC system consisting of a nickel-based superalloy IN 792 CC as the substrate, the MCrAlY bond coating LCO22, and an air plasma sprayed (APS) yttrium-stabilized-zirconia (YSZ) TBC, see section 4.3.

## 2.4.2 Fiber laser

Fiber laser systems offer a laser emission with an intensity of  $10^8 \text{W/cm}^2$  and a pulse width in the range of few 100  $\mu\text{s}$  to a few ms. Material removal process is dominant by melting similar to flash lamp laser. Fiber laser emission sources are available since 2011 with pulse power greater than 6 kW. In comparison with flash lamp laser, the higher pulse-to-pulse stability and reproducibility (38 % less tolerance of hole diameter [17]) makes the fiber laser method standing out to produce holes with constant diameter [110]. Moreover, the

effectiveness of this laser source is with 28 % around 14 times higher, production costs are 2 times less, and the pulse intensity larger than flash lamp drilling [106]. As for flash lamp laser, the focus diameter of the laser beam is dependent on the pulse energy or power, whereas for fiber laser these two parameters are independent leading to more flexibility. Nevertheless, the maintenance and adjustment of such laser systems due to use of flexible glass fibers is more difficult.

Fig. 2.39 shows the main components of a fiber laser. There are several laser diodes which pump up the laser beam into the active fiber using pump coupling. Active fiber acts as an amplifying medium, which is doped with rare earth elements such as Erbium, Ytterbium etc. At the ends of the active fiber there are two Fiber-Bragg-Gratings (FBG), where one of them acts as the end mirror, and the other acts as a filter for passing the required wave length, with nearly no loss in the coupling of active and passive fibers. The laser beam is afterwards driven by passive fiber lasers to the fiber coupling and optic processor units, and finally the specimen surface for machining [111]. Using the fiber coupling unit, different fiber laser cables with various diameters can be used for laser beam handling. The optic processor unit has the task to guide the laser beam with suitable parameters to the specimen surface, see section 3.1.2 for more explanations.

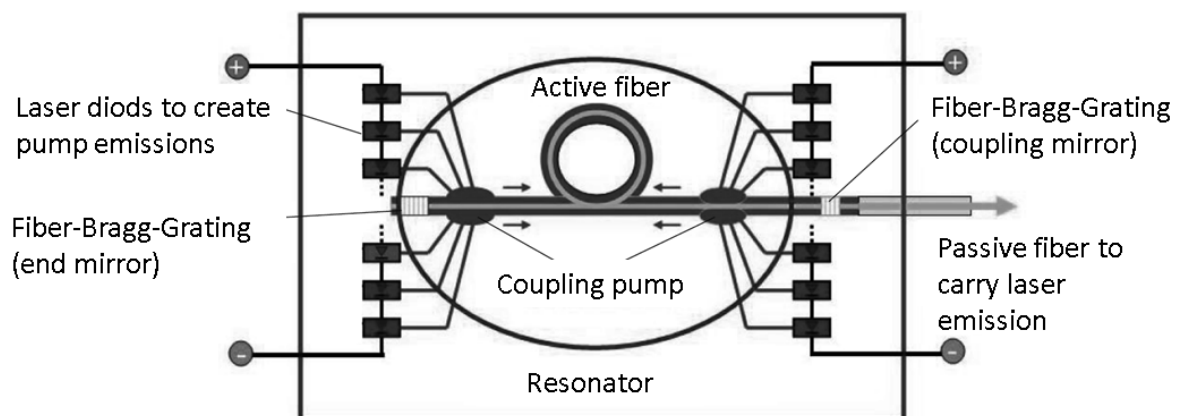


Figure 2.39: Components of a fiber laser system [111].

### 2.4.3 Ultra-short pulsed (USP) laser

First USP laser systems provided ultra-short laser pulses (a few 100 fs) with very small pulse energy and mean power (a few Watts). To enhance the pulse power, the MOPA (Master Oscillator Power Amplifier) principle was later used, where a master oscillator (seed laser) emits pulses with high frequency but with small pulse energy. In the next step, an electronic optical modulator (EOM) reduces the pulse frequency and passes to the power amplifier. The amplifier boosts the pulses, increasing the pulse energy and mean power [106].

The material removal process by ultra-short pulsed laser is vapor dominated. By using this method, the thermal effect on the hole wall is minimum [18]. Since the pulse width is in range of the threshold necessary for heat transfer between atoms, and the conducted heat is negligible, this method provides a perfect quality of laser-drilled hole. According

to the work of Dou et al. [112], at least 1.5–3 picoseconds pulses are necessary so that the heat travels between the electrons and the lattice.

The drilling time increases for USP drilling due to its much smaller pulse widths. Measurements [113] have shown that optimized quality of hole geometry and minimum thermal effect can be achieved for pulse widths around 5–10 ps. Using USP laser nearly no delamination or micro-defect as well as no HAZ, recast- and oxide layer was found on the drilled cross-sections [16], see Fig. 2.40.

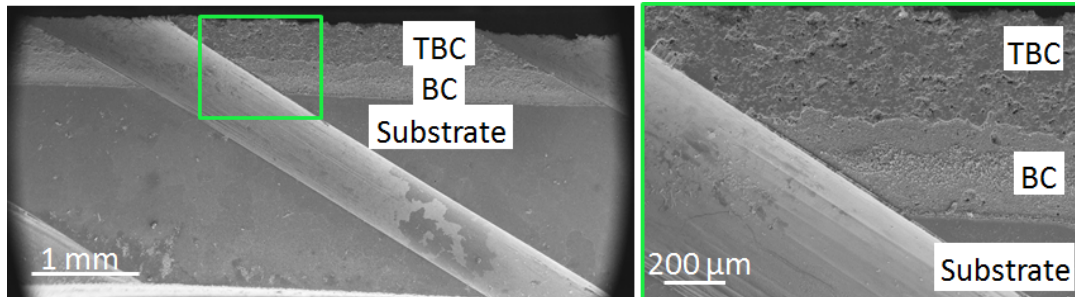


Figure 2.40: Microscopic images of cross-sectional view of a hole, drilled by a picosecond laser method where no crack can be observed at the interfaces; TBC system consists of an APS TBC, MCrAlY bond coating, and a IN792 superalloy, see section 4.3. The images are produced by the Chair of Laser Technology in RWTH Aachen University,

#### 2.4.4 Percussion and trepanation drilling

Laser drilling might be carried out in two modes. By percussion drilling, multiple pulses are emitted to the specimen surface, whereas the laser nozzle position is fixed, see Fig. 2.41a. Using this drilling mode, there is a recast layer on the hole wall, as well as a tapering in the hole geometry which is sometimes not needed [105]. By trepanation drilling, the laser nozzle moves in a circular way, see Fig. 2.41b. This method is essentially percussion drilling and a subsequent cutting in a circular movement. In order to obtain more precise hole geometry as well as holes with larger diameter, this method is preferred [105].

Trepanation drilling has been suggested in literature [10–12] as a method to provide better quality holes than percussion drilling. Trepanation can also be used to drill larger holes with good quality, as it is more similar to a conventional cutting process. However, a detailed comparison of these two drilling modes appears not to be available in literature, which is hence one of the focuses of this study.

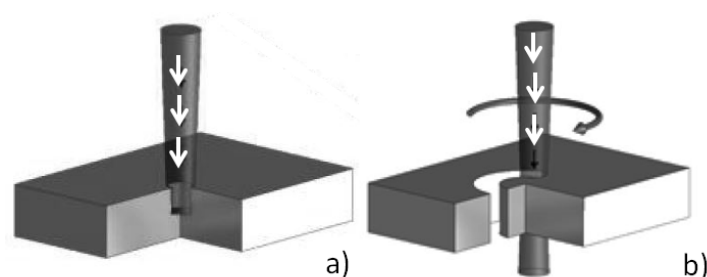


Figure 2.41: (a) Percussion and (b) trepanation drilling [106].



# Chapter 3

## Experimental method and FEM modelling of thermomechanical response of TBC-coated superalloy

### 3.1 Laser drilling systems

In this section, the chosen laser systems for drilling of cooling holes in specimens tested in this thesis are described. The laser processing has been performed by the Chair of Laser Technology in RWTH Aachen University.

#### 3.1.1 Flash lamp laser

The flash lamp laser drilling system was a Lasag FLS 652 N, illustrated in Fig. 3.1. The specifications of this system are listed in Table 3.1. The FLS-N laser system series provides a pulsed Nd:YAG laser with an averaged power of 300-600 W and a max pulse power up to 50 kW. Holes in the range of 0.02 to 1.5 mm can be drilled with flash lamp laser in percussion drilling mode.

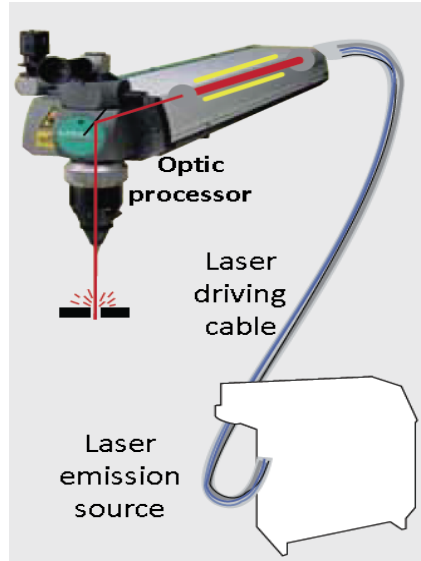


Figure 3.1: Fundamental system of flash lamp laser method.

Laser emission source: Lasag FLS 652 N	
Laser type	pulsed Nd:YAG solid-state laser
Wave length	1064 nm
Pulse width	0.1 - 20 ms
Repetition rate	0.1 - 1000 Hz
Pulse energy	60-150 J
max. power in average	300-600 W

Table 3.1: Features of the flash lamp laser emission source Lasag FLS 652 N.

### 3.1.2 Fiber laser

The system used for performing fiber laser drilling consists of 4 components; fiber laser source, radiation driving fiber, fiber coupling, and the optic processor.

The experiments were performed with a YLS-600/6000-QCW from the company IPG Photonics. The parameters of the laser source are listed in Table 3.2.

Laser emission source: IPG YLS-600/6000-QCW	
wave length	1068 - 1072 nm
Pulse width	0.2 - 10 ms
Repetition rate	10 - 500 Hz
max. power in CW-mode	600 W
max. power in pulsed mode	6000 W
Power stability	$\pm 1\%$
Output fiber core diameter	50 $\mu\text{m}$

Table 3.2: Features of the fiber laser emission source IPG YLS-600/6000-QCW

Flexible glass fibers are used to transport the laser emission from the source, which can be



called emission driving fibers. Through fiber coupling, the laser beam can be transferred from such fibers to the process fibers, which can have different core diameters such as 50, 100, 150, 200, 300 and 400  $\mu\text{m}$  [106].

In order to couple emission driving and process fibers, a coupling system with a fiber to fiber coupling unit (FFC) from the company Optoskand has been used. The laser emission enters the FFC and will be collimated, see Fig. 3.2. Afterwards, the laser emission will be focused into the process fibers using a focus lens. With a 5 kW input power, for example, the lost power should not be more than 100 W, which yields an efficiency of 98 % of the coupling system.

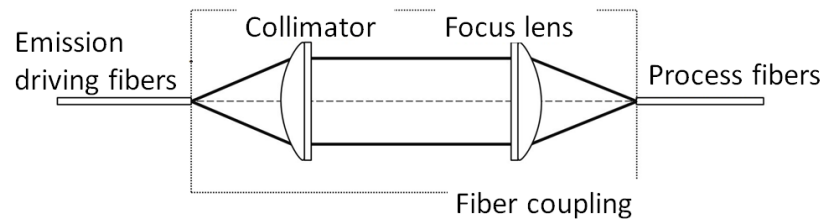


Figure 3.2: Fundamental system of laser coupling [114].

Different sections of the optic processor are shown in Fig. 3.3. The laser beam is basically received by the receiver part of the processor. Afterwards, the beam will be collimated by the collimator, and then distributed using an emission divider module. The next section is installed to provide inert gas to the processor in order to get a better machining quality. In the following step, the laser beam will be focused on the nozzle module and emitted for machining. Using a specific adapter the nozzle distance can be changed according to the desired focal length [106].

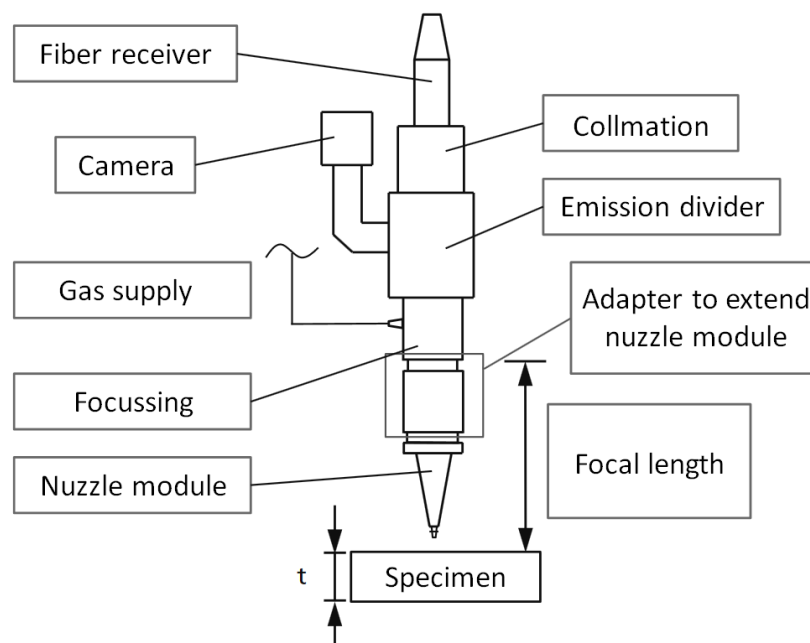


Figure 3.3: Components of an optic processor [106].

### 3.1.3 USP laser

Fig. 3.4 shows the laser system used for ultra-short pulsed laser drilling, which includes a laser emission source, deflection mirrors, Galvo scanner, and gas supply section.

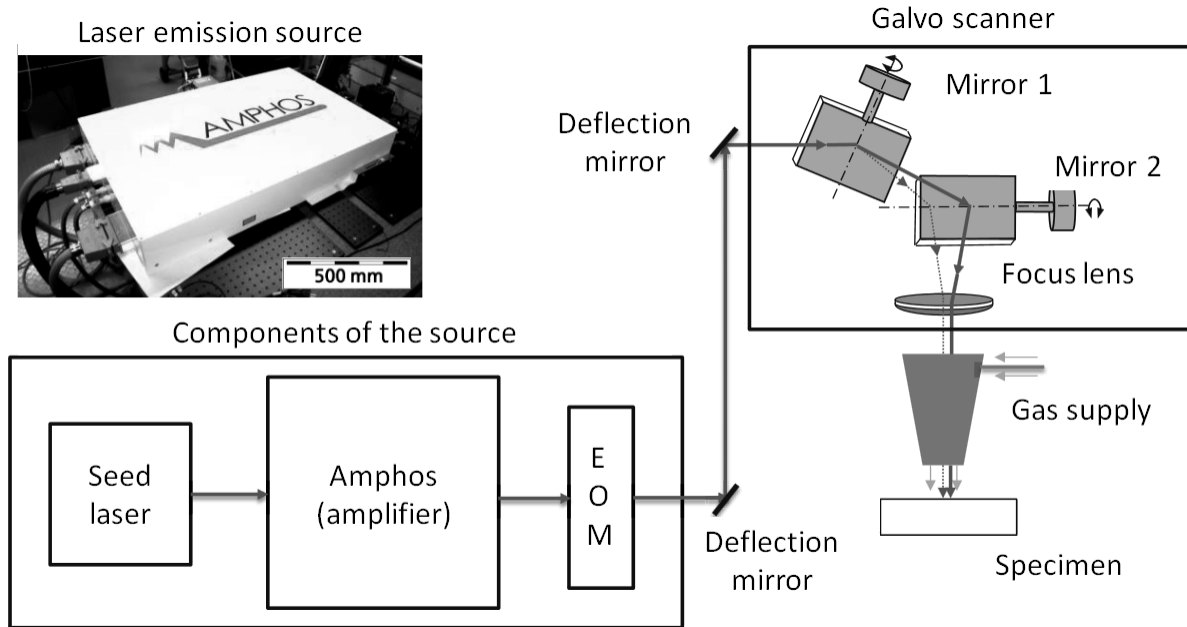


Figure 3.4: Components of the ultra-short pulsed laser system [106].

The laser emission source for ultra-short pulsed laser was from Amphos company. The emission source consists of three parts: seed-laser, electro-optic modulator (EOM) and an amplifier. The seed-laser emits pulses in the range of 0.70 to 7.65 ps with small pulse energy of around 90 nJ and a high frequency of 1.43 to 56.8 MHz. Afterwards, the amplifier increases the averaged power and pulse energy up to 400 W and 256  $\mu\text{J}$  [106]. In the next step, the EOM reduces the pulse frequency of the emitted pulses from the seed-laser by the so-called pulse picking process, where the EOM receives only a specific part of the pulses. The features of this laser source are given in Table 3.3. The mentioned specifications are related to laser drilling of the flat specimens, see section 3.2.

Laser emission source: Amphos 400	
Wave length	1030 nm
Pulse width	0.69 - 7.65 ps
Repetition rate of Seedlaser	1.43 - 56.8 MHz
Repetition rate of pulse picking	100 - 1000 kHz
max. averaged power	400 W
Pulse energy	$\leq 285 \mu\text{J}$

Table 3.3: Features of the laser emission source Amphos 400.

Ultra-short laser pulses cannot be transferred by glass fibers, since such laser emission, after passing the amplifier, might have a very high pulse peak power, in the range of

several 10 MW, and hence can damage such fibers. Therefore, the laser emissions are transferred by using deflection mirrors, which are specific for certain wave lengths. As for optic processor, a Galvo scanner from Aerotech company was used. There are two rotating mirrors in this scanner that can be adjusted electronically. These mirrors will rotate the laser beam onto the specimen surface. The focal length of the focus lens in the scanner is 163 mm [106].

A compilation of the laser processing parameters for drilling of the specimens are shown in Table 3.4. Please note that in this work, the number of pulses required for drilling a vertical hole is around half of the pulses needed for drilling an inclined hole.

Laser parameters	Flash lamp, percussion, 90° & 30°	Flash lamp, trepanation, 90° & 30°	Fiber, trepanation, 90° & 30°	Fiber, percussion, 90° & 30°
Power, kW	7.3	10	5.5	6
Pulse width, ms	0.75	0.6	0.5	0.7
Repetition rate, Hz	20	13	100	60
Process gas, bar	5 bar/compressed air	8 bar/compressed air	5 bar/compressed air	5 bar/compressed air

Table 3.4: Laser parameters used for drilling the specimens

For USP laser drilling of flat specimens, see section 3.2, the mean power and repetition rate are 80 W and 238 kHz, respectively, whereas for the LCF specimens, see section 3.4, these parameters are 45 W and 50 kHz.

## 3.2 Laser drilling of TBC systems

Flat specimens, provided by Siemens AG, were laser drilled with fiber laser and flash lamp laser including trepanation and percussion drilling modes, as well as ultra-short pulsed laser. The base material was a PWA 1483 nickel-based superalloy, the BC Sicoat 2464 (180- 300  $\mu\text{m}$ ), and the TBC was deposited from an IKH powder with a porosity of 18+/-4% (500  $\mu\text{m}$ ). The diameter of all the holes was 500  $\mu\text{m}$ . To understand the influence of the drilling angle, both vertical and inclined (30° with respect to TBC surface) holes were drilled. The specimens were drilled according to the test matrix in Table 3.5. The laser parameters used for drilling are listed in Table 3.4. Parameters for USP-drilled specimens are described below Table 3.4 as well.

Specimen type	hole diameter (mm)	Angle
Fiber laser,percussion	0.5	90
	0.5	30
Fiber laser,trepanation	0.5	90
	0.5	30
Ultra-short pulsed laser	0.5	90

Table 3.5: Test matrix for laser-drilled TBC systems.

### 3.3 Cyclic oxidation of laser-drilled TBC systems

Thermal cycling tests were performed in order to understand the effect of different laser drilling methods on the coating adherence of a TBC system based on a coated superalloy with and without cooling holes. The chosen TBC system consists of IN792 substrate with two types of bond coating: aluminized LCO22 and not aluminized PWA286, and an APS TBC coating, see Table 3.6. The TBC coating consisted of yttria-stabilized zirconia with the percentage ratio 92%/8%. It should be mentioned that the results presented are based on one sample for each laser drilling process.

Substrate	IN 792/0.7±0.3 mm	
BC	LCO22 / 200 µm/with Al	PWA 286/ 200 µm / no Al
TBC	APS/300µm	
Length of the specimens	ca. 22 mm	
Number	6	4

Table 3.6: Composition of the specimens tested with cyclic oxidation.

To study the influence of the hole angle on the cyclic oxidation behavior of the TBC system, the cooling holes were drilled using flash lamp laser (see Table 3.1 for the properties of the laser system) with percussion mode at 90° (200 pulses) and 30° (400 pulses) degree with respect to the surface of TBC, as well as with fiber laser using percussion mode and trepanation modes, see the fiber laser system in Table 3.2 and the test plan in Table 3.7. The laser parameters used for drilling holes with different methods can be found in Table 3.4. The hole diameter was in all cases 500 µm. The specimens had a cylindrical geometry with three rows of holes with a 120° shift with respect to each other, as well as two holes on every row, see Fig. 3.5. Specimens had a diameter of 7.8 mm.

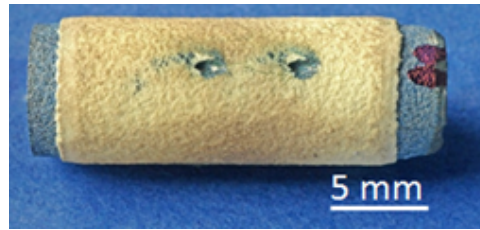


Figure 3.5: A cyclic-oxidation specimen with laser-drilled holes.

Specimen type	bond coating type			
	LCO22		PWA 286	
	hole diameter (mm)	Angle	hole diameter (mm)	Angle
Flash lamp, percussion	0.5	90	0.5	90
	0.5	30	0.5	30
Fiber, trepanation	0.5	30	0.5	30
Fiber, percussion	0.5	30	0.5	30

Table 3.7: Test matrix for cyclic oxidation tests.

Two other specimens were also tested to see the influence of hole diameter by considering the values 0.5 mm and 1 mm. A second specimen with cooling holes of a diameter of 0.5 mm was tested until the midlife in order to analyze deeper the failure progress. The TBC system consists similarly of IN792 substrate with LPPS LCO22 BC and an APS TBC coating. The specimens were drilled with fiber laser and trepanation mode with the laser processing parameters shown already in Table 3.4.

Specimen type	hole diameter (mm)	Angle (degree)
Fiber, trepanation	0.5	30
	1	30

Table 3.8: Test matrix for cyclic oxidation tests for analysis of the influence of cooling hole diameter.

Cyclic oxidation tests were performed using a tube furnace (Carbolite-Gero GmbH, Model 301), with a minimum temperature of 100°C and a maximum of 1050°C, including a heating time of 2 hours and 12 min as well as a cooling time of 5 min. Failure was defined as the number of cycles at which a segmentation macro-crack was observed by human eye. The components of the furnace are shown in Fig. 3.6. The furnace is controlled using a computer program, written in LabView, which is implemented in the corresponding furnace regulator. As the heating phase starts, the furnace lid opens and the slide moves on the rail and enters the specimen into the furnace. When the heating period ends, the slide moves out until the cooling phase finishes. The temperature profile at the specimen, measured by thermoelements, is shown in Fig. 3.7.

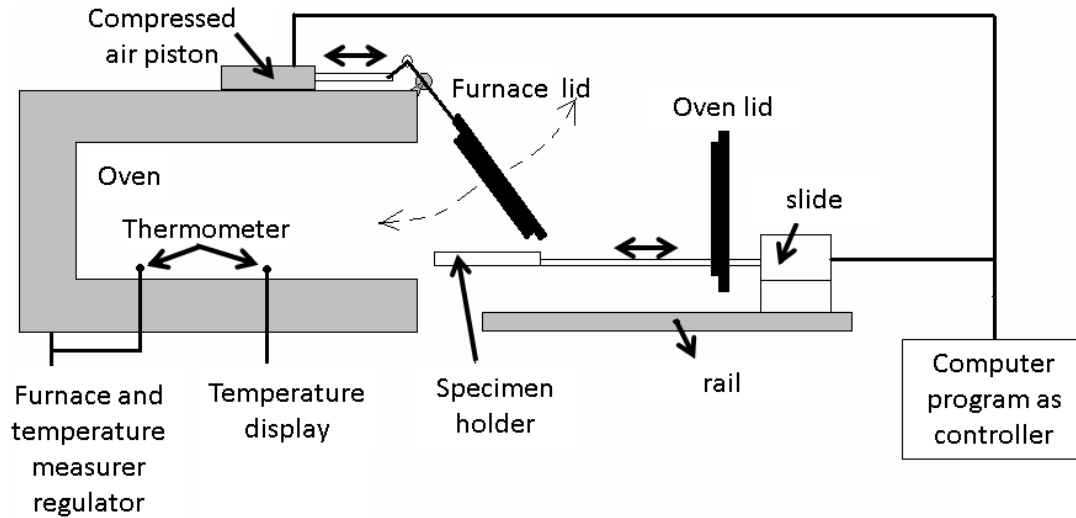


Figure 3.6: Components of the furnace used for cyclic oxidation tests.

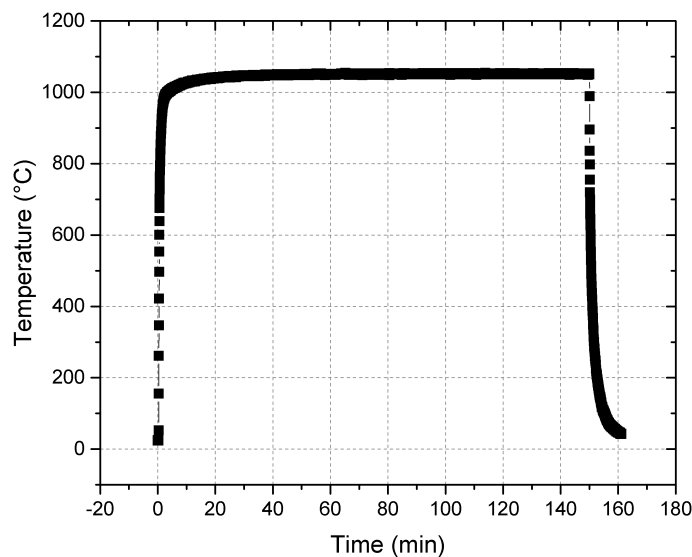


Figure 3.7: Measured specimen's temperature in the cyclic oxidation furnace.

After defined number of cycles, thermography images were recorded using an infrared camera (FLIR, ThermaCam SC3000). For thermography images, the samples were heated in 0.4 s with two flash lamps, and during cooling-down 20 images are recorded with a frequency of 50 Hz. The thermography images were obtained using temperature profile analysis available in the software ThermoLab [115]. At positions where the coating potentially delaminated from BC or substrate, the heat flux decreases leading to a higher temperature compared with the surroundings. These images are typically presented in a greenish format, where green areas represent regions with interface in-contact and yellow to red areas represent delaminated regions, see Fig. 3.8 as an example.

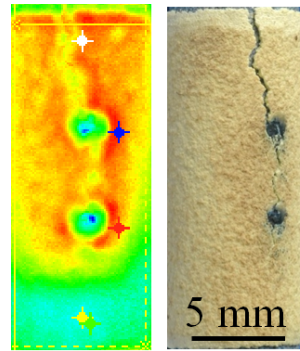


Figure 3.8: Thermography image can be seen on the left, where the delaminated region is shown in red. An image of the coated specimen is shown on the right for the same region. The arrows indicate the position of the crack.

To perform microscopy investigations, specimens were embedded in a mixture of epoxy and hardener solution. After hardening of the epoxy, specimens were cut at the laser holes (using ISOMET 4000 cutting machine, from Buehler company). Afterwards, the specimen were grinded and then polished successively with 6, 3, 1  $\mu\text{m}$ , and very fine diamond suspensions.

After the necessary preparation of the specimens, microstructural analysis was performed using secondary electron microscopy (SEM), using a Zeiss SUPRA 50 VP, electron backscattered diffraction (EBSD) using the machine Oxford Instruments X-Max, and energy dispersive spectroscopy (EDS) by Oxford Instruments Nordlys.

### 3.4 Influence of LCF loading on life time of laser-drilled TBC systems

With the purpose to understand the influence of hole quality especially in the base alloy under mechanical fatigue, LCF tests have been performed on undrilled and laser-drilled TBC-coated superalloy at 850  $^{\circ}\text{C}$ , to be able to simulate the operation conditions in a gas turbine optimally. The advantage of LCF tests is the lower time consumption of these experiments, which is the reason that the focus was more on such mechanical tests in comparison with TMF tests.

In order to analyze the material behavior at different application-relevant loading conditions, two distinct mechanical strain ranges in LCF regime were chosen, 0.38 % and 0.67 %, with  $R = -1$ , see loading profile in Fig. 3.9, and a standard strain rate of 6 %/min, see Table 3.9. The failure criterion was rupture or 30 % stress reduction from the maximum stress of 100<sup>th</sup> cycle where the material response has been stabilized. This is a mutual failure criterion regarding the tests performed by the industrial partners.

The TBC system consisted of a APS TBC coating, a LPPS CO-211 BC, and IN 792 CC nickel-based superalloy, which had a thickness of  $500 \pm 75 \mu\text{m}$ ,  $240 \pm 60 \mu\text{m}$ , and 1.75 mm respectively, see Table 3.10.



LCF Parameters				
T, °C	R= $\epsilon_{min}/\epsilon_{max}$	mechanical strain range, %	strain rate	failure criterion
850	-1	0.38 or 0.67	6%/min	30% stress reduction

Table 3.9: Test parameters for LCF tests

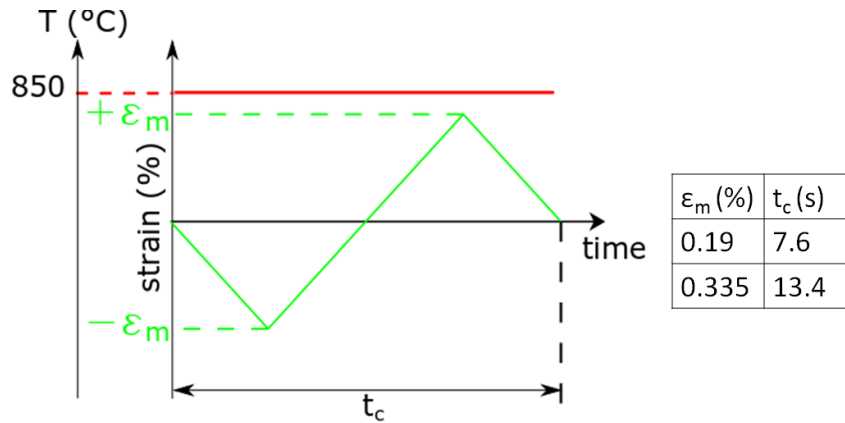


Figure 3.9: LCF loading profile.

Material system		Thickness
Substrate	IN 792 CC	1.75 mm
BC	LPPS: CO-211, Ra 11±2 $\mu m$	240±60 $\mu m$
TBC	APS TBC	500±75 $\mu m$

Table 3.10: Material data of the TBC system for LCF tests.

The sample sketch for LCF tests is shown in Fig. 3.10. The specimen is hollow and the measurement length is 35 mm long where the substrate thickness is 1.75 mm. The TBC coating is deposited overall the specimen to prevent heat absorption by the uncoated surface.

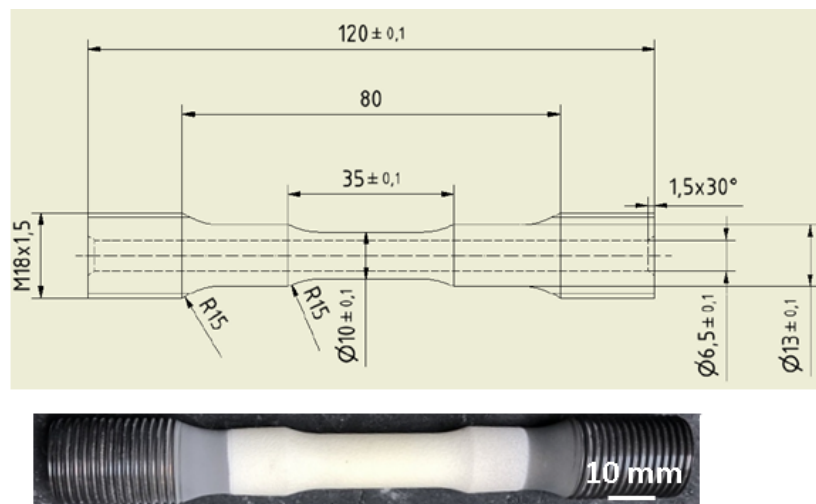


Figure 3.10: Sketch of an undrilled LCF specimen.

For drilled specimens, three cross sections were laser drilled. At each section, 3 cooling holes were drilled with  $120^\circ$  angle with respect to each other. The ordering of the laser-drilled cooling holes is shown in Fig. 3.11.

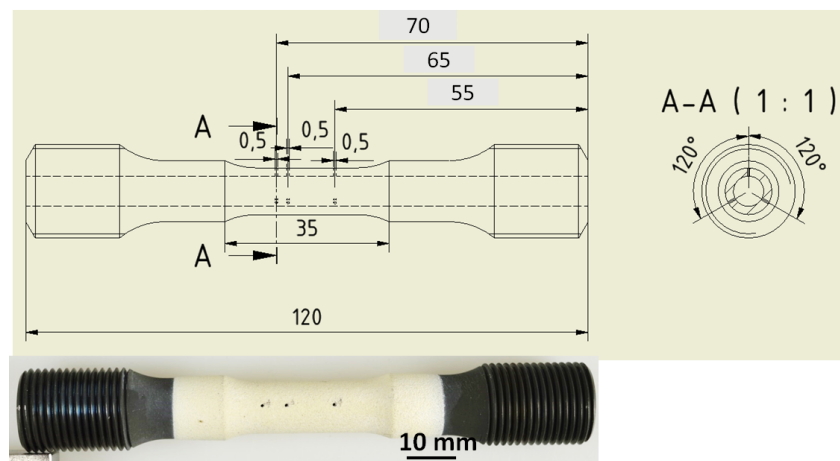


Figure 3.11: Sketch of the laser-drilled cooling holes in a LCF specimen.

The LCF test matrix is shown in Table 3.11. Specimens were drilled with flash lamp (FL) in trepanation mode, as the current state of technique, as well as USP laser as the most advanced method. Specimens were drilled at  $30^\circ$  and  $90^\circ$  angles with the purpose of analyzing the influence of inclination under mechanical cyclic loading. For both higher strain range, undrilled specimens were tested to understand the effect of cooling hole on life time and failure mechanism.

The LCF tests were performed using a universal testing machine (Instron, model 8802) with a 100 kN load cell (50 kN dynamic / 100 kN static) equipped with a 24 KW-infrared furnace (24 halogen lamps, 1 kW each) from Xerion GmbH. To obtain the desired temperature distribution over the coating with a gradient with respect to the

strain range, %	specimen type	
0.67	undrilled	
	FL, 30°	USP, 30°
	FL, 90°	USP, 90°
0.38	undrilled	
	FL, 30°	USP, 30°
	FL, 90°	USP, 90°

Table 3.11: Test matrix for LCF experiments, FL: flash lamp laser, USP: ultra-short pulsed laser.

superalloy, IR lamps were arranged in 3 circuits, each containing 8 lamps. Using compressed air, cooling and heating can be applied with adjustable rate. The temperature was calibrated using 3 pyrometers and Pt/Pt-Rh-thermocouples. The temperature profile during the test was measured by the pyrometers. Deformation was measured with 2 high-temperature extensometers from MTS systems GmbH, installed at 2 points on BC outside of measurement length. An overview of the LCF testing equipment is given in Fig. 3.12.

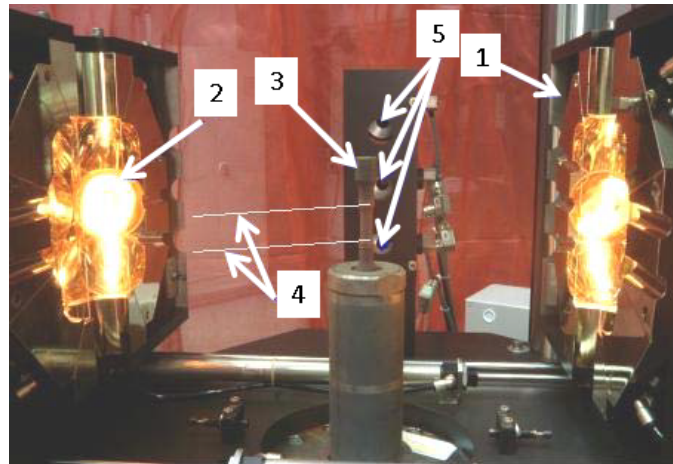


Figure 3.12: Overview of the LCF testing equipment: 1- furnace half; 2- lamp with reflector; 3- specimen; 4- extensometers; 5- optical pyrometers [19].

### 3.4.1 Measurement of temperature gradient during LCF test at 850°C

The temperature gradient was measured using a calibration TBC-coated LCF specimen shown in Fig. 3.13. Three thermoelement holes, of the diameter 0.6 mm, were machined using EDM at different distances; 50 mm, 60 mm, and 70 mm with respect to the specimen end. Thermoelements of type S were used for these measurement. Three elements were installed on TBC surface at the distances mentioned above, and three other elements were inserted into the thermoelement holes. The nominal temperature on the specimen was set to 850°C.

The average temperature values for the last 10 min are shown in Fig. 3.14a. The

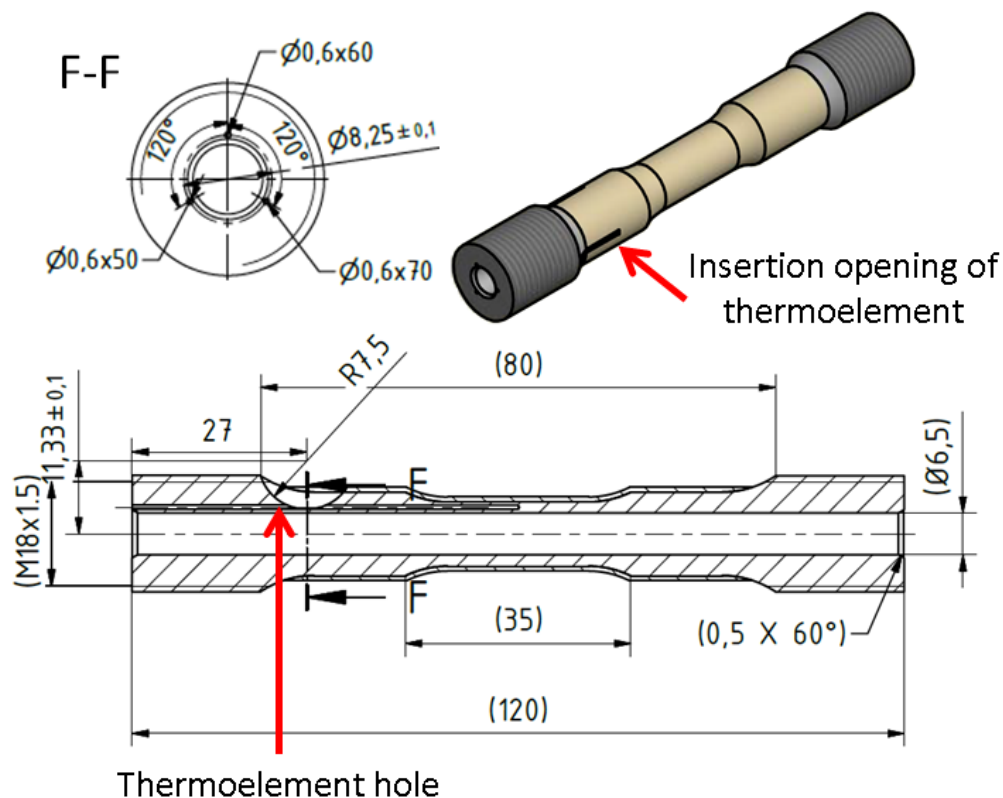


Figure 3.13: Sketch of the calibration TBC-coated specimen used for the measurement of the temperature gradient by machining 3 thermoelement holes with EDM (Units are in mm).

temperature gradient is maximum at the middle section, 34°C. The temperature gradient at the upper and lower section are 7°C and 2°C. The superalloy experiences the maximum temperature in the middle section. The positioning of the specimen in the test machine is shown in Fig. 3.14b. The results of the whole measurement of the temperature gradient are shown below, see Fig. 3.15. It can be observed that after around one hour, the temperatures become stable.

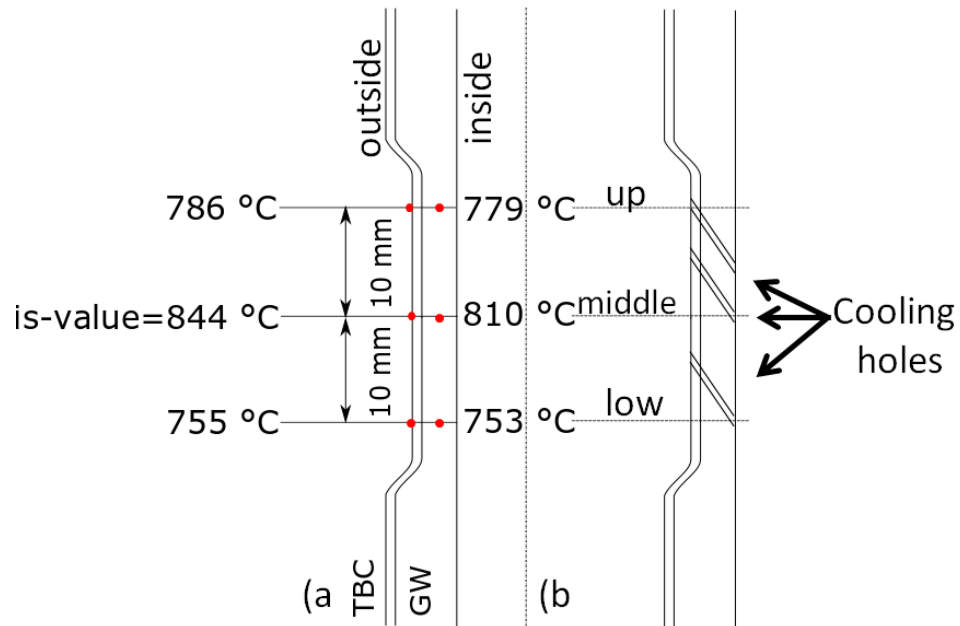


Figure 3.14: a) Average temperature of the last 10 min at the three sections, "up", "middle", and "low", on TBC surface and in superalloy as shown with red points, b) the schematic of cooling holes during the LCF test.

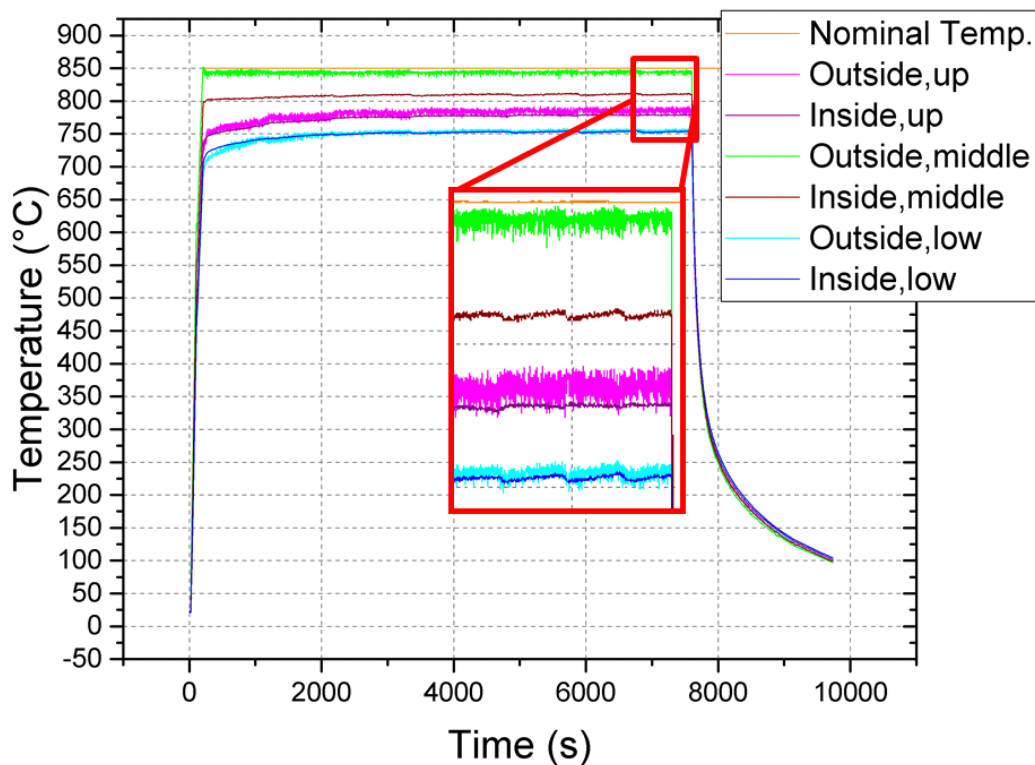


Figure 3.15: Measurement of the temperature gradient of the TBC-coated IN 792 CC with the nominal test temperature 850 °C.

## 3.5 FEM simulations

In the following, the FEM simulations of laser-drilled TBC systems under thermal loading conditions are described in details. Simulation of the FEM model under LCF loading was not the project's plan.

### 3.5.1 Material system

A visco-elastic model for TBC layer and substrate, and visco-plastic (ideal plasticity) for TGO and BC were chosen in the FEM model. In Table 3.12, the temperature-dependent material parameters:  $E$ -modulus, Poisson ratio  $\nu$ , Yield strength  $\sigma_y$ , and coefficient of thermal expansion CTE  $\alpha$  are listed. In regard with the values not shown for BC and substrate (marked with  $\vdots$ ), refer to Bednarz [23]. For the other temperatures not listed in the table, the values will be inter- or extrapolated by ABAQUS. The creep rates are chosen as an average values for simplification, as listed in Table 3.13. The data in these two tables are used in the reference simulation, and some of the properties are changed in the sensitivity analysis, which will be explained in details later, see Table 3.14.

Layer	$T(^{\circ}\text{C})$	$E(\text{GPa})$	$\nu$	$\sigma_y(\text{MPa})$	$\alpha \times 10^{-6}(\text{K}^{-1})$
TBC	25	17.5	0.2		9.68
	400				
	800				9.88
	1000	12.4			10.34
TGO	25	380	0.27	1200	5.1
	800	338			
	1000	312			9.8
BC	25	152.4	0.311	868	12.3
	50	151.1	0.312		12.8
	$\vdots$	$\vdots$	$\vdots$		$\vdots$
	1000	58.5	0.352		19.4
	1100	41.07	0.354	38	20.2
Substrate	25	130.7	0.363		11.7
	50	128.9	0.3633		11.8
	$\vdots$	$\vdots$	$\vdots$		$\vdots$
	1000	78.78	0.3869		13.8
	1100	76.64	0.3887		13.9
References	[23, 116–118]	[116–118]	[118]	[116, 119]	[116–118]

Table 3.12: Material properties of the TBC system. For the values not shown for BC and substrate (marked with  $\vdots$ ), refer to Bednarz [23].

A simple Norton power law model was used for creep simulation, similar as used in

several other reports [25, 26]:  $\dot{\epsilon} = B\sigma^n$ , where  $\dot{\epsilon}$  and  $\sigma$  are creep strain rate and creep stress, respectively, and  $B$  and  $n$  Norton law coefficients.

Layer	T(C)	B(S <sup>-1</sup> MPa <sup>-1</sup> )	n
TBC[120]	1000	1.8e-7	1
TGO[23]	1000	7.3e-4	1
BC[117]	600	6.54e-19	4.57
	700	2.2e-12	2.99
	800	1.84e-7	1.55
	850	2.15e-8	2.45
Substrate[23]	10	4.85e-36	1
	1200	2.25e-9	3

Table 3.13: Creep properties of TBC system

### 3.5.2 Axisymmetric model

In order to study the effect of TBC and BC/substrate recast layer on the hole wall (diameter 500 $\mu\text{m}$ ), an axisymmetric model with 4-node axisymmetric continuum solid element CAX4R was used to reduce computational time, see Fig. 3.16. The axis of symmetry, the yellow dash line in Fig. 3.16, is the hole axis, so that the left edge in the model simulates the hole edge. The analysis was performed only for 1 cycle with a specific TGO thickness of 0.5  $\mu\text{m}$ , which represents a more realistic case since BC temperature is typically around 950° C in a gas turbine and the oxidation rate is moderate. For the TBC/BC interface, a sinusoidal model was used with an amplitude of 15  $\mu\text{m}$  and a wavelength of 60  $\mu\text{m}$ . Thickness of TBC, BC, and substrate were 500  $\mu\text{m}$ , 250  $\mu\text{m}$ , and 1.75 mm, respectively.

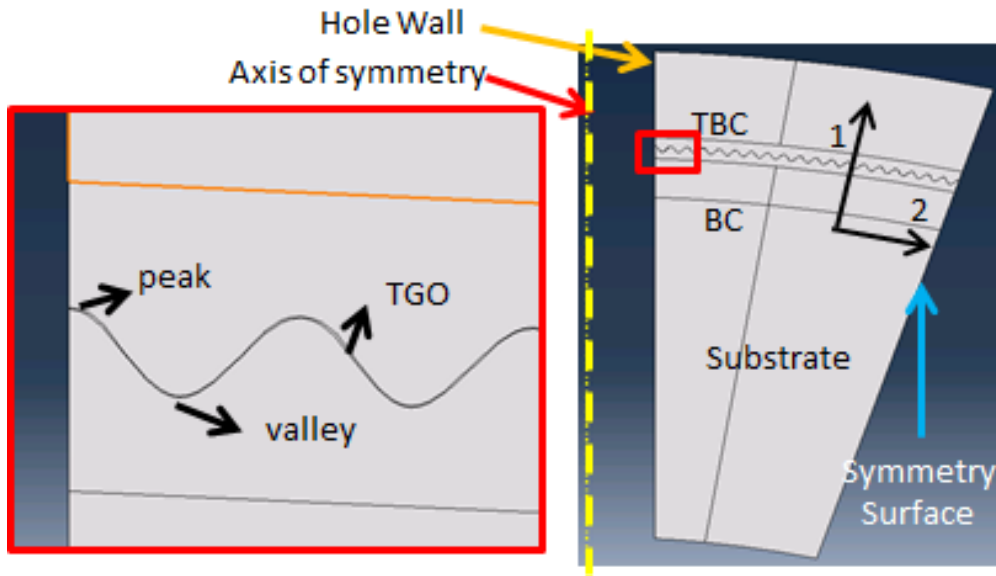


Figure 3.16: The axisymmetric model of a TBC system showing the wavy structure of TBC/BC interface in peak and valley positions.



The 2D-model, which considers the TBC system with recast layer, is shown in Fig. 3.17. The recast layer represents resolidified zirconia with a thickness of 24  $\mu\text{m}$ . This layer has a negligible pore density (as verified from experimental results), see in Fig. 3.18b the recast TBC layer at a laser-drilled hole. Therefore, the  $E$ -modulus ( $E$ ) is higher than that of the porous TBC; i.e. around 200 GPa [121]. The BC/substrate recast layer, 30  $\mu\text{m}$  thick, is located on the hole wall, which usually includes oxide particles, see Fig. 3.18c. This recast layer has a much smaller grain size. Hence, the creep rate [122, 123] of such layers should be higher at high temperatures compared with the base alloy.

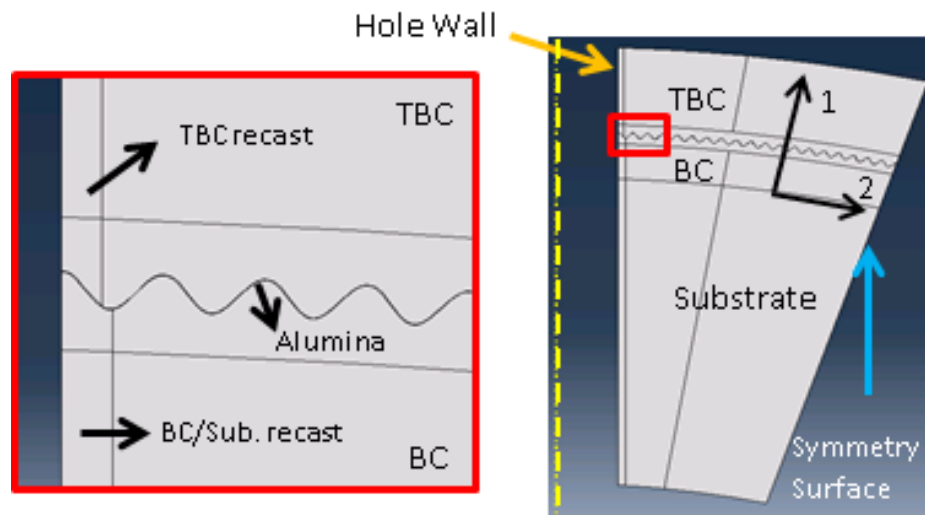


Figure 3.17: The axisymmetric model of a TBC system showing the TBC recast as well as BC/substrate (BC/Sub.) recast.

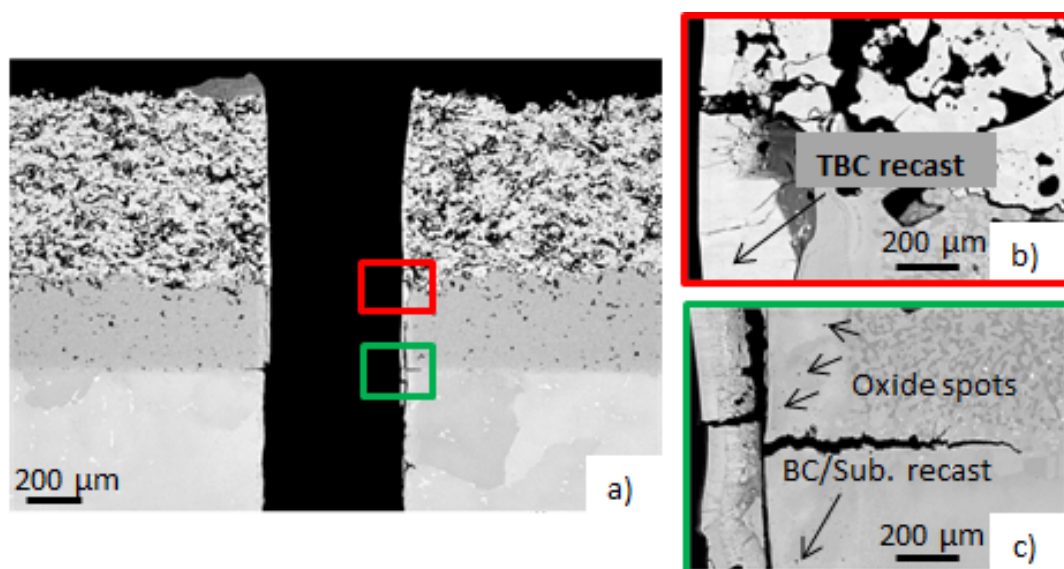


Figure 3.18: Typical defects at (a) a laser-drilled hole of a TBC system made of a PWA 1483 substrate, a Sicoat 2464 BC, and a APS TBC; (b) TBC recast layer with negligible pore density; (c) BC/substrate recast layer.

As for boundary condition, the degree of freedom of all the nodes on the symmetry surface, see Fig. 3.16 and Fig. 3.17, are constrained in tangential direction (direction 2) to apply cyclic symmetry. For loading, a homogeneous temperature distribution is assigned to every node. The thermal loading profile is shown in Fig. 3.19. The thermal loading starts at 200 °C, which is the free stress state after the coating deposition.

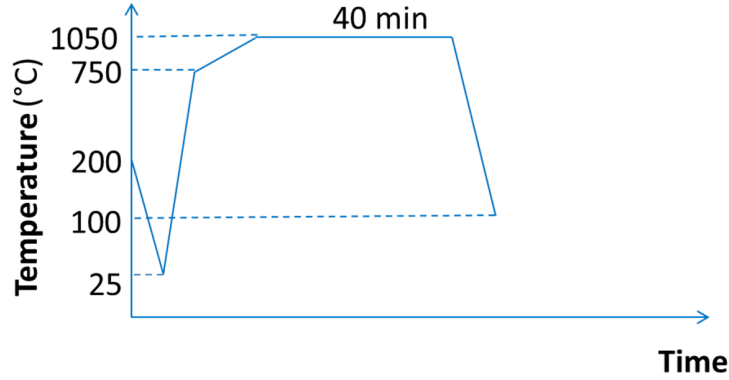


Figure 3.19: The thermal loading profile in the simulations.

A sensitivity analysis has also been performed on the effect of parameter variations in CTE, creep resistance, and elastic modulus on stress response of the system, according to the plan outlined in Table 3.14. The properties  $\{\alpha_{TBC}, \alpha_{Sub}, E_{Sub}\}$ , and  $\{B_{TBC}, B_{Sub}\}$  are listed in Tables 3.12 and 3.13, respectively.

Recast layer	Creep strain rate, B			CTE			$E$ (GPa)	
TBC recast	$0.75B_{TBC}$	$B_{TBC}$	$1.25B_{TBC}$	$0.75\alpha_{TBC}$	$\alpha_{TBC}$	$1.25\alpha_{TBC}$	-	-
BC/substrate recast	-	$B_{Sub}$	$1.25B_{Sub}$	$0.75\alpha_{Sub}$	$\alpha_{Sub}$	$1.25\alpha_{Sub}$	$E_{Sub}$	$1.25E_{Sub}$

Table 3.14: Parameters for the sensitivity analysis.

Afterwards, the FEM results for the ideal situation without any recast layers and the case with both recast layers are compared. For the latter case, the only properties where the TBC and substrate differ from their corresponding recast layers in the FEM model are TBC elastic modulus, because of very low porosity of the TBC recast, and substrate creep rate, because of finer grains of BC/substrate recast, see Table 3.15. Finally, two analyzes were performed with TGO layer having 0.5 and 5  $\mu\text{m}$  thickness in order to analyze the influence of TGO layer thickness.

Properties	TBC	TBC recast	Substrate	BC/substrate recast	T (°C)
$E$ (GPa)	17.5	200	-	-	25
	12.4	141.7	-	-	1000
Creep coeff. B ( $\text{s}^{-1}\text{MPa}^{-1}$ )	-	-	$4.85\text{e-}36$	$4.85\text{e-}36$	10
	-	-	$2.25\text{e-}9$	$2.25\text{e-}8$	1200

Table 3.15: Difference in properties of TBC components and their recast layers in the FEM model.

### 3.5.3 Influence of cooling hole diameter under thermal loading on stress distribution at cooling hole

The influence of the cooling hole diameter on the stress distribution around the hole has been studied. The TBC system with no cooling hole, and with cooling hole having diameters of 0.5, 0.75 and 1 mm have been considered. Axisymmetric FEM models of the mentioned cases were used to reduce simulation time, see Fig. 3.20.

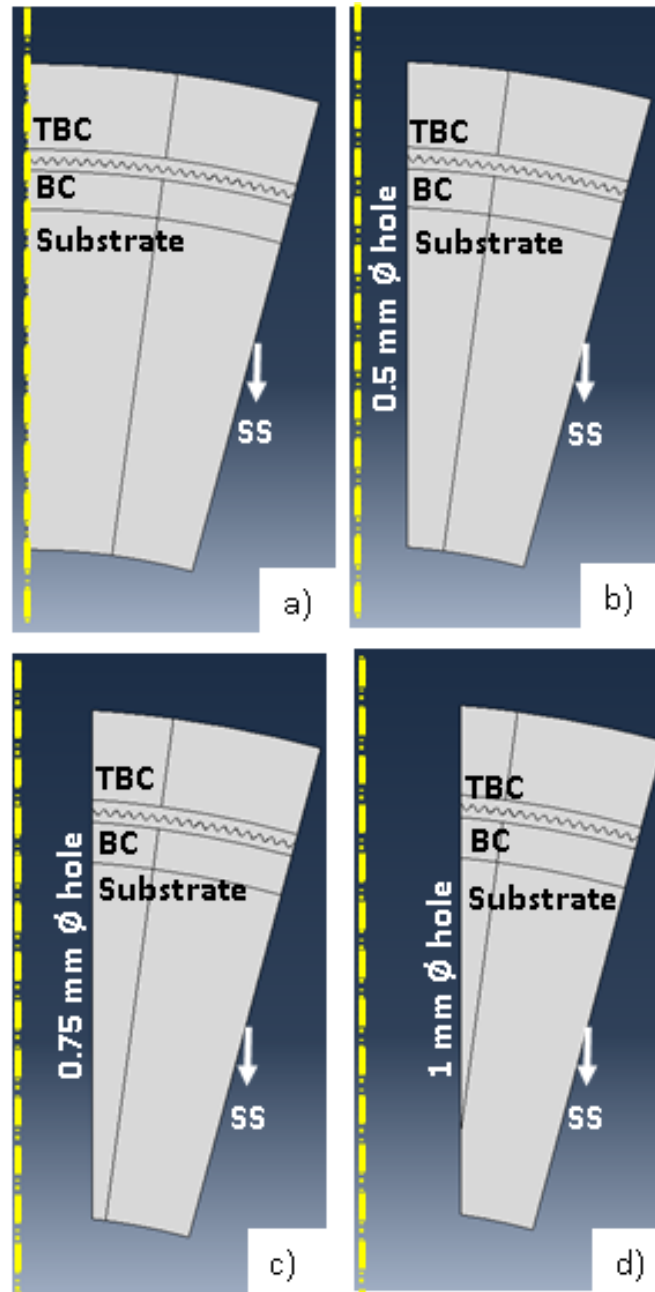


Figure 3.20: Axisymmetric FEM models for understanding the influence of the diameter. SS: Symmetry Surface

### 3.5.4 3D FEM model

In order to analyze more precisely the influence of the angle as well as the effect of recast layer on the stress distribution at the hole, a 3D model was created for FEM analysis. 10-node quadratic tetrahedral elements, C3D10, were used in the analysis. In order to save computational time, two/three symmetry surfaces have been defined for the model with vertical/inclined hole, as marked in Fig. 3.21. The TGO thickness was also assumed to be negligible in the 3D model to reduce computation time.

For inclined hole, symmetry surface SS1 (opposite side of hole) is defined to simulate the cyclic symmetry, i.e. simulating the hole as a part of a cylinder. SS2 is the symmetry surface (at hole) with respect to 1-3 ( $r - z$ ) plane in cylindrical coordinate system, see Fig. 3.21b. For cyclic symmetry surfaces the degree of freedom in tangential direction (2) was constrained. In other symmetry surfaces the freedom was constrained in the normal direction of the plane.

As for a vertical hole, SS1, similar to inclined hole, is the cyclic symmetry surface, whereas SS2 and SS3 are the symmetry surfaces with respect to 1-3 ( $r - z$ ) and 1-2 ( $r - \theta$ ) planes, respectively, see Fig. 3.21a. Additionally, Fig. 3.21 shows the paths where the stress distributions for vertical and inclined ( $30^\circ$ ) holes will be compared; the red path is in the TBC layer at the TBC/BC interface, and the blue path is in the substrate at the BC/substrate interface. With respect to the loading, a homogeneous temperature distribution was assigned to every node, reducing from the free stress state at  $1050^\circ\text{C}$  to  $100^\circ\text{C}$  over 211 s. Similar to an axisymmetric model, the hole diameter, TBC, BC, and substrate thickness were 0.5 mm, 500  $\mu\text{m}$ , 250  $\mu\text{m}$ , and 1.75 mm, respectively.

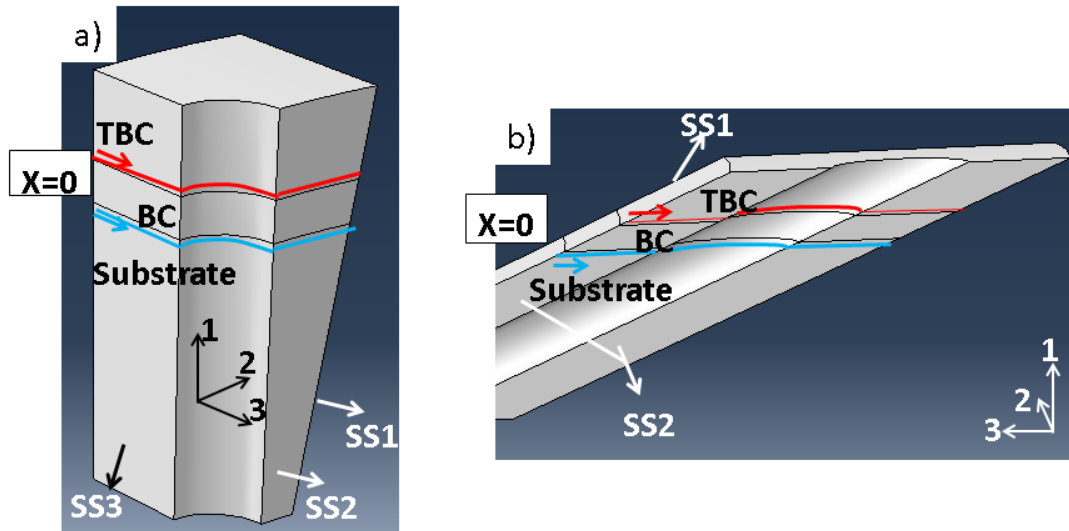


Figure 3.21: The paths over which the stress distributions are shown for (a) vertical and (b) inclined; TBC/BC interface is in red, BC/substrate interface is in blue

In order to assess the influence of a recast layer on 3D stress distribution, a few additional simulations were done. For each angle, 3 simulations have been performed; with no recast layer, with a recast layer using the reference  $\text{CTE}_{\text{TBC}}$ , see Table 3.12, and with a higher

CTE ( $1.25 \times \text{CTE}_{\text{TBC}}$ ). Fig. 3.22 shows the 3D model of vertical and inclined laser-drilled holes with the recast layer which is  $15 \mu\text{m}$  thick. The stress distribution will be compared in the described cases at TBC/BC and BC/substrate interfaces, and along the TBC recast layer at the hole (green path in Fig. 3.22).

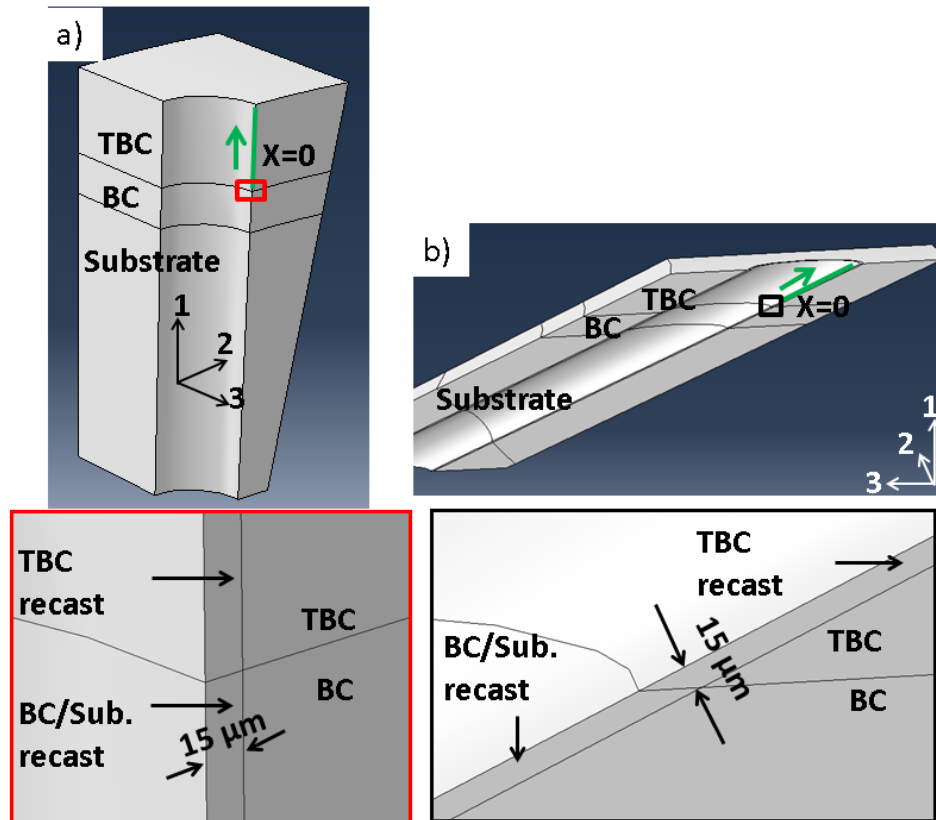


Figure 3.22: 3D FEM model considering the recast layers at the laser-drilled hole, including (a) vertical and (b) inclined hole. For each figure, there is a magnified image at TBC/BC interface near the hole showing the thickness of recast layer:  $15 \mu\text{m}$ .

# Chapter 4

## Results and Discussion

In this chapter, the microstructural analysis of the laser-drilled specimens and the quality of different laser drilling methods in the initial state before thermal cycling is presented based on metallographic examination. Afterwards, the results regarding the influence of cyclic oxidation and LCF loading conditions on laser-drilled TBC systems, drilled with different laser methods, are analyzed. FEM simulation results regarding the influence of different parameters, such as recast layer, CTE, creep strain rate, elastic modulus, and TGO thickness on the stress distribution at the hole, are also presented. The effect of the hole angle and hole diameter on the induced stresses at the laser-drilled hole is also discussed based on the FEM results.

### 4.1 Laser drilling of TBC systems

Microstructural analysis of specimens drilled with different laser methods, as explained in section 3.2, are presented in the following.

First, microstructural images of an undrilled specimen are shown in Fig. 4.1. It is observed that oxidation merely occurs between TBC and BC, as explained in more detail in section 2.2.1. As opposed to the case after drilling, the BC/substrate interface is intact and no oxidation is observed at this location.

Cross-sections of the specimens having vertical and inclined holes, drilled with fiber laser, in both percussion and trepanation mode, provide useful information about typical imperfections at such holes. For both percussion and trepanation drilling with fiber laser, inclined holes showed longer cracks, see Fig. 4.2. Comparing percussion and trepanation drilling, it can be observed that a better hole quality with shorter crack lengths can be achieved using trepanation drilling. It is important to note that interfaces between TBC and BC, and between BC and substrate are prone to crack initiation and propagation during the drilling process.



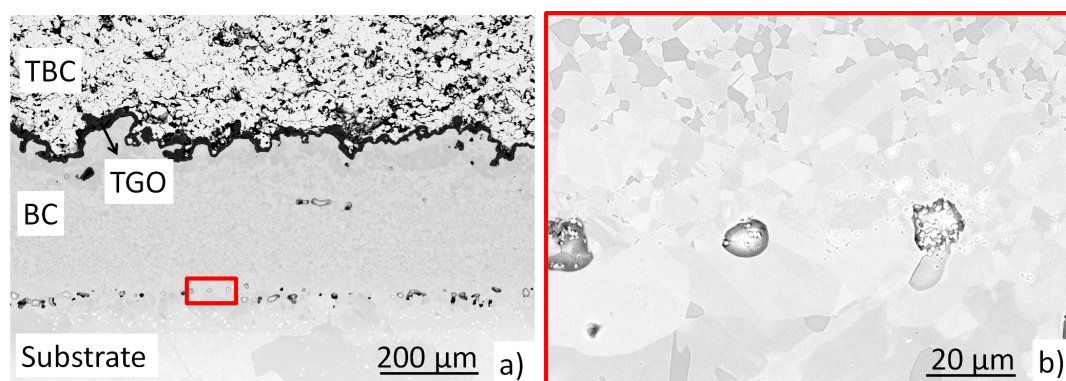


Figure 4.1: SEM images of (a) undrilled specimen as well as (b) the magnification of BC/substrate interface, including existing pores.

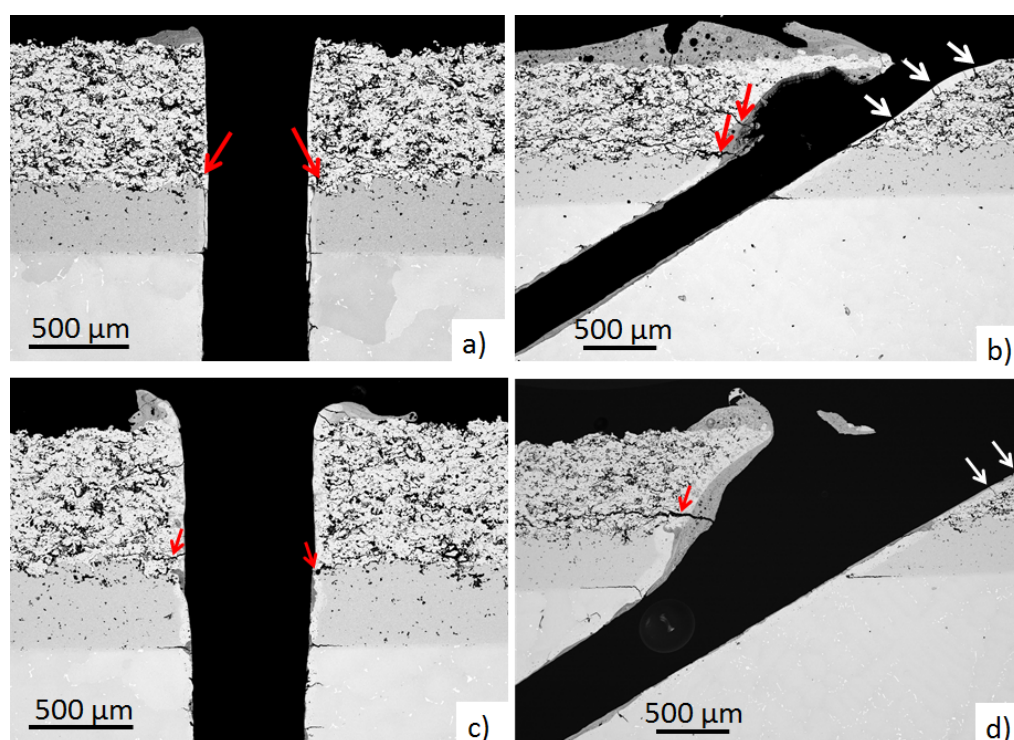


Figure 4.2: SEM images of specimens drilled with fiber laser using trepanation mode for (a) 90° and (b) 30° hole, and percussion mode similarly for a (c) 90° and (d) 30° hole. Arrows in red show cracks at TBC/BC interface, and arrows in white show cracks in TBC recast layer.

Typical microstructural defects of the specimen drilled with long-pulsed laser sources are shown in Fig. 4.3, where the TBC recast layer with negligible pore density as well as the BC/substrate recast layer including the oxide particle can be observed.



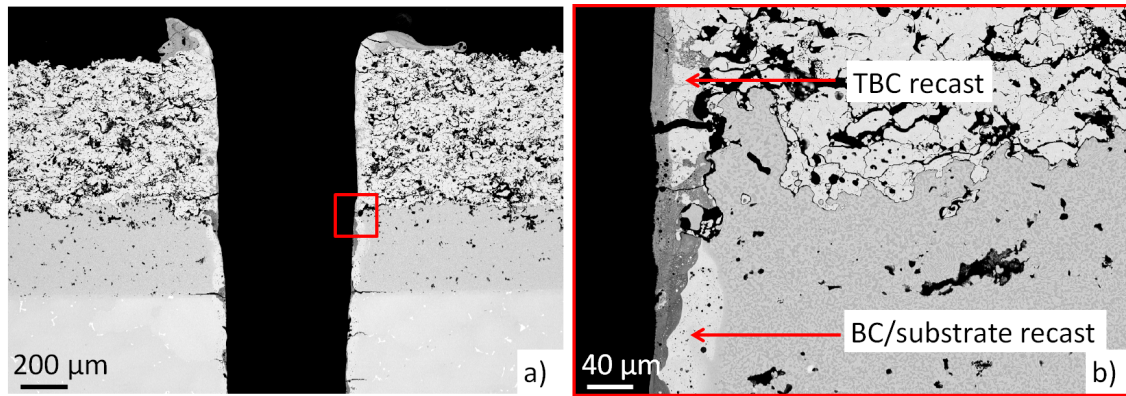


Figure 4.3: a) SEM images of specimens drilled with fiber laser, percussion mode, b) magnified image of red marked area in (a) at TBC/BC interface.

Fig. 4.4 shows the SEM images of the specimen drilled with ultra-short pulsed laser. It can be observed that the density of the defects at the hole is negligible in comparison with other laser methods. However, this method is still not fully developed, as imperfection in the hole geometry, such as in the TBC layer, can be observed.

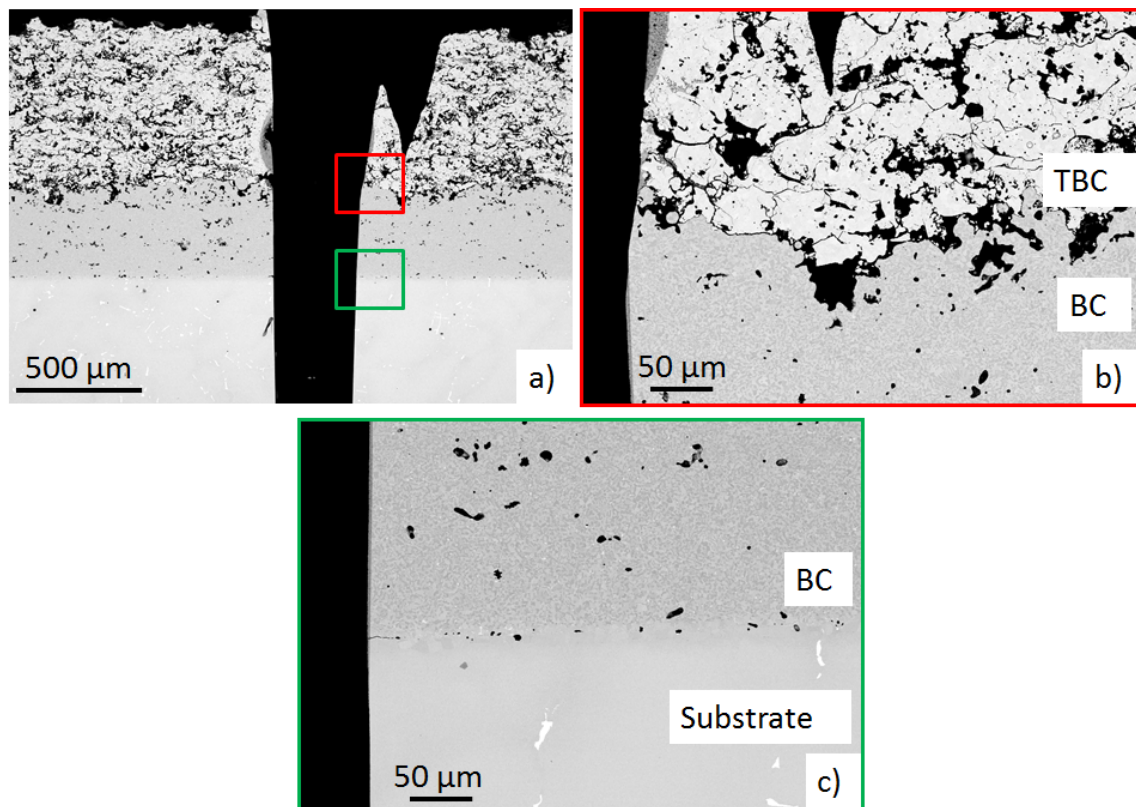


Figure 4.4: SEM images of specimens drilled with (a) ultra-short pulsed laser, and magnified image (b) at TBC/BC interface, and (c) at BC/substrate interface.

In the following, crack lengths for specimens drilled with fiber laser, percussion and trepanation mode, flash lamp, percussion, as well as ultra-short pulsed laser, as measured using analySIS Pro software, are presented, see Table 4.1. It can again be verified that

cracks are longer in case of percussion drilling in comparison with the trepanation mode. Moreover, ultra-short pulsed laser drilling demonstrates better quality with a negligible defect density. It is clear from this table that larger defects occur for inclined holes, except for flash lamp laser. Additionally, in case of percussion drilling, fiber laser, probably due to the applied higher pulse frequency, induces more defects at the hole compared with flash lamp laser. See Appendix A, section A.1, for microstructural images of flash lamp laser-drilled holes, Fig. A.2.

Crack length, $\mu m$	Fiber, trep., 90°	Fiber, trep., 30°	Fiber, perc., 90°	Fiber, perc., 30°	Flash, perc, 90°	Flash, perc, 30°	USP, 90°
TBC	37 ± 31	103 ± 94	142 ± 70	337 ± 436	94 ± 74	100 ± 107	41 ± 33
BC-Sub int.	71 ± 15	138 ± 42	156 ± 7	400 ± 50	47 ± 22	136 ± 35	20 ± 10
Substrate	42 ± 9	52 ± 5	58 ± 22	91	78 ± 12	50 ± 26	0

Table 4.1: Measurement of averaged crack length, in TBC layer, at BC/substrate interface (shown as BC-Sub int.), and in substrate. *trep.*: trepanation, *perc.*: percussion.

The averaged thicknesses of the TBC recast and BC/substrate recast layers are analyzed using the same software. As shown in Table 4.2, percussion drilling of vertical holes results in thicker recast layers at TBC as well as at BC and substrate near the hole, in comparison with trepanation drilling. Regarding inclined holes drilled using percussion, a thicker recast layer is also observed compared with trepanation, but only with regard to BC/substrate recast. The TBC recast thickness was comparable for these two cases. In case of fiber laser, inclined holes showed thicker recast layers in comparison with vertical holes, which is agreement with the data in literature [6]. On the other hand, ultra-short pulsed laser offers a better quality especially at the BC/substrate interface. Moreover, flash lamp laser, percussion mode, caused a reduction in recast layer thickness in comparison with fiber laser drilling, probably due to the less pulse frequency as mentioned earlier.

Recast thickness, $\mu m$	Fiber, trep., 90°	Fiber, trep., 30°	Fiber, perc., 90°	Fiber, perc., 30°	Flash, perc, 90°	Flash, perc, 30°	USP, 90°
TBC recast	19 ± 8	83 ± 46	56 ± 17	77 ± 24	35 ± 12	33 ± 12	33 ± 19
BC-Sub recast	23 ± 8	27 ± 10	46 ± 20	60 ± 21	29 ± 20	20 ± 13	0

Table 4.2: Measured averaged thickness of TBC and BC/substrate recast layers. *trep.*: trepanation, *perc.*: percussion

By comparing the percussion and trepanation drilling modes using fiber laser, the former caused larger cracks, which appears to be due to higher pulse energy of such drilling mode. By trepanation, the recast layer is observed to be thinner since the melt ejection is likely accelerated by vaporization of the melt due to the higher pulse intensity in this mode. By percussion drilling, fiber laser caused lager defects at the hole compared with flash

lamp laser, perhaps due to higher pulse frequency by the former laser method. Inclined laser drilling showed thicker recast layers and larger cracks in comparison with vertical holes, in case of fiber laser. USP laser drilling delivered the best quality for drilling of the cooling holes, where no recast layer and cracks at the hole were observed.

## 4.2 Cyclic oxidation of TBC systems

### 4.2.1 Thermography measurements of specimens drilled with different parameters and hole angle

It has been verified in the publication of Schweda [20] that thermography is a useful tool to analyze the delamination of TBCs. Thermography images obtained for specimens with defined number of thermal cycles are presented and discussed in the following. In Fig. 4.5, as an example, the initiation and development of delamination for two specimens with 90° and 30° holes drilled with flash lamp laser are compared. Thermography measurements for other specimen types, including fiber laser and flash lamp laser for both BC types, with similar observations can be found in Appendix A, section A.2.1. Although thermography images of specimens with LCO22 bond coating are shown, a similar evolution of the delamination mechanism was observed also for specimens with PWA 286 BC, see Fig. A.5 in Appendix A. It can be observed that, for specimens with inclined holes, the delaminations are more pronounced close to the holes due to larger pre-defects after drilling [6], see Table 4.1 and Fig. 4.5, as well as higher stress concentration at the holes, see in Fig. 4.41, which is based on the FEM simulations. Taking into consideration the direction of inclined holes, one can see that initial defects at the coating interface occur mainly at the leading edge, where one reason can be the higher stress magnitude at this site. For specimens with 90° holes, the situation with respect to delamination seems to be less critical at the holes, due to lower thermal stresses at TBC/BC interface, see Fig. 4.41b.

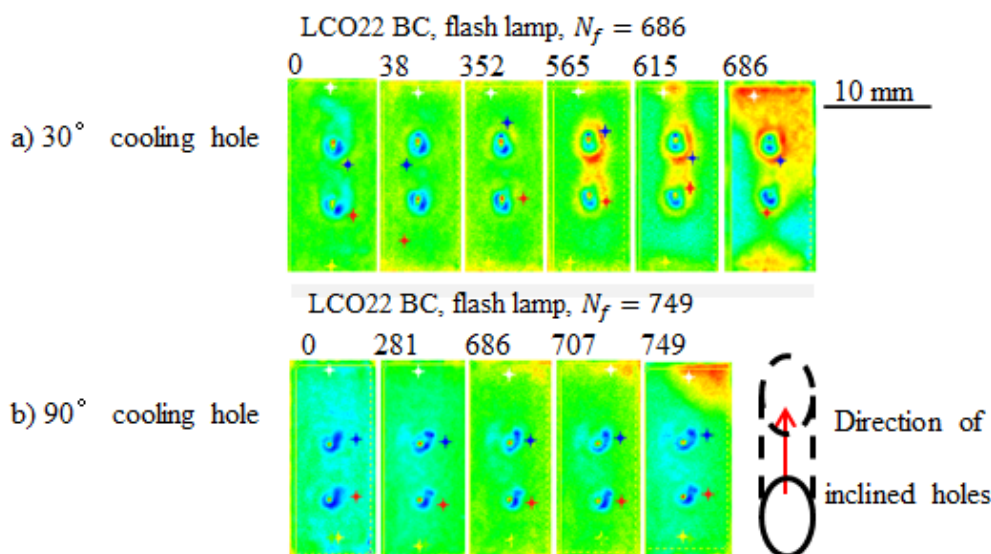


Figure 4.5: The development of delamination for specimens drilled with flash lamp laser at 30° [upper row] and 90° [lower row].

In Fig. 4.6, the thermography images after laser drilling of 30° holes and 90° holes, before and after cycling are presented, where in contrast to 90° holes, delaminated areas at the inclined holes can already be observed after drilling, see white arrows in the figure. The images are shown for flash lamp and fiber laser for both specimen types with LCO22+Al (type 1) and PWA286 (type 2) BC.

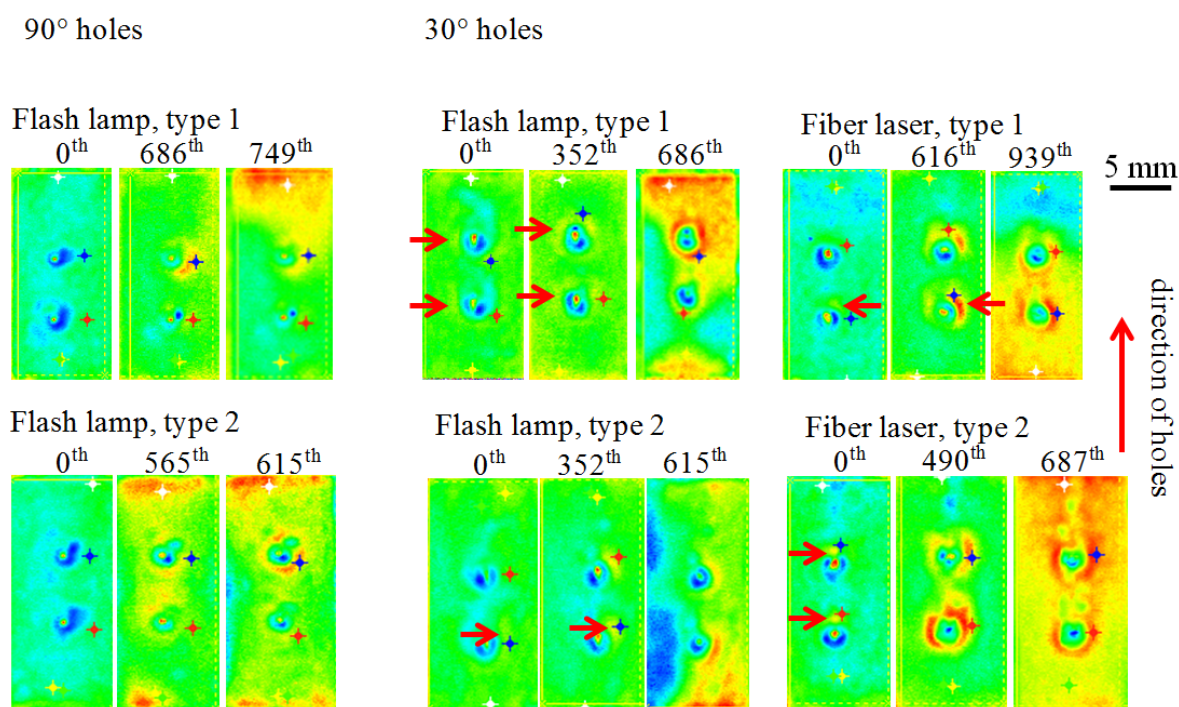


Figure 4.6: The development of delamination for the specimen after laser drilling.

The delaminated regions mostly occur at the leading edge as well as at the sides of the hole, which reveals to be a critical crack initiation position for inclined holes that has not been reported in previous works. Fig. 4.7 illustrates the schematic of the critical position for crack initiation and propagation at TBC/BC interface for an inclined hole based on the experimental observations in Fig. 4.7.

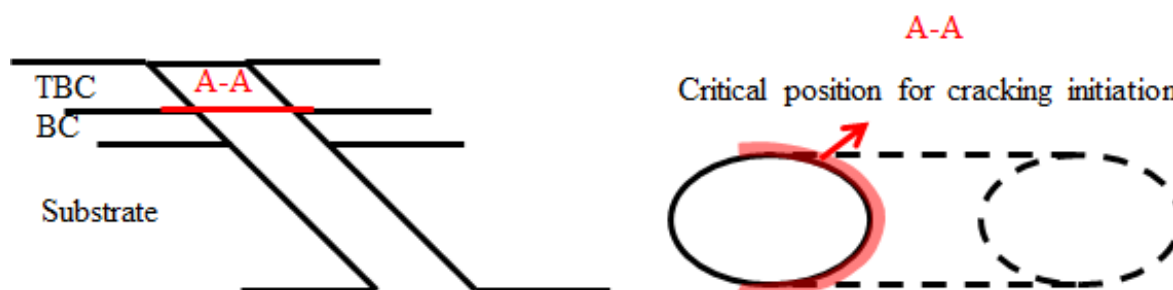


Figure 4.7: Schematic presentation of an inclined hole with the critical position at the TBC/BC interface for crack initiation and propagation.



## 4.2.2 Microstructure analysis of laser-drilled TBC-coated superalloy before and after cyclic oxidation tests

In the following, microstructural images are presented and compared for the specimen with LCO22 BC in the as-drilled and tested state, where cooling holes have been produced using fiber laser, trepanation mode. The microstructural images for other specimens, drilled with fiber laser and for other BC type PWA286, are shown in Appendix A, section A.2.2. For all tested samples, the influence of the drilling mode, i.e. percussion and trepanation, on the damage mechanisms during cyclic oxidation is discussed.

In Fig. 4.8, microstructural images of an as-drilled specimen, close to the hole cross-section, are shown. Typically this kind of large delamination crack shown in the image is observed at the leading edge after laser drilling. As already described in [107], such cracks can be a result of a combination of mechanical stresses arising during melt rejection, induced by recoil pressure during subsequent laser pulses, thermal stresses during cool-down, and the geometry of the hole. The cracks indicated in Fig. 4.8, which are formed at the hole, are critical for failure. Such cracks are usually constraint within recast layer and HAZ region. They can lead to further propagation and oxidation in the BC and substrate, see Fig. 4.11a, hence, they should be avoided. The BC/substrate recast layer consists mainly of  $\gamma$  phase (red) and has normally much finer grains in comparison with the substrate, see Fig. 4.9. On top of this recast layer, either a TBC type recast layer or an oxide layer can be observed. This oxide layer is formed most probably as a result of the high temperature exposure of the recast layer during laser drilling.

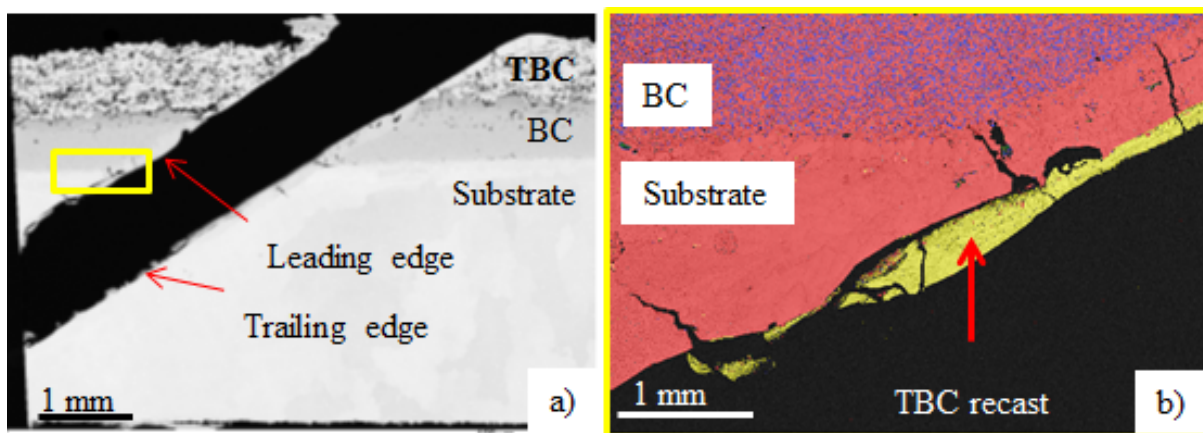


Figure 4.8: (a) SEM image of the specimen drilled with fiber laser, trepanation mode; (b) magnification of the yellow marked area in (a), where yellow:  $ZrO_2$  (cubic), red: Ni-fcc, blue:  $\beta$  - NiAl

In Fig. 4.9, EBSD orientation mappings of the leading edge for the same specimen after drilling are shown. Grains in the metallic recast layer are elongated in the direction perpendicular to the hole wall, which makes this layer prone to crack initiation in the direction parallel to hole edge. Small cracks can also be observed at the BC/substrate interface as well as in the recast layers. As mentioned earlier, the grain size of the BC/substrate recast layer is finer in comparison with substrate, resulting in a lower creep resistance.

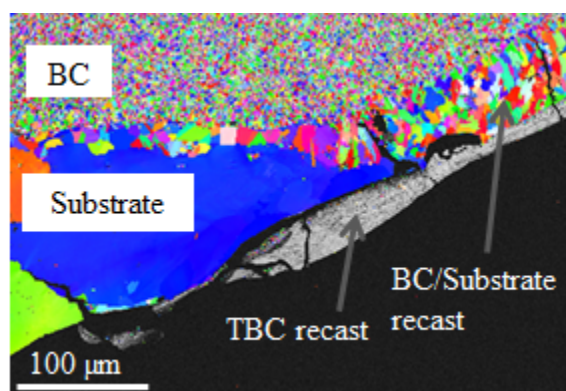


Figure 4.9: EBSD orientation mapping for a specimen drilled with fiber laser, trepanation mode, position BC/substrate for the leading edge.

In Fig. 4.10a, the enhanced Cobalt concentration, observed in the EDS mapping at the leading edge, is a result of molten BC and substrate during drilling, which flows most likely downward in the final phase of the trepanation drilling process due to breakthrough of substrate by the laser pulses [4]. In Fig. 4.10b, Al is also found in the TBC recast layer, which originates probably from the mixing of molten BC and TBC during laser drilling [5].

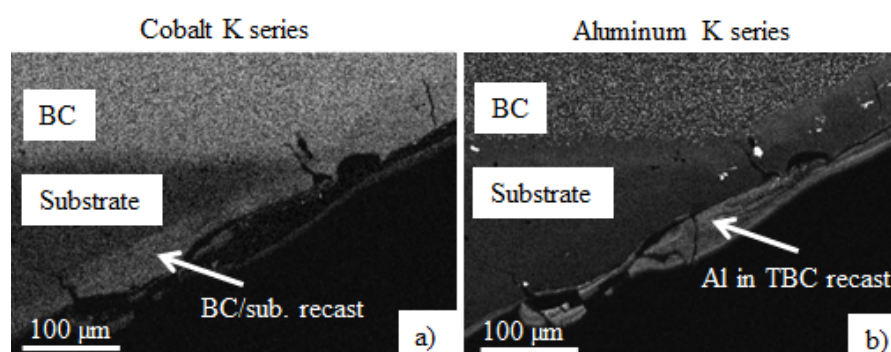


Figure 4.10: EDS mapping for specimen drilled with fiber laser, trepanation mode, of (a) Cobalt and (b) Aluminum.

In Fig. 4.11, microstructural images of a tested specimen, drilled with fiber laser, trepanation, are shown. It can be deduced that the failure of TBC coating occurs predominately at the TBC/BC interface (Fig. 4.11b), where a mixture of delamination at TGO layer (black failure) and delamination in TBC (white failure) can be seen. The strong oxidation of substrate and also BC can be easily observed. The substrate is oxidized and also eroded at the lower parts of the hole, see Fig. 4.11c.

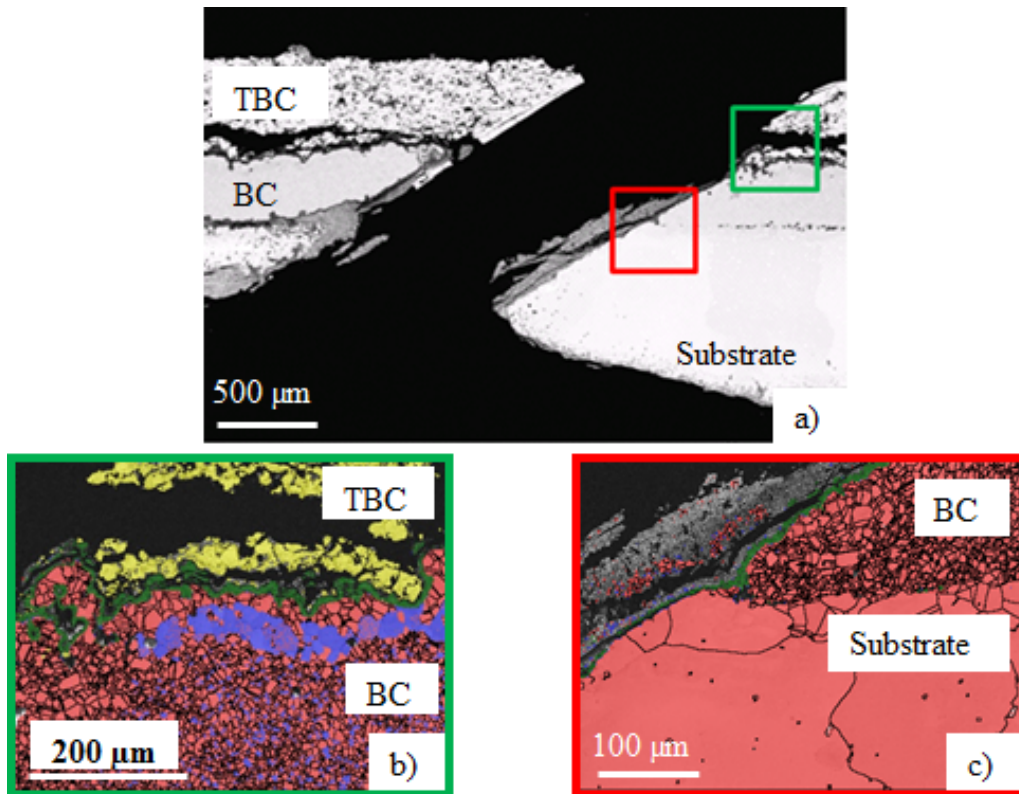


Figure 4.11: Microstructural images of a specimen drilled with fiber laser, trepanation mode, after cyclic oxidation test; (a) SEM image of the hole, (b) EBSD phase mapping at the delamination crack near TBC/BC interface, (c) EBSD phase mapping of the trailing edge at BC/substrate interface. Yellow: ZrO<sub>2</sub> (cubic), red: Ni-fcc, blue: β – NiAl, green: Al<sub>2</sub>O<sub>3</sub>.

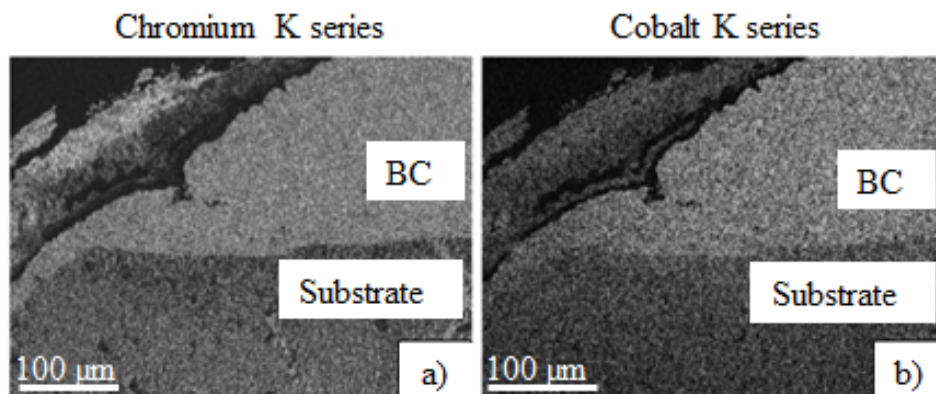


Figure 4.12: EDS mapping of the oxide layers on the hole wall for a specimen drilled with fiber laser, trepanation mode, after cyclic oxidation test.

The size of oxidized regions in the BC for different specimens after failure was measured using the software analysis Pro. As shown in Table 4.3, oxidation for inclined holes is more severe in the case of specimens drilled via percussion mode in comparison with trepanation drilling. The reason is probably the lower quality of the hole wall, in terms



of observed larger crack lengths, leading to more pronounced oxidation. Compared with vertical holes, inclined holes experienced stronger oxidation, which is due to their larger defects after laser drilling, see Table 4.1.

Oxidation attack area ( $\text{mm}^2 \times 10^{-3}$ )	Percussion				Trepanation	
	LCO22		PWA286		LCO22	PWA286
Flash lamp	30°	90°	30°	90°	30°	30°
	$20 \pm 22.4$	$10 \pm 13$	$19 \pm 11$	$3.1 \pm 1.2$	-	-
Fiber laser	EF*		$20 \pm 25$	-	$7 \pm 5.4$	$3.6 \pm 6$

Table 4.3: Comparison of oxidized areas in BC at the hole wall of failed specimens. \*EF: Experimental set-up failure

The difference between percussion and trepanation drilling of specimens drilled with fiber laser (trepanation and percussion mode) after cyclic oxidation can be assessed on the basis of Fig. 4.13. It can be seen that the number of oxidized cracks at the hole wall is higher in the case of percussion drilling, which is due to the lower quality of the hole after drilling. Moreover, the stronger oxidation for the specimen drilled with percussion mode, can be also observed.

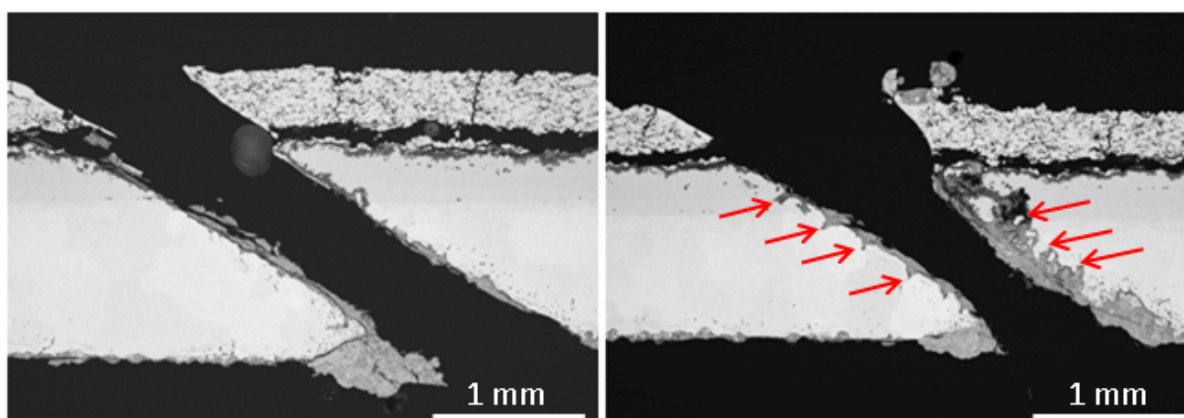


Figure 4.13: Comparison of specimens, with the BC PWA 286, drilled with fiber laser using trepanation drilling (left) and percussion drilling (right); red arrows show the oxidized cracks at the hole wall

The resulting life times for the tested specimens, at 1050 °C with a 2 hour hold time at max. temperature, are shown in Table 4.4. As shown, specimen drilled with fiber laser using trepanation mode had the longest life time together with the undrilled specimen. Overall, the drilled specimens had shorter life times than the undrilled specimens, which shows the influence of laser-drilled cooling holes on life time under cyclic oxidation loading conditions. The life time results agree with the microstructural analysis of the specimens. It should be mentioned that one specimen was tested for each specimen type.

Specimen type	LCO22- Type Bondcoat	PWA286- Type Bondcoat
Flash lamp, 30°	686	615
Flash lamp, 90°	749	615
Fiber, Percussion, 30°	EF*	687
Fiber, Trepanation, 30°	939	687
Undrilled	949	-

Table 4.4: Test matrix for cyclic oxidation tests for analysis of diameter influence.

### 4.2.3 Thermography measurements of specimens drilled with different diameters

In this part, thermography measurements of the specimens drilled with different diameters with an inclination of 30° with respect to TBC surface are presented. As demonstrated in Fig. 4.14, the delamination started at the holes, mainly at the leading edge. At the next step, delamination cracks at the holes coalesce together and apparently propagate further to the edge. Generally, macroscopic spallation happens when these huge delaminations join together.

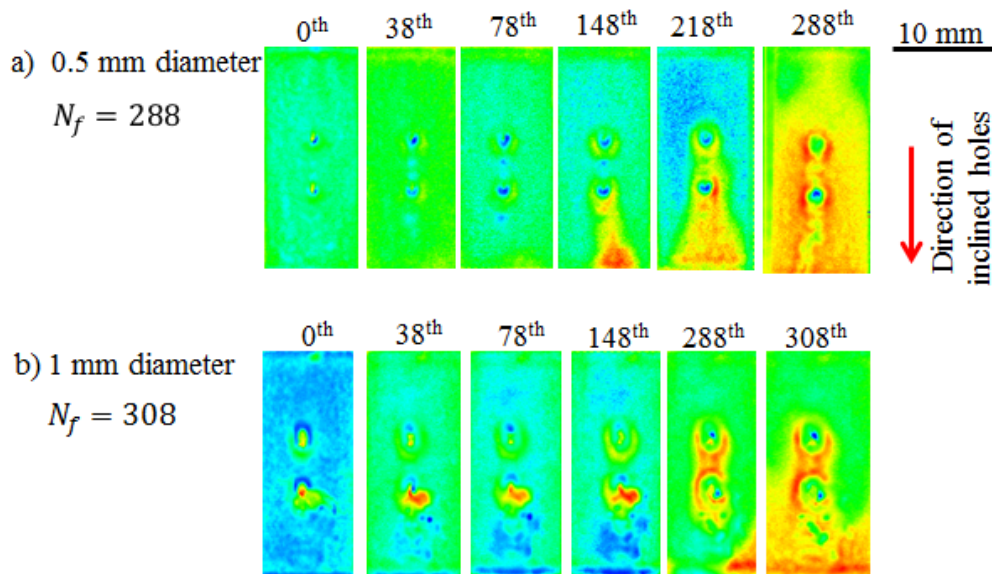


Figure 4.14: The development of delamination for specimens drilled with fiber laser, trepanation, with 0.5 mm [upper row] and 1 mm diameter [lower row].

#### 4.2.4 Microstructure analysis of specimens drilled with different diameters

Fig. 4.15 presents the laser-drilled TBC system with a 1 mm diameter cooling hole, where a typical delamination crack at the leading edge is observed. Microstructure of the laser-drilled specimen with 0.5 mm cooling hole has been already discussed in Fig. 4.8. In Fig. 4.15b, a crack in the superalloy which has initiated in HAZ and propagated into  $\gamma/\gamma'$  microstructure is shown. The formation of BC recast layer has induced cracking, which is propagated into BC/substrate interface and resulted in delamination cracking after laser drilling.

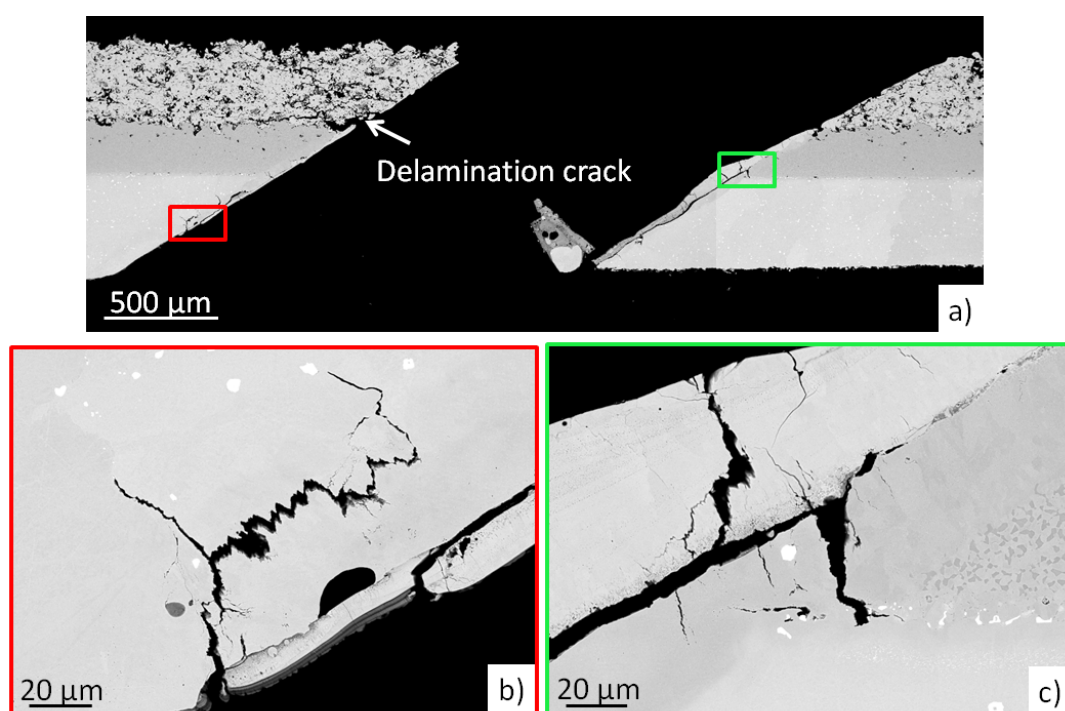


Figure 4.15: a) SEM image of laser-drilled hole with 1 mm hole, b) crack in superalloy initiated from the HAZ, c) cracking in BC recast leading to delamination crack at BC/substrate interface.

Fig. 4.16a shows the EDS mapping of chromium at the BC/substrate interface which demonstrates the HAZ area of base alloy on the leading edge. This is shown by the misorientated region shown by the EBSD analysis of the same spot in Fig. 4.16b, where a recast layer of BC can be observed as well. It is worth to note the very small nucleated grains near the laser-induced cracks in Fig. 4.16b, which may have promoted the formation of such defects. The crack at the lower left part of Fig. 4.16b is shown with high resolution in Fig. 4.15b, where it can be seen that crack propagation mainly occurs along grain boundaries of the base material. The EDS and EBSD images of the HAZ on the trailing edge are presented by Fig. 4.16a and Fig. 4.16d. The HAZ is shown by the misorientation phase (light green area) in Fig. 4.16d.

The SEM image in Fig. 4.17 shows a laser-drilled hole with 1 mm diameter after failure. As demonstrated, the oxide attack at TBC/BC interface at the life time has grown

extremely due to high growth rate of spinel type oxide scales.

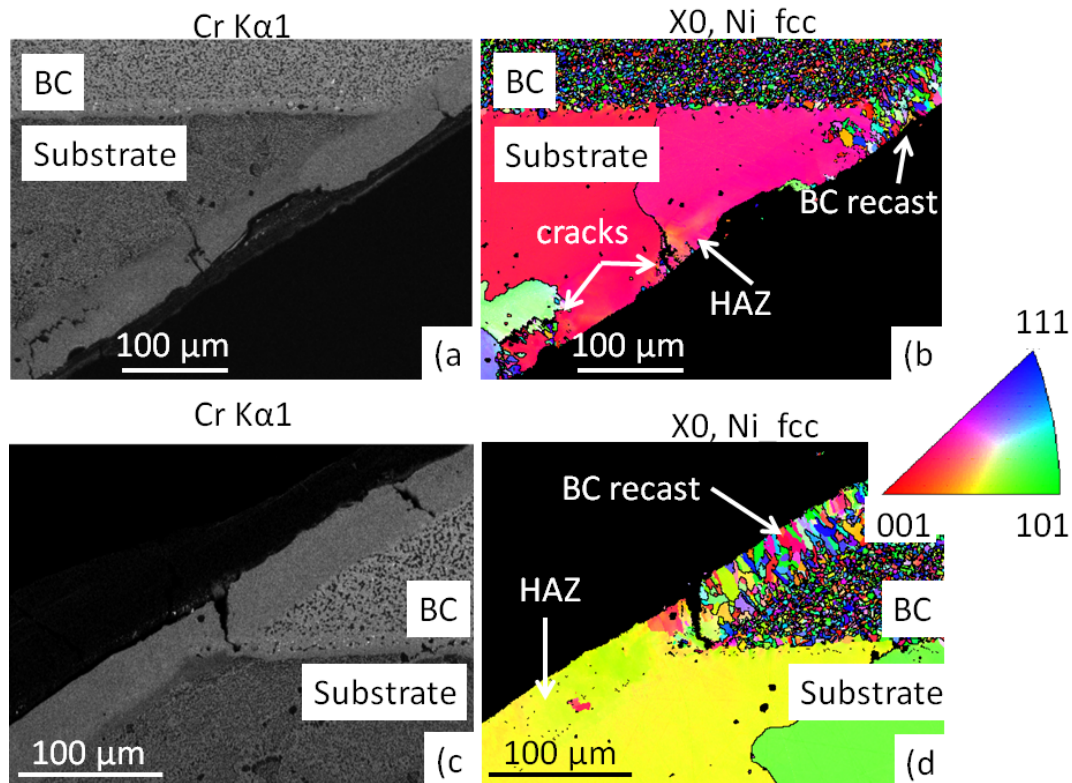


Figure 4.16: a, b) EDS and EBSD orientation mapping of image of BC/substrate interface on the leading edge, c, d) EDS and EBSD orientation mapping of image of BC/substrate interface on the trailing edge.

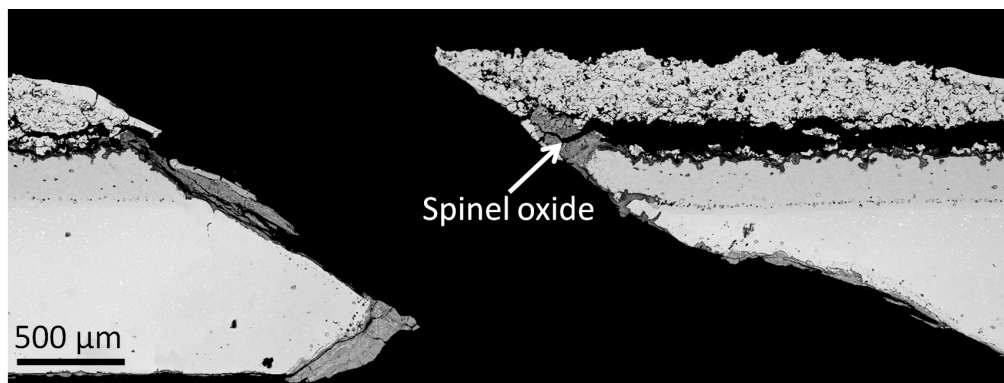


Figure 4.17: a) SEM image of the laser-drilled specimen with 1 mm hole after 308 cycles and reaching failure.

Fig. 4.18a shows the microstructure of the specimen cycled only to the middle of life time. It can be observed that delamination is developed fully near the laser-drilled hole by coalescing of smaller cracks together. The oxide attack at TBC/BC interface at the hole leads to extreme growth of spinel type oxides as shown in green by the EBSD phase map in Fig. 4.18b. This phenomenon appears to be important for accelerating TBC separation,



see Fig. 4.18b and Fig. 4.18c. Growth of spinel oxide in the current experiments is due to the long time exposure of the superalloy under extreme high temperatures, which is different than gas turbine components which experience lower temperatures due to film cooling.

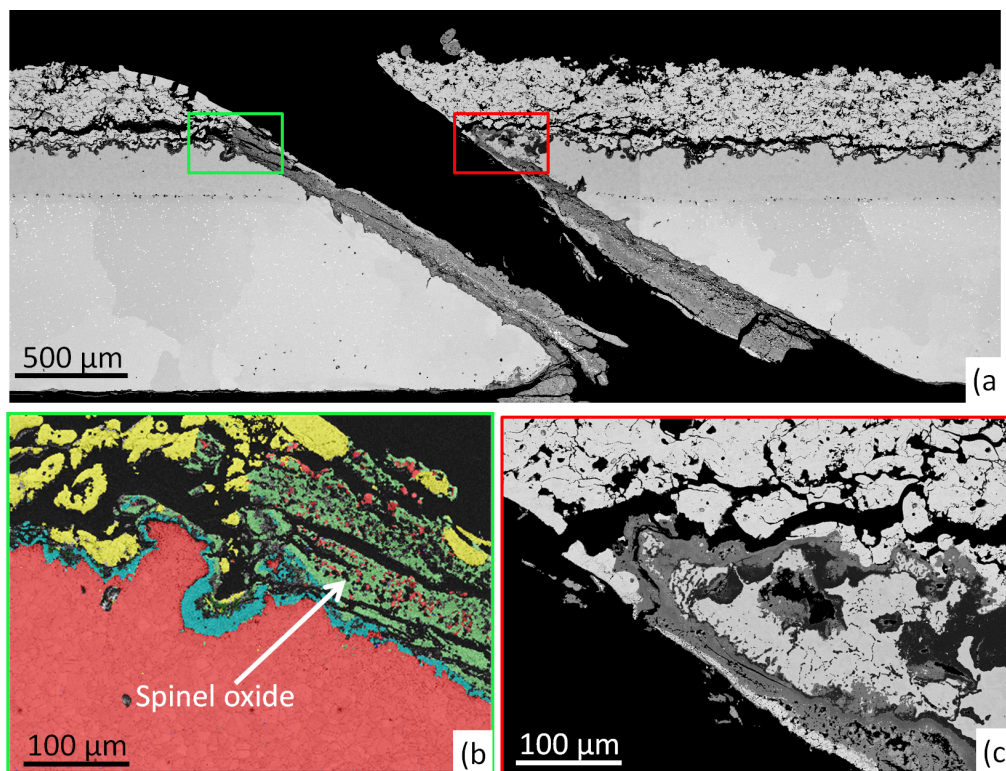


Figure 4.18: a) SEM image of the laser-drilled specimen with 0.5 mm hole at the mid-life, 156<sup>th</sup> cycle, b) magnified image of TBC/BC interface on the leading edge with strong oxidation, c) oxidation on trailing edge at TBC/BC interface.

Recast layer thickness and crack length for the specimens with the different cooling hole diameters of 0.5 and 1 mm have been measured and are shown in Table 4.5. The delamination crack at TBC/BC interface on the leading edge as well as the averaged crack length in BC or substrate are comparable for both diameters. The thickness of the BC recast layer is also not significantly different for these two diameters. The change in diameter due to oxidation is also measured and presented in Table 4.6. The diameters of the laser-drilled holes increase due to formation of spinel type oxides. Such oxides are prone to break away after extended growth, leading into an increase in hole diameter. As shown in Table 4.7, the life time of the specimens with cooling hole diameters of 0.5 mm and 1 mm are almost in the same range, which probably means that the influence of cooling hole diameter on life time of TBC-coated superalloys under cyclic oxidation is low, which agrees with the FEM results of the 2D stress distribution of a TBC system with vertical cooling holes under thermal cyclic loading.

Hole diameter (mm)	Crack length ( $\mu\text{m}$ )		BC recast thickness ( $\mu\text{m}$ )
	0.5	TBC	
BC-Sub.		$33 \pm 25$	
1.0	TBC	596	$32 \pm 10$
	BC-Sub.	$42 \pm 32$	

Table 4.5: Average crack length in TBC, BC and substrate, and BC recast thickness for 0.5 and 1 mm cooling holes.

Oxidation effect	Hole diameter (mm)	
	Before test	After test
0.5	463	663
1.0	1071	1452

Table 4.6: Influence of oxidation on the diameter of cooling hole.

Hole diameter (mm)	Life time, cycles
0.5	288
1.0	308

Table 4.7: Life time of specimens with laser-drilled cooling holes with 0.5 and 1 mm diameter.

The results of cyclic oxidation experiments performed on TBC-coated superalloys show that the presence of cooling holes results in moderate reduction of TBC-life by TBC delamination around cooling holes. This can be attributed to the laser drilling processes, which induce small visible damages at the cooling hole including delamination at TBC/BC interface as well as micro-cracks in the superalloy at the cooling hole. Percussion as well as inclined laser drilling induced stronger oxidation attacks compared with trepanation, and vertical laser drilling, respectively. Influence of the cooling hole diameter on life time behavior under the cyclic oxidation tests was observed to be insignificant. In contrast to the current experiments, which have been performed without cooling air at uniform temperature, air-cooled TBC coated vanes and blades will exhibit significant lower temperature at cooling holes, resulting in lower oxidation rate of the bond coating and improved probably improved TBC adherence.

### 4.3 LCF testing of undrilled and laser-drilled TBC systems

In the following, the results of LCF experiments using undrilled and drilled TBC coated specimens performed at 850 °C are presented and discussed.

Firstly, the microstructural images of the untested TBC-coated superalloy IN 792 laser drilled with flash lamp, trepanation mode, and USP, has been investigated to characterize cooling hole quality, recast layer and crack formation.

Fig. 4.19 shows the microdefects at the laser-drilled cooling holes with flash lamp using trepanation mode, illustrating the delamination cracks as well as cracks in the superalloy. Similar to the results shown in section 4.1, a delamination crack at the TBC/BC interface on the leading edge can be observed, which is due to the melt ejection process promoted by gas pressure during the drilling process, see Fig. 4.19b. Fig. 4.19c shows a crack in the superalloy, which has initiated from the cooling hole, propagated through the HAZ/recast layer, and stopped in the  $\gamma/\gamma'$  phase. Hard particles at the cooling holes, i.e. carbides, promote crack initiation and propagation [124, 125], see also Fig. 4.19c.

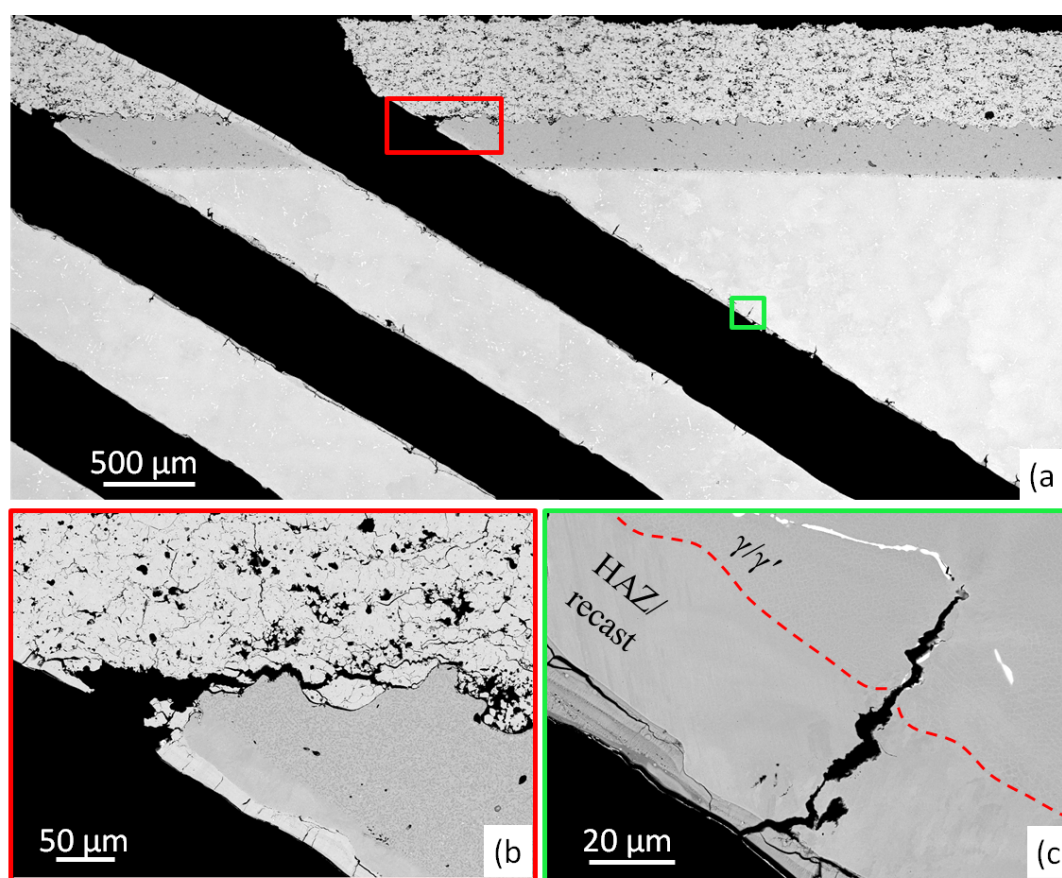


Figure 4.19: SEM images of the TBC coated IN 792 laser drilled at 30° with flash lamp trepanation.

Metallographic images of the specimen drilled with USP laser are shown in Fig. 4.20. No delamination cracks or defects in the base alloy can be observed, indicating the high quality of this laser drilling method.



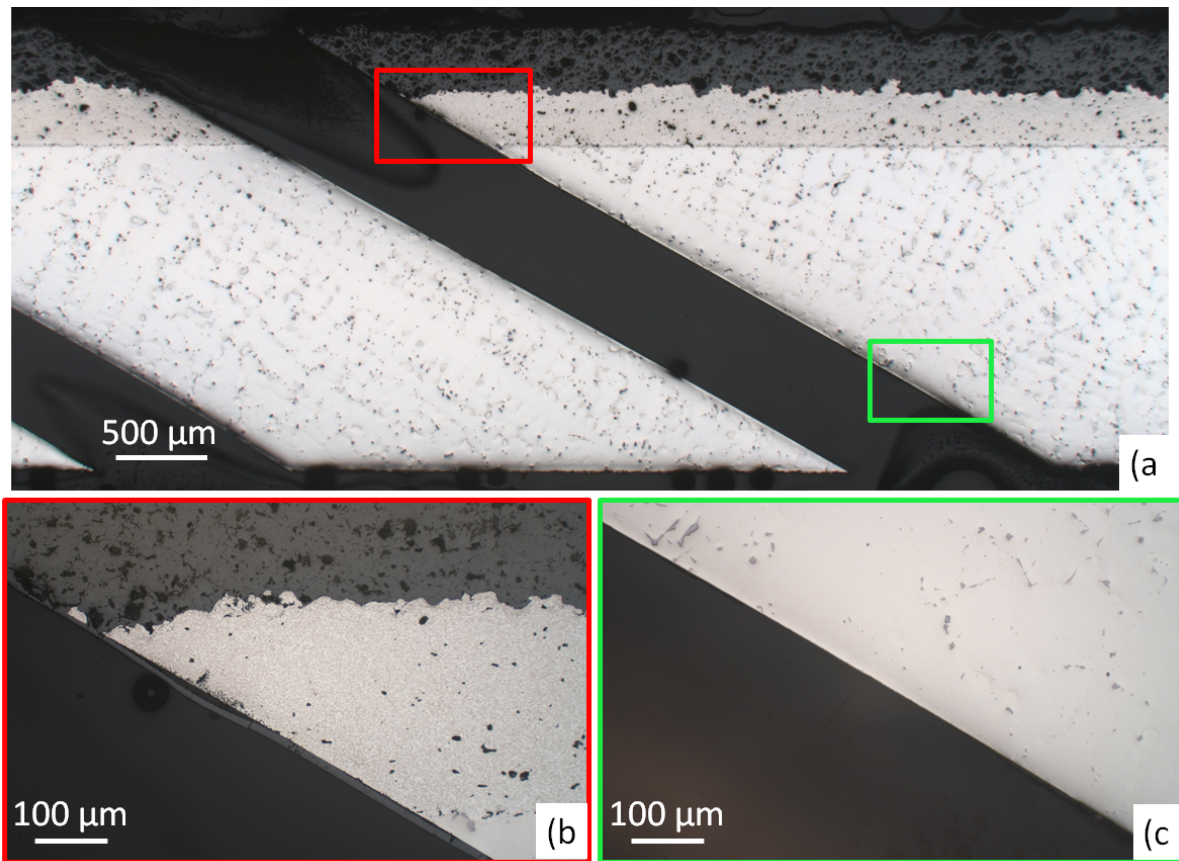


Figure 4.20: Metallographic images of the TBC coated IN 792 laser drilled at 30° with USP.

The SEM images of a cooling hole laser drilled at 90° hole with flash lamp trepanation mode are shown in Fig. 4.21. Delamination at the cooling hole near the TBC/BC interface can be observed in Fig. 4.21b. Fig. 4.21c shows the HAZ/recast layer on the substrate's  $\gamma/\gamma'$  microstructure at the hole.

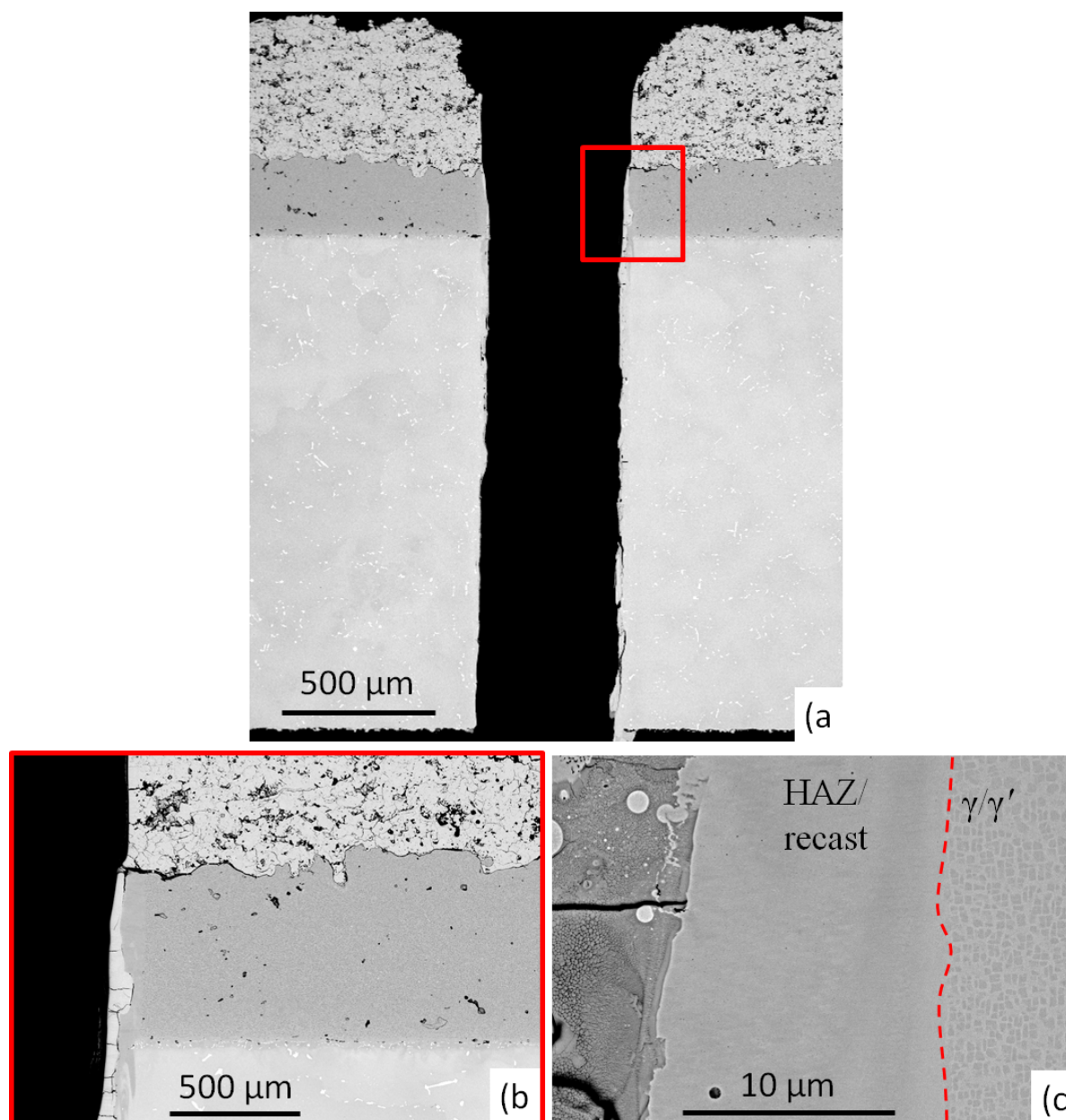


Figure 4.21: SEM images of the TBC coated IN 792 laser drilled at  $90^\circ$  with flash lamp, trepanation mode.

Fig. 4.22 illustrates the laser-drilled TBC system. Due to the high quality of this method, no delamination cracks were observed at the interfaces, see Fig. 4.22b. Additionally, no defects could be found at the hole wall, as can be seen in Fig. 4.22c. The  $\gamma/\gamma'$  microstructure of the superalloy can be detected up to the hole wall, where no HAZ/recast is existing.

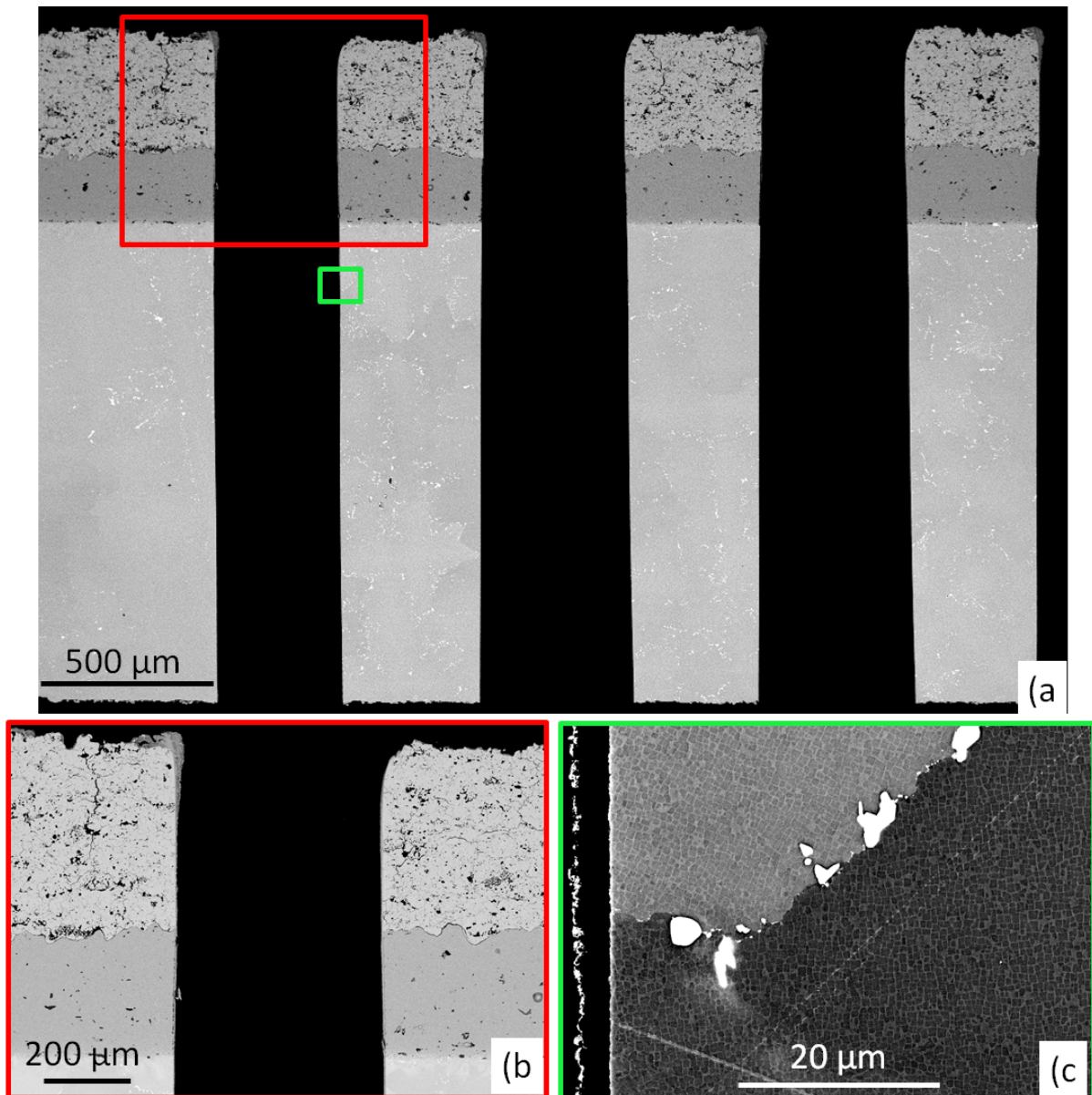


Figure 4.22: SEM images of the TBC coated IN 792 laser drilled at 90° with USP.

Fig. 4.23 shows the stress-strain hysteresis loops of the LCF tests performed with the two strain ranges 0.38 % and 0.67 % for both samples laser drilled with flash lamp, trepanation, at 30° with cooling holes of 0.5 mm diameter. As expected the plastic work is larger using a higher mechanical strain range, as indicated by the corresponding area of the stress-strain hysteresis loops. Cyclic softening occurs near the end of the life time.



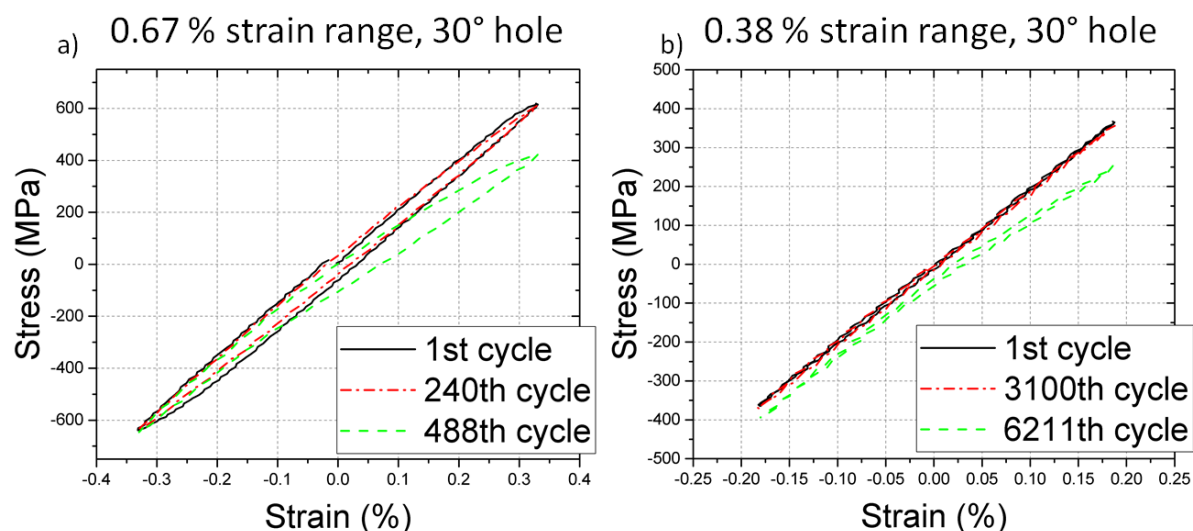


Figure 4.23: Stress-strain hysteresis loops of specimens laser drilled with flash lamp, trepanation, at  $30^\circ$ , tested by LCF at  $850^\circ\text{C}$  with a) 0.67% and b) 0.38% strain ranges.

Stress amplitudes of the tested specimens are presented in Fig. 4.24. As expected, higher strain ranges induce larger stresses in the material. In case of the higher strain range, 0.67%, laser-drilled holes reduced the life time, see Fig. 4.24 and Fig. 4.25.  $90^\circ$  holes caused a larger reduction in the life time than  $30^\circ$  holes, indicating the more criticality of these holes in case of mechanical loading. The results presented in Fig. 4.25 clearly show good reproducibility of LCF behavior of undrilled as well as drilled specimens. The results also indicate that the quality of laser drilling with respect to uniformity of cooling holes, with negligible or no recast or HAZ layer as well as micro-cracks, has a significant influence on the life time of TBC-coated superalloys under LCF conditions at high temperatures. USP laser drilling process is superior compared with the flash lamp (FL) trepanation method. LCF testing of undrilled and USP-drilled specimens at the high strain range, 0.67%, showed similar life times. Heckmann [39] performed LCF tests on TBC-coated superalloy IN 792 at  $950^\circ\text{C}$  with 0.67% mechanical strain range, where a shorter life time,  $N_f = 582$ , was achieved, in comparison to the undrilled specimens tested in this work at  $850^\circ\text{C}$ . This can be attributed to higher test temperature of  $950^\circ\text{C}$ .

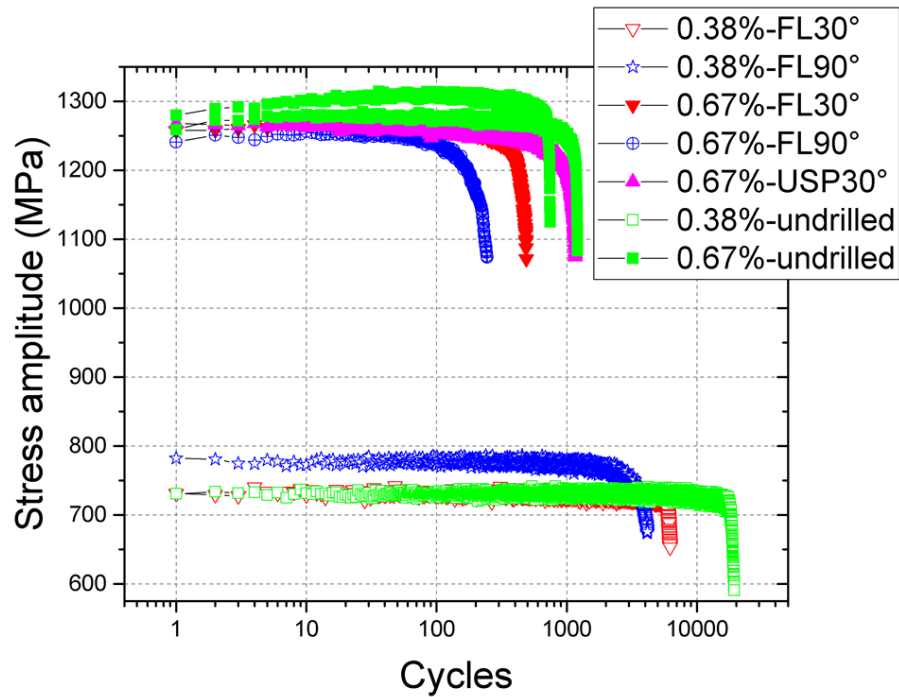


Figure 4.24: Stress amplitude versus failure cycle for specimens with 90° and 30° laser-drilled holes tested by LCF at 850°C with both 0.67% and 0.38% strain ranges. FL: flash lamp.

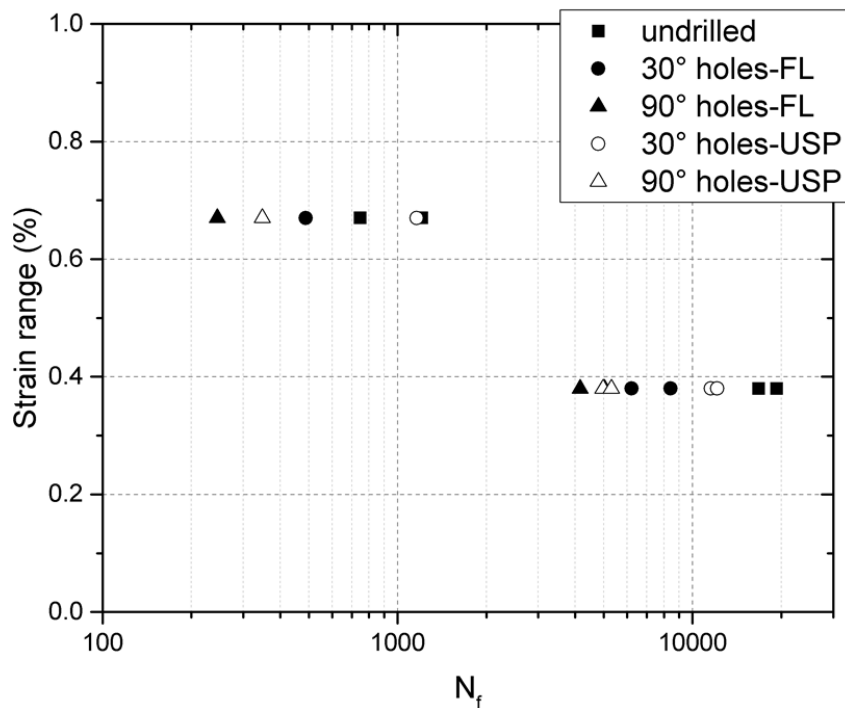


Figure 4.25: The Wöhler curve of LCF tests performed on laser-drilled TBC-coated superalloy IN 792 CC for different hole angles and mechanical strain ranges at 850°C. FL: flash lamp.

J. Klabbers [3] performed LCF tests of uncoated single crystal superalloy CMSX-4, as well as CM186 LC DS/SX with and without laser-drilled holes at 950 °C, which showed a reduction of life time for the specimen with cooling holes, similar to the current results.

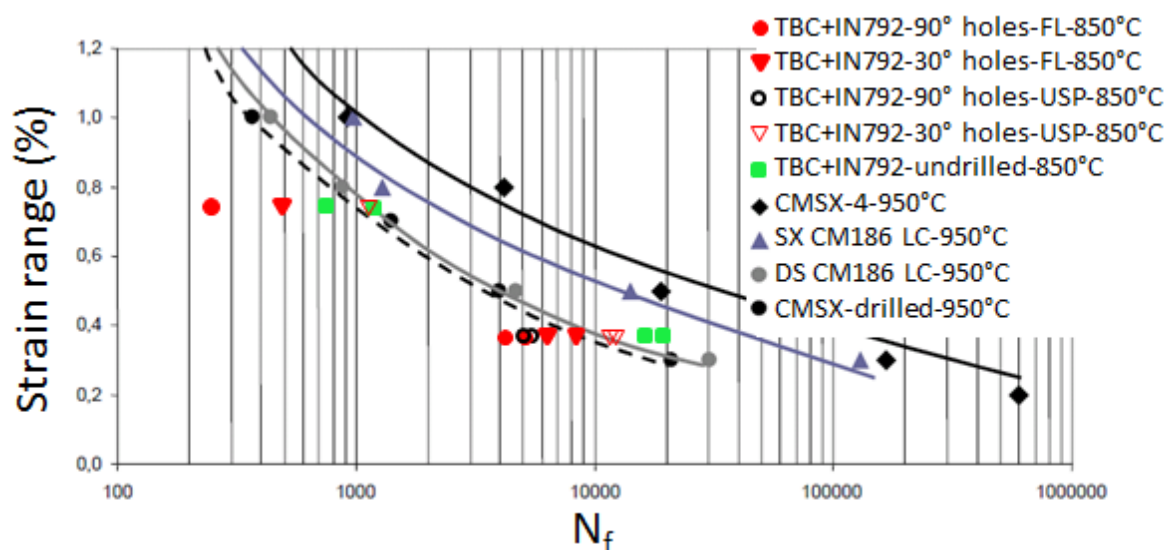


Figure 4.26: Comparison of LCF test results on undrilled and laser-drilled nickel-based superalloys at 850°C and 950°C performed in this thesis and by Klabbers [3], respectively. FL: flash lamp.

### 4.3.1 Damage analysis by microstructural investigation of LCF tests

The undrilled specimen tested with 0.67 % mechanical strain range is shown in Fig. 4.27. The TBC coating is almost intact, however a small delaminated region can be seen in the thermography images almost at the middle section, where a segmentation crack was observed in TBC, as indicated in the magnified image in Fig. 4.27. 1<sup>st</sup> thermography image is shown with the red frame on the failed specimen, whereas 2<sup>nd</sup> 3<sup>rd</sup> are the thermography images of the 120° rotation in the directions shown.

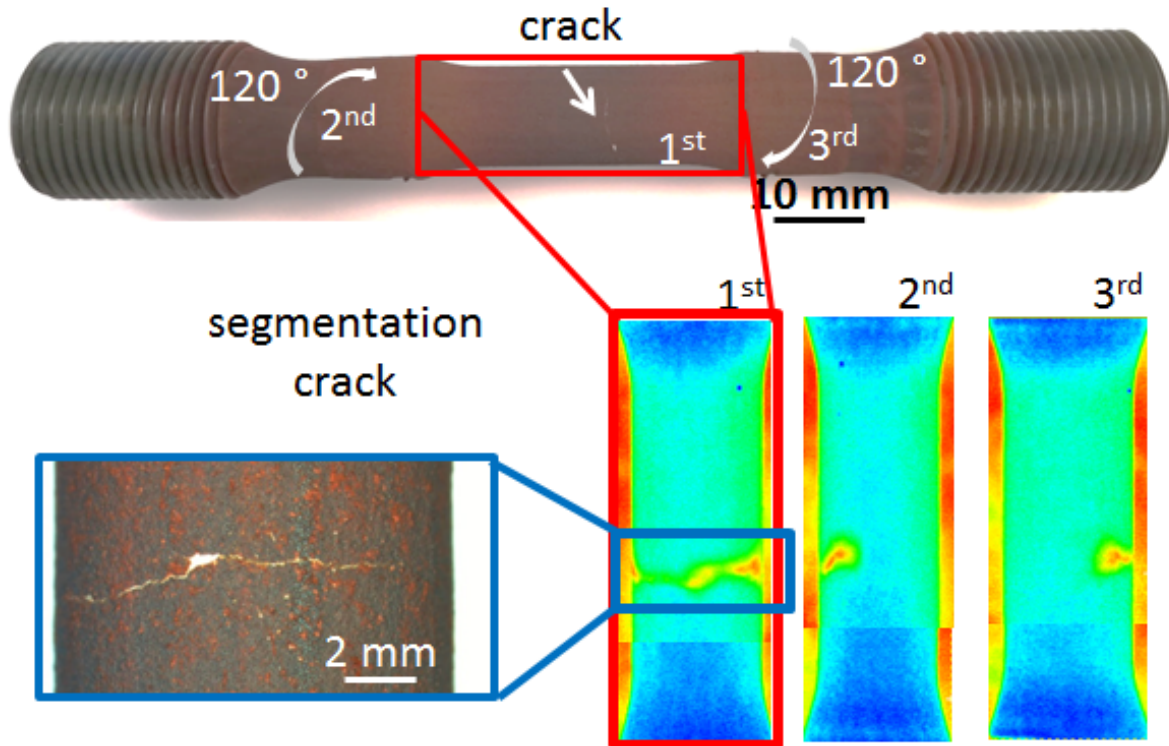


Figure 4.27: Failed undrilled specimen tested with 0.67 % mechanical strain range as well as thermography measurement, 1<sup>st</sup> thermography measurement is shown with the red frame on the failed specimen, 2<sup>nd</sup> and 3<sup>rd</sup> images are thermography measurement of the 120° rotation in the directions shown above.

At the location where delamination was observed by thermography measurement, a longitudinal section was prepared and analyzed via SEM. A primary crack can be observed in Fig. 4.28 propagating perpendicular to the loading direction, which has caused the local delamination of TBC, whereas moving away from the crack no delamination can be observed, which agrees with thermography measurements. EDS mapping of the primary crack shows, as expected, the influence of oxidation on the crack path, which has promoted the crack propagation mechanism. This has been shown by the LCF tests performed by Heckmann [39] at high and low temperatures, where testing at the lower temperature had a longer life time. The primary crack has initiated from the inner surface of the tubular specimen.



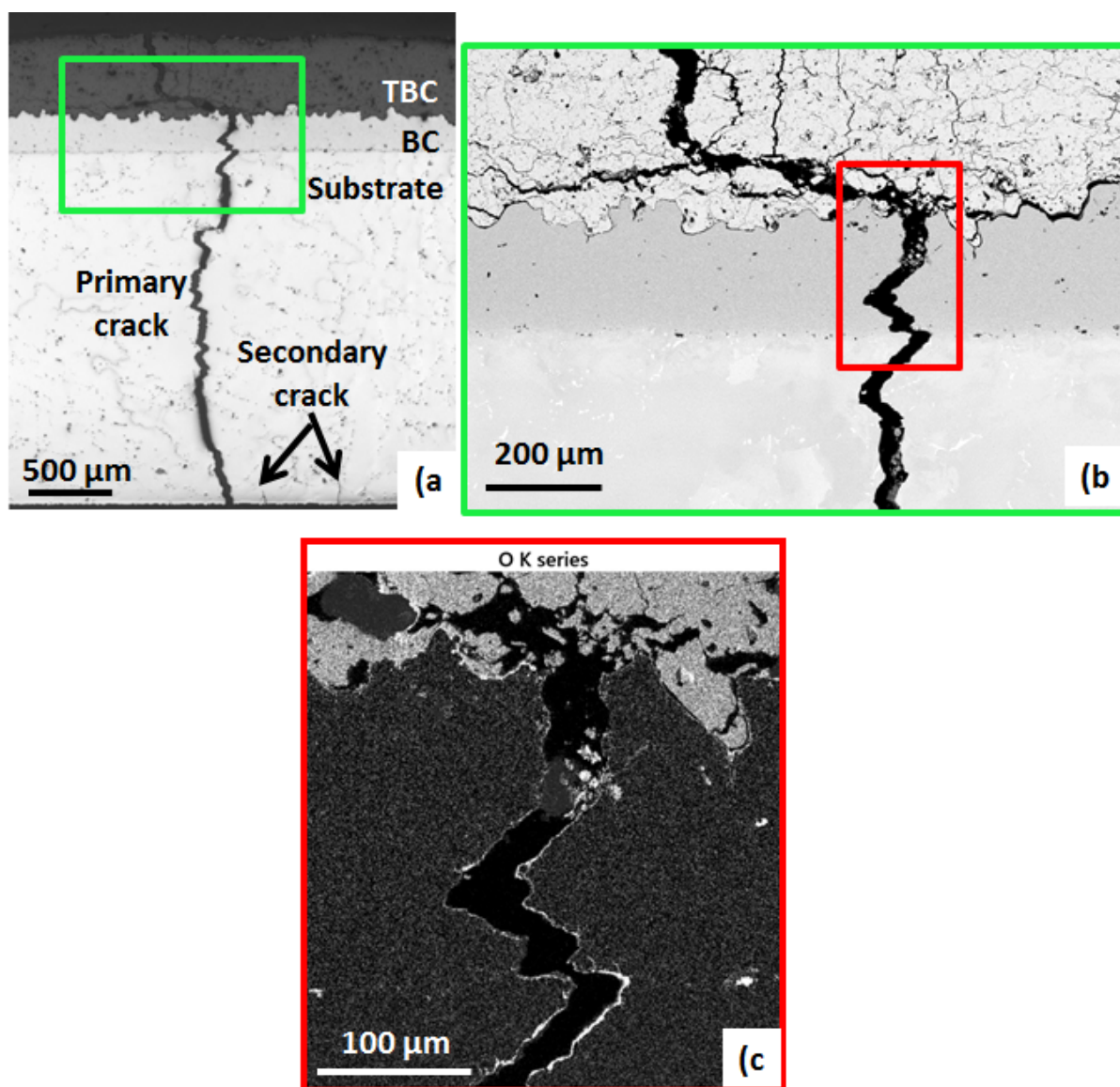


Figure 4.28: a) Primary crack causing failure of undrilled specimen, b) delamination occurred at the end of life time, c) Oxygen EDS mapping at the primary crack showing the influence of oxidation.

Secondary cracks as well as the primary crack, perpendicular to loading direction, are initiated at the base alloy inner surface which shows the criticality of the uncoated side, see Fig. 4.29a. The oxidation observed on the crack surfaces might have accelerated the crack propagation, see Fig. 4.29b.

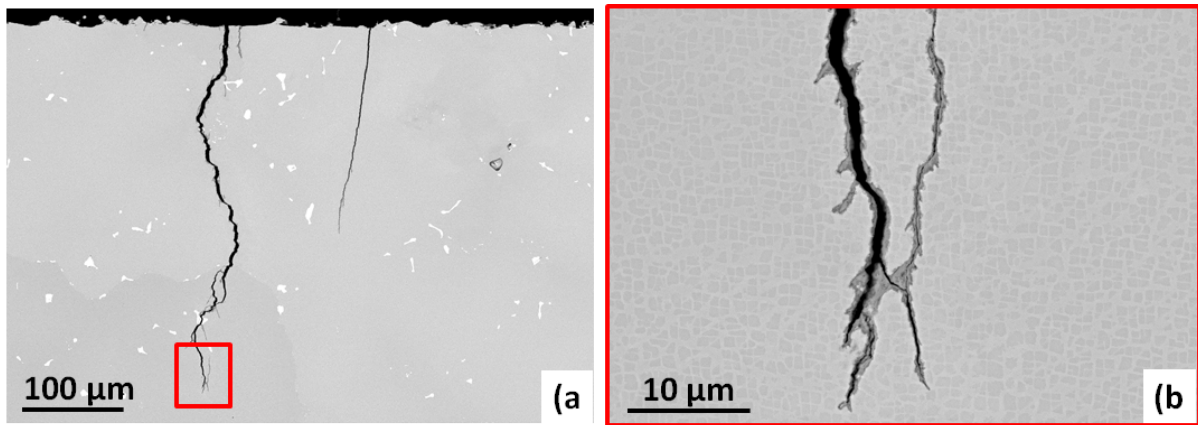


Figure 4.29: a) Secondary crack in the failed undrilled specimen, b) magnification of crack tip showing oxidation influence.

At TBC/BC interface, small cracks can be observed, as shown in Fig. 4.30. The oxidation effect can also be observed on the crack surfaces.

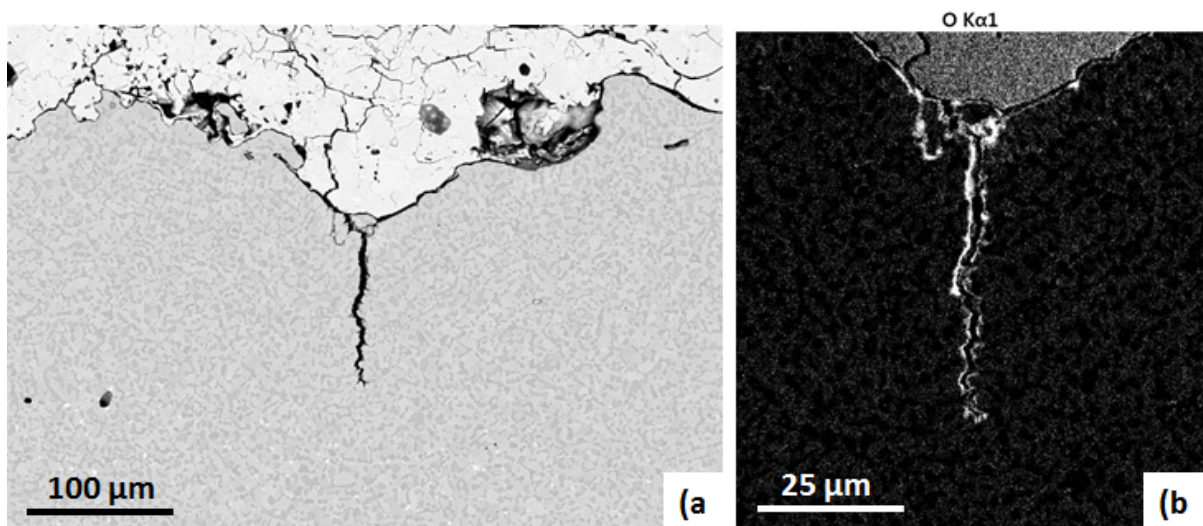


Figure 4.30: a) Small cracks at TBC/BC interface, b) Oxygen EDS mapping of the crack.

Fig. 4.31 shows the failed specimen with inclined holes, drilled with flash lamp laser using trepanation, tested with 0.67 % mechanical strain range. A segmentation crack in the TBC can be observed at the laser-drilled hole marked with blue rectangle.

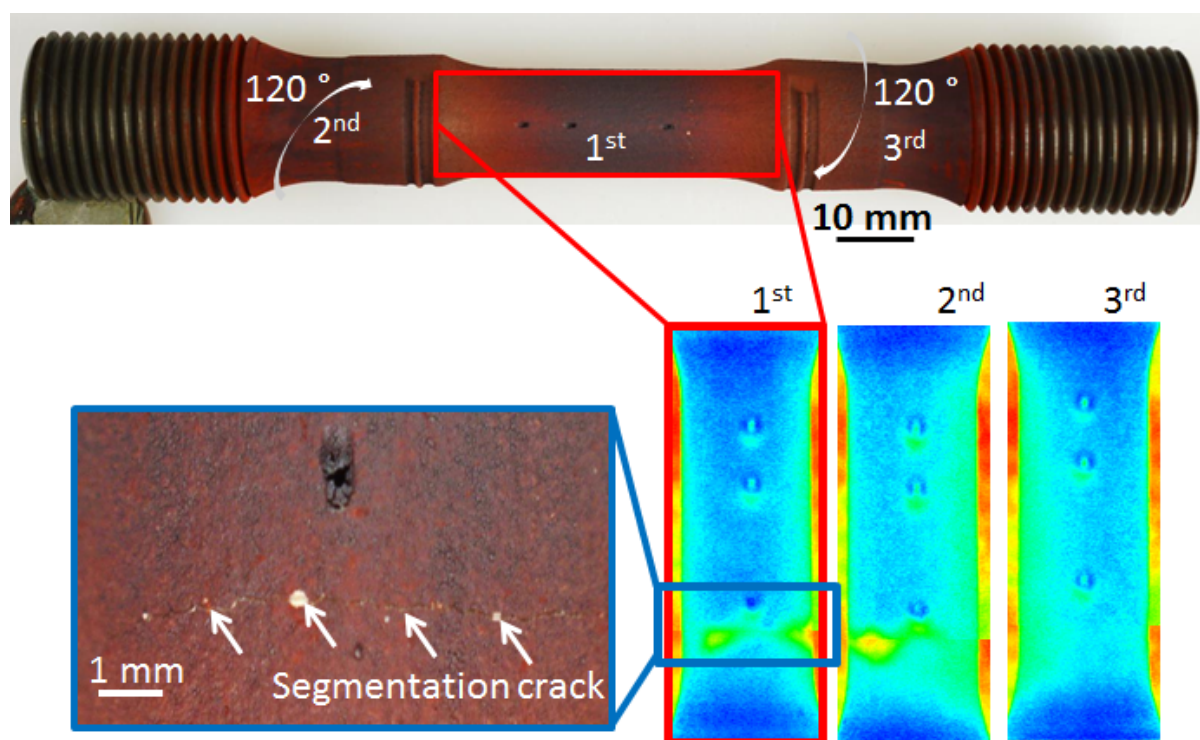


Figure 4.31: Failed drilled specimen with inclined holes, laser drilled with flash lamp using trepanation mode, tested with 0.67 % mechanical strain range as well as thermography measurement.

The SEM images of the failed specimen, illustrated in Fig. 4.31, with inclined cooling holes tested with 0.67 % are shown in Fig. 4.32. The SEM images are related to the cooling hole marked in blue in Fig. 4.32. A secondary crack can be observed near the primary crack, see Fig. 4.32b and Fig. 4.32c. Fig. 4.31b shows the secondary crack at the leading edge. It seems that the secondary crack has propagated through a crack in the HAZ or recast layer, formed during laser drilling. As illustrated by Fig. 4.32c, the direction of the crack propagation seems to be towards the BC and TBC, and it has stopped in the BC. In Fig. 4.32d and Fig. 4.32e, the delamination of TBC and partly BC can be seen as a consequence of the formation and propagation of the primary crack in the substrate, BC, and TBC. These observations agree with the thermography measurements of the specimen which showed a delamination at the same location.



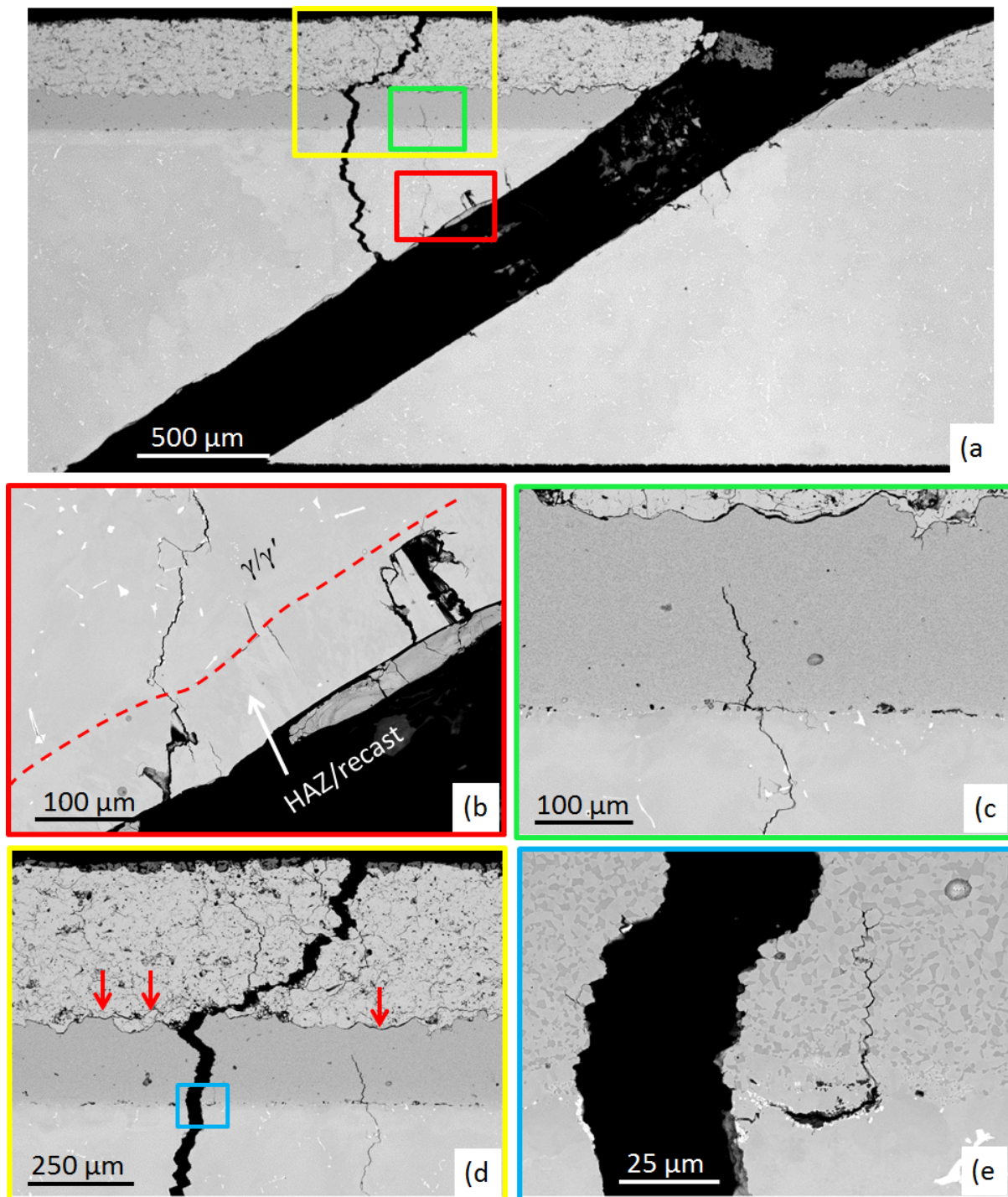


Figure 4.32: a) SEM image of the cooling hole, laser drilled with flash lamp using trepanation mode, marked in blue in Fig. 4.31, from the LCF test with 0.67 % mechanical strain range, b) secondary crack at the cooling hole, c) penetration of the secondary crack into BC, d) delamination of TBC coating due to penetration of primary crack, e) branching of a small crack into BC/substrate interface and its further propagation into the BC.

A SEM image of a crack at the cooling hole, laser drilled with flash lamp using trepanation mode, related to the specimen in Fig. 4.31, at the end of the life time can be seen in Fig.

4.33 with a higher magnification. It can be seen that the crack is mainly in the HAZ or recast layer having a different microstructure than the cubic  $\gamma/\gamma'$  microstructure of the base alloy, see Fig. 4.33a. In Fig. 4.33b, the penetration of the crack into the  $\gamma/\gamma'$  microstructure is visible. This is probably the mechanism which led to the failure shown in Fig. 4.32.

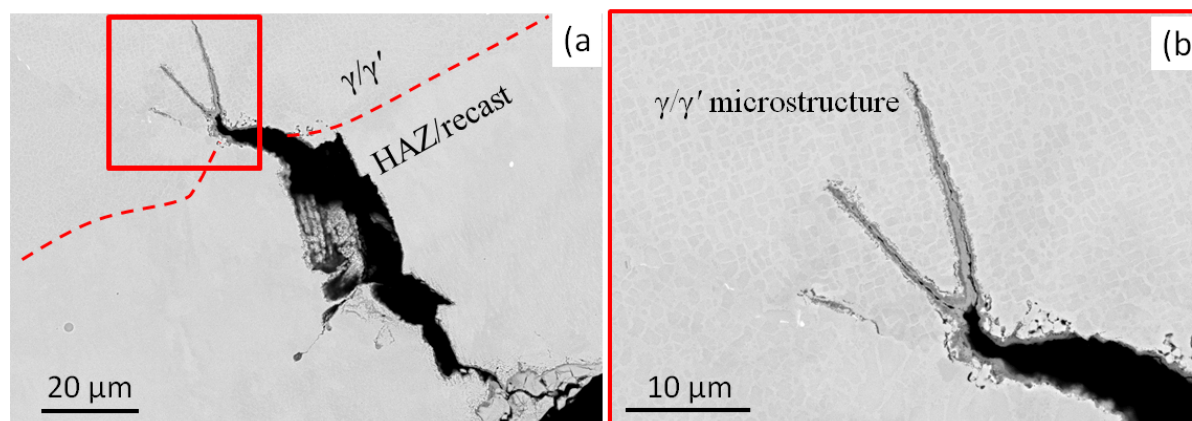


Figure 4.33: a) A crack at the leading edge of an inclined cooling hole, laser drilled with flash lamp using trepanation mode, in the failed specimen tested with 0.67 % mechanical strain range, b) magnified image of the crack tip.

Fig. 4.34 shows the failed specimen with inclined cooling holes, drilled with flash lamp laser using trepanation, tested with 0.38 % mechanical strain ranges. As in the previous cases, a segmentation crack can be observed at the marked cooling hole. However, the delaminated area is not significant in comparison with the specimen tested with higher strain range, see the red arrows in Fig. 4.35c.

The primary crack in the specimen with inclined cooling holes tested with 0.38 % mechanical strain range, was observed at a similar location with respect to the hole, see Fig. 4.35a. Secondary cracks were found near the primary crack, which have coalesced together, see Fig. 4.35b. Similarly, it seems that the cracks in HAZ/recast layer have promoted the initiation or propagation of primary or secondary cracks, as shown in Fig. 4.35d. In Fig. 4.35e, other tertiary cracks at the cooling hole can be seen, which propagated into the base alloy mainly along carbide precipitates.

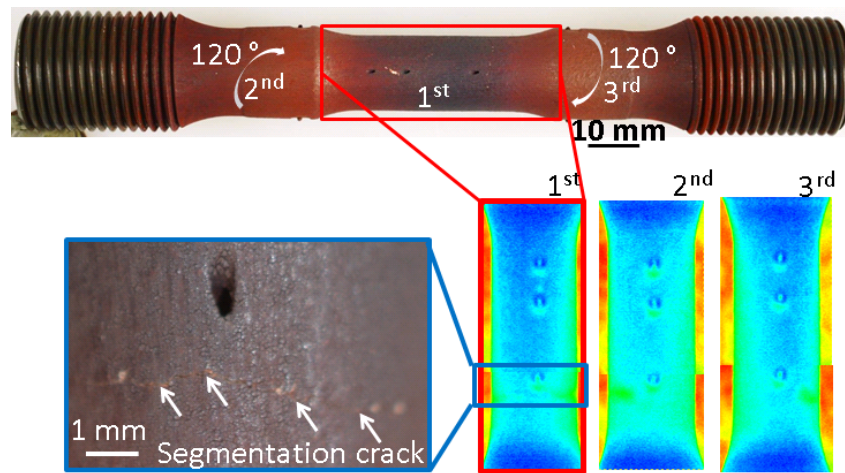


Figure 4.34: Failed specimen with inclined holes, laser drilled with flash lamp using trepanation mode, tested with 0.38 % mechanical strain range as well as thermography measurement.

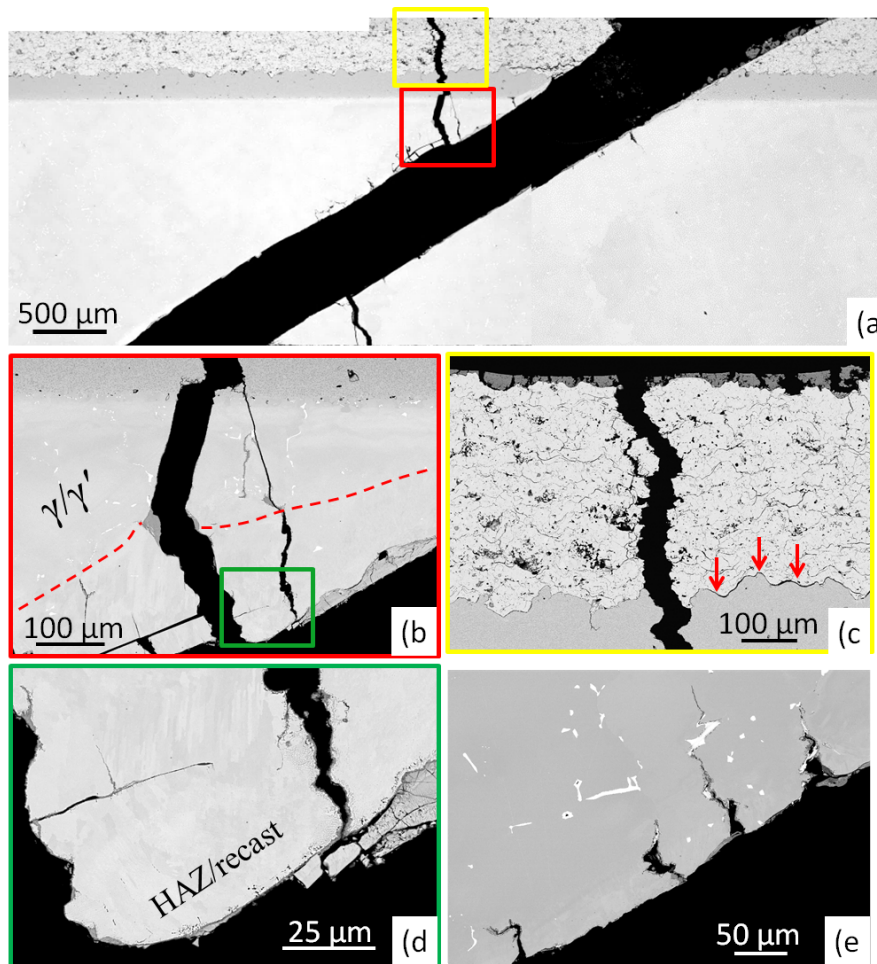


Figure 4.35: a) SEM image of the inclined cooling hole marked in blue in Fig. 4.34, from the LCF test with 0.38 % mechanical strain range, b) Secondary crack coalescing the primary crack, c) delamination at TBC/BC interface at the primary crack, d) changed microstructure of  $\gamma/\gamma'$  structure in the HAZ/recast layer promoting crack initiation, e) tertiary cracks at the carbides.



The crack numbers for three cooling holes belonging to the both specimens having holes, laser drilled with flash lamp using trepanation mode, and tested with the strain ranges 0.38% and 0.67%, have been illustrated for different crack length intervals in Fig. 4.36. It can be concluded that the number of cracks regarding the specimen tested with the lower strain range were higher compared with the specimen tested with the higher strain range.

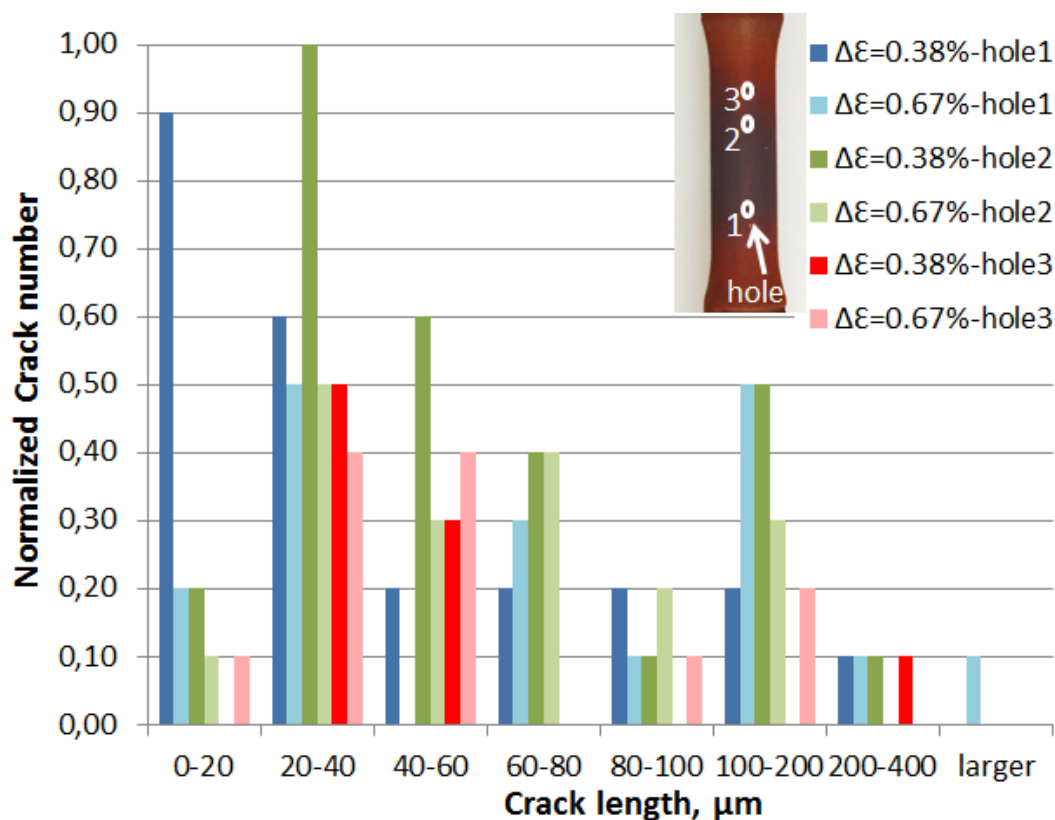


Figure 4.36: Normalized crack number for three cooling holes, laser drilled with flash lamp using trepanation mode, of the two specimens tested with 0.67 % and 0.38 % strain ranges.

The total crack numbers for the three cooling holes of the specimens tested with the two strain ranges, 0.67 % and 0.38 % are 44 and 59, respectively. This is a similar phenomenon observed by Klabbbers [3], where testing by a lower strain range induced a larger crack density, as shown in section 2.2.5.1. This probably means that the lower strain range is more sensitive to laser-drilled hole quality.

Fig. 4.37 shows the USP-drilled specimen after failure, which was tested with the strain range of 0.67 %. As shown, no TBC spallation was observed, similar to the other cases. A segmentation crack can be observed in the middle section of the specimen.

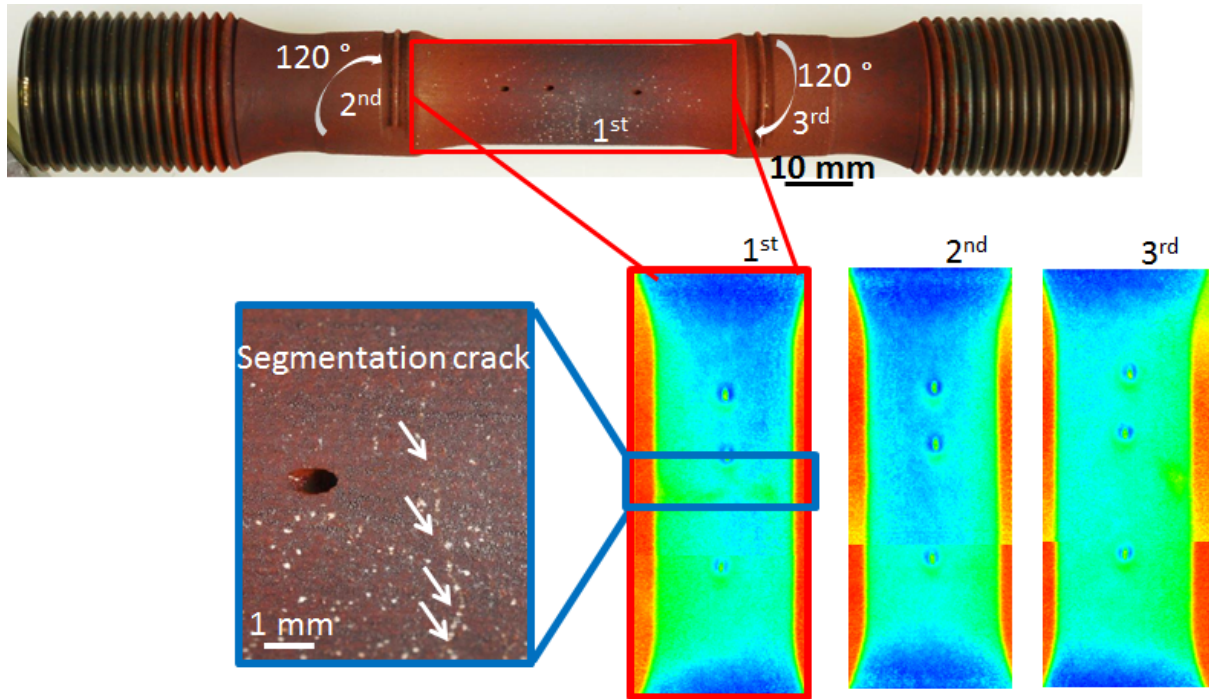


Figure 4.37: Failed specimen with USP-drilled inclined cooling holes, tested with 0.67 % mechanical strain range as well as thermography measurement.

Fig. 4.38a shows the SEM images of the cooling hole marked in blue in Fig. 4.37. Similar to the specimens drilled with flash lamp, trepanation mode, the primary crack can be observed at the similar spot of the hole, which suggests that stress concentration at this location of the inclined holes is the most critical. However, the crack density is negligible in comparison with the other laser drilling method, which is due to the high quality of the USP method. As shown in Fig. 4.38b and Fig. 4.38c, it can be seen that there is no recast layer or HAZ after the failure. The secondary crack can be found near the primary crack, where the crack surfaces are oxidized. A similar crack was found in BC on the leading edge, where only the pure  $\gamma/\beta$  phase could be found, with no recast layer or HAZ.

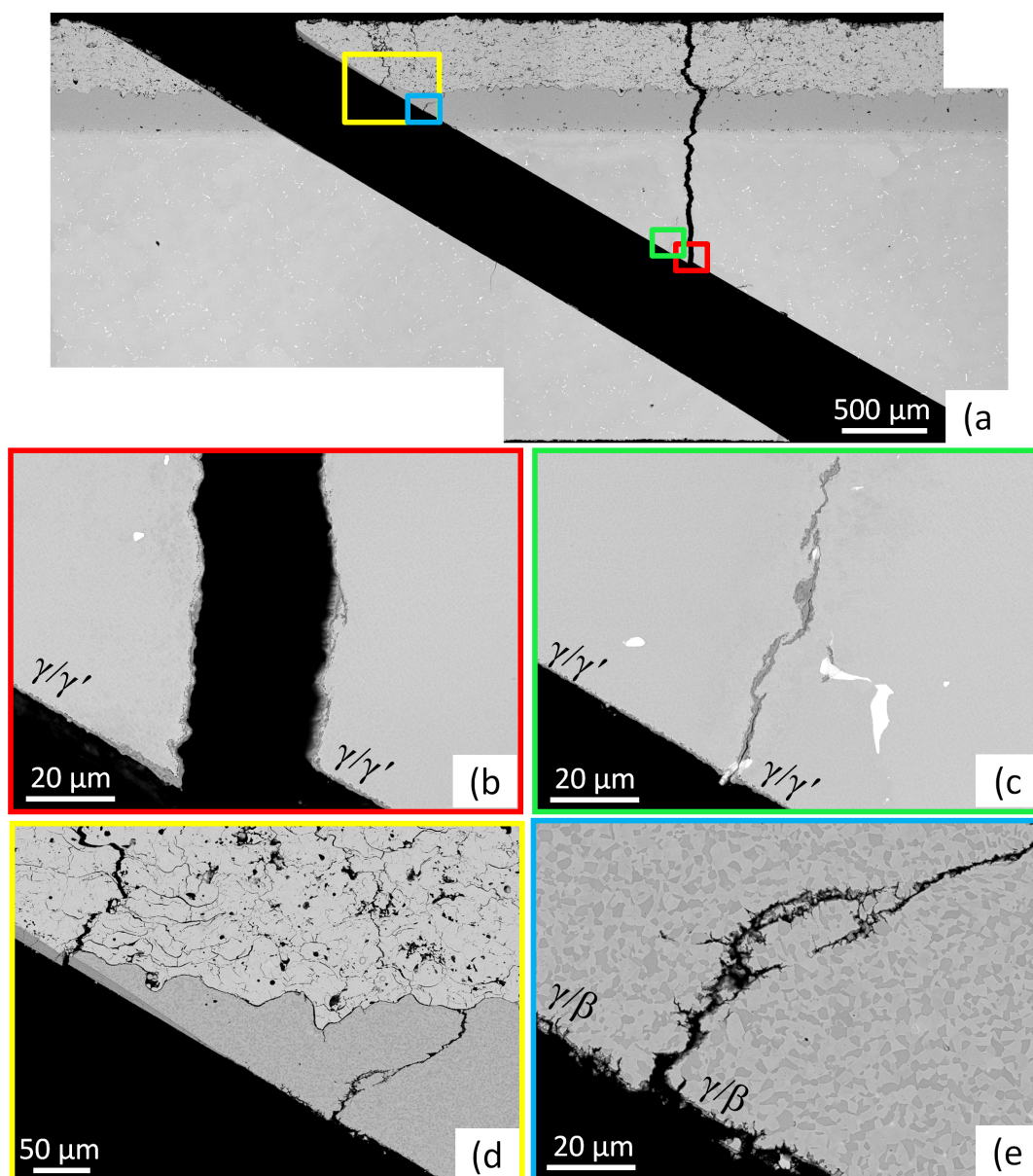


Figure 4.38: a) SEM images of the marked inclined cooling hole, laser drilled with USP, marked in blue in Fig. 4.37, from the LCF test with 0.67 % mechanical strain range, b) the  $\gamma/\gamma'$  microstructure near the primary crack directly at the hole wall, b) tertiary cracks at the trailing edge c) the TBC/BC interface at the trailing edge with no HAZ/recast layer, d) the intact  $\gamma/\beta$  structure of BC at a cooling hole.

Fig. 4.39 presents the failed specimen with vertical cooling holes, laser drilled with flash lamp using trepanation mode, tested at 0.67 % mechanical strain range. A localized delaminated area, marked in blue in thermography measurements, as well as a segmentation crack at the marked cooling hole in Fig. 4.39 can be observed.

Fig. 4.40a and Fig. 4.40b shows the cross section of the vertical cooling holes after failure, where Fig. 4.40c illustrates a vertical cooling hole in the longitudinal section. It can be observed that the crack density on the cross sections are much higher than on the longitudinal section, which is due to the larger stress concentration at this location. The

same behavior was observed for the specimen tested with the lower strain range.

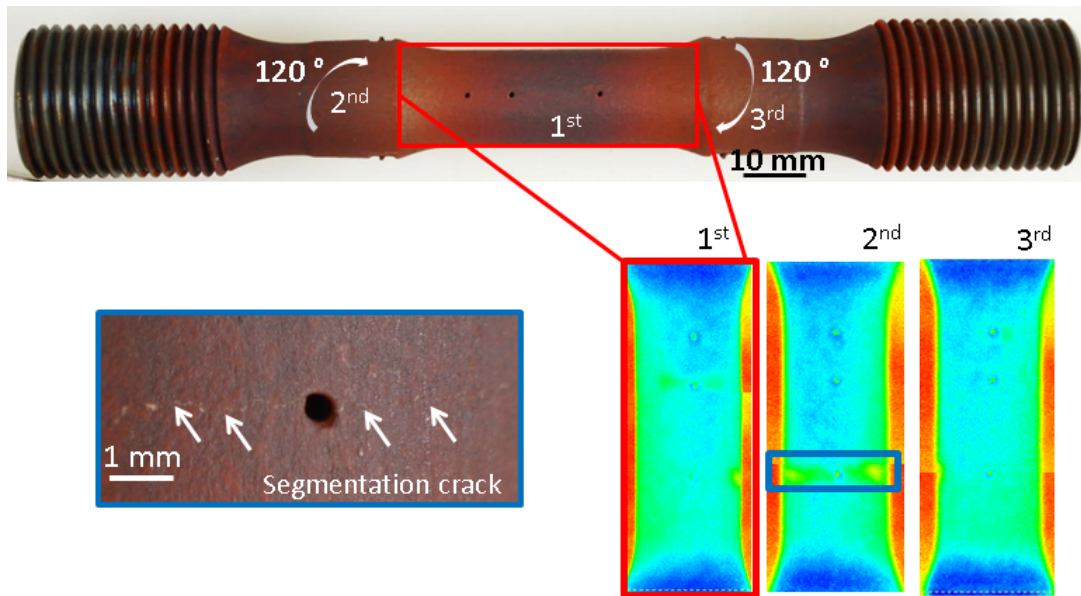


Figure 4.39: Failed specimen with vertical cooling holes, laser drilled with flash lamp using trepanation mode, tested with 0.67 % mechanical strain range as well as thermography measurement.

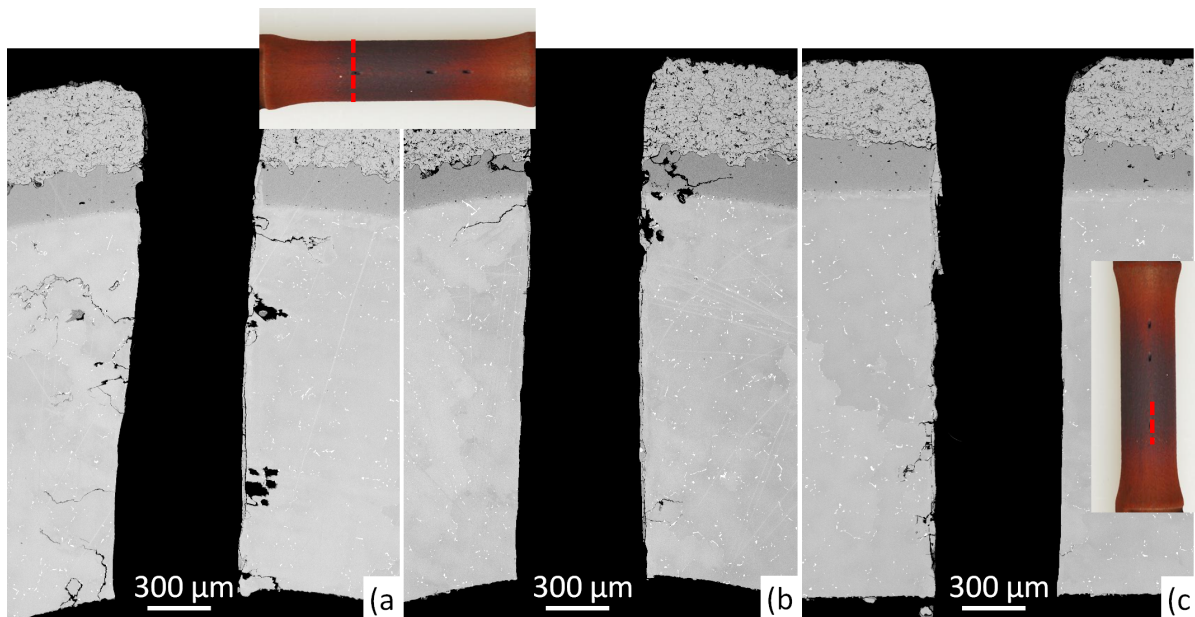


Figure 4.40: SEM images of the vertical cooling holes, laser drilled with flash lamp using trepanation mode, from the LCF test with 0.67 % mechanical strain range, a,b) SEM images of the vertical cooling holes on the cross section with a large defect density, c) SEM image of the vertical cooling hole on the longitudinal section with much less defects compared with the holes on cross section.

Cooling holes, laser drilled using USP, with no recast layer and defect density caused the



minimum reduction of the life time, for each hole angle, in comparison with undrilled specimens. A better laser drilling quality had a larger influence on life time for the specimens with inclined cooling holes in comparison with the ones having vertical holes, where the influence of stress concentration was probably larger than the hole quality. Vertical cooling holes caused a shorter LCF life time compared with inclined holes, due to dominance of the stress concentration effect at the holes. TBC spallation was not observed after the failure, which is in agreement with the literature results. Micro-cracks in the superalloy at the cooling hole had a significant influence on the LCF life time at high temperature, where delamination cracks were not important as a failure mechanism.

## 4.4 FEM results of TBC systems with cooling holes under thermomechanical loading

A FEM model based on thermocyclic loading of TBC-coated nickel-based superalloy, involving oxide growth kinetics has been developed by Bednarz et al. [23], that predicts the evolution of stress distribution with good precision, as described in Fig. 2.30. A key parameter in this model is the alumina scale thickness which affects local stress development as a function of oxidation time. In this model, the influence of cooling holes on stress distribution within the TBC-coated superalloy has not been considered.

The goal of the FEM calculations performed in the following section is to calculate the influence of cooling holes with different angles and diameters, as well as the effect of recast layer due to laser drilling process on the normal and shear stress distribution in an TBC-coated nickel-based superalloy, assuming an alumina scale of  $0.5 \mu\text{m}$  thickness, which is typical after short term oxidation at around  $1000^\circ\text{C}$  in air. A sensitivity analysis has also been performed in order to understand the impact of creep, CTE, elastic modulus, and TGO thickness on the stress distribution close to the hole.

### 4.4.1 Influence of angle with 3D FEM model

In this part, the stress distribution in the 3D model for the case of vertical and inclined hole is analyzed. In section 4.1, experimental results revealed a larger defect density for inclined holes, see Table 4.1 and Fig. 4.13. In the following it is attempted to understand in more details the underlying reasons of the differences in crack densities for different angles. The stress distribution is studied at the TBC/BC interface (over the red path in Fig. 3.21), BC/substrate interface (blue path), and along the TBC recast layer (green path in Fig. 3.22). Fig. 4.41a shows the normal stress at the TBC/BC interface for both inclined and vertical holes. A higher normal tensile stress can be observed for the inclined hole, which is one of the reasons for the observed longer cracks in the experiments, as shown in Fig. 4.2. It should be noted that at the BC/substrate interface, the normal stresses for vertical and inclined holes are in the same range, see Fig. 4.41b.

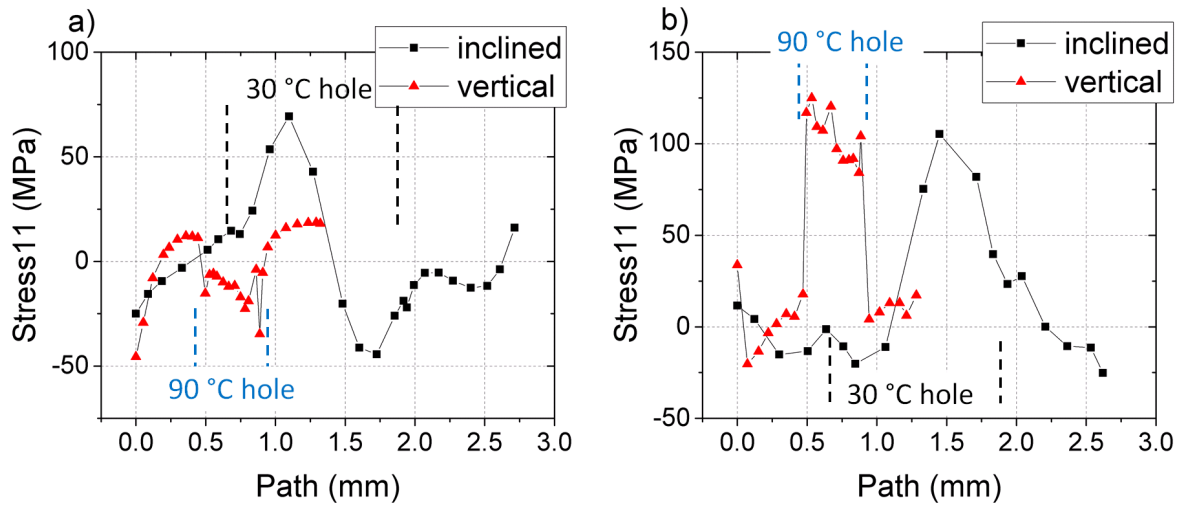


Figure 4.41: Comparison of stress distribution for vertical and inclined holes at (a) TBC/BC interface and (b) BC/substrate interface.

In Fig. 4.42, a difference in stress distribution can be observed in the 3D FEM model. As can be seen in this and the previous figure, the stress on the leading edge is higher than in the case of a vertical hole, where larger cracks were also observed based on experimental results, see Fig. 4.2.

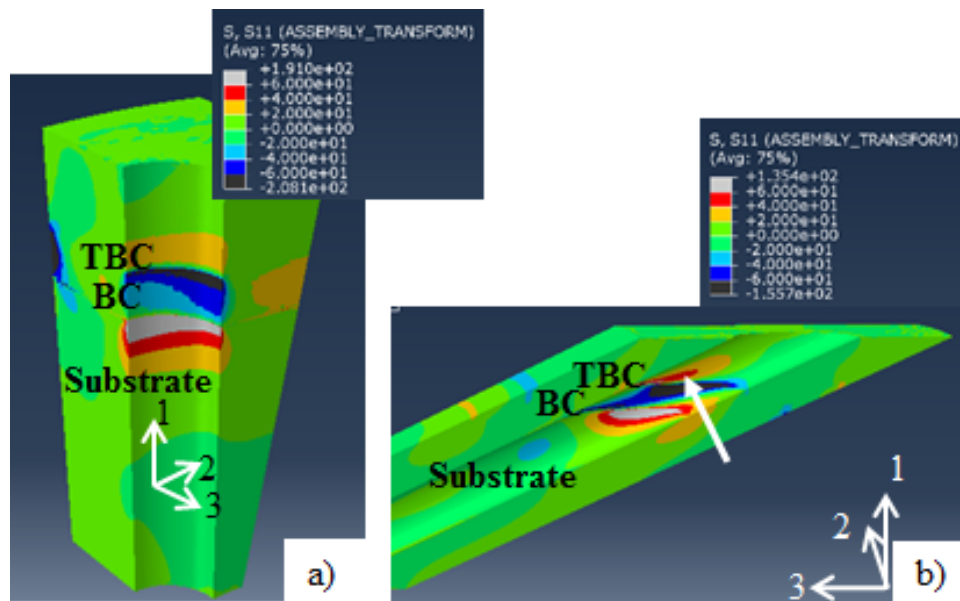


Figure 4.42: Normal stress distributions (11 direction) are shown for vertical (a) and inclined hole (b).

#### 4.4.2 Influence of hole diameter with 2D FEM model

In this part, the results on the stress distribution at TBC/BC interface near holes with different diameters are reported and compared with the undrilled case. The stress



distribution is studied over the paths shown in Fig. 4.43.

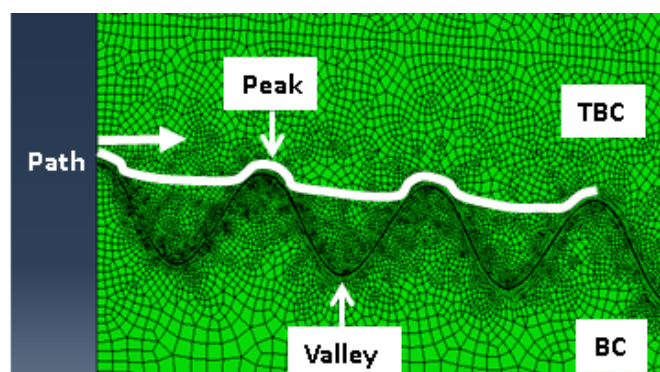


Figure 4.43: Path over which the stress distribution is studied.

Fig. 4.44 shows the normal stress profile over this path for the considered cases. It can be seen that the normal stress at the hole edge for a cooling hole of diameter 0.5 mm is higher than for the case with no hole. For the cooling hole of diameter 0.75 mm, the stress at the hole edge is comparable with the case of no hole. Further away from the hole edge, the stresses are less tensile at peaks as well as more compressive at valleys than in the case of the undrilled material. However, this difference decreases as we move away from hole till the distributions merge. It should be mentioned that stresses for the cooling hole of smaller diameter are slightly higher than for holes with larger diameters.

Fig. 4.45 shows the shear stress along such path. It can be seen that the shear stresses have increased by around a factor of two in cases of drilled holes. The maximum stress occurs at off peak position.

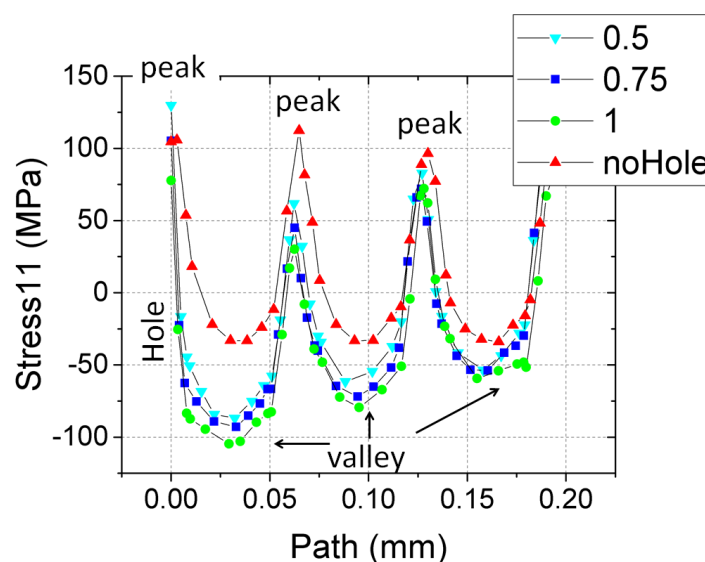


Figure 4.44: Normal stress for the TBC-coated superalloy without and with cooling hole of diameters of 0.5, 0.7, and 1 mm.

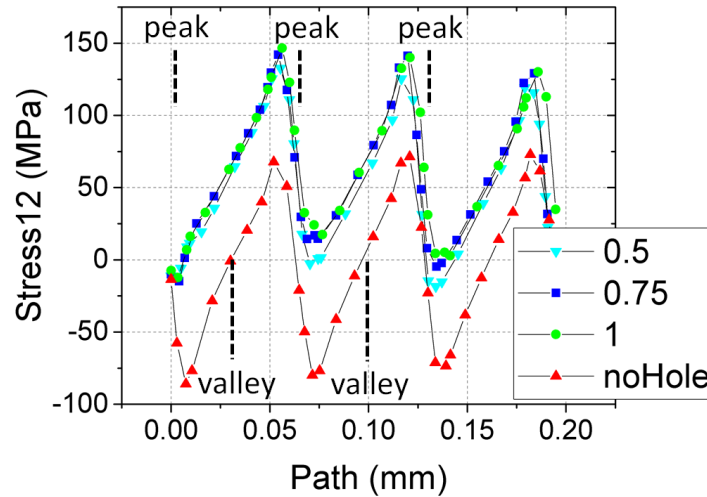


Figure 4.45: Shear stress for the case with no hole, and for holes having diameters of 0.5, 0.7, and 1 mm.

The simulation results are supported by the outcome of the cyclic oxidation results of the specimens with laser-drilled holes of 0.5 and 1 mm diameter, showing that the effect of the cooling hole diameter on life time is low. However, different results were obtained by [28], where perhaps due to using a pure elastic model an influence of diameter was observed.

#### 4.4.3 Influence of recast layer with 3D model

In this section, the influence of recast layers in a 3D model for both vertical and inclined holes is studied. In the following, three cases are analyzed: without recast layer (WORC), with TBC recast layer (RC), and with a higher CTE (25 %) of TBC recast layer (RCHCTE). Fig. 4.46a shows the influence of recast layer at a vertical hole along the TBC recast layer, see the green path in Fig. 3.22a. The stresses become higher with an existing recast layer, which is supported by experimental cross-sections revealing the cracks in TBC recast layer of vertical holes, see Fig. 4.2a and c. A higher normal stress can be seen in the simulation results for the TBC/BC interface, see Fig. 4.46b. Therefore, a thicker recast layer increases probably the stress at TBC/BC interface and TBC recast layer.

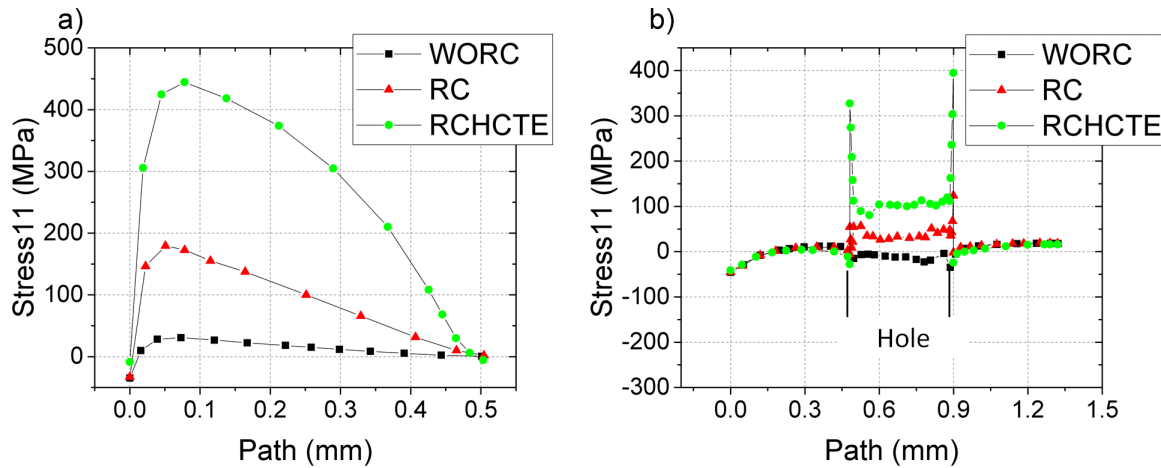


Figure 4.46: Influence of recast layers for a vertical hole on the stress in 11 direction, (a) on the TBC recast layer at the hole edge (over the green path in Fig. 3.22a) and (b) at the TBC/BC interface (over the red path in Fig. 3.21). Without recast layer (WORC), with TBC recast layer (RC), with a higher CTE (25 %) of TBC recast layer (RCHCTE).

Fig. 4.47 presents the influence of a recast layer on an inclined hole. In Fig. 4.47a, it is shown that with a higher CTE of a TBC recast layer the normal tensile stress increases, making formation of cracks at this position more likely. As for the TBC/BC interface, the recast layer causes a larger stress concentration at the hole, see Fig. 4.47b. Fig. 4.48 shows the shear stress distribution at the hole with and without recast layer. Similar to the normal stresses, the recast layers intensifies shear stresses at the hole, either along the TBC recast layer, see Fig. 4.48a, or at the TBC/BC interface, see Fig. 4.48b. Considering the TBC/BC interface, the normal tensile stress on leading edge is higher compared with trailing edge, see Fig. 4.47b. The shear stress is also higher on leading edge. As shown by experimental observations Fig. 4.2b and d, the crack length on the leading edge at TBC/BC interface is larger; hence, one of the underlying reasons is such a stress concentration.

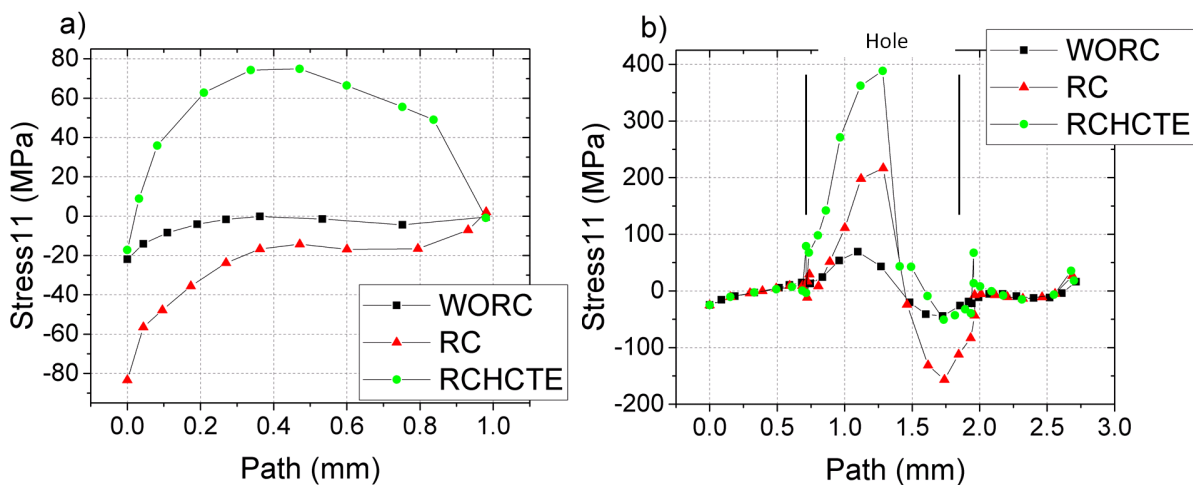


Figure 4.47: Influence of recast layers on normal stress distribution at an inclined hole (a) on TBC recast layer at the hole edge (over the green path in Fig. 3.22b) and (b) at TBC/BC interface (over the red path in Fig. 3.21).

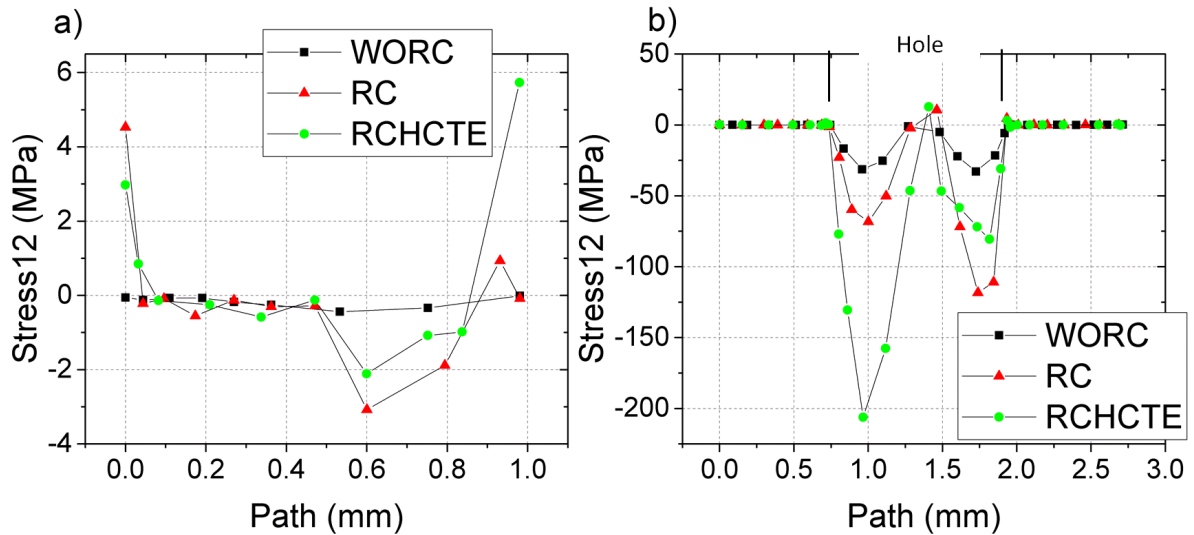


Figure 4.48: Influence of recast layers on shear stress distribution at an inclined hole (a) on TBC recast layer at the hole edge (over the green path in Fig. 3.22b) and (b) at TBC/BC interface (over the red path in Fig. 3.21).

#### 4.4.4 Influence of recast layer with 2D model

Laser drilling can cause crack initiation at interfaces as well as at grain boundaries of the base alloy [69, 124]. Hence, the normal and shear stress distributions are shown at interfaces near the hole for the path indicated by red lines in Fig. 4.49. Stress distribution in the superalloy at the cooling hole will be discussed later, too.

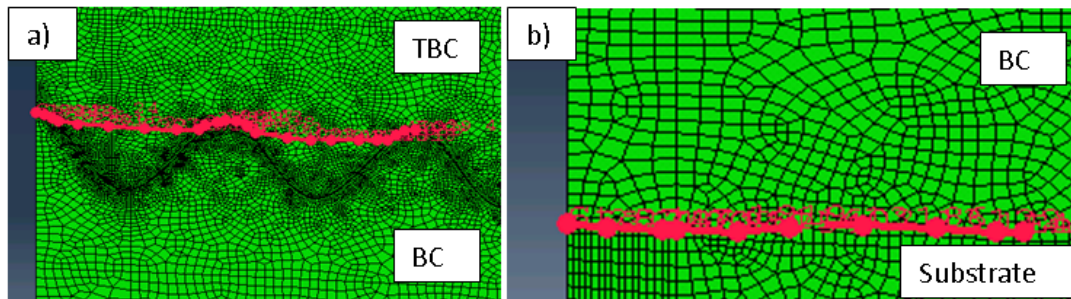


Figure 4.49: Stress distributions in the following are shown over the paths at TBC/BC interface (left) and at BC/substrate interface (right).

In the following, three cases are studied: without recast layer (WORC), with TBC recast layer (TRRC), and with a (25 %) lower (TRCLCt) and (25 %) higher (TRCHCt) CTE of TBC recast layer (RCHCTE). In Fig. 4.50a, it is shown that over the path shown in Fig. 4.49a the normal stresses increases drastically in the non-porous recast layer which induces cracks parallel to the interface. FEM results of two additional cases are shown as well: 25 % lower and 25 % higher CTE with respect to the  $CTE_{TBC}$ , see Table 3.12. A higher CTE of the non-porous layer leads to higher normal, and shear stresses, see Fig. 4.50a and Fig. 4.50b. In Fig. 4.50c and Fig. 4.50d, it can be seen that in comparison

with ms-pulsed laser drilling, femto second laser drilling provides a better hole quality. Hence, it can be concluded that the existence of the TBC recast layer can cause cracks parallel to interface.

In order to assess the influence of the creep rate of the TBC recast layer on stress distribution over the path shown in Fig. 4.49a, two additional simulations with 25% higher (TRCHCr) and 25% lower (TRCLCr) creep rates with respect to that of TBC (given in Table 3.13) were performed, see Fig. 4.51. It can be observed that the normal stress in this case is not strongly affected by the creep behavior, and only the shear stress has increased slightly with a higher creep rate. Hence, it is worth to mention that stresses within the TBC system are more sensitive to CTE variations than to the creep rate.

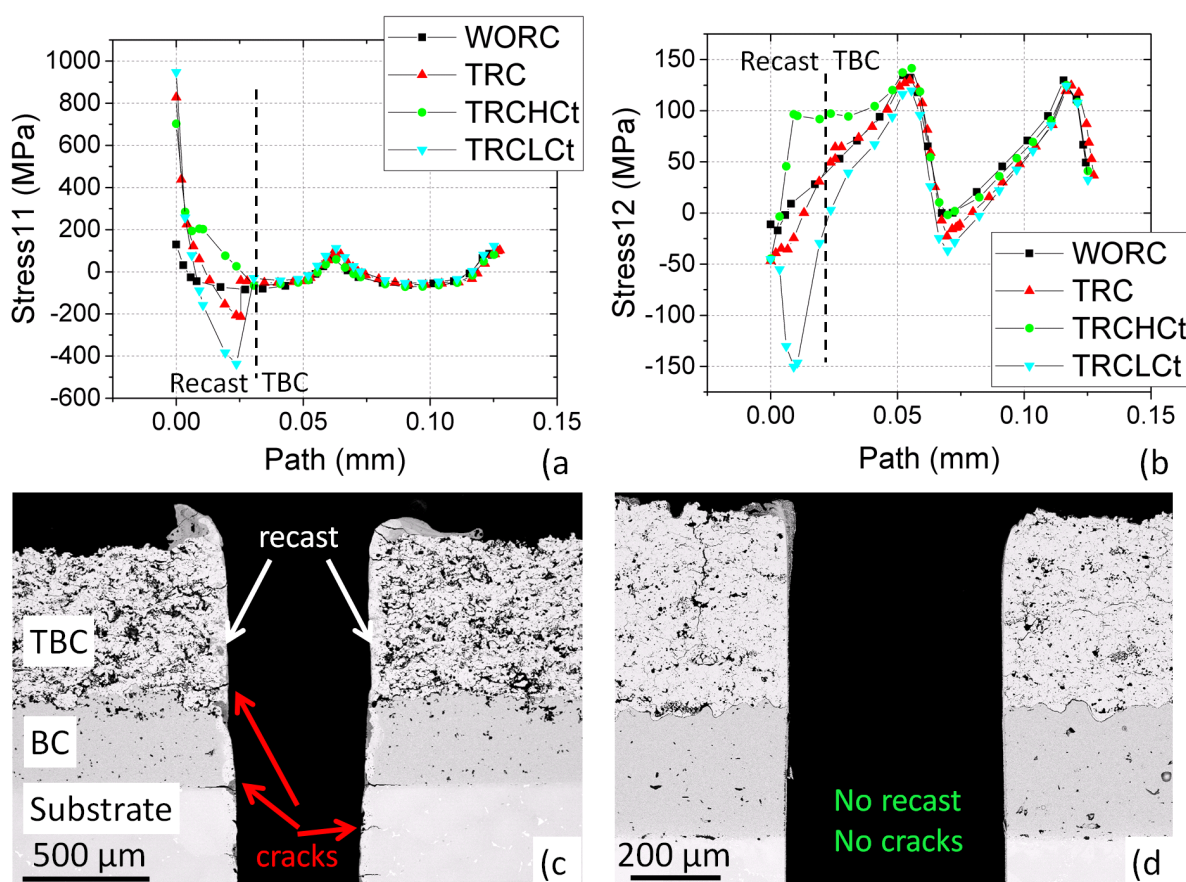


Figure 4.50: Comparison of (a) normal and (b) shear stress distribution for the TBC system at TBC/BC interface near the hole, see Fig. 4.49a, without recast layers (WORC), with TBC recast layer (TRC) together with higher (TRCHCt) and lower (TRCLCt) CTE. TBC systems drilled with (c) ms-pulsed laser method and (d) fs-pulsed laser method are also to be compared with numerical results.



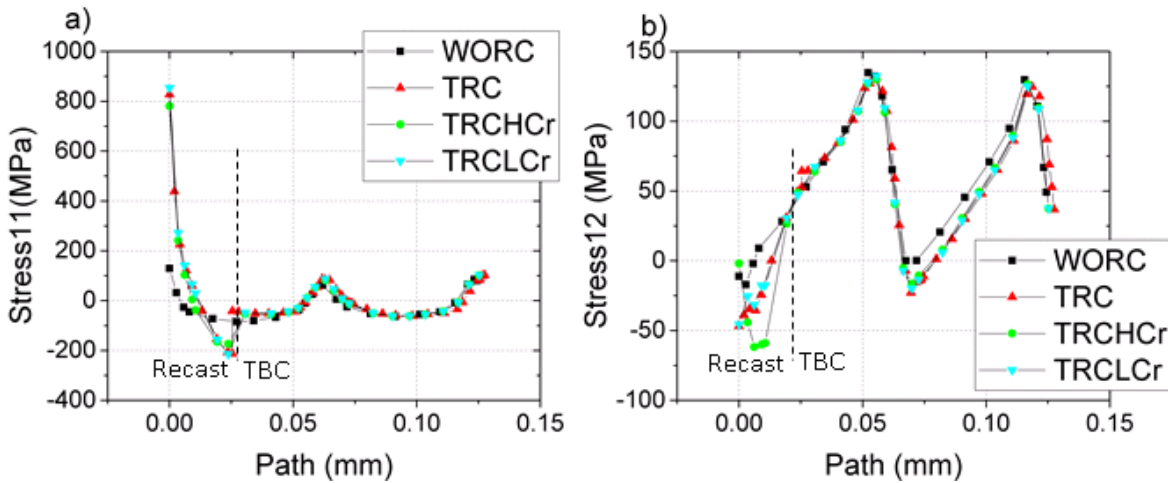


Figure 4.51: Comparison of (a) normal and (b) shear stress distribution, over the path shown in Fig. 4.49a, for the TBC system without recast layers (WORC), with TBC recast layer (TRC) together with high (TRCHCr) and low (TRCLCr) creep strain rate.

The influence of substrate recast layer (SRC) was also studied, see Fig. 4.52. Normal and shear stresses in the BC increase above BC/substrate interface, especially at the recast-BC line. This increase can induce cracks after laser drilling, which were also observed in Fig. 4.50 at this position. Based on the current results, the normal stresses in the recast layer reduce at BC/substrate interface near the hole, see Fig. 4.52a, however, shear stresses increase, see Fig. 4.52b. With a creep rate, 25 % higher (SRCHCr) than that of the substrate, due to the smaller grains of this layer, stresses decrease. With an elastic modulus, 25 % higher (SRCHE) than that of substrate, stresses increase as expected. However, stresses might be still high enough to cause cracks.

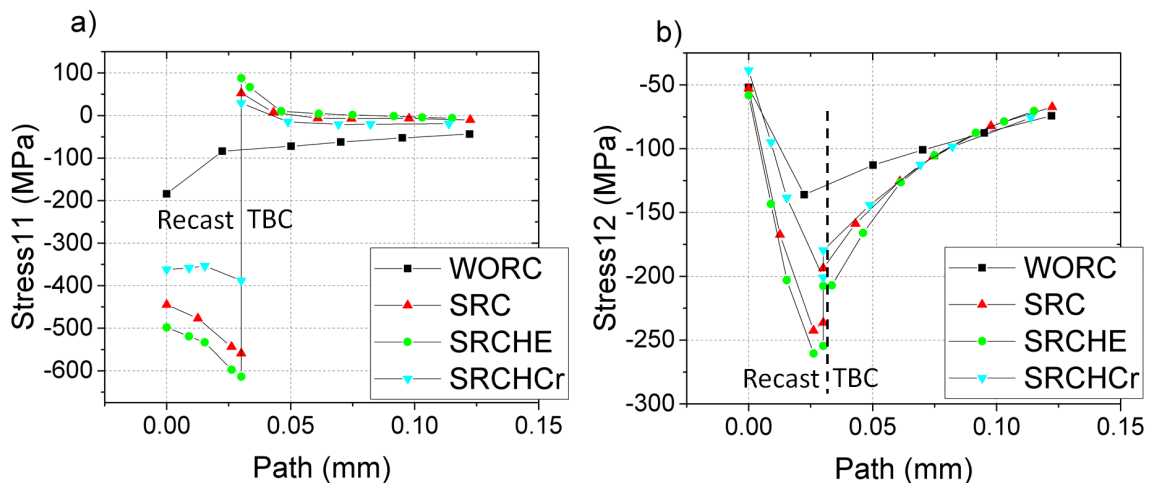


Figure 4.52: Comparison of (a) normal and (b) shear stress distribution for the TBC system, over the path shown in Fig. 4.49b, without recast layers (WORC), with BC/substrate recast layer (SRC) together with higher elastic modulus (SRCHE) and higher creep strain rate (TRCHCr).

Fig. 4.54a shows the influence of a 25 % higher (SRCHCTE) and lower (SRCLCTE)



CTE of BC/substrate recast layer, than that of substrate, on the normal stress over a path shown in Fig. 4.53.

A relative higher CTE of the recast layer in comparison with the substrate's reference value enhances the normal stresses, which could initiate cracks as observed by the experimental results, see Fig. 4.54b. On the other hand, a lower CTE decreases the normal stress into the compressive region.

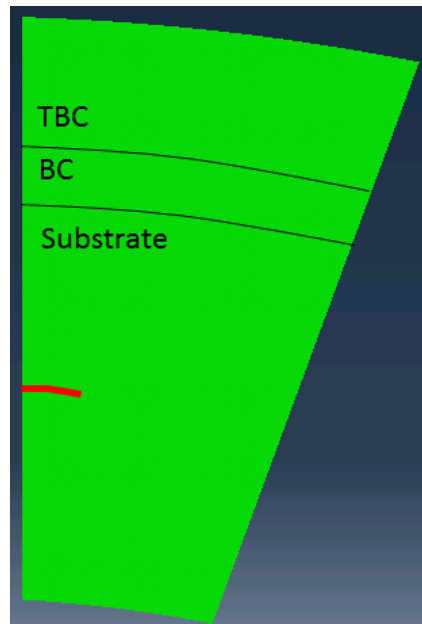


Figure 4.53: Stress distributions in Fig. 4.54 are shown over the shown red path in substrate with certain distance from BC/substrate interface.

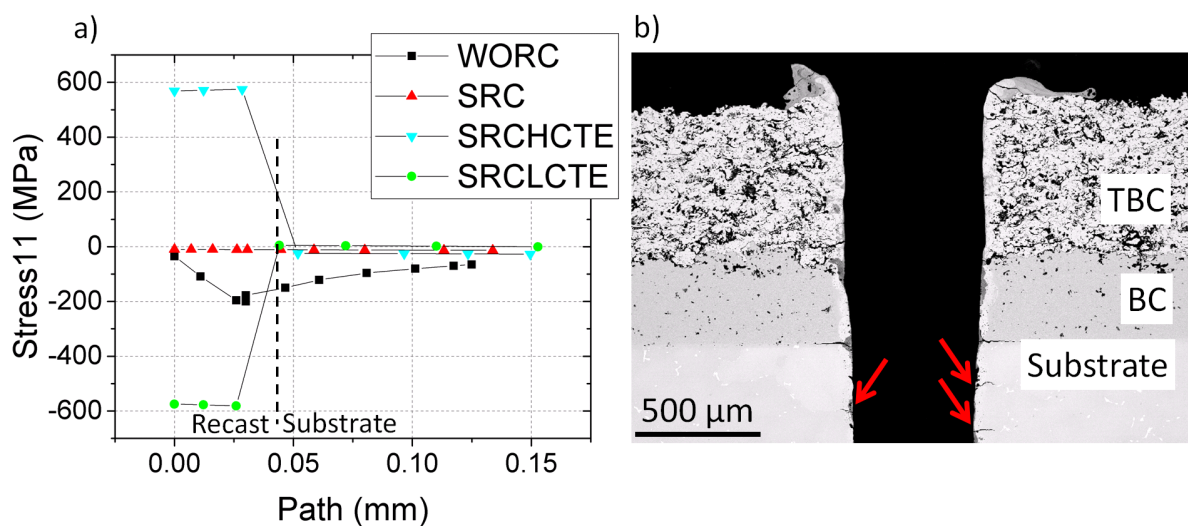
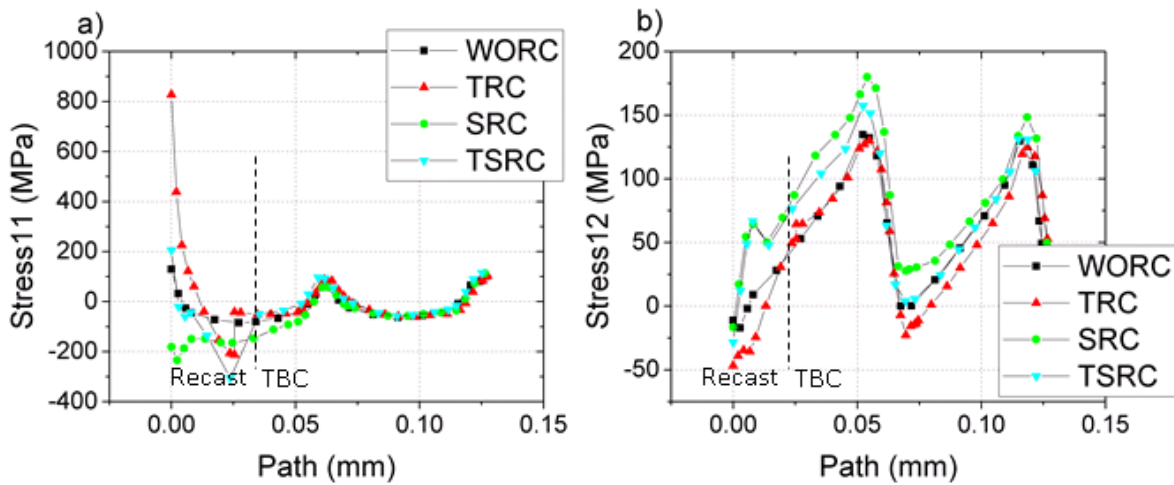


Figure 4.54: (a) Comparison of normal stress distribution for the TBC system, over the path shown in Fig. 4.53, without recast layers (WORC), with BC/substrate recast layer (SRC) together with high (SRCHCTE) and low (SRCLCTE) CTE. (b) SEM image of specimen drilled with fiber laser, percussion mode with cracks in substrate at the cooling hole wall.

In the case of existence of both TBC and BC/substrate recast layers (TSRC), the stress distribution at TBC/BC interface can be compared for the cases with no recast layers (WORC), only TBC recast (TRC) or BC/substrate recast layer (SRC), respectively, see Fig. 4.55. Regarding the TSRC case, a TBC recast layer has a higher  $E$ -modulus due to its low porosity than the porous TBC. Moreover, the BC/substrate recast layer has also an assumed 25 % higher creep rate with respect to substrate, due to its fine grains, see Table 3.15. At the TBC/BC interface the normal stress increases close to the hole considering both recast layers (TSRC), however, decreases afterwards, see Fig. 4.55a. Additionally, shear stresses in this case are increased more, especially at the hole, see Fig. 4.55b. At the BC/substrate, normal and shear stresses in the BC increase in the case of both recast layers (TSRC), see Fig. 4.55c and d.

TBC/BC interface:



BC/substrate interface:

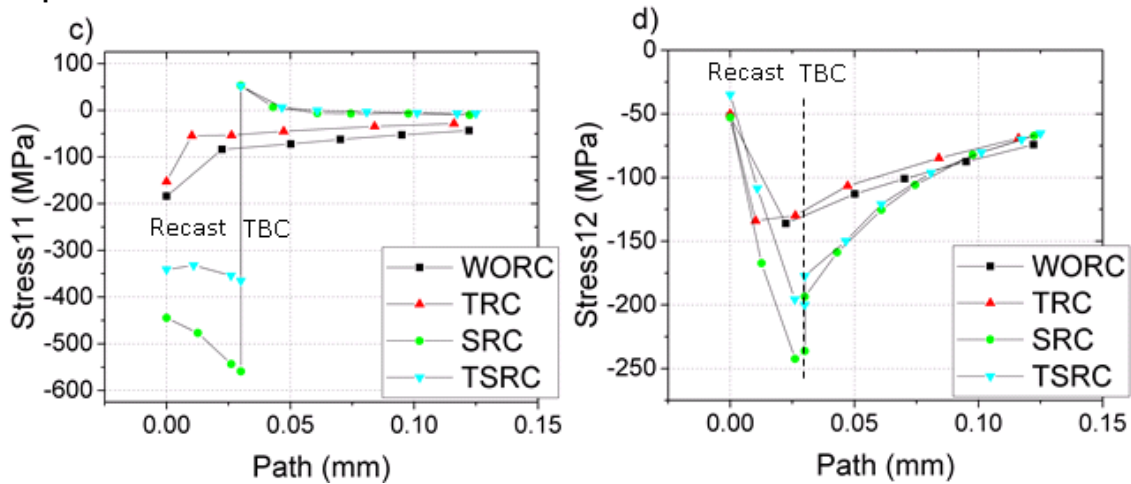


Figure 4.55: Comparison of (a) normal and (b) shear stress distribution for the TBC system without recast layers (WORC), with TBC recast layer (TRC), with BC/substrate recast layer (SRC), and the case with both layers.

In Fig. 4.56a, the influence of BC oxidation and TGO formation is shown at the TBC/BC interface. When TGO thickness is  $0.5\mu\text{m}$ , the normal stress is very high at

peaks, especially at the hole edge, see Fig. 4.56. At valleys, the compressive stress is considerable as well. Due to TGO thickening, the normal tensile stress decrease at the hole edge, hence, crack initiation is more likely when the TGO layer is thin, which is the case for a gas turbine after thousands of hours operation. On the other hand, the normal stresses over valleys has switched from compression to tension range, which causes linkage of the cracks and finally delamination [23, 24]. As for shear stress at the hole edge Fig. 4.56b, the shear stress is higher for a thicker TGO, which shows the deteriorating effect of BC oxidation and formation of the TGO oxide layer. These results are in agreement with the simulations performed by P. Bednarz [23].

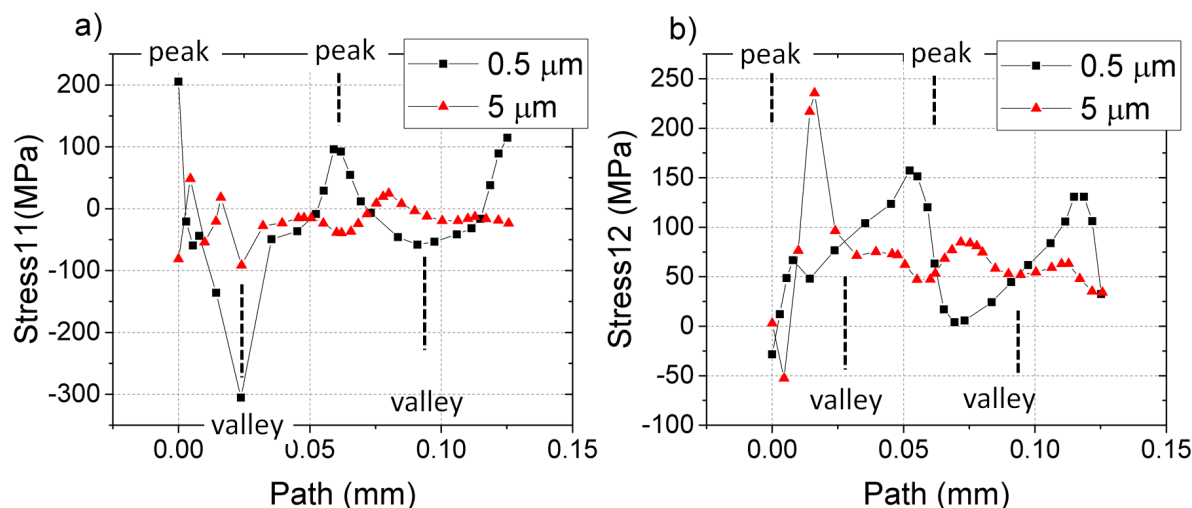


Figure 4.56: Comparison of stress distribution at TBC/BC interface in (a) normal and (b) shear direction as- received and oxidized TBC system.

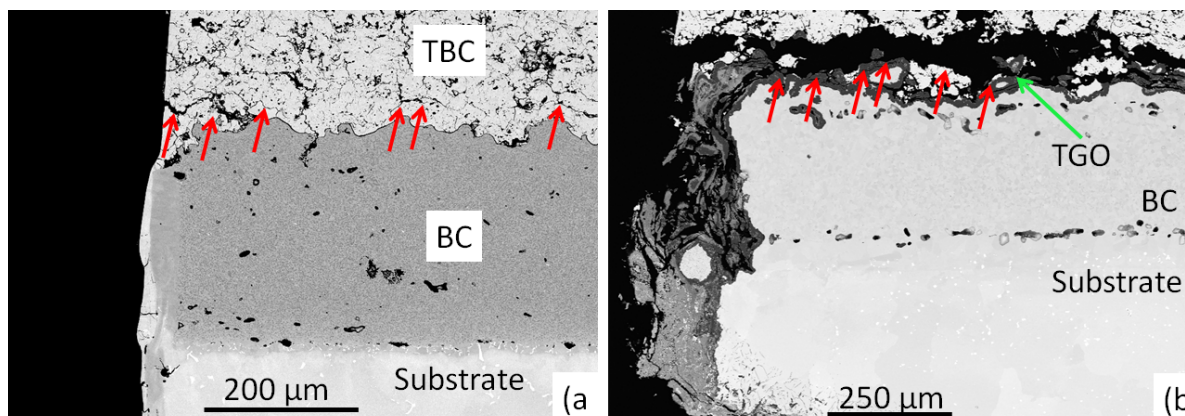


Figure 4.57: a) micro-cracks at the TBC/BC interface in TBC at the cooling hole wall as well as above peaks for a TBC coated IN 792, laser drilled with flash lamp using trepanation, (b) delamination crack at the TBC/BC interface propagated through TGO and TBC for a TBC coated IN 792 laser drilled with flash lamp using percussion mode and cyclic oxidized at 1050°C.

It was shown that normal stresses at the TBC/BC interface are higher for inclined holes, explaining one of the reasons for more critical situation of such holes verified

experimentally by the performed thermography measurements, see Fig. 4.5. As for the inclined holes, higher stresses are observed near the leading edge with the maximum stress slightly away from the edge. The influence of recast layers on the stress distribution at the hole was also studied. By considering the higher E-modulus of the dense TBC recast layer, it was observed that this recast layer increased the normal and shear stresses at TBC/BC interface for both vertical and inclined holes. The BC/substrate recast layer with a higher creep rate due to its much smaller grain size caused also higher stresses in BC at the BC/substrate interface. These observations are one of the reasons of the larger cracks observed with long-pulsed laser drilling with recast layers. These numerical results are helpful to obtain an understanding of the difference in the defect density of the TBC systems laser drilled with long-pulsed and ultra short pulsed laser methods, compare Fig. 4.3 and Fig. 4.4. The influence of oxidation and the formation of alumina scale between TBC and BC (TGO) on the stress distribution at the cooling hole was also studied. As long as the TGO is thin, the normal stresses at the hole wall as well as at peaks are higher compared with a thicker TGO. The micro-cracks at these spots have been shown for a TBC coated IN 792, laser drilled with flash lamp using trepanation mode in Fig. 4.57a by the red arrows. In case of a thicker TGO, the normal stresses at valleys are higher in the tensile region which contribute to coalescence of smaller cracks which have been initiated with thinner TGO. This leads to larger delamination cracks propagating at the TBC/BC interface through the TBC and TGO layers, which is shown by the red arrows in Fig. 4.57b. The shear stress at the hole wall also increased in case of a thicker TGO, where moving away from the hole the shear stress becomes less than in the case of a thinner oxide scale.

# Chapter 5

## Conclusion and Outlook

TBC coated nickel-based superalloys drilled with different laser methods as well as different angles were prepared and tested, in order to choose best laser drilling conditions for gas turbine applications.

First set of specimens were drilled with fiber laser, flash lamp laser, ultrashort pulsed laser or USP, and the quality of the holes were examined. Comparing the average crack lengths for each laser method, laser drilling of inclined holes caused larger cracks than vertical holes, which is as a result of the forces due to melt ejection and recoil pressure of assist gas during the laser drilling process, as well as the thermal stresses induced by the thermal mismatches of TBC, BC, and the superalloy [6, 109]. Inclined cooling holes, drilled using fiber laser, induced thicker recast layers compared with vertical holes [6]. Comparing percussion and trepanation drilling modes by fiber laser, the former caused larger cracks as well as larger recast thickness, probably due to its higher pulse energy. Trepanation drilling resulted in thinner recast layer which can be most likely related to its higher pulse intensity, i.e. energy per area, which helps to evaporate the melt out of the hole. Moreover, fiber laser with percussion mode caused larger defects at the hole compared with flash lamp laser, which is probably due to higher pulse frequency used for fiber laser drilling. On the other hand, USP laser drilling provided the best quality of the holes in terms of crack length and recast layer thickness, due to its ultra-short pulses.

A second set of specimens was drilled with different angles by flash lamp and fiber laser, and the specimens were cyclically oxidized with a hold time of 2 hours at 1050°C in order to understand the influence of cyclic oxidation. Cyclic oxidation tests were interrupted to perform thermography measurements, in order to examine the damage state of the coatings. These tests verified the more critical situation for inclined holes, where already delamination cracks could be observed at the leading edge as well as the side wall of the hole in the as-drilled state. Considering the direction of inclined holes, it was observed from the thermography images that delamination cracks were formed initially mainly at the leading edge and sidewalls and propagated over the next cycles. As expected, the oxidized area was larger for fiber laser percussion mode than trepanation mode. Moreover, the average oxidized area was larger for inclined holes, which is in agreement with previous findings. Two specimens with different cooling hole diameters, 0.5 mm and 1 mm, were also cyclically oxidized at 1050°C. However, no considerable influence of diameter on the life time of the TBC-coated superalloy under this loading condition could be observed.



LCF tests at 850°C were performed at two mechanical strain ranges, 0.67% and 0.38%, on a third set of specimens, i.e. undrilled and laser drilled TBC-coated nickel-based superalloys. The drilling process was performed by flash lamp laser method using trepanation mode as well as USP laser. The LCF tests were performed with a standard strain rate of 6%/min, and were stopped after 30% stress reduction with respect to the maximum stress. Based on the results, the specimens with cooling holes having negligible recast layer and defect density caused the minimum reduction of the life time, compared with undrilled specimens. USP laser drilling resulted in higher life time than flash lamp laser method, for specimens with vertical and inclined cooling holes.

The inclined cooling hole, laser drilled with USP laser, had a similar life time at the higher strain range, 0.67%, in comparison with undrilled specimen. The higher laser drilling quality of USP laser had the largest influence on the of life time of the specimens with inclined cooling holes, where the influence of stress concentration is probably less dominant as it is for vertical holes, making the quality of laser drilling more important. The specimens with vertical cooling holes had a shorter life time than the inclined cooling holes, due to a larger stress concentration effect, i.e. a smaller cross section of the specimen at the holes in comparison with the case of having inclined holes. This means that the superalloy is under higher stress concentration at the vertical cooling holes than the inclined ones. It should be mentioned than under cyclic oxidation, a more critical situation was observed for the inclined holes. Under this loading condition, the TBC/BC interface is the weakest spot, which has more damages around the inclined cooling hole due to the laser drilling process, compared with the case of a vertical hole.

Neither spallation nor a large scale delamination of TBC was observed at the failure after LCF testing, which is in agreement with literature results [3, 39]. A local delamination at the TBC/BC interface was merely found at the primary crack, which had led to a segmentation crack in the TBC. Such local delamination was larger for the higher strain range. For the undrilled specimen tested at the higher strain range, cracks were initiated at the uncoated inner surface of the superalloy as well as at the TBC/BC interface in the BC, which propagated perpendicular to the loading direction. Compared with the cracks at the TBC/BC interface, the cracks initiated at the uncoated inner surface of the superalloy had a larger length, suggesting that these cracks caused the failure. Regarding the specimens with inclined cooling holes tested at both strain ranges, the primary crack was observed to have initiated from the cooling holes, due to the laser-drilling induced defects as well as stress concentration. The specimen with USP-drilled cooling holes, tested at the higher strain range, experienced the same type of cracking, where the crack density on the hole compared with the other laser method was negligible, which emphasizes the influence of stress concentration effects.

A 3D FEM model was developed for a vertical and inclined hole in order to analyze the differences in stress distribution under thermal loading conditions. The model consisted of a visco-elastic TBC and substrate, as well as a visco-plastic BC. The model was numerically cooled down from the stress free high temperature state to room temperature. In comparison with vertical cooling holes, it was shown that especially normal stresses at TBC/BC interface are higher for inclined holes, explaining one of the reasons for more critical situation of such holes observed in cyclic oxidation experimental results. As for the inclined holes, the higher stresses are observed near the leading edge with the maximal stress slightly away from this edge, which can be observed only with a 3D model.



The 3D FEM model with recast layers was simulated under thermal loading conditions to understand the influence of such layers on stress distribution at the hole as well. It was observed that with the existence of such layers, the normal and shear stresses increase at TBC/BC interface for both vertical and inclined holes. This is one of the reasons of the larger cracks observed with long-pulsed laser drilling with recast layers.

Additionally, a sensitivity analysis regarding CTE, creep rate, elastic modulus, and TGO thickness was performed on a 2D FEM model under the same thermal loading as previous simulations. A TBC recast layer with various values for CTE was implemented in the FEM model, from which it was concluded that with higher CTE values, higher stresses at TBC/BC interface near the hole wall were induced. On the contrary, assigning different creep rates to the TBC recast layer did not have a large influence on stress distribution at this interface near the cooling hole. Moreover, the influence of creep rate, CTE, and elastic modulus was studied for BC/substrate recast layer at the BC/substrate interface near the cooling hole. In case of an existent recast layer at the cooling hole, higher normal and shear stresses in the BC at the BC/substrate interface were observed near the hole. The stresses in BC above the BC/substrate interface increased with the BC/substrate recast layer of a higher elastic modulus and creep rate.

The influence of oxidation, resulting in TGO growth, on the stress distribution near the cooling hole was also analyzed. With a thinner TGO, it was observed that there is a higher normal tensile stress at the hole which could initiate cracks. However, the shear stress increased at the hole edge with thickening of such layer, while moving away from the hole wall such stresses became smaller than that of thinner TGO. With a thicker TGO, normal tensile stresses at peaks decreased and normal compressive stresses at valleys shifted partly to tensile regions. The results are in agreement with those reported by Bednarz [23].

## Highlights

Key results of this thesis with respect to future gas turbine development are:

1. Among the different laser drilling methods investigated, USP drilling offers the best cooling hole quality with respect to
  - minimized recast layer formation
  - nearly no crack formation at TBC/BC and BC/substrate interface as well as at the grain boundaries of the superalloy at the hole.
  - uniformity of cooling hole diameter
2. Based on LCF investigations at low and high strain ranges, the life time of TBC-coated IN 792 with cooling holes generally decreases compared with undrilled components.
3. The type of laser drilling has a significant influence on the LCF-life. USP laser drilling shows the lowest reduction in LCF life of TBC coated IN 792.
4. Specimens with inclined holes showed longer LCF life time compared with those having vertical holes, probably due to a less stress concentration at the holes.

5. Comparing the TBC coated specimens laser drilled by percussion and trepanation drilling modes using fiber laser, the former caused larger cracks. By trepanation, the recast layer is observed to be thinner.
6. Percussion as well as inclined drilling caused stronger oxidation of BC during cyclic oxidation tests, in comparison with trepanation and vertical drilling, respectively.
7. For inclined holes, delamination was more critical under cyclic oxidation in comparison with vertical holes. Thermography images of thermally cycled inclined holes have shown that delamination occurs at the leading edge of the hole as well as at the sidewall near the edge, which is in agreement with the performed 3D FEM calculations of normal stresses at the TBC/BC interface for vertical and inclined cooling holes.
8. No influence of diameter could be observed for the specimens with 0.5 mm and 1 mm cooling holes after cyclic oxidation tests at 1050°C.
9. Based on the FEM calculations, recast layer increased the stresses at the TBC/BC as well as BC/substrate interfaces near the cooling hole.
10. Based on the FEM simulations, a thinner TGO induces higher normal stresses at the hole as well as at the peaks, where as a thicker TGO facilitates coalescence of smaller cracks which are formed in the previous phases.

## Outlook

The following works are suggested for future studies:

1. In-phase and out-of-phase thermomechanical fatigue tests with temperature gradient using an internal cooling air flow in order to simulate more effectively real operation conditions.
2. Simulation of stress development under LCF loading conditions with controlled cooling air flow and temperature gradient within the coated component

# Appendix A

## Additional Results

### A.1 Laser drilling of TBC systems

Below, microstructural images of the specimens drilled with flash lamp laser, percussion mode at different angles, are shown.

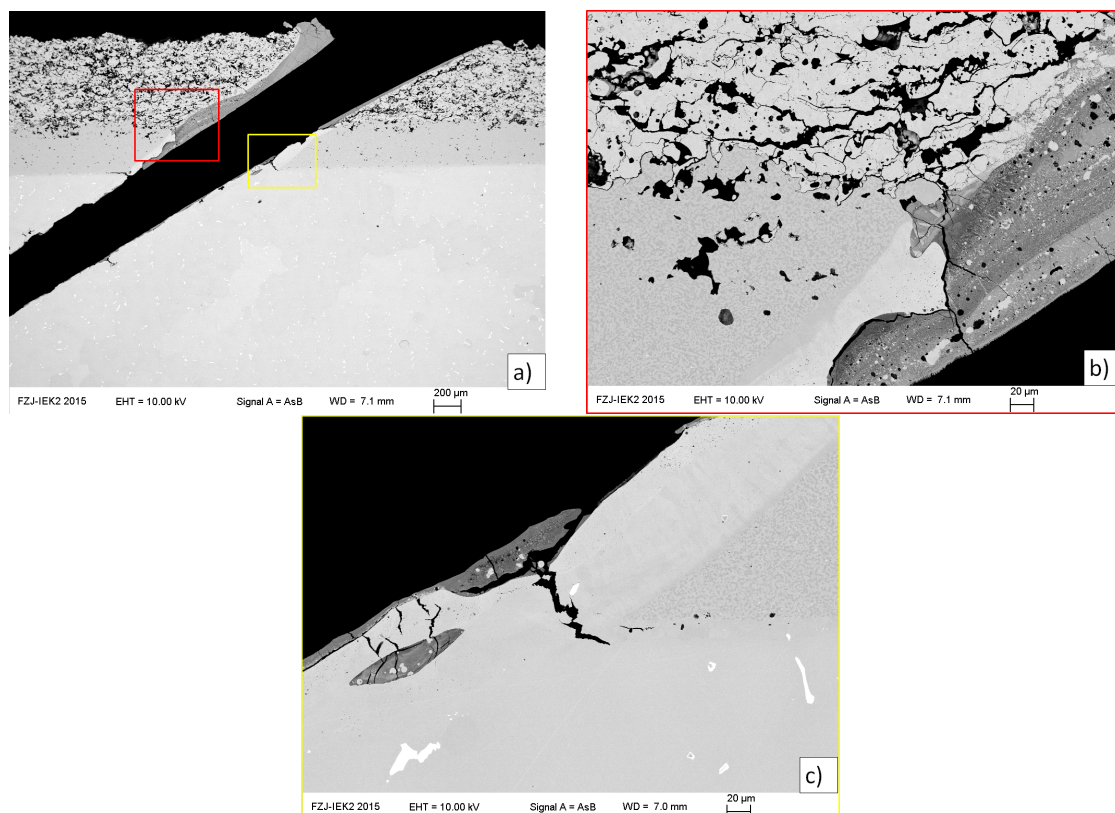


Figure A.1: a) SEM images of the specimen drilled at 30° angle with flash lamp, percussion mode, including the b) magnification of TBC-BC interface, and c) BC-substrate interface.

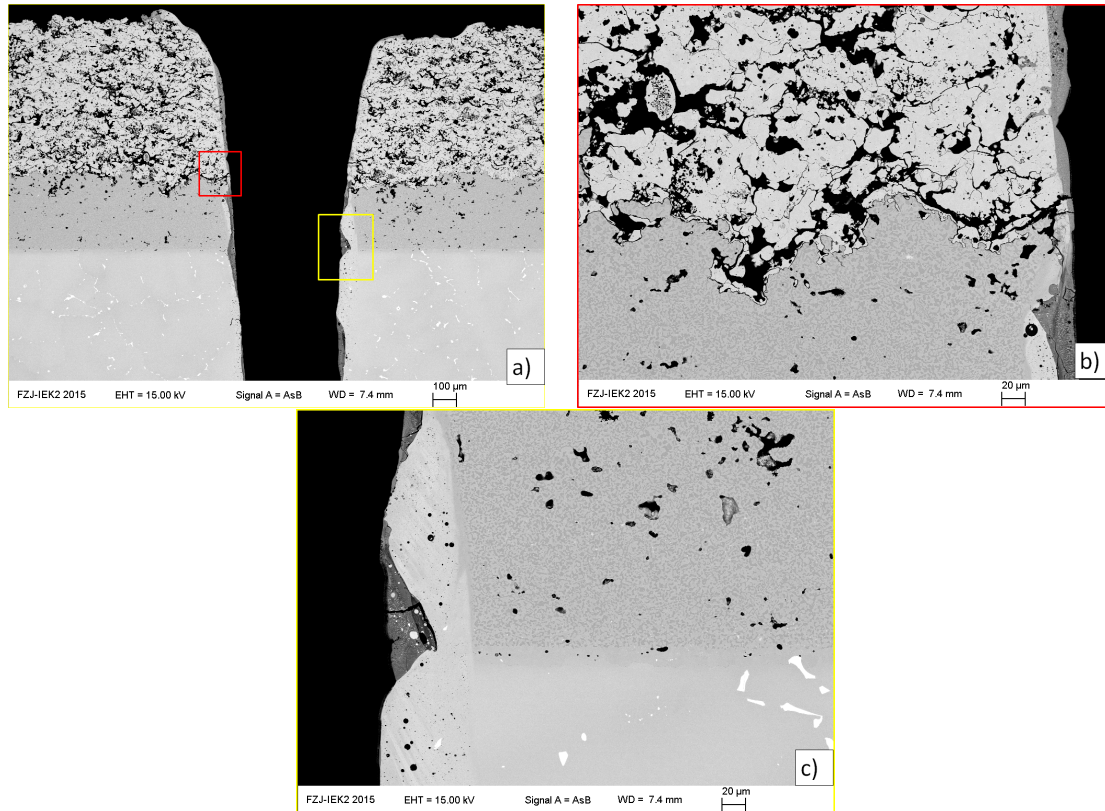


Figure A.2: a) SEM images of the specimen drilled at  $90^\circ$  angle with flash lamp, percussion mode, including the b) magnification of TBC-BC interface, and c) BC-substrate interface.

## A.2 Cyclic oxidation of laser drilled TBC systems

### A.2.1 Thermography measurements

In the following, thermography images of the specimens drilled with different methods are shown. As already explained in section 4.2.1., one can observe usually more critical situation for inclined holes, where delamination happens typically at both holes starting from earlier cycles. It can also be observed, taking the direction of the inclined holes, that delamination usually appear at the leading edge, showing the criticality of this position.

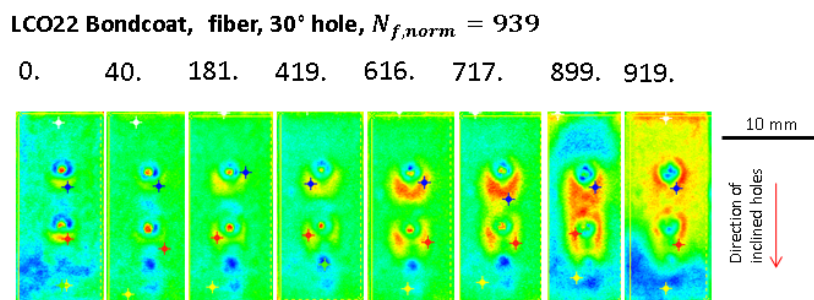


Figure A.3: Thermography images of the specimen drilled at 30° angle with fiber laser and LCO22 BC

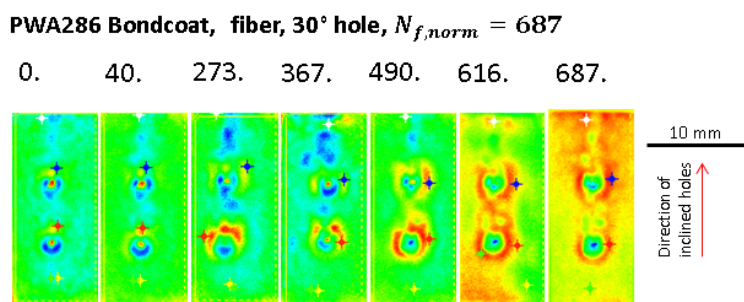
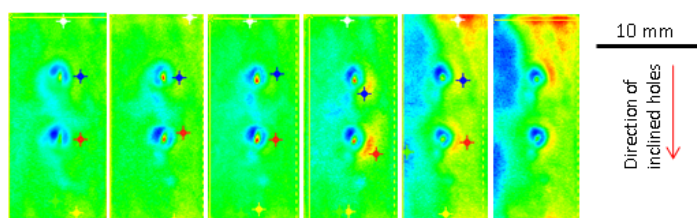


Figure A.4: Thermography images of the specimen drilled at 30° angle with fiber laser and PWA286 BC

**PWA286 Bondcoat, flash lamp, 30° hole,  $N_{f,norm} = 615$**

0. 38. 155. 425. 565. 615.



**PWA286 Bondcoat, flash lamp, 90° hole,  $N_{f,norm} = 615$**

0. 38. 155. 425. 490. 615.

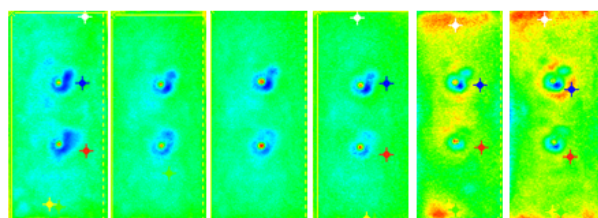


Figure A.5: Thermography images of the specimen drilled at 30° and 90° angle with flash lamp and PWA286 BC



### A.2.2 Microstructure analysis

In the following, SEM images of the specimens drilled with different laser methods are presented. Please note that only the initial state of the specimens drilled with flash lamp, percussion, and fiber laser, trepanation, with LCO22 BC have been available due to limited available specimens.

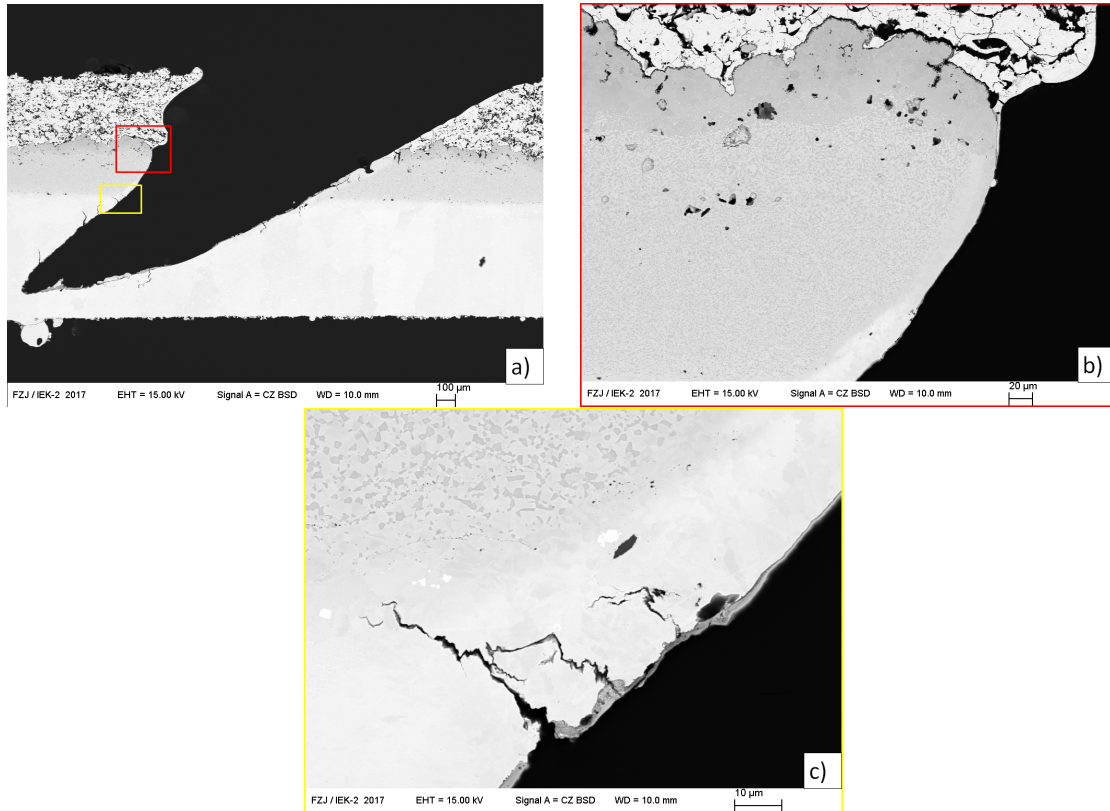


Figure A.6: As-received state of the specimen drilled at  $30^\circ$  angle with flash lamp and LCO22 BC

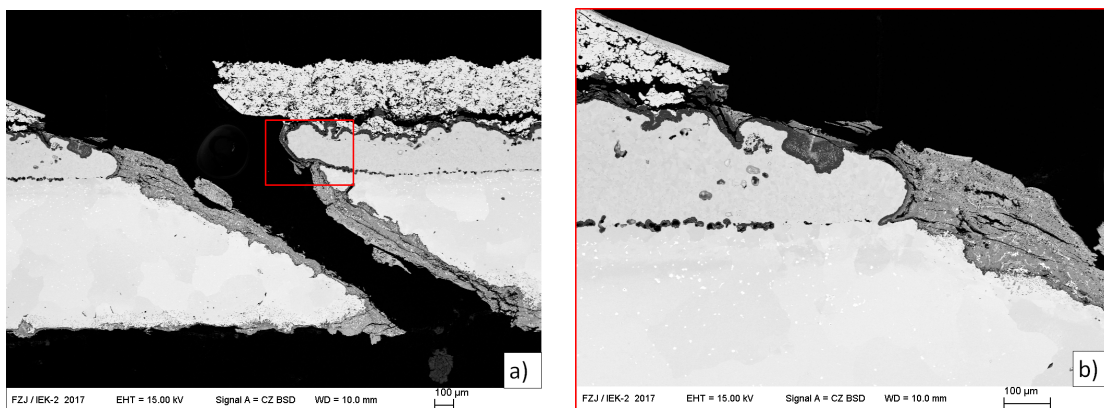


Figure A.7: Failure state of the specimen drilled at  $30^\circ$  angle with flash lamp and LCO22 BC

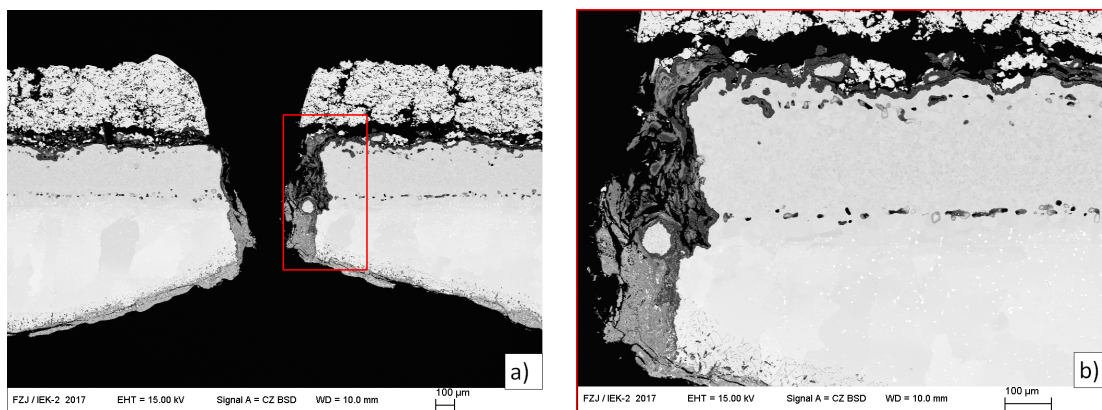


Figure A.8: Failure state of the specimen drilled at 90° angle with flash lamp and LCO22 BC

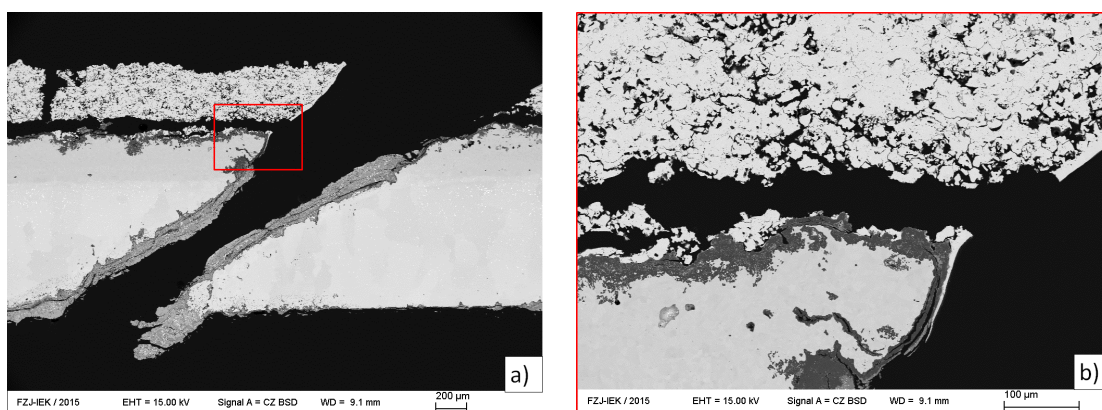


Figure A.9: Failure state of the specimen drilled at 30° angle with flash lamp and PWA286 BC

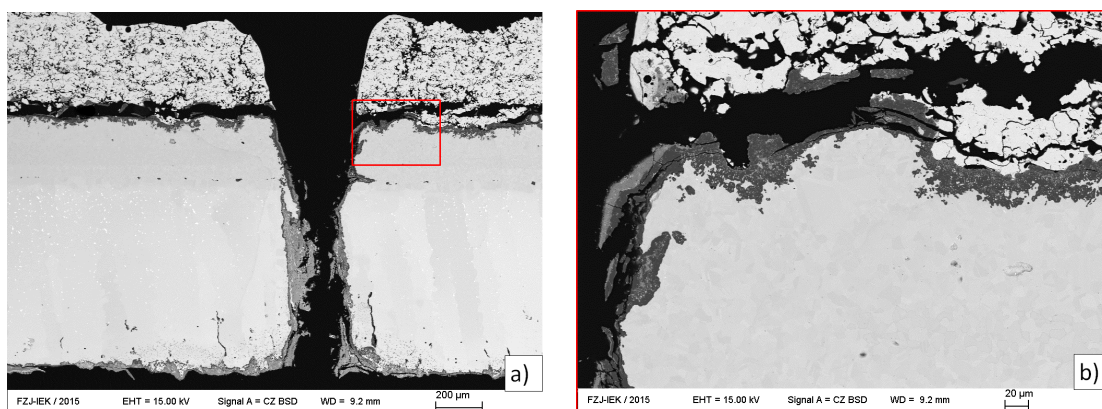


Figure A.10: Failure state of the specimen drilled at 90° angle with flash lamp and PWA286 BC

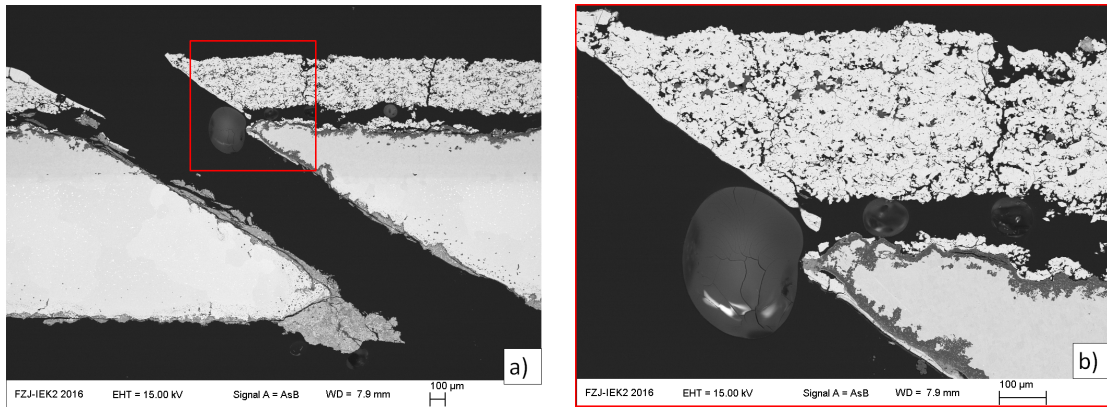


Figure A.11: Failure state of the specimen drilled at  $30^\circ$  angle with fiber laser, trepanation, and PWA286 BC

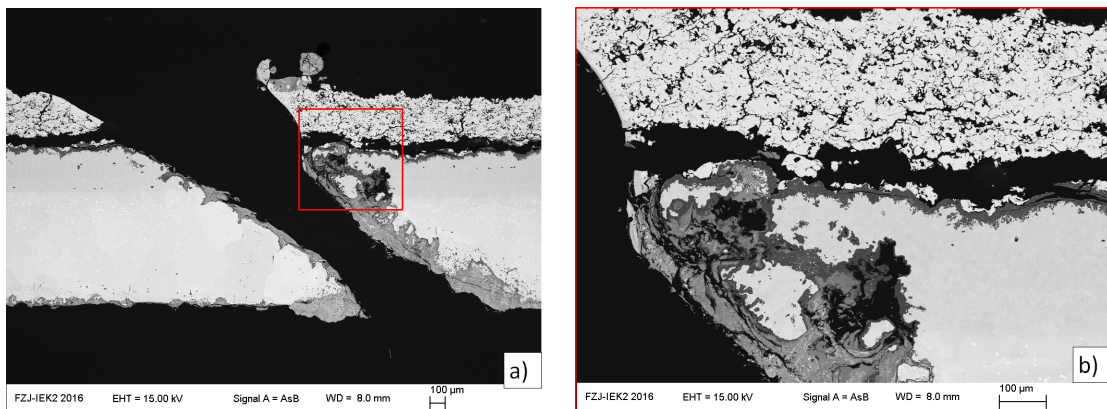


Figure A.12: Failure state of the specimen drilled at  $30^\circ$  angle with fiber laser, percussion, and PWA286 BC

# Bibliography

- [1] International Energy Agency. World energy outlook 2014 factsheet. pages 1–5, 2014.
- [2] P. Caron et al. Third generation superalloys for single crystal blades. *Procs. 6th Conf. on Materials for Advanced Power Engineering*, 53:897, 1998.
- [3] Jürgen J. Klabbbers-Heimann. Anwendungsgrenzen von modernen Nickelbasis-Superlegierungen in effusionsgekühlten Bauteilen zukünftiger Gasturbinen. PhD thesis, RWTH Aachen University, 2003.
- [4] M. Antar et al. High speed edm and laser drilling of aerospace alloys. *Procedia CIRP*, 42:526–531, 2016.
- [5] H.K. Sezer et al. An investigation into delamination mechanisms in inclined laser drilling of thermal barrier coated aerospace superalloys. *Journal of Laser Applications*, 17:225–234, 2005.
- [6] H.K. Sezer et al. Effect of beam angle on HAZ, recast and oxide layer characteristics in laser drilling of TBC nickel superalloys. *International Journal of Machine Tools and Manufacture*, pages 1972–1982, 2006.
- [7] G.D. Gautam et al. Pulsed Nd:YAG laser beam drilling: A review. *Optics Laser Technology*, 100:183–215, 2018.
- [8] N.I. Morar et al. Investigation of recast and crack formation in laser trepanning drilling of CMSX-4 angled holes. *The International Journal of Advanced Manufacturing Technology*, 95:4059–4070, 2018.
- [9] K.T. Voisey et al. Melt ejection during laser drilling of metals. *Materials Science and Engineering: A*, 356:414–424, 2003.
- [10] W.T. Chien et al. Investigating the recast layer formed during the laser trepan drilling of Inconel 718 using the Taguchi method. *International Journal of Advanced Manufacturing Technology*, 33:308–316, 2007.
- [11] C.Y. Yeo et al. A technical review of the laser drilling of aerospace materials. *Journal of Materials Processing Technology*, 42:15–49, 1994.
- [12] D. Ramanathan et al. Micro- and Sub-Micromachining of Type IIa Single Crystal Diamond Using a Ti:Sapphire Femtosecond Laser. *Journal of Materials Processing Technology*, 124:389–396, 2002.



- [13] M. Tanaka et al. Thermomechanical fatigue damage evolution in a superalloy/thermal barrier system containing a circular through hole. *Journal of the American Ceramic Society*, 94:128–135, 2011.
- [14] D.K. Das et al. Femtosecond laser machining of cooling holes in thermal barrier coated CMSX4 superalloy. *Journal of Materials Processing Technology*, 209:5661–5668, 2009.
- [15] E. Lugscheider et al. Laser Drilled Microholes in Zirconia Coated Surfaces using Two Variants to Implement the Effusion Cooling of First Stage Turbine Blades. *Advanced Engineering Materials*, 7:145–152, 2005.
- [16] Q. Feng et al. Femtosecond laser machining of single-crystal superalloys through thermal barrier coatings. *Materials Science and Engineering A*, 430:203–207, 2006.
- [17] J. Dietrich. Synchrone Produktivitäts- und Qualitätssteigerung beim Perkussionsbohren. PhD thesis, RWTH Aachen University, 2012.
- [18] R. Poprawe. Lasertechnik für die Fertigung: Grundlagen, Perspektiven und Beispiele für den innovativen Ingenieur. Springer, 2005.
- [19] Olena Trunova. Effect of thermal and mechanical loadings on the degradation and failure modes of APS TBCs. PhD thesis, RWTH Aachen University, 2006.
- [20] Mario Erhardt Schweda. Optimierung von APS-ZrO<sub>2</sub>-Wärmedämmschichten durch Variation der Kriechfestigkeit und der Grenzflächenrauigkeit. PhD thesis, RWTH Aachen University, 2013.
- [21] E. Tzimas et al. Failure of thermal barrier coating systems under cyclic thermomechanical loading. *Acta Materialia*, 48:4699–4707, 2000.
- [22] H. Aleksanoglu et al. Determining a critical strain for APS thermal barrier coatings under service relevant loading conditions. *International Journal of Fatigue*, 53:40–48, 2013.
- [23] P. Bednarz. Finite Element Simulation of Stress Evolution in Thermal Barrier Coating Systems. PhD thesis, RWTH Aachen University, 2007.
- [24] M. Ranjbar-Far et al. Simulation of the effect of material properties and interface roughness on the stress distribution in thermal barrier coatings using finite element method. *Materials and Design*, 31:772–781, 2010.
- [25] M. Ranjbar-Far et al. Impact of the non-homogenous temperature distribution and the coatings process modeling on the thermal barrier coatings system. *Materials and Design*, 32:728–735, 2011.
- [26] S. Wei et al. Lifetime prediction of plasma-sprayed thermal barrier coating systems. *Surface and Coatings Technology*, 217:39–45, 2013.
- [27] L. Wang et al. Finite element simulation of residual stress of double-ceramic-layer La<sub>2</sub>Zr<sub>2</sub>O<sub>7</sub>/8YSZ thermal barrier coatings using birth and death element technique. *Computational Materials Science*, 53:117–127, 2012.



- [28] Y. Jiang et al. Finite element modeling of residual stress around holes in the thermal barrier coatings. *Computational Materials Science*, 49:603–608, 2010.
- [29] T. Beck et al. Damage mechanisms and lifetime behavior of plasma-sprayed thermal barrier coating systems for gas turbines Part II: Modeling. *Surface and Coatings Technology*, 202:5901–5908, 2008.
- [30] ed. by J.R. Davis. Metallurgy, Processing, and Properties of Superalloys. ASM Speciality Handbook: Heat-Resistant Materials, 1997.
- [31] A. Szczotok et al. Effect of Heat Treatment on Chemical Segregation in CMSX-4 Nickel-Base Superalloy. *Journal of Materials Engineering and Performance*, 23:2739–2747, 2014.
- [32] T. Niendorf R. Bürgel, H.J. Maier. Handbuch Hochtemperatur-Werkstofftechnik. Springer Vieweg, 2011.
- [33] H.F. Aldinger et al. Einfluß von Lösungsglüh-temperatur auf das Umformverhalten und die Dauerfestigkeit von geschweißtem IN 718. *DGM-Informationsgesellschaft*, 7:391–396, 1996.
- [34] D.M. Shah et al. The Effect of Orientation, Temperature and Gamma Prime Size on the Yield Strength of a Single Crystal Nickel Base Superalloy. *TMS Superalloys, fifth international symposium*, 5:105–114, 1984.
- [35] Y.M. Wang-Koh et al. Understanding the yield behaviour of L12-ordered alloys. *Materials Science and Technology*, 33:934–943, 2016.
- [36] P. Beardmore et al. On the temperature dependence of the flow stresses of nickel-base alloys. *Transactions of the Metallurgical Society of AIME*, 245:1537–1545, 1969.
- [37] F.C. Campbell. Manufacturing Technology for Aerospace Structural Materials. Elsevier Science, 2006.
- [38] S. Heckmann. Eigenschaften von Schichtverbundsystemen unter isothermer LCF- und TMF-Belastung. Master's thesis, RWTH Aachen University, 1999.
- [39] S. Heckmann. Ermittlung des Verformungs- und Schädigungsverhaltens von Wärmedämmschichtsystemen. PhD thesis, RWTH Aachen University, 2003.
- [40] F. Schubert et al. Modelling of the mechanical behaviour of the single-crystal alloy CMSX-4 during thermomechanical loading. *Modelling and Simulation in Materials Science and Engineering*, 8:947–957, 2000.
- [41] S. J. Marz. Birth of an Engine Blade. *Machine Design*, pages 39–44, 1997.
- [42] W.J. Quadakkers et al. The significance of bond coat oxidation for the life of TBC coatings. *Elevated temperature coatings: Science and Technology*, 3:119–130, 1999.
- [43] I.G. Wright et al. Factors affecting the performance of bond coatings. *Turbomat*, 2002.

- [44] R. Anton et al. Untersuchungen zu den Versagensmechanismen von Wärmedämmschicht-Systemen im Temperaturbereich von 900°C bis 1050°C bei zyklischer Temperaturbelastung. PhD thesis, RWTH Aachen University, 2002.
- [45] N.S. Cheruvu et al. Evaluation, degradation and life assessment of coatings for land based combustion turbines. *Energy Materials: Materials Science and Engineering for Energy Systems*, 1:33–47, 2013.
- [46] W.J. Quadackers et al. Growth mechanisms of oxide scales on ODS alloys in the temperature range 1000–1100 °C. *Werkstoffe und Korrosion*, 41:659–668, 1990.
- [47] K.J. Kang et al. Creep properties of a thermally grown alumina. *Materials Science and Engineering A*, 478:154–162, 2008.
- [48] B. Gudmundsson et al. Structure formation and interdiffusion in vacuum plasma sprayed CoNiCrAlY coatings on IN 738 LC. *Materials Science and Engineering*, 100:207–217, 1988.
- [49] R. Kowalewski et al. Thermomechanische Ermüdung einer beschichteten, stengelkristallinen Nickelbasis-Superlegierung. PhD thesis, Erlangen-Nürnberg University, 1997.
- [50] G. Kerkhoff. Vergleich zwischen experimentell beobachteten Versagensmustern und berechneten Spannungsverteilungen in thermisch belasteten ebenen und gekrümmten 8YSZ Wärmedämmschichten. Technical report, Forschungszentrum Jülich, 2000.
- [51] H. Kirchner et al. Mechanisches Verhalten des Schutzschicht-Grundwerkstoff-Verbundes von Gasturbinenschaufeln unter zyklischer Beanspruchung. PhD thesis, TU Darmstadt, 1995.
- [52] H. Lau et al. Influence of bondcoat pre-treatment and surface topology on the lifetime of EB-PVD TBCs. *Surface and Coatings Technology*, 165(3):217–223, 2003.
- [53] M. Bartsch et al. Fatigue cracks in a thermal barrier coating system on a superalloy in multiaxial thermomechanical testing. *International Journal of Fatigue*, 30:211–218, 2008.
- [54] F. Mauget et al. Damage mechanisms in an EB-PVD thermal barrier coating system during TMF and TGMF testing conditions under combustion environment. *International Journal of Fatigue*, 99:225–234, 2017.
- [55] D. Schwingel et al. Mechanical and thermophysical properties of thick PYSZ thermal barrier coatings: correlation with microstructure and spraying parameters. *International Journal of Fatigue*, 108–109:99–106, 1998.
- [56] C. Fredin et al. Versagen von Plasmaspritzschichten aus Y<sub>2</sub>O<sub>3</sub>-stabilisiertem ZrO<sub>2</sub> zur Wärmedämmung im Motor unter Thermoschockbeanspruchung. *Tech. wiss. Ber. MPA Stuttgart*, 93/03:1537–1545, 1993.

- [57] H.B. Guo et al. Thermophysical properties and thermal cycling behavior of plasma-sprayed thick thermal barrier coatings. *Surface and Coatings Technology*, 192:48–56, 2005.
- [58] H.G. Scott et al. Phase relationships in the zirconia-yttria system. *Journal of Materials Science*, 10:1527–1535, 1975.
- [59] R. Vassen et al. The influence of the microstructure of thermal barrier coatings systems on sintering and other properties. *Proceedings of International Thermal Spray Conference*, pages 879–883, March 2002.
- [60] H. Salmang et al. *Keramische Werkstoffe*. Springer, 1983.
- [61] J. DeMasi-Marcin et al. Protective coatings in the gas turbine engine. *Surface and Coatings Technology*, 68/69:1–9, 1994.
- [62] R. Steinbrech et al. Thermomechanical behaviour of plasma sprayed thermal barrier coatings. *26th Annual Conference on Composites, Advanced Ceramics, Materials, and Structures*, pages 397–407, 2002.
- [63] G. Thurn et al. High-temperature deformation of plasma-sprayed zirconia thermal barrier coatings. *Materials Science and Engineering*, 233:176–182, 1997.
- [64] T.A. Cruse et al. Mechanical properties testing and results for thermal barrier coatings. *Journal of Thermal Spray Technology*, 6:57–66, 1997.
- [65] J.T. DeMasi et al. Thermal barrier coating life prediction model development, phase i. Technical report, NASA Lewis Research Center, 1989.
- [66] M. Beghini et al. Determination of thermal sprayed coatings elastic modulus using four point bending test. *WIT Transactions on Engineering Sciences*, 17, 1997.
- [67] G. Blandin. Thermomechanisches Verhalten von plasmagespritzten Schichtsystemen zur Wärmedämmung. PhD thesis, RWTH Aachen University, 2001.
- [68] M. Schütze. *Protective oxide scales and their breakdown*. Wiley, 1997.
- [69] A. Rabiei et al. Failure mechanisms associated with the thermally grown oxide in plasma-sprayed thermal barrier coatings. *Acta Materialia*, 430:3963–3976, 2000.
- [70] E.A.G. Shillington et al. Spallation failure of a thermal barrier coating associated with aluminium depletion in the bond coat. *Acta Materialia*, 47:1297–1305, 1999.
- [71] D.R. Clarke et al. Precursor to TBC failure by constrained phase transformation in the thermally grown oxide, in: Elevated temperature coatings. *Science and Technology*, 3:67–78, 1999.
- [72] H.E. Eaton et al. Sintering studies of plasma-sprayed zirconia. *Surface and Coatings Technology*, 32:227–236, 1987.

- [73] G. Thurn et al. Toughness anisotropy and damage behavior of plasma sprayed zirconia thermal barrier coatings. *Surface and Coatings Technology*, 123:147–158, 2000.
- [74] D. Zhu et al. Thermal conductivity and elastic modulus evolution of thermal barrier coatings under high heat flux conditions. *Journal of Thermal Spray Technology*, 9:175–180, 1999.
- [75] J.A. Thompson et al. Effect of heat treatment on the stiffness of zirconia top coats in plasma-sprayed TBCs. *Acta Materialia*, 49:1565–1575, 2001.
- [76] J.A. Thompson et al. Sintering of the top coat in thermal spray tbc systems under service conditions. pages 685–692, 2000.
- [77] G. Thurn et al. Hochtemperatureigenschaften und Schädigungsverhalten plasmagespritzter ZrO-Wärmebarrieren. PhD thesis, Universität Stuttgart, 1997.
- [78] A.J. Allen et al. Microstructural characterization studies to relate the properties of thermal spray coatings to feedstock and spray conditions. *Surface and Coatings Technology*, 146-147:544–552, 2001.
- [79] Sung R. Choi et al. Effect of sintering on mechanical and physical properties of plasma-sprayed thermal barrier coatings. *Journal of American Ceramic Society*, 88:2859–2867, 2004.
- [80] L. Hu et al. Effect of Sintering Temperature on Compressive Strength of Porous Yttria-Stabilized Zirconia Ceramics. *Ceramics International*, 36:1697–1701, 2010.
- [81] H. Echsler et al. Mechanical behaviour of as sprayed and sintered air plasma sprayed partially stabilised zirconia. *Materials Science and Technology*, 20:869–876, 2013.
- [82] D. Zhu et al. Sintering and creep behavior of plasma-sprayed zirconia- and hafnia-based thermal barrier coatings. *Surface and Coatings Technology*, 108-109:114–120, 1998.
- [83] D. M. Nissley et al. Thermal barrier coating life modeling in aircraft gas turbine engines. *Journal of Thermal Spray Technology*, 6:91–98, 1997.
- [84] Y. Yamazaki et al. The determination of the delamination resistance in thermal barrier coating system by four-point bending tests. *Surface and Coatings Technology*, 201:744–754, 2006.
- [85] Y. Yamazaki et al. Evaluation of interfacial strength by an instrumented indentation method and its application to an actual TBC vane. *Acta Metallurgica Sinica (English Letters)*, 24:109–117, 2011.
- [86] R. Herzog et al. Contribution to life prediction of thermal barrier coatings: a conception of accumulated damage. *Journal of Materials Processing Technology*, 117, 2001.
- [87] M. Li et al. Thermal shock behavior of EB-PVD thermal barrier coatings. *Surface and Coatings Technology*, 201:7387–7391, 2007.

- [88] A.N. Khan et al. Thermal cyclic behavior of air plasma sprayed thermal barrier coatings sprayed on stainless steel substrates. *Surface and Coatings Technology*, 201:4653–4658, 2007.
- [89] D. Zhu et al. Effect of layer-graded bond coats on edge stress concentration and oxidation behavior of thermal barrier coatings. Technical report, NASA Lewis Research Center, 1998.
- [90] J. N. Reddy. *An Introduction to Continuum Mechanics*. Cambridge University Press, 2007.
- [91] G.C. Chang et al. Behaviour of thermal barrier coatings for advanced gas turbine blades. *Surface and Coatings Technology*, 30:13–28, 1987.
- [92] R. Vassen et al. Development of a micromechanical life prediction model for plasma sprayed thermal barrier coatings. *Materials Science and Engineering A*, 303:100–109, 2001.
- [93] M. Bäker et al. A parametric study of the stress state of thermal barrier coatings, part ii: Cooling stresses. *Acta Materialia*, 53:469–476, 2005.
- [94] J. Cheng et al. Thermal/residual stress in an electron beam physical vapor deposited thermal barrier coating system. *Acta Materialia*, 46(16):5839–5850, 1998.
- [95] A. M. Freborg, B.L. Ferguson, W.J. Brindley, and G.J. Petrus. Modeling oxidation induced stresses in thermal barrier coatings. *Material Science and Engineering A*, 245:182–190, 1998.
- [96] M. Ahrens et al. Stress distributions in plasma-sprayed thermal barrier coatings as a function of interface roughness and oxide scale thickness. *Surface and Coatings Technology*, 161:26–35, 2002.
- [97] C.H. Hsueh et al. Residual stresses in thermal barrier coatings: effects of interface asperity curvature/height and oxide thickness. *Material Science and Engineering A*, 283:46–55, 2000.
- [98] M. Gupta et al. Influence of topcoat-bondcoat interface roughness on stresses and lifetime in thermal barrier coatings. *ASM International*, 23:170–181, 2013.
- [99] T. Bäcker et al. A guide to finite element simulations of thermal barrier coatings. *Journal of Thermal Spray Technology*, 26:1146–1160, 2017.
- [100] R. Eriksson et al. TBC bond coat–top coat interface roughness: Influence on fatigue life and modelling aspects. *Surface and Coatings Technology*, 236:230–238, 2013.
- [101] L. Wu et al. Numerical and experimental investigation of residual stress in thermal barrier coatings during APS process. *ASM International*, 23:653–665, 2013.
- [102] C.A. McNally et al. Laser drilling of cooling holes in aeroengines: state of the art and future challenges. *Materials Science and Technology*, 20:805–813, 2004.
- [103] H.W. Yankee et al. *Manufacturing Processes*. Pearson College Div, 1978.



- [104] M. Bass et al. *Laser Materials Processing*. Elsevier, 2012.
- [105] S. Dhar et al. A review on laser drilling and its techniques. *Proceedings: International Conference on Advances in Mechanical Engineering*, 2006.
- [106] Hermann Uchtmann. Modulares hybrides Laserstrahl-Bohren. PhD thesis, RWTH Aachen University, 2016.
- [107] J. Girardot et al. Investigation of delamination mechanisms during a laser drilling on a cobalt-base superalloy. *Journal of Materials Processing Technology*, 213:1682–1691, 2013.
- [108] K. T. Voisey et al. Laser drilling of cooling holes through plasma sprayed thermal barrier coatings. *Surface and Coatings Technology*, 176:296–306, 2004.
- [109] J. Kamalu et al. Variable angle laser drilling of thermal barrier coated Nimonic. *Journal of Materials Processing Technology*, 122:355–362, 2002.
- [110] Hermann Uchtmann. Vergleich von dioden- und blitzlampengepumpten Festkörperlasern zum Bohren mit Einzelpulsen. Master's thesis, RWTH Aachen University, 2011.
- [111] M. Grupp al. Faserlaser - Das energieeffiziente Werkzeug : Verschiedene industrielle Anwendungen im Überblick. *Laser Technik Journal*, 6:38–41, 2009.
- [112] K. Dou et al. Femtosecond study of surface structure and composition and time-resolved spectroscopy in metals. *Applied Physics A*, 76:303–307, 2003.
- [113] F. Dausinger. Femtosecond technology for precision manufacturing: Fundamental and technical aspects. *Proc. SPIE 4830, Third International Symposium on Laser Precision Microfabrication*, 4830:471–478, 2003.
- [114] Fiber to fiber coupling unit 1239. Technical report, Optoskand AB, Mölndal, Sweden, 2012.
- [115] M. Schweda et al. Thermal cycling damage evolution of a thermal barrier coating and the influence of substrate creep, interface roughness and pre-oxidation. *International Journal of Materials Research*, 103:40–49, 2012.
- [116] M. Bialas et al. Finite element analysis of stress distribution in thermal barrier coatings. *Surface and Coatings Technology*, 208:6002–6010, 2008.
- [117] J. Aktaa et al. Assessment of TBC systems failure mechanisms using a fracture mechanics approach. *Thin Solid Films*, 53:4399–413, 2005.
- [118] K. Sfar et al. Numerical investigation of residual stress fields and crack behavior in TBC systems. *Materials Science and Engineering A*, 333:351–360, 2002.
- [119] S. Widjaja et al. Modeling of residual stresses in a plasma sprayed zirconia/alumina functionally graded-thermal barrier coating. *Thin Solid Films*, 434:216–27, 2003.
- [120] J. Rösler et al. A parametric study of the stress state of thermal barrier coatings, Part I: creep relaxation. *Acta Materialia*, 52:4809–4817, 2004.

- 
- [121] D.N. Boccaccini et al. Influence of porosity on mechanical properties of tetragonal stabilized zirconia. *Journal of the European Ceramic Society*, 38:1720–1735, 2018.
- [122] A. Lasalmonie et al. Influence of grain size on the mechanical behaviour of some high strength materials. *Journal of Materials Science*, 21(6):1837–1852, 1986.
- [123] J.P. Sah et al. Grain-size effects during dynamic recrystallization of Nickel. *Metal Science*, 8(1):325–331, 1974.
- [124] W. Österle et al. Influence of heat treatment on microstructure and hot crack susceptibility of laser-drilled turbine blades made from Ren 80 . *Material Characterization*, 59:1564 – 1571, 2008.
- [125] A. Neidel et al. Hot cracking in the HAZ of laser-drilled turbine blades made from René 80. *Materials Testing*, 47:553–559, 2005.

# Acknowledgements

I wish to express my gratitude to Prof. Dr.-Ing. Lorenz Singheiser for making it possible for me to work on this project in the Institute of Energy and Climate Research, department of Mechanics of Materials (IEK-2), and supporting me throughout this challenging work. I would also like to thank Prof. Dr.-Ing. Manja Krüger for examining and giving helpful remarks on my work. I also thank Prof. Dr.-Ing. Bernd Markert, for accepting the chairmanship of the examination process. Many thanks go to my supervisor as well, Dr. Jürgen Malzbender for his great support.

I would also like to express my appreciation to Dr. Hermann Uchtmann and Dennis Haasler, from the Chair of Laser Technology in RWTH Aachen university, for helping me a lot regarding the experimental part of the work, and the friendly discussions. I am as well very grateful for the provided specimens and the helpful remarks by Dr. Werner Stamm from Siemens AG, as well as Dr. Roland Herzog from MAN Energy Solutions.

I am very thankful to my kind colleagues Harald Reiners, Alexander Moser, Daniela Liebert, Burkhard Werner, Dr. Egbert Wessel, Dr. Daniel Grüner, Volker Gutzeit, and Jörg Bartsch, for their great help and support regarding the performed experiments throughout this project. I want to acknowledge the friendly environment that my colleagues provided for me here in the institute, especially Marita Offermann, Torsten Fischer, Masoud Fakouri, and Goran Pecanac, to name a few.

The biggest gratitude I owe to my love, Medisa Jabbari, who kept believing in me and motivating me, made many beautiful moments during this period, and helped me with editing of this work, too. My wholeheartedly gratitude goes also to my friends, who made these years more pleasant.

As the last but not least, I want to thank enormously my parents and sisters, who have stayed always with me and kept faith in me.

# Lebenslauf

## Persönliche Daten

Vahid Ebrahimzade

Geb. am 28. 12. 1987, Esfahan, Iran  
verheiratet, iranisch

## Studium

- 10/2006–09/2011 Maschinenbau, B.Sc.,  
Technische Universität Isfahan, Iran, *Note: 2.3*,  
Schwerpunkt: Festkörpermechanik, Finite-Element-Methode
- 10/2011–07/2014 Computational Engineering, M.Sc.,  
Ruhr-Universität Bochum, *Note: 1.0*,  
Schwerpunkt: Finite-Element-Methode

## Wissenschaftliche Tätigkeiten

- 07/2010–03/2011 Finite-Elemente- und Schädigungsanalyse der Verbundwerkstoffe, Maschinenbau Fakultät, Technische Universität Isfahan
- 06/2012–03/2013 Modellreduktion, Surrogate Modellierung, studentische Hilfskraft, Lehrstuhl für Statik und Dynamik, Ruhr-Universität Bochum
- 10/2013–07/2014 Finite-Elemente-Analyse dynamischer Rekristallisierung in polykrystalline Materialien, Institut für Material-Theorie, Ruhr-Universität Bochum
- 10/2014–09/2019 Mechanische Untersuchung und Finite-Elemente-Simulation von lasergebohrten TBC-Systemen, Werkstoffstruktur und -eigenschaften (IEK-2), Institut für Energie und Klimaforschung, Forschungszentrum Jülich GmbH